Winter 1996

Numerical Simulation of Complex, Three-Dimensional, Turbulent-Free Jets

Robert V. Wilson
Old Dominion University

NUMERICAL SIMULATION OF COMPLEX, THREE-DIMENSIONAL, TURBULENT FREE JETS

By

Robert V. Wilson
B.S., June 1991, Old Dominion University
M.S., December 1993, Old Dominion University

A Dissertation submitted to the Faculty of
Old Dominion University in Partial Fulfillment of the
Requirement for the Degree of

DOCTOR OF PHILOSOPHY
MECHANICAL ENGINEERING

OLD DOMINION UNIVERSITY
DECEMBER 1996

Approved by:

Dr. Ayodeji O. Demuren (Director)

Dr. Dennis M. Bushnell

Dr. Tom L. Jackson

Dr. Arthur C. Taylor III.

Dr. Suren N. Tiwari

ABSTRACT

NUMERICAL SIMULATION OF COMPLEX, THREE-DIMENSIONAL, TURBULENT FREE JETS

Robert Vance Wilson
Old Dominion University, 1996
Director: Dr. Ayodeji O. Demuren

Three-dimensional, incompressible turbulent jets with rectangular and elliptical cross-section are simulated with a finite-difference numerical method. The full Navier-Stokes equations are solved at low Reynolds numbers, whereas at high Reynolds numbers filtered forms of the equations are solved along with a sub-grid scale model to approximate the effects of the unresolved scales. A 2-N storage, third-order Runge-Kutta scheme is used for temporal discretization and a fourth-order compact scheme is used for spatial discretization. Although such methods are widely used in the simulation of compressible flows, the lack of an evolution equation for pressure or density presents particular difficulty in incompressible flows. The pressure-velocity coupling must be established indirectly. It is achieved, in this study, through a Poisson equation which is solved by a compact scheme of the same order of accuracy. The numerical formulation is validated and the dispersion and dissipation errors are documented by the solution of a wide range of benchmark problems. Three-dimensional computations are performed for different inlet conditions which model the naturally developing and forced jet. The experimentally observed phenomenon of axis-switching is captured in the numerical simulation, and it is confirmed through flow visualization that this is based on self-induction of the vorticity field. Statistical quantities

such as mean velocity, mean pressure, two-point velocity spatial correlations and Reynolds stresses are presented. Detailed budgets of the mean momentum and Reynolds stress equations are presented to aid in the turbulence modeling of complex jets. Simulations of circular jets are used to quantify the effect of the non-uniform curvature of the non-circular jets.

ACKNOWLEDGEMENTS

I would like to express my deep gratitude to my advisor Dr. Ayodeji O. Demuren for his encouragement and valuable guidance during my research. His advice and encouragement in the final stages of this research is especially appreciated. In addition, I would also like to thank my technical monitor, Mr. Dennis Bushnell for his helpful comments that improved my research. I would like to thank Mr. Mark Carpenter of NASA Langley Research Center for providing consultation on the numerical formulation. My research has benefited through numerous fruitful discussions with Dr. Gordon Erlebacher of Florida State University. Flow visualization of the numerical results through animation was performed by Kwan-Liu Ma of the Institute for Computer Applications in Science and Engineering (ICASE) which was beneficial and greatly appreciated.

I gratefully acknowledge the financial support of the Government Student Researcher's Program (GSRP) at NASA Langley Research Center. In addition, I acknowledge the financial support of the Institute for Computational and Applied Mechanics (ICAM) which is funded by NASA Langley Research Center through grant number. LAG-1-363. Also, I am grateful to ICASE for the use of their computers and facilities which were always outstanding. The numerical simulations were performed on CRAY supercomputers at NASA Langley Research Center and the National Aerodynamic Simulator (NAS) at NASA Ames Research Center.

I would like to express my sincere thanks to my family for their help and support during the course of this research. In particular, my parents for always supporting me, my wife, Donna, for her endless patient and love, and to my daughter, Brittany, for all the joy she has brought me.

TABLE OF CONTENTS

LIST OF TABLES

LIST OF FIGURES

LIST OF SYMBOLS

Roman Symbols

a	coefficient of compact scheme
a_i	Fourier coefficient of velocity perturbation
a^M	coefficient of Runge Kutta scheme
A	coefficient matrix for Poisson equation
AR	aspect ratio
A_{xx}	LHS coefficient matrix for numerical approximation to second derivative
b	coefficient of compact scheme
b^M	coefficient of Runge Kutta scheme
B_{xx}	RHS coefficient matrix for numerical approximation to second derivative
c_{bl}	buffer layer parameter
C	coefficient of Smagorinsky model
D	jet diameter
D_e	equivalent jet diameter
f	general variable in filtering operation
f_{bl}	buffer layer factor
f_{cr}	buffer layer parameter
F	vector containing source terms for Poisson equation
F_i	normalized spectrum function
G	spatial filter
h_x, h_y	grid spacing in x and y coordinate directions
H_i	sum of convection and diffusion terms

i	imaginary number
k	wavenumber
L	individual block in A_{xx} coefficient matrix
L_x, L_y, L_z	computational domain dimensions in the x, y, z direction
M	sub-stage level
n	exponent of super-elliptic coordinate system
N	time level
p	instantaneous pressure
P	vector containing unknown pressure for Poisson equation
q_{ij}	anisotropic part of subgrid stress
Q	number of sub-stages of the Runge Kutta scheme
r	minimum directed distance
R	individual block in B_{xx} coefficient matrix
Re_{De}	Reynolds number based on equivalent jet diameter
S_{ij}	strain rate tensor
t	time
T	time interval
u, v, w	instantaneous velocity components
U, V, W	time-averaged velocity components
U_C, U_L, U_H	convective, ambient, and core velocities
u_j	velocity component in the jth direction
U_o	jet core velocity
x, y, z	streamwise, transverse, and lateral coordinates
x_{cr}	buffer layer parameter
x_j	spatial coordinate in the jth direction
$x_{1/2}$	buffer layer parameter

LIST OF SYMBOLS

Greek Symbols

α	perturbation wavenumber
γ	randomly generated phase angle
$\bar{\Delta}^2$	square of the length scale of subgrid model
Δt	time step
$\Delta x, \Delta y, \Delta z$	grid spacing
δ_{ij}	Kronecker delta function
θ	momentum thickness
λ	wavelength
ν	molecular viscosity
ν_t	turbulent viscosity
ϕ	pseudo pressure
Ω	region of the computational domain
ω	angular frequency

Chapter 1

INTRODUCTION

1.1 Motivation

Turbulent jets are present in many physical processes and technological applications. Turbulent jets can be found in combustors where the fuel and oxidizer are introduced as co-flowing jets, where the efficiency of such a process is largely determined by the mixing of the jets. Recently, jet aircraft noise has received much attention due to plans for a high-speed civil transport. A critical issue for the project's success is reducing jet noise to acceptable levels near populated areas. The belief is that acoustic patterns can be altered by manipulating the large scale structures in turbulent jet flows through external forcing. Non-circular jets can also be used to enhance the mixing of hot jet gases with the surroundings in aerospace applications and thus avoid aircraft detection. In industrial applications, efficient mixing is required to mix pollution issuing from smokestacks with the ambient surroundings to avoid its harmful effects.

In the laboratory, turbulent jets usually originate from a high pressure stagnation chamber. Typically, the flow is then expanded through either a contoured nozzle or an orifice plate which caps the stagnation chamber. The jet is then allowed to mix with the ambient surroundings and to develop in the streamwise direction.

Experiments have shown that three-dimensional (3-D) jets can be used to enhance mixing and entrainment rates compared to nominally two-dimensional (2-D) jets. A

fundamental understanding of the dynamics of complex, turbulent jets is required for their prediction and control. The present study is concerned with understanding the spatial evolution of incompressible 3-D jets in the near to medium field.

1.2 Survey of Previous Work - Experimental

Early experimental studies of three-dimensional, turbulent jets issuing from nozzles and orifices (Sforza et al. 1966, Trentacoste and Sforza 1967, and Sfeir 1976) revealed a phenomenon known as axis switching whereby the orientation of the jet major and minor axes at the nozzle exit switch at a downstream location.

Sforza et al. (1966) and Trentacoste and Sforza (1967) studied the mean flow of 3-D jets issuing from round, elliptical, and rectangular orifices of various aspect ratios. They characterized the streamwise development of the mean velocity using three distinct regions: *(i)* potential core, *(ii)* characteristic decay, and *(iii)* axisymmetric decay regions. In the potential core region, the mixing layer separating the jet core from the ambient surroundings at the orifice exit, has not spread to the jet centerline. As a result, the streamwise velocity near the jet centerline is constant in this region. In the second region, the velocity profiles in the plane containing the minor dimension of the orifice were found to be similar whereas those in the major plane are non-similar. Because the decay of centerline velocity was found to be dependent on orifice geometry, this region is referred to as the characteristic decay region. A third region is characterized by an axisymmetric decay of the centerline velocity which is proportional to the inverse of the streamwise coordinate. Velocity profiles in both major and minor planes were found to be similar and mostly independent of initial geometry. The results show that the length of the potential core region is roughly 5 diameters for rectangular and elliptical geometries of aspect ratio, AR = 10. The start of the axisymmetric decay region was roughly 50 diameters

downstream of the exit. Saddle-shaped streamwise velocity profiles (the maximum value occurs away from the jet centerline) were observed in the minor axis plane in the characteristic decay region. One axis switching was reported at 40 equivalent diameters downstream of the exit for the rectangular orifice of $AR = 10$.

Sfeir (1976) extended the earlier results by studying rectangular jets issuing from both nozzles and orifices for aspect ratios of $AR = 10$, 20, and 30. Axis switching and saddle-shaped velocity profiles were found for both orifice and nozzle jets. In general, jets from orifices showed axis switching locations closer to the exit when compared to jets from nozzles of equal aspect ratio. The saddle-shaped velocity profiles were more pronounced for jets from orifices.

Krothapalli et al. (1981) performed experiments of rectangular jets from a moderate aspect ratio nozzle, $AR = 16.7$ at Reynolds number of 12,000. In the characteristic or two-dimensional region, they found self-similar profiles for the mean velocity, Reynolds shear and normal stresses and a linear growth of the jet width in the minor axis plane. The shape of the self-similar profiles was found to be insensitive to aspect ratio, for $AR > 10$. However, the location where the self-similar profiles begin was found to be directly influenced by aspect ratio. Non-similar profiles were found in the major axis plane.

Tsuchiya et al. (1985) studied the effect of exit shape on the mean velocity field of rectangular jets of aspect ratios, $AR = 2$ and 5. Smoothly contoured nozzles of various lengths and sharp-edged orifices were utilized as exit shapes. Only the jets issuing from orifice configurations produced saddle-shaped velocity profiles. All three configurations produced at least one axis switching event with the orifice jet the closest to the jet exit. In a later study, Tsuchiya et al. (1989) reported the saddle-shaped velocity profiles in nozzle jets as well.

Ho and Gutmark (1987) studied jets issuing from elliptic nozzles with AR =2. Entrainment rates for the elliptic jet were found to be several times larger than equivalent area plane or axisymmetric jets. The increased entrainment rate was explained in terms of vortex induction due to the non-uniform azimuthal curvature of the shear layer. Fluid was found to be preferentially entrained at the minor axis plane as this portion of the vortex moved outward, thus resulting in an axis switching. Three such events were observed before the jet approached a circular shape.

Hussain and Husain (1989) extended the study of elliptic jets to include the effect of initial condition of the boundary layer at the jet exit plane, such as azimuthal variation of momentum thickness, turbulence level and effect of forcing. Axis switching was reported for up to 100 equivalent diameters. Subsequent studies explained the vortex ring pairing process (Husain and Hussain 1991) and the preferred mode coherent structure (Husain and Hussain 1993).

Zaman (1996) used azimuthal and streamwise vorticity dynamics to explain the presence (or absence) of axis-switching in low aspect ratio, AR =3, rectangular jets. The study also investigated the effect of adding vorticity generating tabs at the nozzle exit. It was shown that contracting nozzles upstream of the jet exit plane could produce two pair of counter-rotating streamwise vortices which eject fluid form the jet core to the ambient. This sense of rotation did not promote axis-switching within the measurement domain. Tabs placed on the short sides of the rectangular jet produced two pair of streamwise vortices which pump fluid from the ambient to the jet core resulting in rapid axis switching. Tabs placed on the long sides of the jet produced streamwise vortices of the same sense as that from contracting nozzles, resulting in no axis-switching.

Periodic forcing of the jet was shown to spatially organize the azimuthal vortex structures resulting in the first axis-switching location being closer to the jet exit when compared to the naturally developing jet. This was used to explain axis switching in supersonic screeching jets. The authors note that the effects of azimuthal and streamwise vorticity are not mutually exclusive and that the effect of streamwise vorticity pairs can either stop or augment axis-switching.

1.3 Survey of Previous Work - Analytical

Analytical techniques have been used to study non-circular jets in the literature. These methods fall roughly into two categories: *(i)* linear stability analysis, and *(ii)* vortex methods. In the former method, the governing equations are linearized about a base flow and the perturbation quantity is assumed to be composed of normal modes. The linear stability analysis of non-circular layers is more complex than nominally 2-D, plane shear layers due to the inherent three-dimensionality of the base flow.

The stability of elliptic jets was initially studied by Crighton (1973) using a vortex sheet model. Morris (1988) extended the analysis to finite thickness shear layers. Koshigoe and coworkers (Koshigoe and Tubis 1986, 1987, Koshigoe et al. 1987) studied the instability of circular and elliptical jets using a generalized shooting method. The studies showed that for elliptic jets, instabilities associated with the lower curvature portion of the jet boundary layer are dominate inferring that large scale coherent structures would form first in the minor axis plane.

Tam and Thies (1993) investigated instability waves of rectangular jets using a vortex sheet model which approximates the region very close to the jet exit where the boundary layer thickness is very small. The analysis identified four linearly independent families of instability modes based on mode shape (symmetry considerations). The authors found that

within each family, the first and third modes are associated with jet corner instability. The second mode is associated with instability of the mixing layers of the center of the flat sides of the jet. The second mode was found to have the largest spatial growth rate and is thus expected to be the dominate instability in rectangular jets.

The dynamics of isolated inviscid elliptic vortex rings was studied by Viets and Sforza (1972) and Dhanak and DeBernandis (1981) in an effort to model elliptic jets from nozzles. An analysis using the Biot-Savart law predicts induced velocity perpendicular to the plane containing the vortex core. The magnitude is proportional to the local curvature of the vortex tube, C, and the log of the inverse of the cross-sectional area, A; $\dot{x} \sim C\hat{b}\log(A^{-1})$, where $\hat{b}$ is the local bi-normal vector. Therefore, vortex tubes with high local curvature and small cross-sectional areas will experience larger induced velocities. The analysis predicts that an initially planar elliptic ring will become distorted and switch its major and minor axis. Axis switching in jet issuing from nozzles and orifices is considerably more complex due to viscous and turbulent diffusion, shear, entrainment, and flow instabilities.

1.4 Survey of Previous Work - Computational

Previous computational studies of three-dimensional free jets are reviewed in this section. In comparison to the available experimental studies, the number of computational studies in the literature is sparse.

Early attempts at a numerical solution of 3-D jet flow utilized the Reynolds Averaged Navier-Stokes (RANS) equations whereby the instantaneous Navier-Stokes equations are first time-averaged and a turbulence model is used to close the system of equations (the well-known closure problem). The RANS equations are then solved for the time-averaged velocity and pressure. This procedure was followed by McGuirk and Rodi (1979) in their study of 3-D free jets of aspect ratio, AR = 1, 5, 10, and 20. A $k-\varepsilon$ turbulence model was

used to close the system of equations. The flow was assumed to be parabolic in the streamwise direction, allowing the use of a spatial marching procedure in the downstream direction. While this procedure requires less CPU time and memory than an elliptic solution, a boundary layer analysis shows that the flow is only parabolic in the far field. The computations were unable to reproduce the experimentally observed axis switching and saddle-shaped velocity profiles. One axis switching event was predicted only after an ad-hoc specification of the lateral velocity components at the inflow of the computational domain was made. The saddle-shaped velocity profiles were never predicted. The authors attributed this deficiency to the $k-\varepsilon$ turbulence model which is incapable of capturing the effects of turbulence driven secondary motion.

Quinn and Militzer (1988) utilized a 3-D elliptic solution procedure to solve the RANS equations for the turbulent square jet from a sharp-edged orifice. Unlike the McGuirk and Rodi study, the velocity components at the inflow were specified from the author's experimental results, which were also presented in the paper. The computations were successful in predicting the decay of the centerline velocity in the medium to far field. Results in the near field, $x/D_e < 5$, were only qualitatively predicted, which the authors attributed to a relatively coarse grid. The experimental results showed off-centerline peaks of mean streamwise velocity in the near field, a faster spread rate when compared to a circular jet of equivalent area, and positive mean static pressure in the very near field at the jet centerline. Saddle-shaped profiles were also reported for the normal Reynolds stress components. Detailed velocity profiles from the numerical solution were not provided so that a comparison with the above mentioned trends is not possible.

Only in the last decade an unsteady numerical solution of the Navier-Stokes equations for 3-D jet flows has been possible. In the direct numerical simulation (DNS) approach, all scales of motion are resolved by the computational grid and no modeling is required. In

the large eddy simulation (LES) approach, the energy containing large scales of motion are resolved, while the unresolved small scales are modeled.

Grinstein and DeVore (1992) performed LES of spatially-developing square jets at moderate Reynolds numbers to study large scale coherent structures. The Euler equations of motion were solved (i.e. molecular viscosity is neglected) and an explicit filtering of the velocity was used as a minimal subgrid model for the unresolved scales of motion. The authors explain the jet dynamics in terms of the deformation, merging, and breakdown of initially planar square vortex rings. The deformation of the initially planar rings was attributed to the induced velocity due to azimuthal curvature present in the jet corners. The relative induced velocity results in the corners of the square ring moving ahead and towards the jet centerline, while the flat sides remain behind and move away from the centerline. The deformation results in a switching of the orientation of the square jet by 45^0 at an axial location downstream of the jet exit ($x/D_e \sim 0.8 - 1.0$). Flow visualization of the results revealed pairs of counter-rotating streamwise hairpin vortices in the high strain corner region between two adjacent vortex rings. Pairing of the vortex rings was accompanied by amalgamation of neighboring hairpin vortices which doubled their streamwise extent and led to the eventual breakdown of the rings. Subsequently, the flow was characterized by less organized, small scale vortices, indicative of fully turbulent flow.

Later studies (Grinstein 1993) focused on the LES of the very near field ($x/D_e < 5$) of a 2:1 aspect ratio rectangular jet. Thus, the experimentally observed axis switching at x/D_e = 7 is not captured in the author's computation. Other studies focused on the vorticity dynamics of isolated, rectangular vortex rings (Grinstein 1995) and the effects of compressibility and initial condition (Grinstein 1996).

Miller et al. (1996) performed simulations of non-circular jets at low Reynolds number (Re_D = 800) for a streamwise extent of x/D_e = 9. The jets are forced at the inflow plane with a single sinusoidal mode. Iso-surfaces of instantaneous vorticity magnitude show the flow to be laminar - i.e. composed of smooth, symmetrical structures. Axis-switching is predicted at x/D_e = 3.1 for the 2:1 *AR* elliptical jet and x/D_e = 6.3 for the 2:1 *AR* rectangular jet. Plots of centerline velocity reveal that the end of the potential core is not reached within the computational domain (0 - 9 D_e).

1.5 Summary of Literature Survey

General conclusions from the experimental and computational studies on non-circular jets in the literature are made in this section. Even though there are some conflicting opinions, trends are consistently observed in many experiments.

Early studies showed that the decay of centerline velocity in rectangular jets was characterized by three distinct regions: *(i)* potential core region, ending at roughly four to five diameters, where the centerline velocity is constant, *(ii)* characteristic decay region, ending at roughly 20 - 60 diameters (dependent on aspect ratio), where decay is dependent on initial geometry and profiles in the minor axis plane only are similar, and *(iii)* the axisymmetric region where the decay is proportional to the inverse of the streamwise coordinate and is mostly independent of initial condition. There is evidence that for jet with *AR* > 10, the axis switching location scales linearly with nozzle aspect ratio. The strong skewing of streamlines near the jet exit in orifice jets results in axis switching closer to the jet exit in comparison with equivalent nozzle jets. Pronounced saddle-shaped profiles for streamwise mean and fluctuating velocity were also observed with orifice jets. Less pronounced saddle-shaped profiles were observed for nozzle jets as well. Studies reveal that entrainment

and mixing in non-circular jets can be several times larger in comparison with equivalent area, circular jets. This increase occurs preferentially in the minor axis plane.

Linear stability analysis of rectangular jets indicate that instabilities associated with the center of the flat sides of the jet have larger spatial growth rates compared with corner modes and are thus expected to be dominant.

Numerical studies at lower Reynolds numbers ($Re_D \sim 800$) where the flow is laminar/ transitional, predict axis switching of non-circular jets forced with a single sinusoidal mode. The effect of the spectral content of the forcing function has not been addressed in such studies. Numerical simulation at higher Reynolds numbers are required for comparison with most jet experiments. Spatially-developing LES performed at higher Reynolds numbers are limited to the potential core region and single sinusoidal mode forcing. Axis switching for the rectangular or elliptic jet has not been simulated numerically at higher Reynolds number.

1.6 Objectives of the Current Study

The specific objectives of the current study are given in this section which attempt to address issues not covered in the literature. The objectives of the current study are enumerated below.

(i) Develop a higher-order accurate numerical formulation for the simulation of spatially-developing, unsteady, incompressible flows with improved resolution of high frequency modes.

(ii) Show the effect of initial condition on jet dynamics by altering the spectral content of the forcing function.

(iii) Simulate the potential core and characteristic decay regions of non-circular jets at higher Reynolds numbers ($Re_D \sim 10^5$).

(iv) Demonstrate axis switching at higher Reynolds numbers and explore the axis switching mechanism.

(v) Compute budget terms of the mean momentum and Reynolds stress equations which can be used in the turbulence modeling of complex jets.

A description of the organization of this study is now given. The governing equations for incompressible flow are presented in Chap. 2 along with the necessary subgrid stress model required for large eddy simulation. Boundary and initial conditions for the spatially-developing jet are also presented. The temporal and spatial discretization of the governing equations are presented in Chap. 3, while the details of the solution of the Poisson equation for pressure are presented in Chap. 4. The numerical formulation is validated in Chap. 5 through the solution of a variety of benchmark problems. Results of the direct numerical simulation of rectangular jets are presented in Chap. 6. In Chap. 7, results from the large eddy simulation of rectangular, elliptic, and circular jets at higher Reynolds number are presented, Finally, a summary and conclusions from the study are provided in Chap. 8.

Chapter 2

MATHEMATICAL FORMULATION

The equations governing the conservation of mass and momentum of an isothermal, incompressible, time-dependent fluid are developed in this section. The initial and boundary conditions for the spatially-developing jet are also given.

2.1 Governing Equations

Figure 2.1 shows the computational domain for the jet simulations along with the coordinate system and domain dimensions. The inflow boundary of the computational domain is located at a finite distance downstream of a hypothetical nozzle which produces a thin boundary layer separating the jet core from a stagnant freestream. It is assumed that the streamwise velocity makes a smooth transition from the jet velocity at the core to the ambient velocity and is thus modeled with the hyperbolic tangent function. The fluid then leaves the computational domain through the outflow boundary located a distance, L_x, downstream of the inflow boundary.

Freestream boundaries are located in the y and z coordinate directions where fluid is entrained into the jet. Unless otherwise specified, the governing equations and reported quantities will be normalized using the equivalent jet diameter at the inflow plane, D_e, as the length scale and the jet core velocity at the inflow plane, U_o, as the velocity scale. The equivalent diameter for the non-circular jet is defined as the diameter of a circle having the same area at the inflow plane. Time will be normalized using the time scale, D_e/U_o.

2.1.1 Continuity and Momentum Equations in Physical Space

The Navier-Stokes equations written in non-conservative form for an incompressible fluid are given in this section. The continuity equation in a Cartesian coordinate system written in indicial notation is given by:

$$\frac{\partial u_j}{\partial x_j} = 0 \tag{2.1}$$

where x_j, u_j, $j = 1, 2, 3$, represent the spatial coordinates and instantaneous velocities in the physical Cartesian coordinate system.

The non-dimensionalized momentum equation in a Cartesian coordinate system is given by:

$$\frac{\partial u_i}{\partial t} + u_j \frac{\partial u_i}{\partial x_j} = -\frac{\partial p}{\partial x_i} + \frac{1}{Re_{D_e}} \frac{\partial u_i}{\partial x_j \partial x_j} \tag{2.2}$$

where $Re_{D_e} = (U_o D_e)/\nu$ is the flow Reynolds number, p is the non-dimensional pressure, and ν the kinematic viscosity of the fluid. The momentum equation has three scalar components ($i = 1,2,3$).

The large eddy simulation (LES) approach is explored in this study, in which the large scales of turbulent motion are resolved while the smallest scales are not computed directly and are modeled in terms of the resolved scales. The filtering operation is defined by:

$$\bar{f}(\hat{x}) = \int_{\Omega} f(\xi) G(\hat{x} - \xi) d\xi \tag{2.3}$$

where the integration is extended over the computational domain, Ω, and the general variable f is filtered to yield the spatially averaged value, $\bar{f}$. The variable G, denotes a spatial filter which must satisfy the normalization constraint:

$$\int_{\Omega} G(\vec{x}-\vec{\xi})d\vec{\xi} = 1 \tag{2.4}$$

It is convenient to define a grid filter that commutes with spatial and temporal differentiation, such that:

$$\overline{\frac{\partial f}{\partial t}} = \frac{\partial \bar{f}}{\partial t} \tag{2.5}$$

$$\overline{\frac{\partial f}{\partial x}} = \frac{\partial \bar{f}}{\partial x} \tag{2.6}$$

Applying the grid filtering operation of Eq. (2.3) to the governing equations of motion, Eqs. (2.1) and (2.2), the filtered equations of motion are obtained as

$$\frac{\partial \bar{u}_j}{\partial x_j} = 0 \tag{2.7}$$

$$\frac{\partial \bar{u}_i}{\partial t} + u_j\frac{\partial \bar{u}_i}{\partial x_j} = -\frac{\partial \phi}{\partial x_i} + \frac{1}{Re_{D_e}}\frac{\partial \bar{u}_i}{\partial x_j \partial x_j} - \frac{\partial q_{ij}}{\partial x_j} \tag{2.8}$$

where $\phi = \bar{p} + (1/3)\tau_{kk}$ is the pseudo pressure, $\tau_{ij} = \overline{u_i u_j} - \bar{u}_i \bar{u}_j$ is the unresolved subgrid scale stress due to the non-linearity of the convection terms, and $q_{ij} = \tau_{ij} - (1/3)\delta_{ij}\tau_{kk}$ is the anisotropic part of the subgrid scale stress. The subgrid scale (SGS) models considered in this study are defined in the next section.

2.1.2 Subgrid Scale (SGS) Models

The purely dissipative model of Smagorinsky (1963) is used in the current study. The purpose of the SGS model is to account for the unresolved small scales. The Smagorinsky model has been applied to the LES of many turbulent flows such as homogenous isotropic flow, channel flow, and mixing layer flow. The Smagorinsky model has been one of the most popular SGS models for LES, partly because it correctly models the global transfer of energy from large to small scales. It provides an energy sink such that the large scale

energy is drained from the flow. However, it does not correctly model local effects such as solid boundaries and near-wall regions, localized transfer of energy from small scales to large scales, and laminar and transitional flows.

The anisotropic part of the subgrid stress is modeled in terms of the resolved scales using an eddy viscosity model due to Smagorinsky (1963):

$$q_{ij} = -2\nu_t \bar{S}_{ij} \tag{2.9}$$

where ν_t is the turbulent viscosity predicted by the SGS and $\bar{S}_{ij}$ the strain rate tensor of the resolved scales, given by

$$\bar{S}_{ij} = \frac{1}{2}\left(\frac{\partial \bar{u}_i}{\partial x_j} + \frac{\partial \bar{u}_j}{\partial x_i}\right) \tag{2.10}$$

The turbulent viscosity is given by

$$\nu_t = C\bar{\Delta}^2|\bar{S}_{ij}| \tag{2.11}$$

where $C = 0.01$, $\bar{\Delta}^2$ is the volume of the computational cell, and $|\bar{S}_{ij}| = \sqrt{2\bar{S}_{ij}\bar{S}_{ij}}$ is the magnitude of the resolved strain rate tensor.

2.1.3 Continuity and Momentum Equations in a Mapped Coordinate System

The governing equations given in Sec. 2.1.1 are mapped to an alternate coordinate system through the use of the chain rule which introduces "metric" terms. This approach has the potential for a more efficient use of grid points in resolving the thin boundary layer at the domain inflow. The velocity components are defined using the Cartesian coordinate system while the spatial gradients are defined in terms of the computational coordinate system with uniform grid spacing. The gradient terms can then be discretized using high-order compact finite difference schemes.

Consider the following general mapping of Cartesian coordinates (x_1, x_2, x_3) to the alternate coordinates $(\varepsilon_1, \varepsilon_2, \varepsilon_3)$:

$$\varepsilon_m = \varepsilon_m(x_1, x_2, x_3) \tag{2.12}$$

First derivatives in the Cartesian coordinate system are expressed in terms of derivatives in the alternate coordinate system using the chain rule:

$$\frac{\partial}{\partial x_j} = \frac{\partial \varepsilon_m}{\partial x_j}\frac{\partial}{\partial \varepsilon_m} \tag{2.13}$$

Upon expansion, Eq. (2.13) represents a sum of three products of metrics and derivatives. The Laplacian operator in the alternate coordinate system is expressed as

$$\frac{\partial}{\partial x_j \partial x_j} = \frac{\partial \varepsilon_m}{\partial x_j}\frac{\partial}{\partial \varepsilon_m}\left(\frac{\partial \varepsilon_n}{\partial x_j}\frac{\partial}{\partial \varepsilon_n}\right) \tag{2.14}$$

Equation (2.14) involves 18 terms upon expansion. It is understood that the term $\partial/\partial\varepsilon_m$ operates on the term in parenthesis. Equations (2.13) and (2.14) are used to express spatial gradients appearing in the continuity and momentum equations in terms of gradients in the alternate coordinate system. The continuity equation in the alternate coordinate system is given by

$$\frac{\partial \varepsilon_m}{\partial x_j}\frac{\partial u_j}{\partial \varepsilon_m} = 0 \tag{2.15}$$

The momentum equation in the alternate coordinate system is given by

$$\frac{\partial u_i}{\partial t} + u_j\frac{\partial \varepsilon_m}{\partial x_j}\frac{\partial u_i}{\partial \varepsilon_m} = -\frac{\partial \varepsilon_m}{\partial x_i}\frac{\partial p}{\partial \varepsilon_m} + \frac{1}{Re_{D_e}}\frac{\partial \varepsilon_m}{\partial x_j}\frac{\partial}{\partial \varepsilon_m}\left(\frac{\partial \varepsilon_n}{\partial x_j}\frac{\partial u_i}{\partial \varepsilon_n}\right) \tag{2.16}$$

The non-linear terms present in the momentum equation preclude the exact solution of the governing equations which must be solved numerically. The numerical approximations to the governing equations are given in Chap. 3.

The continuity and momentum equations represent four scalar equations for the four unknown variables (three velocity components in the Cartesian coordinate system and pressure). In the next chapter it is shown that the continuity equation is enforced through the solution of a Poisson equation for pressure. The Poisson equation is obtained by taking the numerical divergence of the discretized momentum equation.

2.2 Boundary Conditions

In order to define a well posed problem, the boundary and initial conditions for the jet simulations are defined. The ellipticity in the spatial terms of the governing equations requires that boundary conditions be defined at all boundaries. A diagram of the boundary conditions is provided in Fig 2.1.

2.2.1 Streamwise Inlet Boundary Conditions

In the laboratory, jet flows are commonly generated by the use of a fan which forces fluid along an enclosed nozzle. The jet leaves the exit plane of the nozzle where it interacts with the ambient fluid. Prior to exit, the jet can be considered as a relatively uniform freestream and a curved boundary layer at the walls of the nozzle. A short distance downstream of the nozzle exit, the boundary layer is smoothed so that the mean streamwise velocity can be modeled using the hyperbolic tangent (tanh) function. The inflow boundary of the computational domain is placed at a short distance downstream of the nozzle exit which is not actually included in the jet simulations.

(a) Mean Inlet Boundary Conditions

The mean or time-averaged streamwise velocity component, U, at the inflow boundary is given by

$$U(0, y, z) = U_c + \frac{(U_H - U_L)}{2} \tanh\left(\frac{r}{2\theta_o}\right) \tag{2.17}$$

where $U_C = (U_H + U_L)/2$ is the convective velocity and U_H and U_L represent the velocities of the jet core and ambient fluid, respectively. The quantity, r, represents the minimum directed distance from the point, $(0, y, z)$ to the line of constant convective velocity of the boundary layer (see Fig. 2.2). Thus, the shape of the line of constant convective velocity determines the jet geometry at the inflow plane. A super-elliptic equation was used to specify all jet geometries in this study:

$$\left(\frac{z}{a}\right)^n + \left(\frac{y}{b}\right)^n = 1 \tag{2.18}$$

where $a = AR*b$ and b represents the semi-major and minor dimensions of the constant convective velocity contour, and n is the exponent in super-elliptic coordinate system. For example, $n = 2$ defines an elliptic contour, while $n >> 1$ defines a rectangular contour with slightly rounded corners. The momentum thickness of the boundary layer at the inflow plane, θ_o is used to normalize the directed distance, r. If the point $(0, y, z)$ is "outside" the boundary layer contour as in Fig. 2.2, r is defined to be negative, while r is defined to be positive if the point lies on the inside of the boundary layer contour. Equation (2.17) produces a constant thickness boundary layer if the momentum thickness, θ_o, is constant at all azimuthal positions along the boundary layer. Non constant thickness boundary layers are generated by specifying the desired variation of θ_o along the contour of the boundary layer.

The mean streamwise velocity at the inflow plane is specified by defining the jet core and ambient velocities (U_H and U_L) and the momentum thickness of the shear layer, θ_o in (2.17). For this study $U_H = 1$, $U_L = 0.01$, and $D_e/\theta_o = 30$, which models the experimental jet profile a short distance ($x/D_e < 1$) downstream from a contoured nozzle. For elliptic jets the value of the exponent of the super elliptic coordinate system is $n = 2$, while for the rectangular jet, $n = 10$ is used which slightly rounds the corners (see Fig. 7.9a). This also models experimental jets where viscous diffusion is known to smooth the shear layer exiting from rectangular nozzles at the sharp corners. The mean transverse velocity components at the inflow plane are set to zero.

(b) Forced Inlet Boundary Conditions

In an effort to model jet experiments, a time dependent forcing function of low intensity is added to the mean velocity components at the inflow boundary to promote unsteady motion. At higher Reynolds numbers and computational lengths, it is speculated that small round-off errors would grow to produce unsteady motion of the unstable shear layers, thus obviating the need for forcing functions.

Two classes of perturbations are used in the current study; *(i)* sinusoidal perturbations of a specified frequency and *(ii)* perturbations having an experimentally measured velocity spectrum and transverse root mean square (*rms*) value, i.e.,

(i) Perturbations from linearized viscous stability theory

The first class of perturbations is derived from the solution of the Orr-Sommerfeld equation (OSE) which governs the instability of the reference hyperbolic tangent profile to spatially developing disturbances. The details of the solution of the OSE are presented in Wilson and Demuren (1996) with the general form of the perturbation velocities being:

$$\tilde{u}(y,t) = \text{Real}\{\phi'(y)e^{i\omega t}\},\quad \tilde{v}(y,t) = \text{Real}\{-i\alpha\phi(y)e^{i\omega t}\} \tag{2.19}$$

where α, $\phi(y)$, ω represent the perturbation wavenumber, eigenfunction, and angular frequency, respectively. The variables, y and t represent the transverse coordinate and time, respectively, while $i = \sqrt{-1}$. The stability equations are solved for the plane mixing layer and the resulting eigenfunctions are adapted to non-circular jets by replacing the transverse coordinate, y, in Eq. (2.19) with the minimum directed distance, r.

(ii) Random perturbations from experimental data

Perturbations which have a broad spectrum are generated based on experimental data for a plane mixing layer. The velocity power spectra and root-mean-square *(rms)* perturbation levels were taken from the experiment of Spencer and Jones (1971). Because phase information is not included in the power spectra, a random phase relationship for the modes comprising the spectra was assumed. The velocity perturbations are found by performing a Fourier transform of the complex Fourier coefficients, $a_i(y,f)$, defined by:

$$a_i(y,f) = \left[\frac{F_i(y,f)\overline{\tilde{u}_i^2}T}{4\pi^2}\right](\cos\gamma(y) + i\sin\gamma(y)) \tag{2.20}$$

where $F_i(y,f)$, $\overline{\tilde{u}_i^2}$, T, and $\gamma(y)$ represent the normalized spectrum function, the *rms* level of the i_{th} velocity component, time interval of the simulation, and the randomly generated phase angle, respectively. The velocity perturbations for the mixing layer represented by Eq. (2.20) are adapted to non-circular jets by replacing the transverse coordinate, y, with the minimum directed distance, r. The complete details of the derivation of time-dependent inlet boundary conditions based on a experimentally measured spectra are given in Wilson (1993).

The random inlet boundary conditions are the spatial analog to the random perturbations generated for initial conditions in temporal simulations. Figure 7.1a shows representative time traces and power spectra for the broad mode forcing function.

It is widely accepted that the proper boundary condition for the Poisson equation for pressure (derived in the next chapter) is the Neumann boundary condition (Gresho and Sani 1987). This condition is derived by applying the normal component of the momentum equation at the boundary. Applying the $i = 1$ component of Eq. 2.2 and solving for the pressure gradient term results in Neumann condition for pressure at the inflow:

$$\left[\frac{\partial p}{\partial x_i}\right]_o = \left[-\frac{\partial u_1}{\partial t} - u_j\frac{\partial u_1}{\partial x_j} + \frac{1}{Re_{D_e}}\frac{\partial^2 u_1}{\partial x_j \partial x_j}\right]_o \tag{2.21}$$

where the subscript "o" is used to denote the inflow boundary plane. The first term on the RHS of Eq. 2.21 is known from the inflow velocity boundary conditions, and the second and third terms are also known before the solution of the Poisson equation as will be shown in the next chapter.

2.2.2 Streamwise Outflow Boundary Condition

A characteristic analysis of the governing elliptic differential equations reveals no real characteristic curves along which disturbances travel. A disturbance is instead propagated in all directions at once. As a result, the solution of elliptic partial differential equations requires the specification of boundary conditions along the entire boundary. Boundary conditions are well defined at the inflow plane and can be reasonably approximated at the freestream boundary which is placed a large distance from the jet dynamics at the centerline. However, the conditions at the outflow boundary are not known a prior and must be

specified such that those errors do not adversely affect the accuracy in the interior of the domain.

Sources of ellipticity in the governing equations that link errors at the boundary to the interior can be traced to pressure and viscous terms. In addition, it is possible to convect errors from the outflow to the interior if flow reversal occurs. The source term for the Poisson equation for pressure also links outflow errors to the interior.

A technique which breaks the link between errors at the outflow boundary and the interior solution is the buffer domain technique proposed by Streett and Macaraeg (1990). This technique is adapted to the current jet simulations whereby the ellipticity of the governing equations is eliminated in a small region (called the buffer layer) which is appended to the solution domain at the outflow. Practically, this is achieved by a factor which turns off those elliptic terms in the buffer layer. The resulting momentum equation becomes:

$$\frac{\partial u_i}{\partial t} + [f_{bl}u_j + (1-f_{bl})U_j]\frac{\partial u_i}{\partial x_j} = -\frac{\partial p}{\partial x_i} + \frac{f_{bl}}{Re_{D_e}}\left(\frac{\partial^2 u_i}{\partial x_1^2}\right) + \frac{1}{Re_{D_e}}\left(\frac{\partial^2 u_i}{\partial x_2^2} + \frac{\partial^2 u_i}{\partial x_3^2}\right) \qquad (2.22)$$

where f_{bl} is the buffer layer factor which gradually changes from unity in the solution domain to zero in the buffer layer through the following function:

$$f_{bl}(x_1) = \frac{1}{2}\{1 - \tanh[c_{bl}(x_1 - x_{1/2})]\} \qquad (2.23)$$

where $c_{bl} = \ln[f_{cr}/(1-f_{cr})]/(2(x_{cr}-x_{1/2}))$ is a constant which controls the rate of transition between the solution and buffer domains while $x_{1/2}$ controls the transition location. For the simulations presented in Chaps. 6 and 7, the following buffer layer parameters are used, $f_{cr} = 0.99999$, $x_{cr} = 0.99L_x$, and $x_{1/2} = 0.9L_x$. This results in a computational domain length of ten diameters and a buffer domain length of two diameters. The convection

velocity in the buffer domain, U_j, is computed from the time-averaged velocity as the computation progresses. In addition, the source term for the Poisson equation for pressure is gradually forced to zero in the buffer domain through the same function. Zero gradient boundary conditions for all velocity components and the pressure are then applied at the outflow.

2.2.3 Freestream Boundary Conditions

The freestream boundary of the jet simulations is located at a large distance from the jet centerline such that the developing structures do not cross this far-field boundary. This permits the freestream boundary to be modeled as a zero-traction boundary where pressure is set to zero and the gradients of the instantaneous velocity field are set to zero in the transverse and lateral directions:

$$p = 0 \tag{2.24}$$

$$\frac{\partial u_i}{\partial n} = 0 \tag{2.25}$$

where n denotes the direction normal to the freestream boundary.

2.3 Initial Conditions

A spatial simulation of turbulent jet flow is performed in this study where a fixed region of the flow is computed and disturbances grow in the streamwise direction. This can be contrasted with a temporal simulation where a small region of the flow is followed in time and the domain moves in the streamwise direction.

As a result of the spatial reference frame, initial conditions are of minor importance because they are quickly convected out of the domain and the dynamics of the jet flow are determined by the forcing functions applied at the inflow plane. Simulations are started on

coarse grids with the velocities specified at the inflow plane used to initialize the velocity field in the interior at $t = 0$. After several flow through times (the time required for a fluid particle to convect from the inflow to the outflow plane at the convective velocity, U_C) the initial conditions are "washed" from the domain. Simulations on finer grids are started from results on coarser grids by prolongating the results using a standard, second-order accurate interpolation formula.

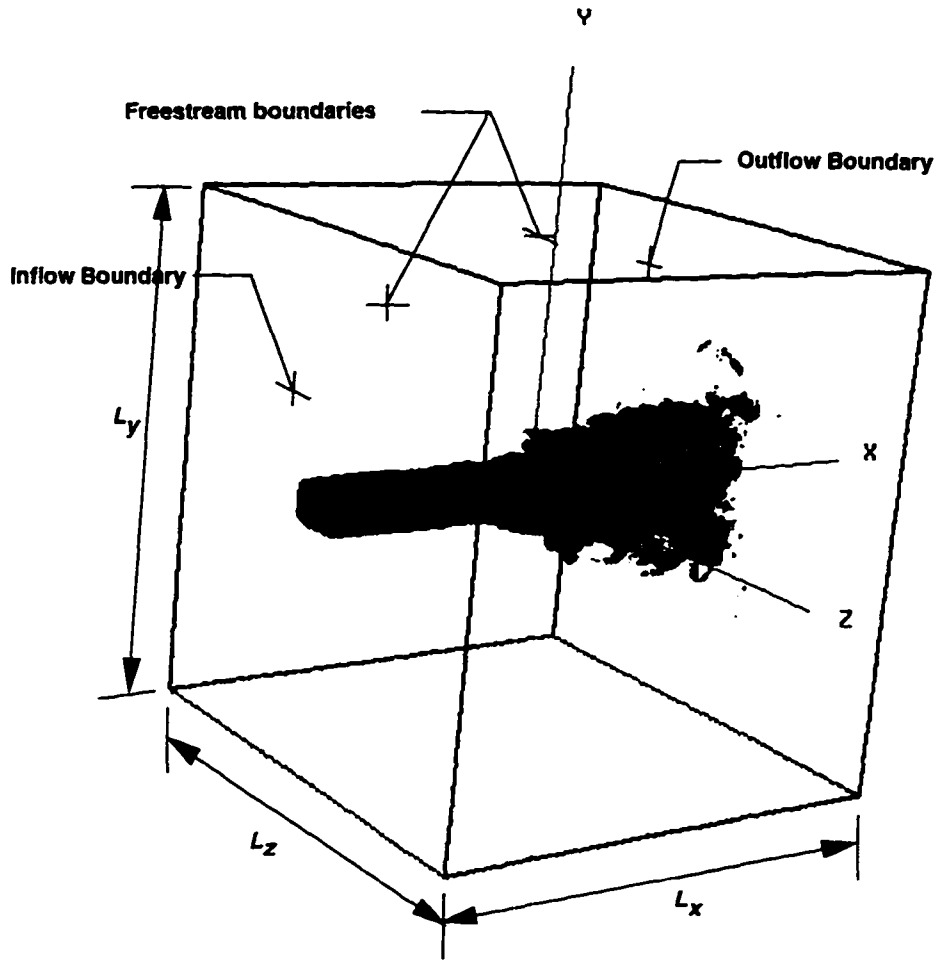

Fig 2.1 **Computational domain and coordinate system for the spatially-developing jet (iso-surface of vorticity magnitude from LES of rectangular jet shown).**

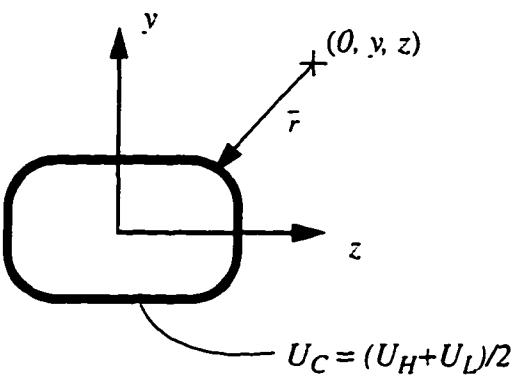

Fig 2.2 **Diagram showing the minimum directed distance, *r*, from the point (*0*, *y*, *z*) to the contour of constant convective velocity, U_C, at the inflow.**

Chapter 3

NUMERICAL FORMULATION

The numerical approximations of the governing equations are described in this chapter. The temporal approximation to the governing equations is given in this section, while the spatial approximations are given in the next section.

3.1 Temporal Discretization

The time advancement scheme used to march the momentum equations in time should possess several qualities; low dispersion and dissipation errors over a wide range of step sizes, low-storage requirements, and a relatively large stability envelope. The family of low-storage, Runge-Kutta schemes proposed by Williamson (1980) possesses these desirable qualities. The scheme is low-storage in the sense that only two storage locations (one for the time derivative and one for the variable itself) are required for time advancement. In comparison, a third-order fully implicit scheme requires four storage locations. For simplicity, the numerical approximations for the governing equations are given in the Cartesian coordinate system with uniform grid spacing. Extension of the formulation to curvilinear grids is accomplished by using the chain rule to replace the derivatives in physical space with derivatives in the uniform computational space and is straightforward.

The additional metric terms are discretized using the same higher-order compact schemes. The momentum equation is advanced from time level, N, to N+1, using Q

substages. The temporal derivative in the momentum equation is discretized using a third- or fourth-order explicit Runge-Kutta scheme:

$$\frac{\partial u_i}{\partial t} \approx \frac{u_i^{M+1} - u_i^M}{b^M \Delta t} = H_i^M - \frac{\partial p^M}{\partial x_i} \tag{3.1}$$

where b^M is a constant of the Runge-Kutta scheme, u_i^M represents the *ith* velocity component at the *Mth* substage ($M = 0$ is the *Nth* time level, $M=Q$ is the $N+1$ time level). The term, H_i^M, denotes the sum of convection and diffusion terms:

$$H_i^M = -u_j \frac{\partial u_i^M}{\partial x_j} + \frac{1}{Re_{D_e}} \left(\frac{\partial^2 u_i^M}{\partial x_j \partial x_j} \right) \tag{3.2}$$

The terms on the right hand side (RHS) of Eq. (3.1) are assumed known from the previous sub-stage or from the initial conditions at $t = 0$. The calculation of the pressure is accomplished by solving a Poisson equation at each sub-stage such that the continuity is enforced. Since the pressure, p^M, is calculated before the advancement of Eq. (3.1), u_i^{M+1}, can be calculated explicitly using Eq. (3.1).

The low-storage requirement is accomplished by continuously overwriting the storage location for the time derivatives and unknown variables at each sub-stage:

$$\hat{H}_i^M \leftarrow a^M \hat{H}_i^{M-1} \tag{3.3}$$

$$u_i^{M+1} \leftarrow u_i^M + b^M \Delta t \hat{H}_i^M \tag{3.4}$$

where $\hat{H}_i^M = H_i^M - [\partial p^M / \partial x_i]$ and the notation $\leftarrow$ is used to indicate that the storage locations, $\hat{H}_i^{M-1}$, u_i^M are overwritten by, $\hat{H}_i^M$, u_i^{M+1}, respectively. Tables 3.1 and 3.2 show the constants, a^M and b^M (to 8 significant figures) for the low-storage, third- and fourth-order schemes, respectively.

Table 3.1 Coefficients of third-order Runge-Kutta schemes from Lowery and Reynolds (1986)

M	a^M	b^M
1	0	0.500
2	-0.68301270	0.91068360
3	-1.33333333	0.36602540

Table 3.2 Coefficients of fourth-order Runge-Kutta schemes from Carpenter and Kennedy (1994) (defined there as solution 3)

M	a^M	b^M
1	0	0.14965902
2	-0.41789047	0.37921031
3	-1.19215169	0.82295502
4	-1.69778469	0.69945045
5	-1.51418344	0.15305724

The stability characteristics of the Runge-Kutta schemes can be analyzed by considering the model equation:

$$\frac{\partial \phi}{\partial t} = \hat{H}(\phi, t) \tag{3.5}$$

where ϕ is the generic unknown to be advanced in time and $\hat{H}$ is the time derivative which contains the spatial terms of the governing equation. Equation (3.5) is transformed from physical space to wavenumber space by decomposing ϕ into Fourier modes:

$$\phi = \tilde{\phi}(t)e^{ikx} \tag{3.6}$$

where $\tilde{\phi}(t)$ is the Fourier coefficient of ϕ, $i = \sqrt{-1}$, and k is the wavenumber. Substituting Eq. (3.6) into Eq. (3.5) yields:

$$\frac{\partial}{\partial t}\tilde{\phi} = \lambda\tilde{\phi} \tag{3.7}$$

where λ (a complex number) is the Fourier symbol of the spatial operator $\hat{H}$. The Runge-Kutta scheme is used to expand the term on the LHS of Eq. (3.7) which gives an amplification factor, $G = \tilde{\phi}^{N+1}/\tilde{\phi}^{N}$ for the third-order scheme:

$$G = 1 + (\lambda\Delta t) + \frac{1}{2}(\lambda\Delta t)^2 + \frac{1}{6}(\lambda\Delta t)^3 \tag{3.8}$$

It can be shown that all three-stage, third-order Runge-Kutta schemes have the same amplification factor given in Eq. (3.8). Solving Eq. (3.7) analytically in time gives the exact amplification factor, G_e:

$$G_e = e^{\lambda\Delta t} \tag{3.9}$$

Comparing Eqs. (3.8) and (3.9), the three-stage, third-order Runge-Kutta scheme is a polynomial approximation to the exact solution to third-order. Similarly, the five-stage, fourth-order Runge-Kutta scheme has amplification factor:

$$G = 1 + (\lambda\Delta t) + \frac{1}{2}(\lambda\Delta t)^2 + \frac{1}{6}(\lambda\Delta t)^3 + \frac{1}{24}(\lambda\Delta t)^4 + \frac{1}{200}(\lambda\Delta t)^5 \tag{3.10}$$

The stability of the Runge-Kutta schemes is shown graphically in Fig. 3.1 by plotting the $|G| = 1$ contour of Eq. (3.8) for the three-stage, third-order scheme and Eq. (3.10) for the five-stage, fourth-order scheme. A selection of $\lambda\Delta t$ in the interior of the closed curve yields $|G| < 1$, i.e. the scheme is stable. Outside the closed curve, $|G| > 1$ and the scheme is unstable. If the Fourier symbol of the spatial operator, λ, is purely imaginary (for example the 1-D convection equation) an inspection of Fig. 3.1 reveals that the region, $-L_I < \lambda\Delta t < L_I$, is stable. If λ is purely real (for example the 1-D diffusion equation) the region, $-L_R < \lambda\Delta t < 0$, is stable. The stability limits for these two extreme cases are given in

Table 3.3 for the third- and fourth-order Runge-Kutta schemes. The fourth-order scheme allows time steps roughly twice that of the third-order scheme.

A temporal stability analysis of the 3-D convection-diffusion equation is used to model the temporal stability of the 3-D Navier-Stokes equations and is postponed until the numerical approximations to the spatial derivatives are defined.

Table 3.3 Stability limits of Runge-Kutta schemes for purely imaginary (L_I) or real (L_R) spatial operators

Spatial Operator	third-order, three stage	fourth-order, five stage
Imag, L_I	1.73	3.34
Real, L_R	2.51	4.65

3.2 Spatial Discretization

The numerical approximations to the spatial derivatives appearing in the semi-discrete momentum equations, Eq. (3.1), are given in this section. Standard second-order finite difference approximations to first derivative suffer from large dispersion errors. Spectral methods offer exact differentiation for resolved modes but suffer from high cost and low flexibility in that simple domains and boundary conditions are required for their implementation. In this study, high-order compact finite differences are used to approximate spatial derivatives because of their excellent combination of high-accuracy, flexibility, and relatively low cost.

3.2.1 Numerical Approximation of First Derivative Terms

The first derivative terms appearing in the governing equations are approximated using fourth- and sixth-order compact finite difference schemes proposed by Lele (1992). High

accuracy is achieved with relatively small computational stencil sizes by treating the derivative terms implicitly:

$$\alpha\phi'_{i-1} + \phi'_i + \alpha\phi'_{i+1} = \frac{a}{2\Delta x}(\phi_{i+1} - \phi_{i-1}) + \frac{b}{4\Delta x}(\phi_{i+2} - \phi_{i-2}) \qquad (3.11)$$

where $\Delta x = L_x/(N_x - 1)$, N_x is the number of grid points, ϕ'_i represents the first derivative of the generic variable ϕ_i with respect to x, and α, a, b are the coefficients of the compact scheme which determine the accuracy. Similar expressions are used for derivatives with respect to the y and z directions. For the fourth-order scheme: $\alpha = 1/4$, $a = 3/2$, and $b = 0$, and for the sixth-order scheme: $\alpha = 1/3$, $a = 14/9$, and $b = 1/9$. The LHS of Eq. (3.11) contains the unknown derivatives at grid points i and $i \pm 1$ while the RHS contains the known functional values ϕ_i at the grid points $i \pm 1$ and $i \pm 2$.

A comparison of explicit central difference and implicit compact approximations to the first derivative is given in Table 3.4. It can be seen that the implicit treatment of the derivative results in a smaller or more "compact" stencil for a given order. Also, the leading truncation error term for the compact scheme is reduced by 1/4 for the fourth-order scheme and 1/9 for the sixth-order scheme compared to explicit central difference schemes of the same order.

Table 3.4 Comparison of explicit central difference and implicit compact approximations to the first derivative

Scheme	Truncation error	Stencil Size
fourth-order central	$(-4/5!)(\Delta x_j)^4\phi^{(5)}$	5
fourth-order compact	$(-1/5!)(\Delta x_j)^4\phi^{(5)}$	3
sixth-order central	$(-36/7!)(\Delta x_j)^6\phi^{(7)}$	7
sixth-order compact	$(-4/7!)(\Delta x_j)^6\phi^{(7)}$	5

Writing Eq. (3.11) at all grid points results in a tridiagonal system of algebraic equations and that is solved efficiently by factoring the LHS into a lower/upper (LU) system

once at the beginning of the simulation. The LU factors are stored and then used to solve Eq. (3.11) for the unknown derivatives.

The resolution properties of the numerical approximation to the first derivative are analyzed by transforming the 1-D convection equation from physical to wavenumber space. In physical space, the 1-D convection equation is given by:

$$\frac{\partial \phi}{\partial t} + |u|\frac{\partial \phi}{\partial x} = 0 \tag{3.12}$$

where $|u|$ is the wave speed which is assumed to be constant. Decomposing ϕ into Fourier modes as in Eq. (3.6) and evaluating $\frac{\partial \phi}{\partial x}$ analytically gives:

$$\frac{\partial \tilde{\phi}}{\partial t} = -i|u|k\tilde{\phi} \tag{3.13}$$

While evaluating the first derivative numerically gives:

$$\frac{\partial \tilde{\phi}}{\partial t} = -i|u|k^*\tilde{\phi} \tag{3.14}$$

where k^* is the numerical wavenumber. For explicit finite difference schemes, $\alpha = 0$, and the numerical wavenumber is given by:

$$k^* = \frac{-i}{\Delta x}\sum_{l=-N}^{N} a_l e^{ilk\Delta x} \tag{3.15}$$

while for the tridiagonal compact scheme, the numerical wavenumber is given by:

$$k^* = \frac{1}{\Delta x}\left[\frac{a\sin(k\Delta x) + \frac{b}{2}\cos(2k\Delta x)}{1 + 2\alpha\cos(k\Delta x)}\right] \tag{3.16}$$

Note that in general the numerical wavenumber, k^*, is complex while the exact wavenumber, k, is real. For the numerical approximation to yield an exact solution, the following two conditions must be met:

$$\text{Real}(k^*) = k \tag{3.17}$$

$$\text{Imag}(k^*) = 0 \tag{3.18}$$

It is easy to show that deviations from Eq. (3.17) indicate dispersion errors due to odd derivative terms appearing in the truncation error. Deviations from Eq. (3.18) indicate dissipation errors due to even derivative terms appearing in the truncation error. The real and imaginary parts of Eq. (3.16) are plotted separately in Fig. 3.2 for the fourth- and sixth-order compact schemes. In addition, some popular explicit numerical approximations to the first derivative are plotted for comparison; the standard second-order central difference scheme and a third-order upwind biased scheme.

From Fig. 3.2a, it can be seen that all four approximations do a reasonable job of approximating the exact wavenumber (i.e. very low dispersion errors) at very low wavenumbers ($k\Delta x \to 0$) and that all four approximations do a poor job at very high wavenumbers ($k\Delta x \to \pi$). For intermediate wavenumbers, the fourth- and sixth-order compact schemes provide a much better approximation to the exact wavenumber over a greater range of wavenumbers than the explicit schemes. The second-order central difference scheme yields a poor approximation to the exact wavenumber for all but the very lowest wavenumbers ($k\Delta x < 0.5$). From Fig. 3.2b it can be seen that the compact and second-order central difference schemes contain no dissipation errors. The third-order upwind scheme adds numerical dissipation errors which are largest at high wavenumbers. Spectral methods yield exact differentiation for all modes which can be resolved on the specified grid and thus correspond to the exact relationship for $k\Delta x$ in Fig. 3.2.

Table 3.5 lists some quantitative measures of resolution for the five schemes. The wavenumber, k_c^*, defines the region of acceptable accuracy, i.e. for $0 < k < k_c^*$, $|k^*\Delta x - k\Delta x| < 0.01$. Modes with k > k_c^*, are not accurately resolved. The quantity, k_{max}^*, defines the maximum value for the modified wavenumber, i.e. for $k < k_{max}^*$, the slope of the curve is zero. Also listed is the number of spatial grids points per wavelength, $PPW = 2\pi/(k_c^*\Delta x)$, to accurately resolve a given mode. From the estimate of PPW, roughly five times as many points are required for the second-order central difference scheme to achieve the same accuracy as the compact schemes.

Table 3.5 Resolution measures of various numerical approximations to the first derivative

Spatial Scheme	$k_c^*\Delta x$	$k_{max}^*\Delta x$	Points per wavelength
second-order central	0.22	1.00	28.6
third-order upwind	0.44	1.27	14.3
fourth-order compact	1.11	1.73	5.6
sixth-order compact	1.55	2.00	4.1
spectral	π	π	2

For non-periodic boundaries, one-sided finite difference expressions are required to close the system of equations at the boundary points; $i = 1$ and $i = N$ for the fourth-order scheme and $i = 1, 2$ and i = N-1, N for the sixth-order scheme. A third-order compact boundary scheme is used at $i = 1$ and $i = N$ with the fourth-order interior scheme:

$$\phi'_1 + \alpha_{bs}\phi'_2 = \frac{1}{\Delta x}\sum_{i=1}^{3} a_{bs_i}\phi_i \qquad (3.19)$$

where $\alpha_{bs} = 2$ and $a_{bs_1} = -5/2$, $a_{bs_2} = 2$, $a_{bs_3} = 1/2$ are the coefficients of the third-order boundary scheme. A similar equation is used at $i = N$.

For the sixth-order scheme, a boundary and near-boundary scheme are required for closure since the interior stencil is pentadiagonal. A fifth-order explicit boundary scheme is used at points, $i = 1$ and $i = N$:

$$\phi'_1 = \frac{1}{\Delta x}\sum_{i=1}^{8} a_{bs_i}\phi_i \tag{3.20}$$

with coefficients:

$$a_{bs_1} = -296/105 \quad a_{bs_5} = -215/12$$

$$a_{bs_2} = 415/48 \quad a_{bs_6} = 791/80$$

$$a_{bs_3} = -125/8 \quad a_{bs_7} = -25/8$$

$$a_{bs_4} = 985/48 \quad a_{bs_8} = 145/336$$

A different fifth-order explicit near boundary scheme is used at points, $i = 2$ and $i = N-1$:

$$\phi'_2 = \frac{1}{\Delta x}\sum_{i=1}^{8} a_{nb_i}\phi_i \tag{3.21}$$

with coefficients:

$$a_{nb_1} = -3/16 \quad a_{nb_5} = 115/144$$

$$a_{nb_2} = -211/180 \quad a_{nb_6} = -1/3$$

$$a_{nb_3} = 109/48 \quad a_{nb_7} = 23/240$$

$$a_{nb_4} = -35/24 \quad a_{nb_8} = -1/72$$

Similar equations for the boundary and near boundary schemes are used at points $i = N$ and $i = N-1$.

3.2.2 Numerical Approximation of the Second Derivative

The second derivative terms present in the viscous terms of the momentum equation and the Laplacian operator of the Poisson equation for pressure are approximated using fourth- and sixth-order compact finite differences. Again, higher accuracy is achieved by treating the derivative implicitly:

$$\alpha\phi''_{i-1} + \phi''_i + \alpha\phi''_{i+1} = \frac{a}{(\Delta x)^2}(\phi_{i+1} - 2\phi_i + \phi_{i-1}) + \frac{b}{4(\Delta x)^2}(\phi_{i+2} - 2\phi_i + \phi_{i-2}) \tag{3.22}$$

where ϕ''_i represents the second derivative of the generic variable ϕ_i with respect to x, and α, a, b are the coefficients of the compact scheme. For the fourth-order scheme: $\alpha = 1/10$, $a = 6/5$, and $b = 0$, and for the sixth-order scheme: $\alpha = 2/11$, $a = 12/11$, and $b = 3/11$. The tridiagonal system of algebraic equations for the second derivatives are solved for in the same manner as the first derivatives. A comparison of explicit central difference and implicit compact approximations to the second derivative is given in Table 3.6. As with the first derivative, the implicit treatment of the second derivative results in a smaller stencil size for a given order. The leading truncation error term for the compact formulation is reduced by 1/2 for the fourth-order scheme and 1/4 for the sixth-order scheme compared to explicit central difference schemes of the same order.

Table 3.6 Comparison of explicit central difference and implicit compact approximations of the second derivative

Scheme	Truncation error	Stencil Size
fourth-order central	$(-8/6!)(\Delta x_j)^4\phi^{(6)}$	5
fourth-order compact	$(-3.6/6!)(\Delta x_j)^4\phi^{(6)}$	3
sixth-order cd	$(-72/8!)(\Delta x_j)^6\phi^{(8)}$	7
sixth-order compact	$(\ -(-16.7/8!))(\Delta x_j)^6\phi^{(8)}$	5

For non-periodic boundaries, one-sided finite differences are required to close the system of equations. At $i = 1$ and $i = N$, a third-order compact boundary scheme is used:

$$\phi''_1 + \alpha_{bs}\phi''_2 = \frac{1}{(\Delta x)^2}\sum_{i=1}^{4} a_{bs_i}\phi_i \tag{3.23}$$

where $\alpha_{bs} = 11$ and $a_{bs_1} = 13$, $a_{bs_2} = -27$, $a_{bs_3} = 15$, and $a_{bs_4} = -1$ are the coefficients of the third-order boundary scheme. For the sixth-order scheme, a near boundary scheme is required at $i = 2$ and $i = N-1$. The fourth-order interior scheme is used at these points since only a three-point stencil is needed.

A similar analysis of the 1-D diffusion equation is used to investigate the resolution qualities of the proposed compact approximation to the second derivative. In physical space, the 1-D diffusion equation is written as:

$$\frac{\partial\phi}{\partial t} = \frac{1}{Re}\frac{\partial^2\phi}{\partial x^2} \tag{3.24}$$

where the term $1/Re$ represents the diffusion coefficient. Equation (3.24) is transferred to wavenumber space by decomposing the solution into Fourier modes. If $\frac{\partial^2\phi}{\partial x^2}$ is evaluated analytically, Eq. (3.24) becomes:

$$\frac{\partial\tilde{\phi}}{\partial t} = -\frac{1}{Re}k^2\tilde{\phi} \tag{3.25}$$

Evaluating the second derivative numerically gives:

$$\frac{\partial\tilde{\phi}}{\partial t} = -\frac{1}{Re}(k^*)^2\tilde{\phi} \tag{3.26}$$

where k^* is the numerical wavenumber. For explicit finite difference schemes ($\alpha = 0$), the numerical wavenumber is given by:

$$(k^*)^2 = \frac{-1}{(\Delta x)^2}\sum_{l=-N}^{N} a_l e^{ilk\Delta x} \tag{3.27}$$

The tridiagonal compact scheme represented by Eq. (3.22) yields a numerical wavenumber:

$$(k^*)^2 = \frac{1}{(\Delta x)^2}\left[\frac{2a[1-\cos(k\Delta x)] + \frac{b}{2}[1-\cos(2k\Delta x)]}{1+2\alpha\cos(k\Delta x)}\right] \tag{3.28}$$

Since explicit central and implicit compact difference schemes for the second derivative have symmetric stencils ($a_l = a_{-l}$), the numerical wavenumber is always a real number. As a result, there are no dispersion errors in the approximation of the second derivative. Only dissipation errors exist. The dissipation errors for the explicit second-order central difference, and fourth- and sixth-order compact schemes are shown in Fig. 3.3 by plotting the numerical wavenumber in Eqs. (3.27) and (3.28). It can be seen that the numerical wavenumber for the compact scheme more closely approximates the exact wavenumber over a wider range of wavenumbers. Quantitative measures of resolution power for the various schemes are given in Table 3.7. It can be seen from the estimate of the PPW that roughly twice as many points are required for the explicit second-order central difference to produce the same accuracy as the compact schemes.

Table 3.7 Resolution measures of various numerical approximations to the second derivative

Spatial Scheme	$(k_c^*\Delta x)$	$(k_{max}^*\Delta x)^2$	Points per wavelength
second-order central	0.57	4.00	11.0
fourth-order compact	1.14	6.00	5.5
sixth-order compact	1.52	6.86	4.1
spectral	π	π^2	2

Upon discretizing the semi-discrete momentum equation using the compact schemes for spatial derivatives outlined above:

$$u_i^{M+1} = u_i^M + b^M \Delta t [H_i - \delta_{x_i} P^M] \tag{3.29}$$

where:

$$H_i^M = -u_j \delta_{x_j} u_i^M + \frac{1}{Re_{D_*}} \delta_{xx_j} u_i^M$$

3.2.3 Stability of Runge-Kutta Schemes for the 3-D Convection-Diffusion Equation

A stability analysis of the 3-D convection-diffusion equation with periodic boundaries and uniform grid spacing using the Runge-Kutta scheme is given in this section. The results of this analysis are used to model the temporal stability of the 3-D Navier-Stokes equations and to select a time step size for the simulations presented in this study. The analysis neglects the effects of non-linearity of the convection terms, non-periodic boundaries, the continuity equation, and grid stretching and therefore cannot predict exact stability limits. The approach is to analyze the convection and diffusion equations separately and then to combine the two results to determine stability limits for the convection-diffusion equation.

Returning to the 1-D convection equation and comparing Eqs. (3.7) and (3.14), it can be seen that the Fourier symbol of the spatial operator, $\frac{\partial \phi}{\partial x}$, is given by, $\lambda = -i|u|k^*$. Recall that k^* is the numerical approximation to the exact wavenumber. The most unstable mode in the temporal integration corresponds to the maximum value of $\lambda \Delta t$ over all wavenumbers:

$$(\lambda \Delta t)_{max} = -i|u|k^*_{max} \Delta t = -iC\left[\frac{|u|\Delta t}{\Delta x}\right] \tag{3.30}$$

where $C = k_{max}\Delta x$ is determined by the numerical approximation to the first derivative and is given in Table 3.5 for the various schemes. From the results of the stability analysis of the model equation presented in Sec. 3.1, the stability limits for the 1-D convection equation are given by:

$$-1 < \frac{C}{L_I}\left[\frac{|u|\Delta t}{\Delta x}\right]_{max_i} < 1 \tag{3.31}$$

where max_i denotes the maximum quantity over all grid points. For the 3-D convection equation, Eq. (3.31) becomes:

$$-1 < \frac{C\Delta t}{L_I}\left[\frac{|u|}{\Delta x} + \frac{|v|}{\Delta y} + \frac{|w|}{\Delta z}\right]_{max_{ijk}} < 1 \tag{3.32}$$

where $|v|$ and $|w|$ are the convection velocities in the y and z directions, respectively.

Considering the 1-D diffusion equation, the Fourier symbol of the spatial operator is found by comparing Eqs. (3.7) and (3.26). The most unstable mode is given by:

$$(\lambda\Delta t)_{max} = -\frac{1}{Re}(k^*_{max})^2\Delta t = -D\left[\frac{\Delta t}{Re(\Delta x)^2}\right] \tag{3.33}$$

where $D = (k^*_{max}\Delta x)^2$ is determined by the numerical approximation to the second derivative and is given in Table 3.7. The stability limit for the 1-D diffusion equation is given by:

$$\frac{D}{L_R}\left[\frac{\Delta t}{Re(\Delta x)^2}\right]_{max_i} < 1 \tag{3.34}$$

For the 3-D diffusion equation, Eq. (3.34), becomes:

$$\frac{D\Delta t}{L_R Re}\left[\frac{1}{(\Delta x)^2} + \frac{1}{(\Delta y)^2} + \frac{1}{(\Delta z)^2}\right]_{max_{ijk}} < 1 \tag{3.35}$$

The stability limits of the diffusion and convection equation are combined to give the stability limits of the convection-diffusion equation. In this case, $\lambda\Delta t$, possesses both real

and imaginary parts. One approach to predicting the stability of the 3-D convection-diffusion equation, once the computational grid is specified, is to substitute the expressions for $\lambda\Delta t$ into Eq. (3.8) or Eq. (3.10) and solve the polynomial equation for Δt at all grid points. Selecting the time step as the minimum computed over all the grid points ensures that $|G| < 1$ for all grid points. However, the solution of such a polynomial equation involves multiple roots (dependent on the order of the polynomial) and is thus difficult to automate.

The present approach is to replace the actual contour, $|G| = 1$, with an ellipse having semi-major and -minor axis lengths of L_R and L_I, respectively. The region inside the ellipse is considered to be stable. The stability criterion from this approach is given by:

$$\Delta t < \frac{1}{[Lim_{conv}^{\ 2} + Lim_{diff}^{\ 2}]_{max_{ijk}}^{1/2}} \tag{3.36}$$

where:

$$Lim_{conv} = \frac{C}{L_I}\left[\frac{|u|}{\Delta x} + \frac{|v|}{\Delta y} + \frac{|w|}{\Delta z}\right]$$

$$Lim_{diff} = \frac{D}{L_R Re}\left[\frac{1}{(\Delta x)^2} + \frac{1}{(\Delta y)^2} + \frac{1}{(\Delta z)^2}\right]$$

For free shear flows at moderate to high Reynolds numbers, one expects the stability to be governed by the inviscid terms. At lower Reynolds number and/or flows with solid boundaries where extremely fine grid spacing must be used, the stability requirements could be governed by the viscous terms. An analysis of grids and Reynolds numbers used in this study indicates that stability is indeed governed by the inviscid limit and thus an explicit time differencing scheme such as the third- or fourth-order Runge-Kutta scheme allows reasonably large time steps to be taken.

Since there are a number of simplifying assumptions made in extending the stability results to the Navier-Stokes equations, the time step used in the simulations is reduced from that predicted by Eq. (3.36):

$$\Delta t < \frac{sf}{[Lim_{conv}{}^2 + Lim_{diff}{}^2]_{max_{ijk}}{}^{1/2}} \tag{3.37}$$

where sf is a safety factor, $0 < sf < 1$. For the simulations in this study, $sf = 0.5$ was used.

In using Eq. (3.36) to estimate the time step requirements for stability, the velocity components of the flow field are required to evaluate the frozen convection coefficients, $|u|, |v|, |w|$. In the absence of a representative flow field (such as at the beginning of a simulation) conservative estimates are used. For non-uniform grids, the local grid spacing ($\Delta x_{ijk}, \Delta y_{ijk}, \Delta z_{ijk}$) is used and it is assumed that the effect of grid stretching on the temporal stability is negligible.

3.3 Enforcement of the Continuity Equation and Poisson Equation for Pressure

An examination of the governing equations reveals four scalar equations (continuity and three scalar components of the momentum equation) in terms of four unknowns (three velocity components and pressure). Time derivatives for the velocity components in the momentum equation are used to march those equations in time. However, no such time derivative exists for pressure, while the continuity equation appears to be an additional constraint on the velocity field. The current approach overcomes this problem by taking the numerical divergence of the discretized momentum equation and substituting for the discretized continuity equation. This results in a Poisson equation for pressure which ensures that the velocity field is divergence free at the $M+1$ sub-stage.

Applying the divergence operator δ_{x_i} to the discretized momentum equation gives:

$$\frac{1}{b^M \Delta t}\{\delta_{x_i}(u_i^{M+1} - u_i^M)\} = \delta_{x_i} H_i^M - \delta_{x_i}\delta_{x_i} p^M \tag{3.38}$$

The term, $\delta_{x_i} u_i^{M+1}$, represents the discretized continuity equation at the $M + 1$ sub-stage and is set to zero to enforce the continuity equation. The term, $\delta_{x_i} u_i^M$, represents the continuity equation at the previous sub-stage M. In practice, this term is retained in the solution of the Poisson equation to "kill off" any accumulating divergence of the velocity field at the previous sub-stage. The term, $\delta_{x_i} H_i^M$, is the source term of the Poisson equation and represents gradients of the convection and diffusion terms which are known from the previous sub-stage. The term, $\delta_{x_i}\delta_{x_i} p^M$, represents the discretized Laplacian operator of the pressure. Solving for the Laplacian of the pressure in Eq. (3.38) gives:

$$\nabla^2 p^M = \delta_{x_i}\left[H_i^M + \frac{u_i^M}{b^M \Delta t}\right] \tag{3.39}$$

The solution details of the Poisson equation for pressure are given in Chap. 4.

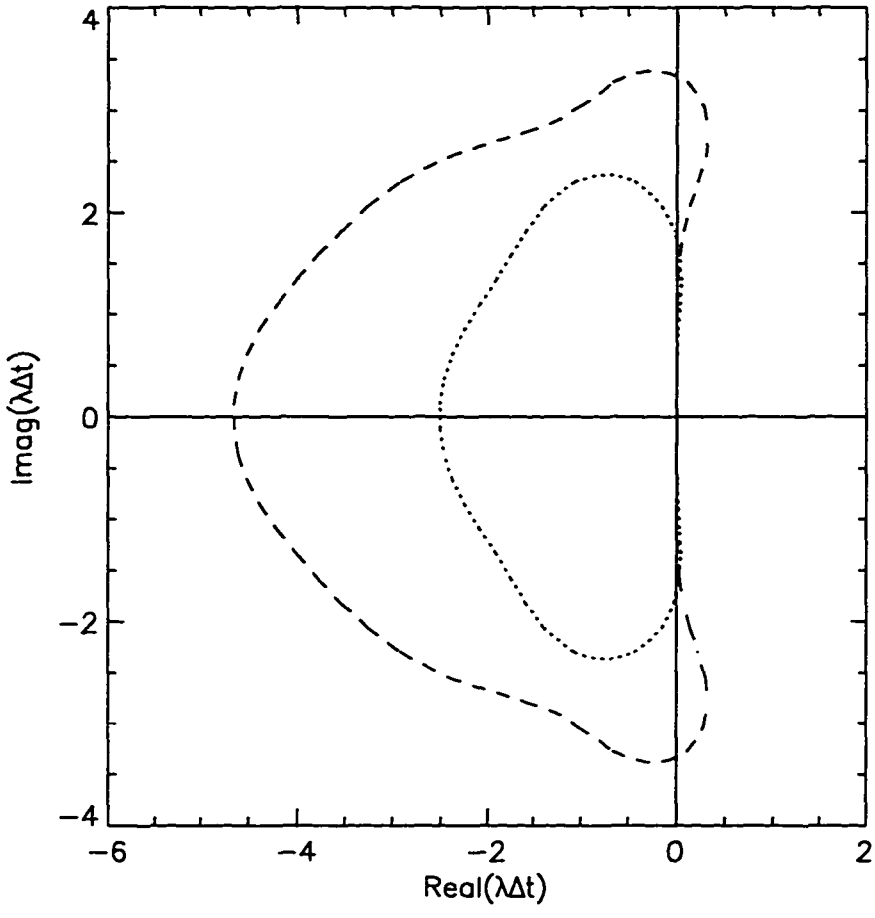

Fig 3.1 Stability diagram for Runge Kutta schemes (dotted line : third-order ; dashed line : fourth-order).

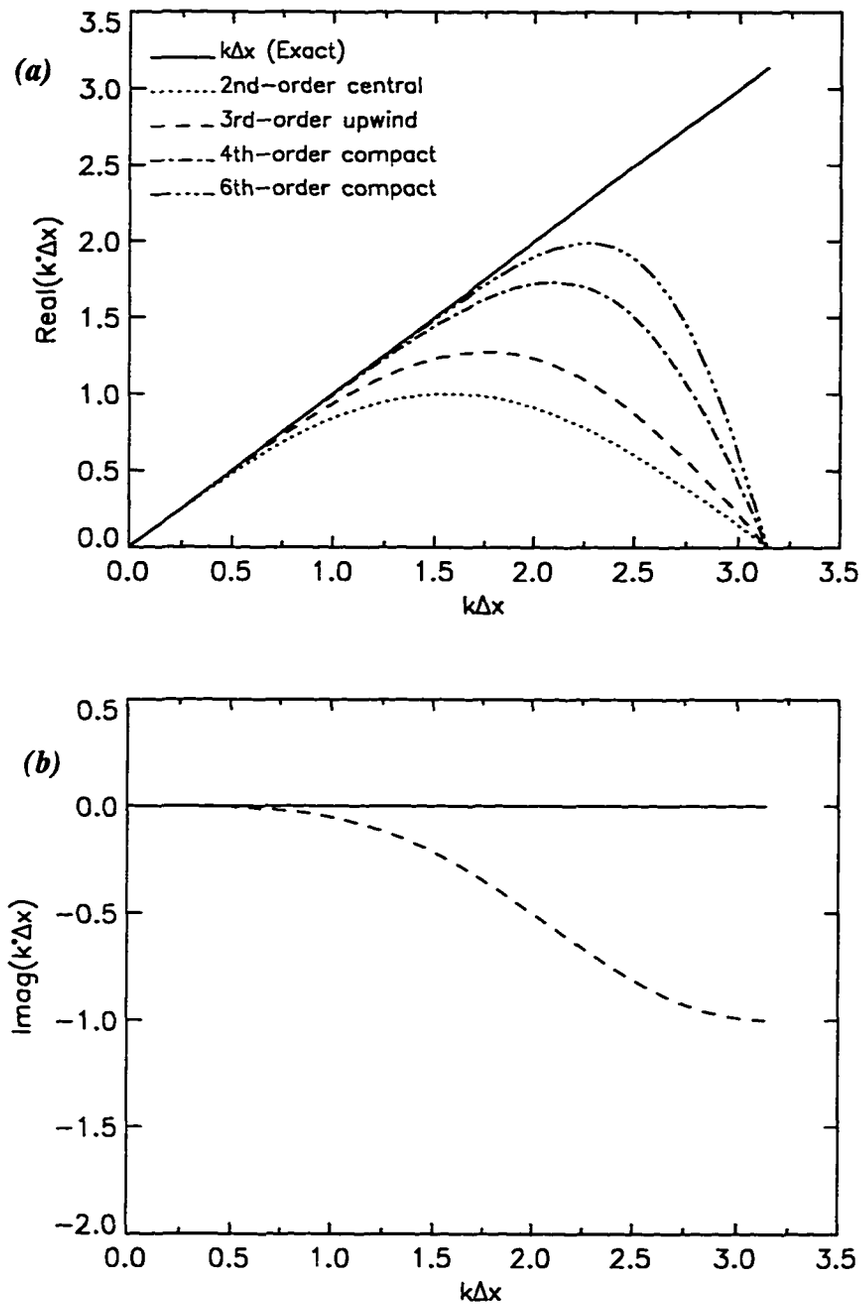

Fig 3.2 **Finite differencing error for numerical approximations of the first derivative *(a)* dispersion errors, *(b)* dissipation errors (zero except for 3rd-order upwind).**

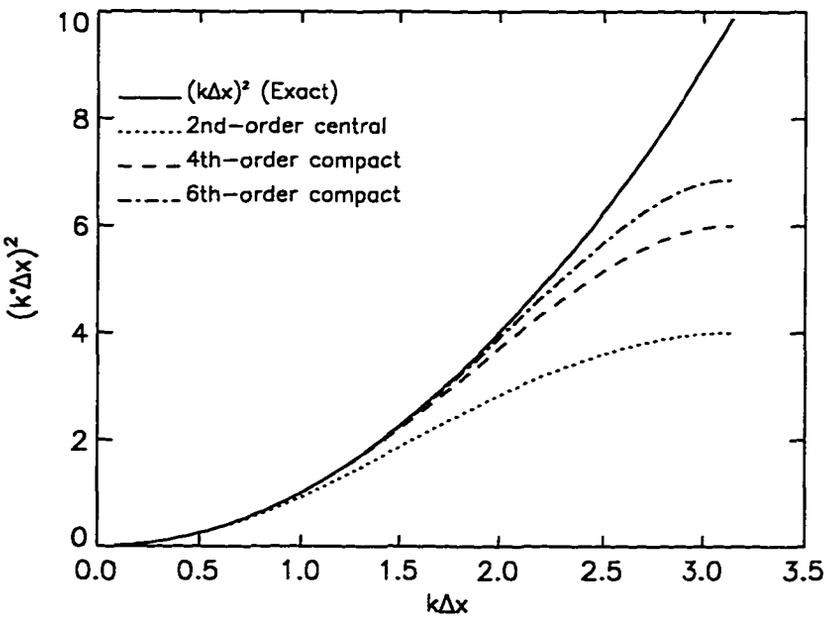

Fig 3.3 Finite differencing error for numerical approximations of the second derivative.

Chapter 4

SOLUTION OF THE POISSON EQUATION FOR PRESSURE

A significant amount of the total computational time required for the solution of the incompressible Navier-Stokes equations (as much as half) is devoted to the enforcement of the continuity equation/solution of pressure. This stems from the fact that evolution equations exist for the velocity components (i.e. the momentum equations) while none exist for the pressure. Instead, an elliptic equation must be solved for the pressure which involves the solution of a system of equations and is expensive. Solutions methods for elliptic equations generally fall into two categories - direct or iterative. Direct methods usually involve some form of Gaussian elimination where the coefficient matrix is first factored into an upper and lower matrix and then the solution is computed using back substitution. The operation count and memory requirements for this procedure can be prohibitively large for the solution of systems involving a large number of unknowns ($\sim 10^6$ in typical 3-D problems). The alternative to a direct solution is an iterative procedure where an initial approximation to the solution is used to yield an improved solution. This process is repeated until the solution is converged within a pre-specified convergence criterion. The operation count and memory requirements of most iterative methods are less than that of Gaussian elimination. Therefore, the iterative solution procedure is used in this study to solve the Poisson equation for pressure. The details of this procedure are outlined in this chapter. The performance of the computer code using uniform and curvilinear grids is also documented and compared with published computational rates of similar codes.

4.1 Discretized Laplacian Operator

The discrete Poisson equation for pressure which was derived in Sec. 3.3 is given by:

$$\delta_{x_i}\delta_{x_i}p^M = \delta_{x_i}\left[H_i^M + \frac{u_i^M}{b^M \Delta t}\right] \tag{4.1}$$

The LHS of Eq. (4.1) represents a discretized Laplacian operator composed of two applications of the first derivative operator, δ_{x_i}. It is well known that using two first derivative operators to represent the Laplacian operator on non-staggered grids can lead to an "odd-even" decoupling of the solution. Indeed, with standard second-order central differencing for the first derivative operator, the solution at even grid points completely decouples from the odd grid points, leading to unphysical results. One remedy is to introduce terms of the same order as the truncation error which in effect replaces the two first derivative operators with a single second derivative operator. This couples the solution at odd and even grid points while maintaining the same formal order of accuracy. The Laplacian operator is discretized using a single second derivative operator to prevent possible decoupling and Eq. (4.1) becomes:

$$\delta_{xx_i}p^M = \delta_{x_i}\left[H_i^M + \frac{u_i^M}{b^M \Delta t}\right] \tag{4.2}$$

where $\delta_{xx_i}p^M$ represents the discrete Laplacian of pressure and is discretized using the compact second derivative operator given by Eq. 3.22.

Writing Eq. (4.2) at all grid points results in a system of equations that is solved at each sub-stage of the time advancement scheme. For simplicity, the system of equations are defined for the 2-D Poisson equation with periodic boundaries on a uniform grid. The Laplacian operator is discretized using the fourth-order tridiagonal scheme defined in Sec.

3.2.2. The solution procedure is easily extended to the 3-D Poisson equation. Equation (4.2) can be written in the form of a system of equations as:

$$AP = [A_{xx}^{-1}B_{xx} + A_{yy}^{-1}B_{yy}]P = F \tag{4.3}$$

$$A_{xx} = \begin{bmatrix} L & & & L \\ & L & & \\ & & \ddots & \\ & & & L \\ L & & & L \end{bmatrix}, \qquad \text{where } L = \begin{bmatrix} 1 & \alpha & & & \alpha \\ \alpha & 1 & \alpha & & \\ & \ddots & & & \\ & & & \alpha & 1 & \alpha \\ \alpha & & & & \alpha & 1 \end{bmatrix}$$

(nj x nj block matrix) (ni x ni scalar matrix)

$$A_{yy} = \begin{bmatrix} I & \alpha I & & & \alpha I \\ \alpha I & I & \alpha I & & \\ & \ddots & & & \\ & & \alpha I & I & \alpha I \\ \alpha I & & & \alpha I & I \end{bmatrix}, \qquad \text{where } I \text{ is the } ni \text{ x } ni \text{ identity matrix}$$

(nj x nj block matrix)

$$B_{xx} = \frac{a}{h_x^2}\begin{bmatrix} \bar{R} & & & \bar{R} \\ & \bar{R} & & \\ & & \ddots & \\ & & & \bar{R} \\ \bar{R} & & & \bar{R} \end{bmatrix}, \qquad \text{where } \bar{R} = \begin{bmatrix} -2 & 1 & & & 1 \\ 1 & -2 & 1 & & \\ & \ddots & & & \\ & & & 1 & -2 & 1 \\ 1 & & & & 1 & -2 \end{bmatrix}$$

(nj x nj block matrix) (ni x ni scalar matrix)

$$B_{yy} = \frac{a}{h_y^2}\begin{bmatrix} -2I & I & & & -2I \\ I & -2I & I & & \\ & \ddots & & & \\ & & I & -2I & I \\ -2I & & & I & -2I \end{bmatrix}$$

(nj x nj block matrix)

$$P = \left[\bar{P}_1\ \bar{P}_2 \cdots \bar{P}_{nj}\right]^T, \qquad \text{where } \bar{P}_j = \left[P_{1,j}\ P_{2,j} \cdots P_{ni,j}\right]^T$$

(nj x 1 block vector) (ni x 1 scalar vector)

$$F = \left[\bar{F}_1\ \bar{F}_2 \cdots \bar{F}_{nj}\right]^T, \qquad \text{where } \bar{F}_j = \left[F_{1,j}\ F_{2,j} \cdots F_{ni,j}\right]^T$$

(nj x 1 block vector) (ni x 1 scalar vector)

where $P_{i,j}$ and $F_{i,j} = \delta_{x_i}[H_i + u_i/(b^M \Delta t)]_{i,j}$ are the pressure and source term at the i,j grid point, respectively. The symbols, $N_x + 1$, $N_y + 1$ denote the number of grid points in the x, y

directions, respectively. Values at $i = N_x+1$ and $j = N_y+1$ locations are replaced by values at $i = 1$ and $j = 1$ since the boundaries are periodic. This change results in a non-zero element in the upper right and lower left corners of the coefficient matrices. The constants, α and a, are from the fourth-order tridiagonal scheme for the second deriviative given in Sec. 3.2.2. The sixth-order compact scheme (with pentadiagonal RHS) can be written in the same manner by including the $i\pm2$ and $j\pm2$ terms in the B_{xx} and B_{yy} matrices.

For non-periodic boundaries, the second derivative boundary scheme given by Eq. 3.23 is used at the boundary points. In addition, the unknown pressures at the boundaries are replaced with their boundary values and those terms are moved and added to the RHS of Eq. (4.3). For Dirchlet boundary conditions, such as the freestream conditions given by Eq. (2.24), this procedure is straightforward. Neumann boundary conditions, such as those applied at the inflow and outflow planes, require that the pressure gradient at the boundary be discretized using a first derivative scheme (Eq. 3.19):

$$\left(\frac{\partial p}{\partial x_1}\right)_{1,j} = \frac{1}{\Delta x}\sum_{i=1}^{3} a_{bs_i} p_{i,j} \tag{4.4}$$

where the subscripts "$1,j$" are used to denote the inflow plane for example. The boundary pressure, $p_{1,j}$ is then solved for:

$$p_{1,j} = \frac{1}{a_{bs_1}}\left[\Delta x\left(\frac{\partial p}{\partial x_1}\right)_{1,j} - \sum_{i=2}^{3} a_{bs_i} p_{i,j}\right] \tag{4.5}$$

Equation (4.5) is then used to substitute for the boundary pressures in Eq. (4.3). The first term on the RHS of Eq. (4.5) is known from the boundary condition and is moved and added to the RHS of Eq. (4.3). The second term on the RHS of Eq. (4.5) contains the unknown pressures, $p_{2,j}$ and $p_{3,j}$, so they are kept on the LHS of Eq. (4.3) and modify the

existing terms of the coefficient matrix, A. The resulting system of equations contains only the interior pressures as unknowns, $p_{i,j}$, $2 \le i \le N_x - 1$ and $2 \le j \le N_y - 1$.

Equation (4.3) results in a "cross" type stencil at the i, j node in which all points along lines passing through the central node contribute to the stencil. The coefficients of this stencil are implicitly defined in the sense that the matrix operations, $[A_{xx}^{-1}B_{xx} + A_{yy}^{-1}B_{yy}]$, in Eq. (4.3) must be performed to determine their values.

Multiplying Eq. (4.3) by $A_{yy}A_{xx}$ gives:

$$[A_{yy}B_{xx} + A_{yy}A_{xx}A_{yy}^{-1}B_{yy}]P = A_{yy}A_{xx}F \tag{4.6}$$

It is easy to show that the matrices A_{xx} and A_{yy} commute, i.e. $A_{yy}A_{xx} = A_{xx}A_{yy}$. Using this property, Eq. (4.6) simplifies to:

$$[A_{yy}B_{xx} + A_{xx}B_{yy}]P = A_{yy}A_{xx}F \tag{4.7}$$

Using the coefficients of the fourth-order compact approximation to the second derivative results in an explicit nine-point, "grid" type stencil for the LHS and RHS of Eq. (4.7):

$$\begin{aligned}
&\left[-2a\left(\frac{1}{h_x^2}+\frac{1}{h_y^2}\right)\right]P_{i,j} + \\
&\left[-2a\left(\frac{\alpha}{h_x^2}-\frac{1}{2h_y^2}\right)\right][P_{i,j+1}+P_{i,j-1}] + \left[-2a\left(\frac{\alpha}{h_y^2}-\frac{1}{2h_x^2}\right)\right][P_{i+1,j}+P_{i-1,j}] + \\
&\left[a\alpha\left(\frac{1}{h_x^2}+\frac{1}{h_y^2}\right)\right][P_{i+1,j+1}+P_{i+1,j-1}+P_{i-1,j+1}+P_{i-1,j-1}] = F_{i,j} + \\
&\alpha[F_{i,j+1}+F_{i,j-1}+F_{i+1,j}+F_{i-1,j}] + \alpha^2[F_{i+1,j+1}+F_{i+1,j-1}+F_{i-1,j+1}+F_{i-1,j-1}]
\end{aligned} \tag{4.8}$$

Using the coefficients of the sixth-order compact approximation to the second derivative results in the same nine-point stencil for the RHS and an explicit twenty-one point stencil on the LHS:

$$\left[-2\left(a+\frac{b}{4}\right)\left(\frac{1}{h_x^2}+\frac{1}{h_y^2}\right)\right]P_{i,j}+ \tag{4.9}$$

$$\left[\frac{-2\alpha}{h_x^2}\left(a+\frac{b}{4}\right)+\frac{a}{h_y^2}\right][P_{i,j+1}+P_{i,j-1}]+\left[\frac{-2\alpha}{h_y^2}\left(a+\frac{b}{4}\right)+\frac{a}{h_x^2}\right][P_{i+1,j}+P_{i-1,j}]$$

$$\left[\frac{b}{4h_y^2}\right][P_{i,j+2}+P_{i,j-2}]+\left[\frac{b}{4h_x^2}\right][P_{i+2,j}+P_{i-2,j}]+$$

$$\left[\frac{b\alpha}{4h_x^2}\right][P_{i+2,j+1}+P_{i+2,j-1}+P_{i-2,j+1}+P_{i-2,j-1}]+$$

$$\left[\frac{b\alpha}{4h_y^2}\right][P_{i+1,j+2}+P_{i+1,j-2}+P_{i-1,j+2}+P_{i-1,j-2}]+$$

$$\left[a\alpha\left(\frac{1}{h_x^2}+\frac{1}{h_y^2}\right)\right][P_{i+1,j+1}+P_{i+1,j-1}+P_{i-1,j+1}+P_{i-1,j-1}]=F_{i,j}+$$

$$\alpha[F_{i,j+1}+F_{i,j-1}+F_{i+1,j}+F_{i-1,j}]+\alpha^2[F_{i+1,j+1}+F_{i+1,j-1}+F_{i-1,j+1}+F_{i-1,j-1}]$$

Thus for uniform cartesian grids, the stencils of Eqs. (4.8) and (4.9) are preferred because they require fewer operations and their coefficients are explicit as compared to the stencil of Eq. (4.3). The commutative property of the A_{xx} and A_{yy} matrices is valid even with non-periodic boundaries. Numerical experiments confirm that the cross-type stencil represented by Eq. (4.3) and the grid-type stencil of Eq. (4.8) or Eq. (4.9) give identical results.

4.2 Iteration Matrix

A point relaxation scheme is used to iteratively solve the system of equations represented by Eq. (4.3) of Eq. (4.8). In this approach, only the value at the central node of the stencil, $P_{i,j}$, is treated as an unknown so that the multi-diagonal system of equations degenerates to a diagonal system for one relaxation sweep, which is trivial to solve. This process can be written in matrix notation by decomposing the matrix, A, into the sum of the diagonal, lower, and upper matrices of A (Briggs 1987):

$$AP = [D - L - U]P = F \tag{4.10}$$

where the matrix, D, is the diagonal matrix of A, and the matrices, L, U, are the lower and upper matrices of A, respectively. The solution at the current iteration level, P^*, is corrected with the increment, P', to yield the solution at the next iteration level, $P = P^* + P'$. For Jacobi iteration the terms, $-LP$ and $-UP$, are assumed to be known from the previous iterate, P^*, and are moved to the RHS so that Eq. (4.10) becomes:

$$DP = F + [L + U]P^* \tag{4.11}$$

Adding the term $-DP^*$ to both sides of Eq. (4.11) casts the equations into incremental form:

$$DP' = F - AP^* = R^* \tag{4.12}$$

where R^* is the residual vector. Equation (4.12) defines one iteration of the Poisson equation. The increment, P', is computed by solving the trivial diagonal system of equations and is then added to the current iterate to yield the solution at the next iteration level:

$$P = P^* + D^{-1}R^* \tag{4.13}$$

This procedure is defined as a Jacobi iteration. Weighted Jacobi iteration can under-relax or over-relax the iterative process by multiplying the increment, P', by a relaxation parameter, ω, so that Eq. (4.13) becomes:

$$P = P^* + \omega D^{-1}R^* \tag{4.14}$$

where $0 < \omega < 1$ denotes under-relaxation, and $\omega > 1$ denotes over-relaxation. Jacobi iteration is equivalent to computing the residual of the current iterate, P^*, at all grid points followed by an update operation. In this regard, information is held and the solution is updated at all grid points simultaneously. Since the computation of the residual vector and the updating of the solution vector are completely separate operations, each operation is

fully vectorizable. This results in an improved computational rate when those operations are performed on vector computers.

Gauss-Seidel iteration makes one modification to Jacobi iteration - the updated solution is used as soon as it is computed. This can be written in matrix form by considering Eq. (4.10). The term, *-UP*, is assumed to be known from the previous iteration and is moved to the RHS requiring the solution of the lower triangular system:

$$[D-L]P = F+UP^* \tag{4.15}$$

In incremental form, Eq. (4.15) becomes:

$$P = P^* + [D-L]^{-1}R^* \tag{4.16}$$

Moving the term, *-UP*, to the RHS in Eq. (4.10) is equivalent to updating the solution vector in an ascending order (i.e., $P_{1,1}, P_{2,1}, \ldots, P_{ni,nj}$). If the term, *-LP*, is moved to the RHS instead, the variables are updated in descending order (i.e., $P_{ni,nj}, P_{ni-1,nj}, \ldots, P_{1,1}$). Many other updating strategies are possible. For instance, if the grid points are colored black or red similar to a checkerboard pattern then during the first sweep all the red points are updated, followed by an update of all the black points. This strategy is referred to as red-black Gauss-Seidel. The order in which the grid points are visited for Jacobi iteration is immaterial since the solution vector is updated only after the residual is computed at every grid point. Similar to weighted Jacobi iteration, Gauss-Seidel iteration can be under- or over-relaxed by multiplying the increment, P', by the relaxation factor, ω:

$$P = P^* + \omega[D-L]^{-1}R^* \tag{4.17}$$

4.3 Multigrid Solution

Relaxation schemes such as Jacobi and SOR applied on a single grid level suffer from poor convergence rates as the number of grid points increase. Through Fourier analysis it can be shown (Briggs 1987) that the high frequency error components (i.e. the difference between the current iterate and the fully convergenced solution) are removed very quickly, while the low frequency components require many iterations to be reduced to an acceptable level. In other words, many relaxation schemes are efficient smoothers (i.e. they remove high frequency error components with a few iteration sweeps) but are poor solvers because they require many iterations to remove low frequency components.

Multigrid methods overcome these deficiencies by utilizing a hierarchy of grids. Smooth error components are transfered to coarser grids where they appear as high frequency error components and are quickly removed by relaxation sweeps. Relaxation sweeps on the coarser grids are also much cheaper to perform.

A coarse grid correction scheme is utilized in the current study to improve the convergence rate of the pointwise relaxation scheme on a single grid. Subscripts are used to denote grid level, i.e. P_h and P_{2h} denotes the solution on the fine and coarse grids, respectively. The symbol, I_h^{2h}, is used to denote transfer from the fine to the coarse grid, while I_{2h}^h is used to denote transfer in the opposite direction. The algorithm for one coarse grid correction is given below and additional details can be found in Briggs (1987).

(1) Smooth the current iterate, P_h^*, on the fine grid ν_1 times:

$$A_h P_h^{(1)} = F_h$$

(2) Calculate the residual on the fine grid:

$$R_h = F_h - A_h P_h^{(1)}$$

(3) Transfer (restrict) the residual to the coarse grid, where it is used as the source term for the error equation:

$$F_{2h} = I_h^{2h} R_h$$

(4) Solve for the error on the coarse grid:

$$E_{2h} = A_{2h}^{-1} F_{2h}$$

(5) Transfer (prolongate) the error to the fine grid and correct the solution:

$$P_h^{(2)} = P_h^{(1)} + I_{2h}^h E_{2h}$$

(6) Perform ν_2 post-relaxation sweeps:

$$A_h P_h = F_h$$

Standard second-order interpolation is used to transfer variables from the coarse to the fine grid, while the full weighting operator is used to transfer variables in the opposite direction. Although the above algorithm utilizes only two grid levels, improved efficiency results from encorporating as many grid levels as possible. In this respect, the direct solution of the error equation in step (5) is performed on a very coarse grid requiring a small number of operations. Simulations presented in Chaps. 6 and 7 utilize five grid levels.

Since the simulations are performed on vector computers, Jacobi iteration was utilized for relaxation sweeps because it is fully vectorizable. Two pre- and two post-relaxation sweeps were performed on each grid. Through numerical experiments, the optimum relaxation factor for the uniform grid formulation was found to be, $\omega = 0.9$. Typically, three

coarse grid corrections were performed for the solution of the Poisson equation which reduced the initial L2 norm of the residual two orders of magnitude. Tests using twice as many corrections resulted in a maximum of 3% difference in the pressure.

4.4 Performance of Computer Code

The computational rate of the computer code on uniform and curvilinear grids is given in this section. The numerical formulation was extended to curvilinear grids which was used to concentrate grid points in the mixing layers of the rectangular jet near the inflow. Downstream of the potential core, the flow is fully turbulent. Clustering of the grid to resolve large gradients due to small scale structures is not possible without the use of time-varying, adaptive grids (which is outside the scope of the present study). Therefore, the grid is gradually relaxed to uniform spacing in this region. As mentioned in Sec. 4.1, uniform grids enable manipulation of the discrete Poisson equation leading to a reduced stencil size and cost as compared with the curvilinear grids making the computational rate roughly one order of magnitude less. Part of the reason for the increase in computational rate is that convergence rates for the multigrid solution of the Poisson equation deteriorate with grid clustering and large aspect ratio. Table 4.1 lists the computational rate for Cartesian and curvilinear formulation. Also listed in the table is the rate of a second-order accurate formulation from Le and Moin (1994). Therefore, the uniform grid formulation was utilized for most of the simulations to be presented in Chaps. 6 and 7.

Table 4.1 Computational rate

Study	Grid	Scheme	Rate (cpu/t.s../pt)
Wilson	Cartesian	fourth-order compact	5.7×10^{-6}
Wilson	curvilinear	fourth-order compact	6.2×10^{-5}
Le & Moin (1992)	Cartesian	second-order central	3.9×10^{-6}

Chapter 5

VALIDATION OF NUMERICAL METHOD

In this chapter, the numerical formulation is validated through the solution of a wide range of benchmark problems. Emphasis is placed on the numerical approximation of spatial derivatives. In particular, the convection terms (containing first derivatives) present the most difficulty in numerical approximation since large dispersion errors exist at high wavenumbers ($k\Delta x \sim \pi$). It is essential that the numerical approximation to the first derivative provide low dispersion errors over a large range of wavenumbers. This is especially true in 3-D simulations where reducing the required number of grid points by half in each coordinate direction leads to eight times fewer total grid points.

In Chap. 3, the theory showed that compact schemes require roughly five times fewer points to accurately resolve a given mode compared to the standard second-order central difference approximation to the first derivative. This theory is tested by solving some practical problems ranging from the 1-D convection equation to the 2-D Navier-Stokes equations.

The purpose of the present chapter is to *(i)* demonstrate the resolution qualities of the compact schemes and *(ii)* compare and contrast results from the compact scheme with results from other popular schemes.

5.1 1-D Convection Equation

The first problem to be solved is the 1-D convection equation, Eq. (3.12), which tests the time advancement scheme and the numerical approximation to the first derivative. The exact solution corresponds to convection of the scalar profile at the constant wave speed, c. Distortion in the shape of the profile indicates dissipation and/or dispersion errors in the solution. The convection of a Gaussian profile was solved using three approximations to the first derivative; *(i)* a second-order central difference, *(ii)* a third-order upwind, and *(iii)* the fourth-order compact approximation outlined in Section 3.2.1. The third-order Runge-Kutta scheme was used to advance the equation in time for all spatial schemes. In addition, the CFL number (and thus the time step) was kept small so that resulting errors are due to the spatial formulation.

The parameters and initial conditions are those proposed at the ICASE/LARC Workshop on Benchmark Problems in Computational Aeroacoustics, Hardin et al. (1995):

$$u(x, 0) = 0.5\exp\left[-\left(\frac{x}{3}\right)^2 \ln(2)\right], \tag{5.1}$$

$$-20 \le x \le 450\,,\ N_x = 470 \text{ grid points}, c = 1$$

Since the specified grid is relatively coarse in comparison with the initial conditions, this problem provides an excellent test of the resolution power of the numerical approximation. Figure 5.1 shows the computed solutions at $t = 400$ after the profile has convected to $x = 400$. There is little discernible difference between the exact solution and the solution with the fourth-order compact scheme. However, the solutions with the second-order central difference and the third-order upwind approximations show greatly reduced peak values and large, dispersive waves trailing the Gaussian profile. The errors from the second-order central difference scheme are the most severe.

It is difficult to determine by inspection what portion of the error is dispersive and what portion is dissipative. The solutions are transformed into wavenumber space using a Fourier transform method and compared with the exact solution in Fig. 5.2 to address this issue. The graph displays the resulting complex Fourier coefficient in polar form with the amplitude displayed in Fig. 5.2a and the phase angle in Fig. 5.2b. It can be seen from Fig. 5.2a that the solutions computed with the second-order central difference and fourth-order compact schemes predict the correct amplitude for all modes. The amplitude of the solution computed with the third-order upwind scheme is reduced or dissipated, especially at higher wavenumbers. Figure 5.2b shows that the fourth-order compact scheme predicts the correct phase angle even for the highest wavenumbers.

The phase angle from the second- and third-order solutions are only correctly predicted for the very lowest wavenumbers ($k < 0.2$ for the second-order solution and $k < 0.3$ for the third-order solution). Large dispersion errors are evident at high wavenumbers. The above trends in the numerical solutions are consistent with the dissipation/dispersion error theory for the 1-D convection equation and show the resolution power of the compact schemes.

The second problem, also proposed at the ICASE/LARC Workshop on Benchmark Problems, is the solution of the 1-D convection equation in a spherical coordinate system. The governing equation takes the form:

$$\frac{\partial u}{\partial t} + \frac{u}{x} + \frac{\partial u}{\partial x} = 0 \qquad (5.2)$$

$$5 \le x \le 450, N_x = 445 \text{ grid points}$$

Initial Conditions:

$$u(x, 0) = 0$$

Boundary Conditions:

$$u(5, t) = \sin\left(\frac{\pi t}{4}\right)$$

Figure 5.3 shows the exact solution at $t = 400$ which corresponds to a damped sine wave due to the addition of the u/x term in the governing equation. Fig. 5.4 shows computational results for the region, $200 < x < 220$ using the third-order upwind approximation to the first derivative on two grids and the fourth-order compact scheme. The solution with 16 points per wavelength shows a greatly reduced amplitude and a phase shift relative to the exact solution. It takes roughly 64 PPW (not shown) to reproduce the exact solution with the third-order upwind approximation. The fourth-order compact approximation is able to reproduce the exact solution with 8 PPW.

5.2 2-D Convection Equation

Multidimensional effects of the numerical formulation are explored by solving for the convection of an inverted cone around a circle. This problem is governed 2-D convection equation:

$$\frac{\partial u}{\partial t} + c_x \frac{\partial u}{\partial x} + c_y \frac{\partial u}{\partial y} = 0 \qquad (5.3)$$

where $c_x = -y$ and $c_y = x$, are the convection speeds in the x and y directions, respectively. The initial conditions are that of an inverted sharp cone centered at $x, y = -0.5, 0$. The exact solution corresponds to the cone being convected counterclockwise in a circular path of radius, $r_o = 0.5$ with a period of 2π. Distortion of the shape of the cone is an indication of dispersion and/or dissipation errors.

Figure 5.5 shows computed results after one revolution of the cone using *(a)* a third-order upwind approximation and *(b)* a fourth-order compact approximation to the first

derivatives on a 32 x 32 grid with uniform spacing. This grid defines the shape of the cone with a maximum of 8 points in each coordinate direction. The exact shape of the cone is included to the right of the computed solution at $x, y = 0.5, 0$ for comparison purposes. The third-order solution (Fig 5.5a) shows that the sharp point of the cone is greatly diffused and that dispersion errors are evident trailing the cone. A grid of 128 x 128 (or 32 points defining the shape of the cone) must be used with the third-order upwind approximation before the shape of the cone is faithfully reproduced. The fourth-order compact solution (Fig 5.5b) shows that the shape of the cone is not distorted as it is convected around the circle on the 32 x 32 grid. Indeed, the only noticeable error is a very small "grid to grid" oscillation due to the absence of physical viscosity in this problem and numerical viscosity in the compact scheme.

Figure 5.6 shows results for the same problem after one revolution obtained by Orszag (1971) using *(a)* second-order Arakawa finite-difference, *(b)* fourth-order Arakawa finite-difference, and *(c)* a spectral approximation to the first derivatives on a 32 x 32 grid. The finite difference solutions show errors similar to the third-order solutions in Fig. 5.5. The spectral method, which provides exact differentiation for all wavenumbers representable on the 32 x 32 grid, convects the cone without distorting its shape. Thus, the solution using the compact scheme is closer to the spectral solution than the solutions obtained with conventional finite difference schemes. The higher accuracy and resolution characteristics are achieved by the implicit treatment of the derivative. Even though the stencil size of the compact scheme is finite, the implicit treatment of the derivatives makes the scheme global much like that of spectral methods.

5.3 2-D Euler/Navier-Stokes Equations

In the previous sections, the effect of numerical approximation on the accuracy of the convection terms was documented. In this section, the accuracy of the enforcement of the continuity equation through the solution of the Poisson equation for pressure is documented by solving the 2-D Euler/Navier-Stokes equations. Since the Navier-Stokes equations contain viscous terms, the numerical approximation to the second derivative is also tested. The test problems chosen for validation contain many features of the 3-D jets which are simulated in the current study. In this respect, the test problems are not merely academic exercises. There benchmark problems are solved; *(i)* a temporally-developing plane mixing layer (2-D Stuart's problem), *(ii)* 2-D viscous wave decay, and *(iii)* the doubly periodic jet. Problems *(i)* and *(ii)* have exact solutions while results of *(iii)* will be compared to a highly resolved spectral simulation.

5.3.1 2-D Temporally-Developing Plane Mixing Layer

Exact solutions to the Euler or Navier-Stokes equations for general flows do not exist due to the non-linearity of the convection terms. However, under special conditions exact solutions may be found. An exact solution for the temporally-developing mixing layer was first published by Stuart (1967). The initial conditions for the 2-D Stuart's problem correspond to a steady hyperbolic tangent function for the streamwise velocity component with a periodic array of vortex cores in the mixing region which cause the solution to vary in time. The wavelength of the disturbance corresponds to the neutral mode such that the disturbance is convected in the streamwise direction with no change in amplitude. The exact solution for the streamwise velocity component, u, and the transverse velocity component, v is given by:

$$u(x, y, t) = c + \frac{C\sinh(y)}{C\cosh(y) + A\cos(x - ct)}$$

$$v(x, y, t) = \frac{A\sin(x-ct)}{C\cosh(y) + A\cos(x-ct)} \tag{5.4}$$

where $A = \sqrt{C^2 - 1}$ is a parameter which controls the strength of the perturbation and c is the convective speed of the mixing layer. The flow is periodic in the streamwise direction with length, $L_x = 2\pi$, $0 \le x \le 2\pi$. The flow is infinite in the transverse direction but in this study is truncated at a finite distance, $-L_y \le y \le L_y$, such that the zero-traction freestream boundary condition outlined in Section 2.2.3 is well approximated. Tests which vary the transverse domain height, $2L_y$, show that $L_y = 10$ is sufficiently large to implement this boundary condition. The exact solution is shown in Fig. 5.7a with parameters, $c = 1, A = 1/2$. A uniform, cartesian grid is used for the simulations in this section. Unless otherwise specified, the third-order Runge-Kutta scheme is used for time advancement and time steps are sufficiently small so that spatial errors are dominant.

Figure 5.7b shows the numerical solution at $t = 20\pi$ (ten flow through times) on a relatively coarse grid of 13 (streamwise) x 41 (transverse) using the fourth-order compact approximation of convection terms and pressure. The solution of pressure involves the computation of the source term and the discretization of the Laplacian operator in Eq. (3.39). In addition, once the Poisson equation is solved for pressure, the gradient of pressure is computed which is required to advance the momentum equation in time. Therefore, the phrase "fourth-order solution of pressure" corresponds to the source and pressure gradient terms computed with the compact first derivative scheme outlined in Section 3.2.1 while the Laplacian operator is discretized using the compact second derivative scheme outlined in Section 3.2.2.

Even though the grid is relatively coarse (13 streamwise points per wavelength and roughly 8 points in the mixing region at $y \sim 0$), there is little discernible difference between the exact and numerical solutions after ten flow through times. It is important to

check the convergence of the error as the grid is refined to expose any coding errors, to demonstrate that the order of error convergence seen in practical computations is that predicted by a Taylor series analysis, and to gain confidence in the numerical formulation. Tables 5.1 and 5.2 give a quantitative measure of the L2 and maximum errors in the velocity components at $t = 0.1$ using the fourth- and sixth-order compact approximations to the convection terms and solution of pressure, respectively. Solution errors from three grids are shown where the grid spacing in the x and y directions is halved from coarsest to finest grid. The results show that the L2 and maximum errors converge at roughly the rate predicted by a Taylor series analysis as the grid is refined. The order, N, is computed using the solution error from three grids of spacing, h, $2h$, and $4h$:

$$N = \frac{\ln\left[\frac{\phi_h - \phi_{2h}}{\phi_{2h} - \phi_{4h}}\right]}{\ln 2} \tag{5.5}$$

where ϕ_h, ϕ_{2h}, ϕ_{4h} are the errors on the h, $2h$,and $4h$ grids, respectively. In using Eq. (5.5) it is assumed that the solution is fully resolved on all three grids and that the leading truncation error term is dominant (Demuren and Wilson 1994).

Table 5.1 Solution errors for 2-D Stuart's Problem at $t = 0.1$ using fourth-order compact approximation for convection terms and solution of pressure.

Grid (ni x nj)	Max U Error	Max V Error	L2 Norm U	L2 Norm V
13 x 41	0.18×10^{-2}	0.21×10^{-2}	0.18×10^{-3}	0.24×10^{-3}
25 x 81	0.86×10^{-4}	0.12×10^{-3}	0.80×10^{-5}	0.11×10^{-4}
49 x 161	0.47×10^{-5}	0.68×10^{-5}	0.57×10^{-6}	0.74×10^{-6}
Order (N)	4.2	4.1	4.5	4.5

Table 5.2 Solution errors for 2-D Stuart's Problem at $t = 0.1$ using sixth-order compact approximation for convection terms and solution of pressure.

Grid (ni x nj)	Max U Error	Max V Error	L2 Norm U	L2 Norm V
13 x 41	0.73×10^{-3}	0.10×10^{-2}	0.97×10^{-4}	0.11×10^{-3}
25 x 81	0.17×10^{-4}	0.20×10^{-4}	0.12×10^{-5}	0.14×10^{-5}
49 x 161	0.15×10^{-5}	0.18×10^{-5}	0.25×10^{-6}	0.45×10^{-6}
Order (N)	5.4	5.7	6.3	6.2

To address the effect of computing the pressure with a lower-order formulation, the 2-D Stuart's problem was solved using second-order central, fourth-order compact and sixth-order compact approximation of the convection terms but a second-order central difference solution of the pressure. The results of the three computations are shown in Tables 5.3 - 5.5. The results of the three computations show that the lower-order solution of pressure results in the overall convergence of the error being second-order, even if the convection terms receive a higher-order treatment. All terms must be discretized using higher-order approximations to achieve higher-order error convergence rates.

Table 5.3 Fourth-order compact approximation for convection terms/ second-order solution of pressure.

Grid (ni x ni)	Max U Error	Max V Error	L2 Norm U	L2 Norm V
13 x 41	0.89×10^{-2}	0.11×10^{-1}	0.20×10^{-2}	0.20×10^{-2}
25 x 81	0.20×10^{-2}	0.25×10^{-2}	0.42×10^{-3}	0.44×10^{-3}
49 x 161	0.51×10^{-3}	0.58×10^{-3}	0.11×10^{-3}	0.11×10^{-3}
Order (N)	2.2	2.2	2.4	2.2

Table 5.4 Sixth-order compact approximation for convection terms/ second-order solution of pressure.

Grid (ni x ni)	Max U Error	Max V Error	L2 Norm U	L2 Norm V
13 x 41	0.87×10^{-2}	0.11×10^{-1}	0.20×10^{-2}	0.20×10^{-2}
25 x 81	0.20×10^{-2}	0.25×10^{-2}	0.42×10^{-3}	0.44×10^{-3}
49 x 161	0.45×10^{-3}	0.60×10^{-3}	0.10×10^{-3}	0.11×10^{-3}
Order (N)	2.1	2.2	2.3	2.2

Table 5.5 Second-order central difference approximation for convection terms/ second order solution of pressure.

Grid (ni x ni)	Max U Error	Max V Error	L2 Norm U	L2 Norm V
13 x 41	0.11×10^{-1}	0.15×10^{-1}	0.21×10^{-2}	0.20×10^{-2}
25 x 81	0.22×10^{-2}	0.38×10^{-2}	0.45×10^{-3}	0.53×10^{-3}
49 x 161	0.61×10^{-3}	0.98×10^{-3}	0.11×10^{-3}	0.13×10^{-3}
Order (N)	2.4	1.9	2.3	2.1

The solution of the 2-D Stuart's problem validates the numerical formulation for the enforcement of the continuity equation and the solution of the Poisson equation for pressure. In addition, it has been shown that the zero-traction freestream boundary condition

for shear flows is a valid approximation provided that the freestream boundary is located a sufficiently far distance from the mixing region.

5.3.2 Viscous Wave Decay

The numerical treatment of viscous terms is validated by solving the 2-D viscous wave decay problem which is governed by the Navier-Stokes equations. The domain for this problem is periodic in both the x and y directions where periodic boundary conditions are applied. The exact solution is given by:

$$u(x, y, t) = -\cos(x)\sin(y)e^{-\left(\frac{2t}{Re}\right)}$$

$$v(x, y, t) = \sin(x)\cos(y)e^{-\left(\frac{2t}{Re}\right)}$$

where $Re = 20$, $L_x = L_y = 1$. The exact solution consists of sinusoidal waves in the x and y directions which decay in time. Table 5.6 shows the L2 norm of the error at $t = 0.025$ using the fourth- and sixth-order compact approximations for convection and diffusion terms and the solution of pressure. The results are compared to the fourth-order, Essentially Non-Oscillatory (ENO) scheme from Weinan and Shu (1992). The error converges at fourth- and sixth-order rates thus validating the numerical treatment of the viscous terms and again validating the convection terms and the solution of pressure. The error of the ENO scheme converges at a fourth-order rate, but is more than two orders of magnitude greater than the fourth-order compact results. The error magnitude of the sixth-order compact formulation on the 128 x 128 grid has reached the round-off error level ($\sim 10^{-13}$) of the Cray supercomputer, indicating that extremely accurate results are obtained on average-sized grids.

Table 5.6 Solution errors for 2-D viscous wave decay.

Grid (ni x nj)	4th oa compact	6th oa compact	3rd(4th) oa ENO
16 x 16	0.14×10^{-6}	0.10×10^{-7}	-
32 x 32	0.77×10^{-8}	0.15×10^{-9}	0.53×10^{-5}
64 x 64	0.47×10^{-9}	0.27×10^{-11}	0.32×10^{-6}
128 x 128	0.71×10^{-10}	0.11×10^{-12}	0.20×10^{-7}
Order(N)	4.0	6.0	4.0

5.3.3. Doubly Periodic Jet

The last validation test is the solution of the doubly periodic jet which is governed by the 2-D Euler equations. The initial conditions correspond to a jet or "top hat" profile for the streamwise velocity component. The initial conditions and problem parameters are:

$$u(x, y, 0) = \begin{pmatrix} \tanh\left[\frac{(y-\pi/2)}{\rho}\right]; y \le \pi \\ \tanh\left[\frac{(3\pi/2-y)}{\rho}\right]; y > \pi \end{pmatrix}$$

$$v(x, y, 0) = \delta \sin(x)$$

where $L_x = L_y = 2\pi$, $\delta = 0.05$, and $\rho = \pi/15$. The flow begins with two parallel, finite-thickness shear layers, one with positive vorticity and the other with negative vorticity. A small amplitude perturbation is provided through the transverse velocity component which causes the shear layers to roll up into vortex cores as they evolve. Between the vortex cores, the shear layers are stretched and thinned as they are wound around the vortex cores. Without viscosity, the scales of motion become smaller and smaller so that eventually resolution is lost on any fixed grid. This problem represents a worst case scenario where the scales of motion cannot be resolved on the grid. Therefore, it is an extremely demanding test of the resolution power of the numerical formulation.

Figure 5.8 shows vorticity contours of the evolution of the doubly periodic jet using spectral methods on a highly resolved grid of 512 x 512 from Weinan and Shu (1992). An 18th-order filter has been used to remove energy at the highest wavenumbers which would otherwise contain aliasing errors. Since spectral methods yield exact differentiation and no unphysical oscillations occur during the time interval, $0 < t < 8$, we can infer that this simulation is extremely accurate during this period. The vorticity contours at $t = 10$ show the beginning of unphysical oscillations or "wriggles" which is a sign that the computations are under-resolved and the smallest scales of motion are determined by the grid and not the physics of the problem.

Figure 5.9 shows vorticity contours for an unfiltered simulation of the doubly periodic jet using the sixth-order compact formulation for convection terms and the solution ot pressure on a 128 x 128 grid. Even though the simulation contains 1/16th the number of grid points used in the spectral simulation, all of the relevant features of the jet are captured. The results show that the location of the braids and details of the vortex cores are well predicted. However, for $t \geq 6$, the results are not as smooth as the spectral simulation and unphysical "wriggles" appear in the braid region at $t = 10$.

Figure 5.10 shows vorticity contours from a simulation using the sixth-order compact scheme where the velocity field is filtered every ten time steps with an explicit sixth-order filter. For this computation, the velocity field is filtered in the x and y coordinate directions to remove energy at the highest wavenumbers ($k\Delta x \sim \pi$). The unfiltered quantity, ϕ, is filtered in the x coordinate direction to produce the filtered quantity, $\hat{\phi}$:

$$\alpha\hat{\phi}_{i-1} + \hat{\phi}_i + \alpha\hat{\phi}_{i+1} = a\phi_i + \frac{b}{2}(\phi_{i+1} + \phi_{i-1}) + \frac{c}{2}(\phi_{i+2} + \phi_{i-2}) + \frac{d}{2}(\phi_{i+3} + \phi_{i-3}) \tag{5.6}$$

where α, a, b, c, and d are the coefficients of the filter. The coefficients for the sixth-order explicit filter are summarized in Table 5.7 along with a second-order explicit and fourth-order compact filter. A similar equation exists for filtering in other coordinate directions. Since the boundaries for this problem are periodic, no additional boundary schemes are required. For problems with non-periodic boundaries, such as the simulations presented in Chap. 7, the following fourth-order boundary filters are used at the first three grid points:

$$\hat{\phi}_1 = \frac{15}{16}\phi_1 + \frac{1}{16}(4\phi_2 - 6\phi_3 + 4\phi_4 - \phi_5)$$

$$\hat{\phi}_2 = \frac{3}{4}\phi_2 + \frac{1}{16}(\phi_1 + 6\phi_3 - 4\phi_4 + \phi_5)$$

$$\hat{\phi}_3 = \frac{5}{8}\phi_3 + \frac{1}{16}(-\phi_1 + 4\phi_2 + 4\phi_4 - \phi_5) \qquad (5.7)$$

By transforming the filter from physical to wavenumber space, its effect on the various modes can be clearly shown. The transfer function defines the filtering operation in wavenumber space (Lele 1992):

$$T(k\Delta x) = \frac{a + b\cos(k\Delta x) + c\cos(2k\Delta x) + d\cos(3k\Delta x)}{1 + 2\alpha\cos(k\Delta x)} \qquad (5.8)$$

The transfer function for the sixth-order explicit filter is plotted in Fig. 5.11 along with a second-order explicit and fourth-order compact filter for comparison. The LES presented in Chap. 7 utilizes the fourth-order compact scheme together with this fourth-order compact filter. It can be seen that the fourth- and sixth-order filters eliminate the highest wavenumber ($k\Delta x = \pi$) while leaving the low wavenumbers unchanged. The fourth-order compact filter is a high-bypass filter in the sense that relatively high wavenumber modes ($k\Delta x < 1.5$) pass through the filter without being changed. Recall from Fig. 3.2 that the approximation to the first derivative is accurate for the low to moderately high

wavenumbers and that wavenumbers, $k\Delta x \sim \pi$, are not well represented. Therefore, the effect of the filter is to remove energy from those modes which are not well represented.

The vorticity contours from the filtered simulation (Fig. 5.10) show that the filtering operation removes the unphysical oscillations while maintaining the fine scale details of the flow. In Fig. 5.12, a simulation using the fourth-order ENO scheme from Weinan and Shu (1992) is shown for comparison purposes.The simulation using the ENO scheme with the same grid shows that the braids and vortex cores are diffused and that information is lost for $t \geq 8$. A simulation of the doubly periodic jet at $t = 10$ using the sixth-order compact scheme and explicit filter is shown in Fig. 5.13 on a 256 x 256 grid.

Table 5.7 Coefficients for filters

Scheme	α	a	b	c	d
second-order, explicit	0	1/2	1/2	0	0
fourth-order, compact	0.475	$\frac{(5+6\alpha)}{8}$	$\frac{(1+2\alpha)}{2}$	$\frac{(1-2\alpha)}{8}$	0
sixth-order, explicit	0	11/16	15/32	-3/16	1/32

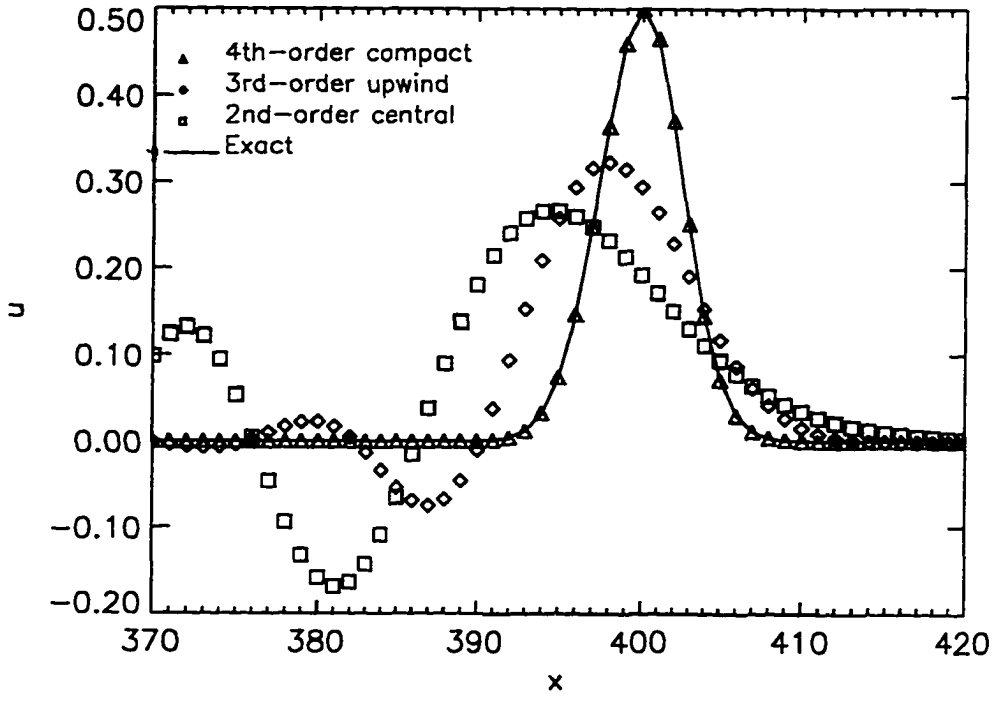

Fig 5.1 **Solution to the 1-D convection equation at $t = 400$ in physical space for various finite difference approximations of the first derivative term.**

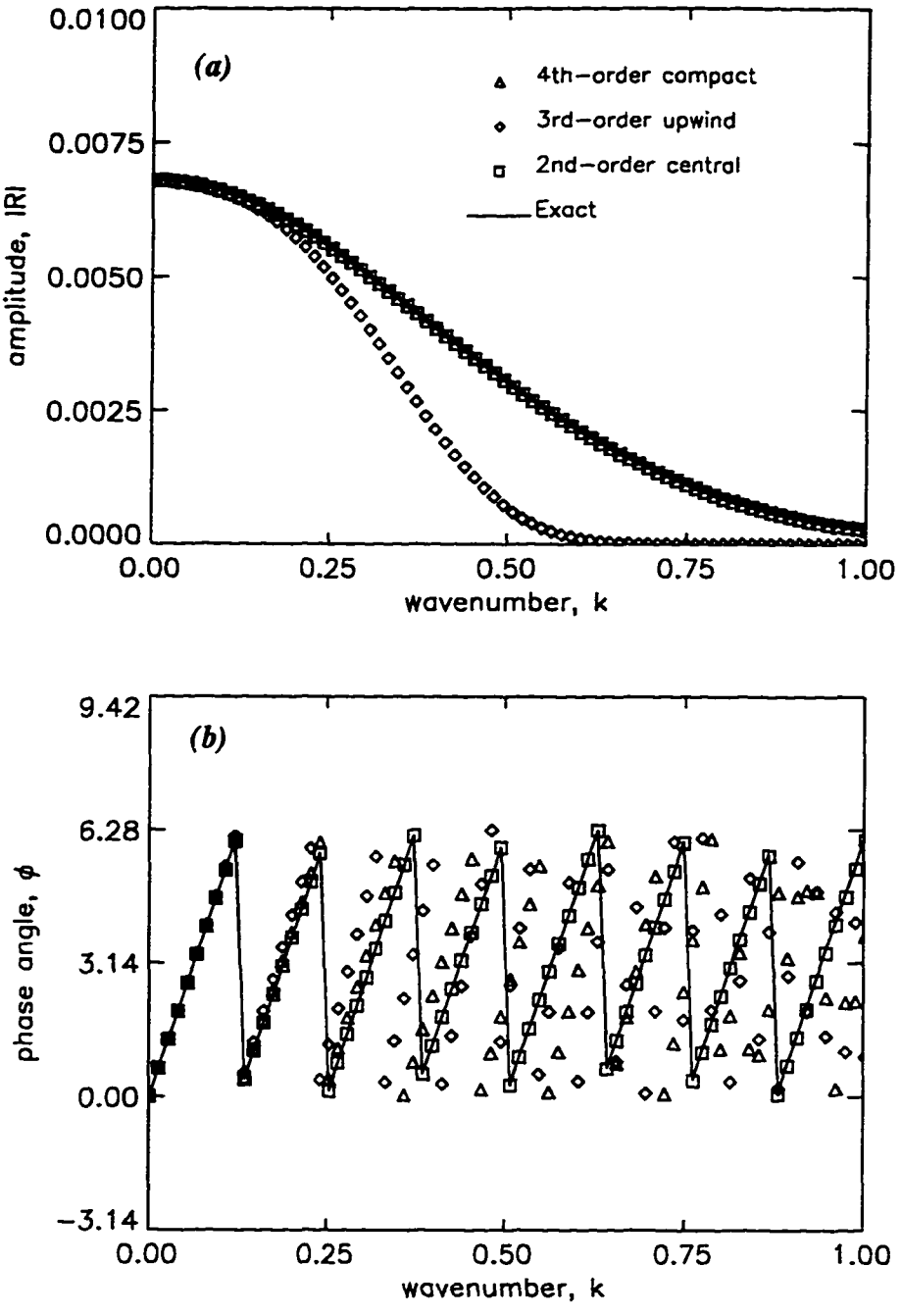

Fig 5.2 **Solution to the 1-D convection equation at t = 400 in wavenumber space for various finite difference approximations of the first derivative term, *(a)* amplitude and *(b)* phase angle.**

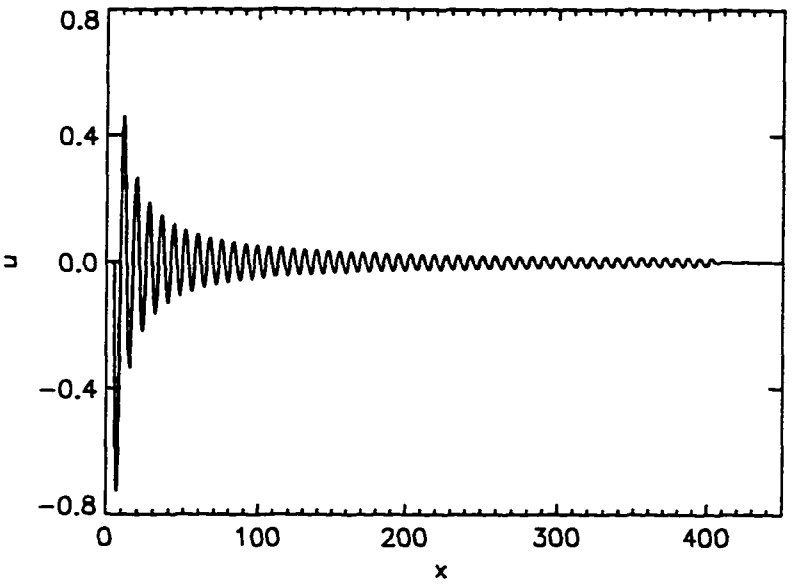

Fig 5.3 Exact solution to the spherical wave problem at $t = 400$.

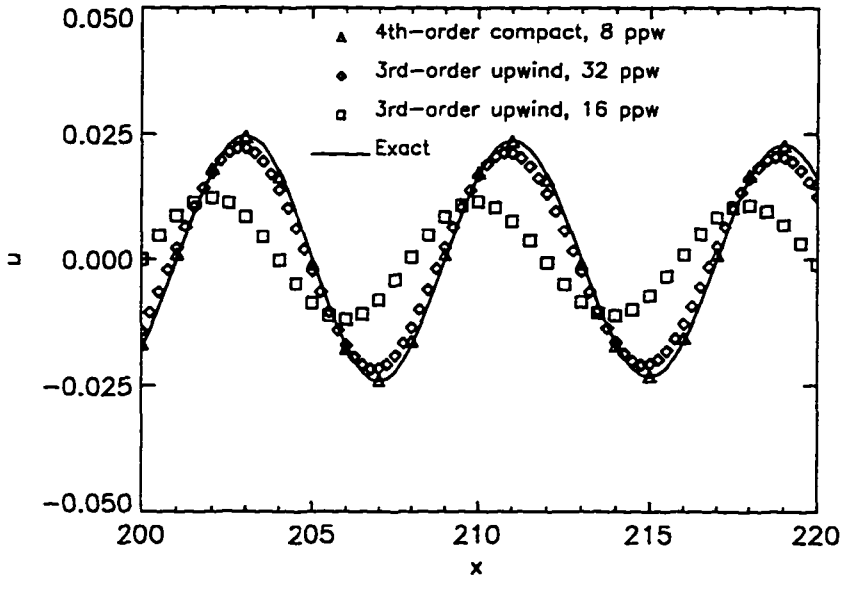

Fig 5.4 Numerical solution of the 1-D spherical wave problem at $t = 400$ for the region, $200 < x < 220$.

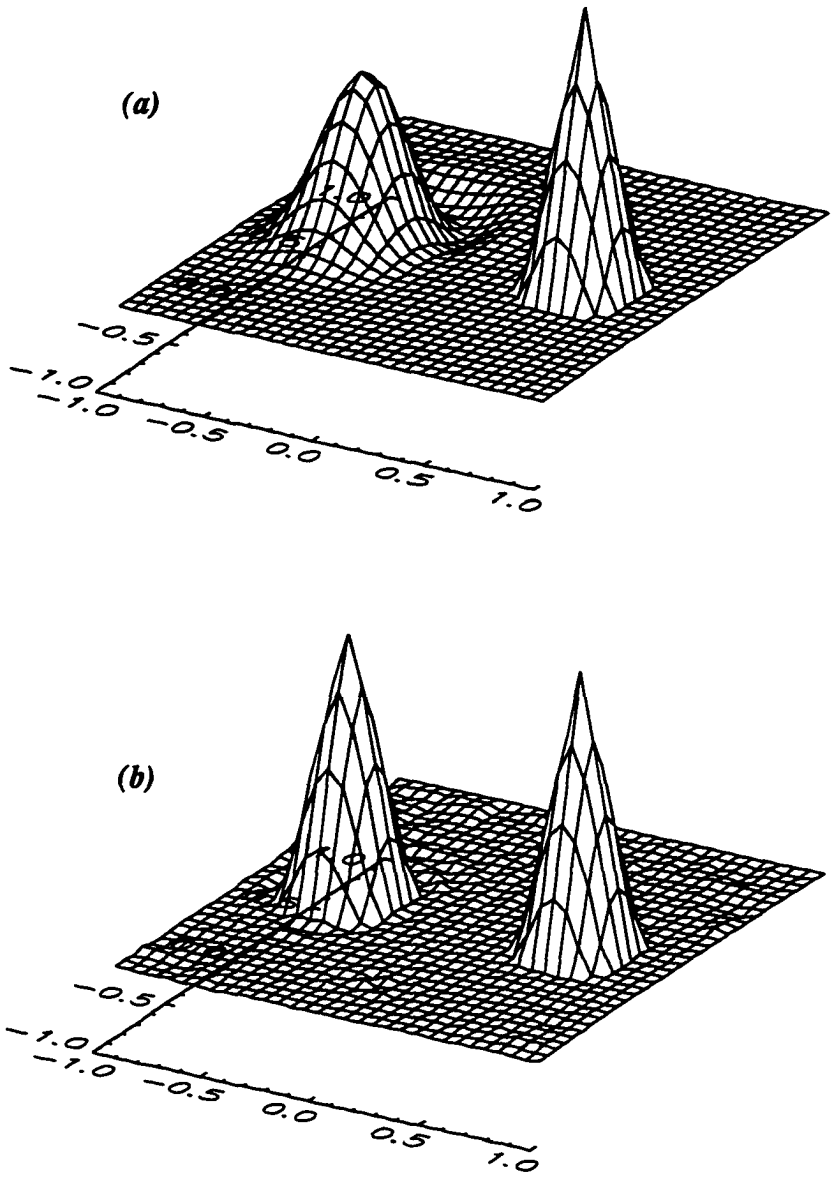

Fig 5.5 **Numerical solution of the rotating cone problem after one revolution on a 32 *x* 32 grid *(a)* third-order upwind scheme, *(b)* fourth-order compact scheme. Numerical solution is shown to the left, exact solution to the right.**

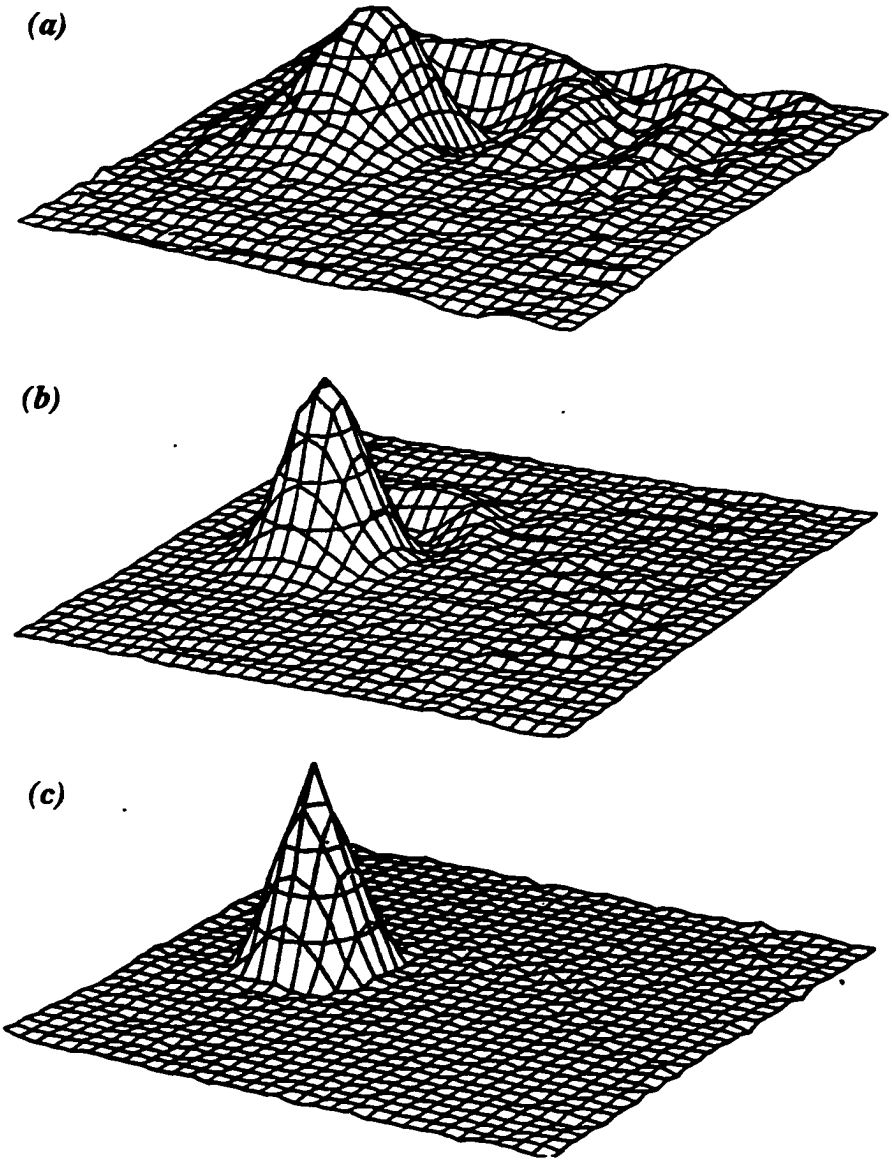

Fig 5.6 **Numerical solution of the rotating cone problem after one revolution on a 32 x 32 grid from Orszag (1971), *(a)* second-order Arakawa scheme, *(b)* fourth-order Arakawa scheme, and *(c)* spectral methods.**

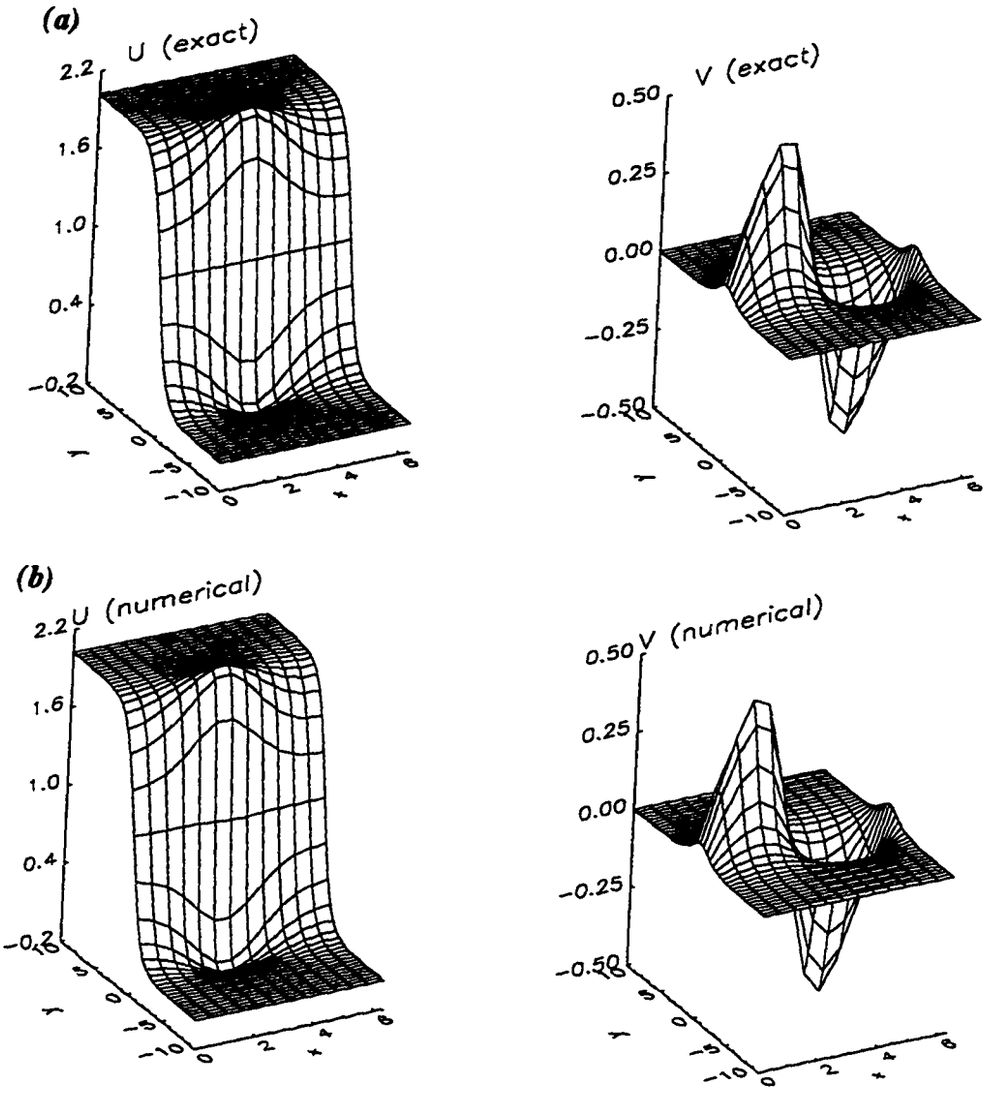

Fig 5.7 **Solution of the Stuart's problem, *(a)* Exact solution and *(b)* numerical solution using fourth-order compact scheme on a 13 x 14 grid at** $t = 20\pi$.

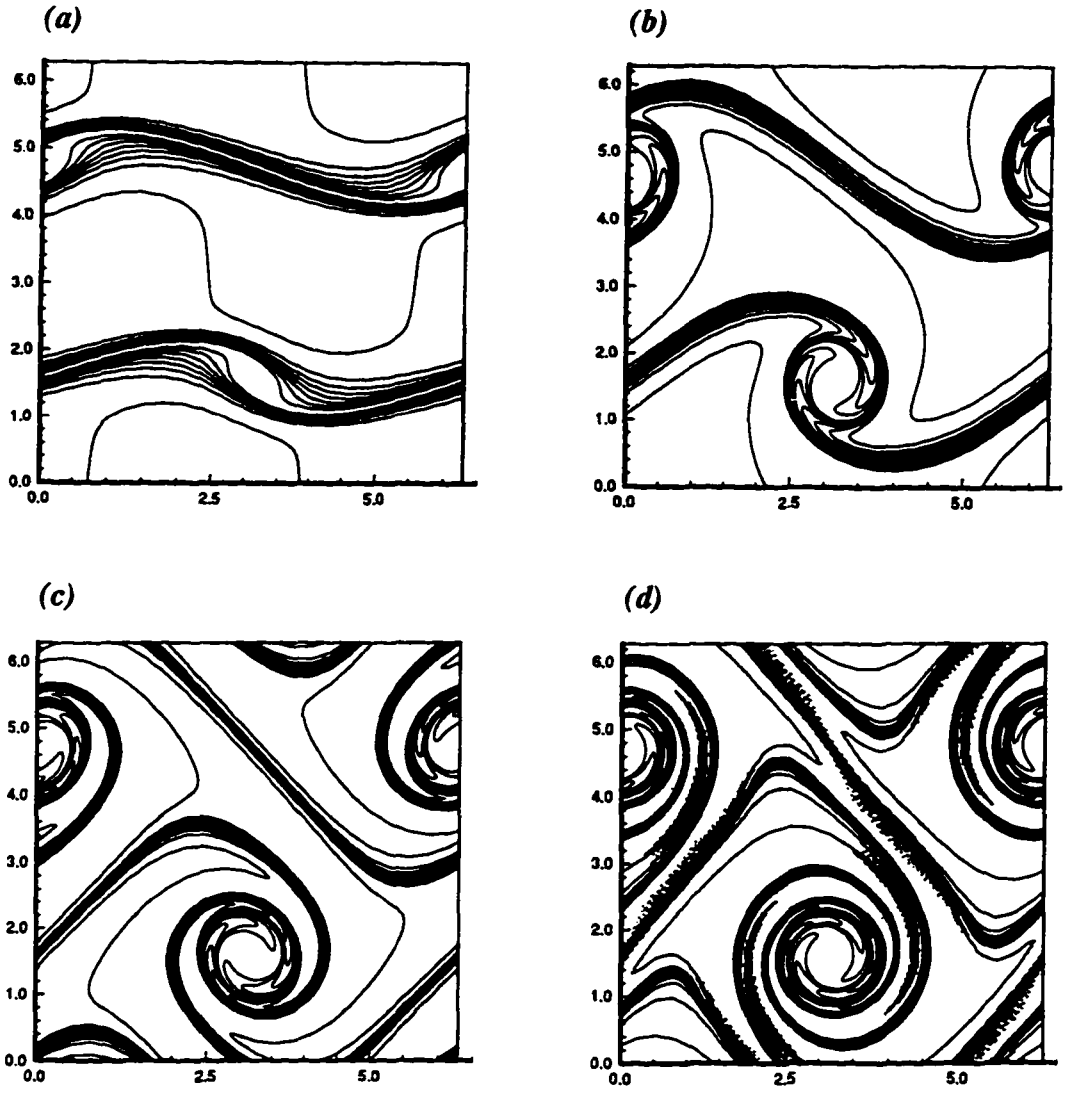

Fig 5.8 **Numerical solution of the double shear layer using spectral methods on a 512^2 grid from Weinan and Shu (1992), *(a)* $t = 4$, *(b)* $t = 6$, *(c)* $t = 8$, and *(d)* $t = 10$.**

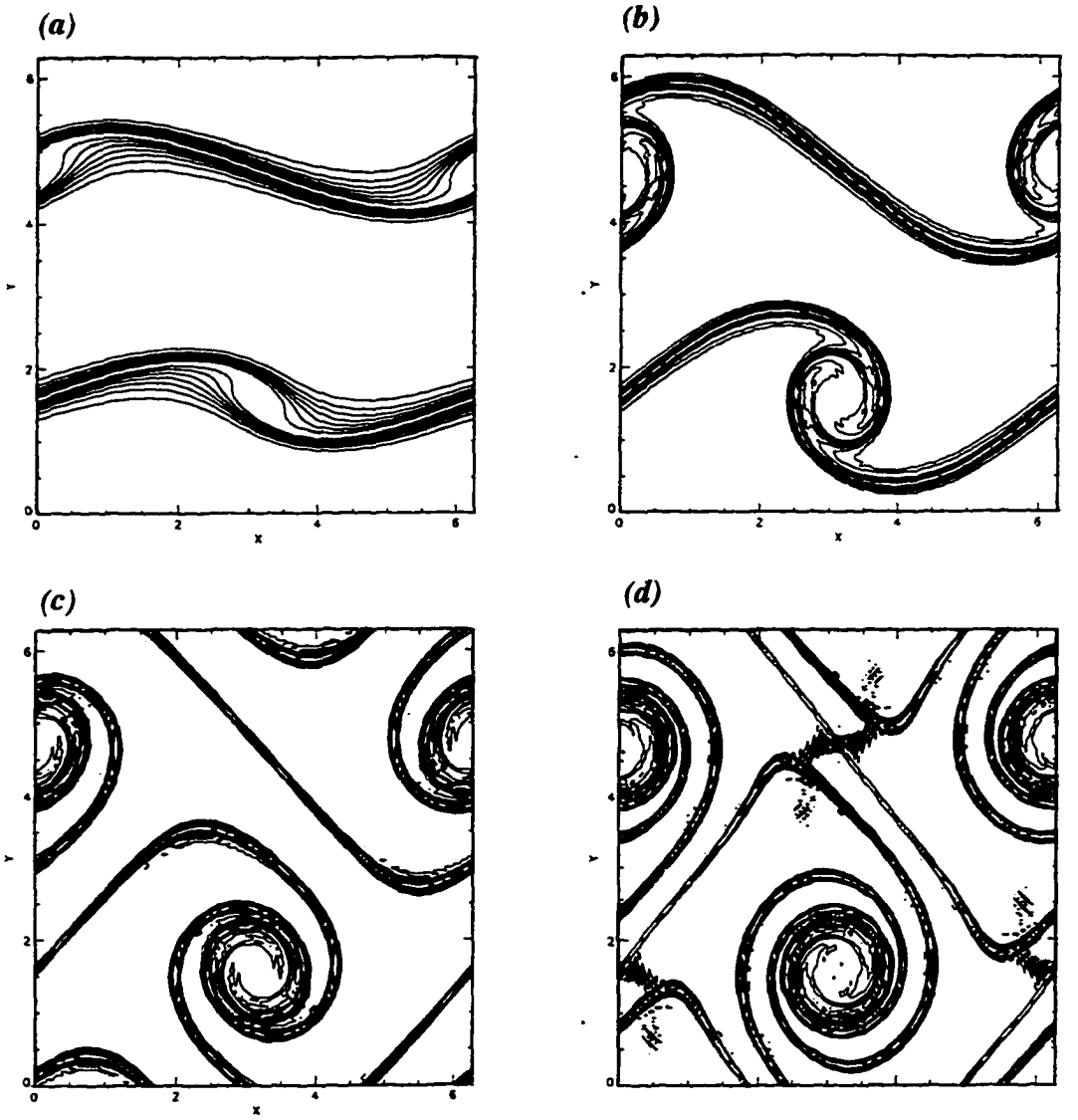

Fig 5.9 **Numerical solution of the double shear layer using the unfiltered, sixth-order compact scheme on a 128^2 grid, *(a)* $t = 4$, *(b)* $t = 6$, *(c)* $t = 8$, and *(d)* $t = 10$.**

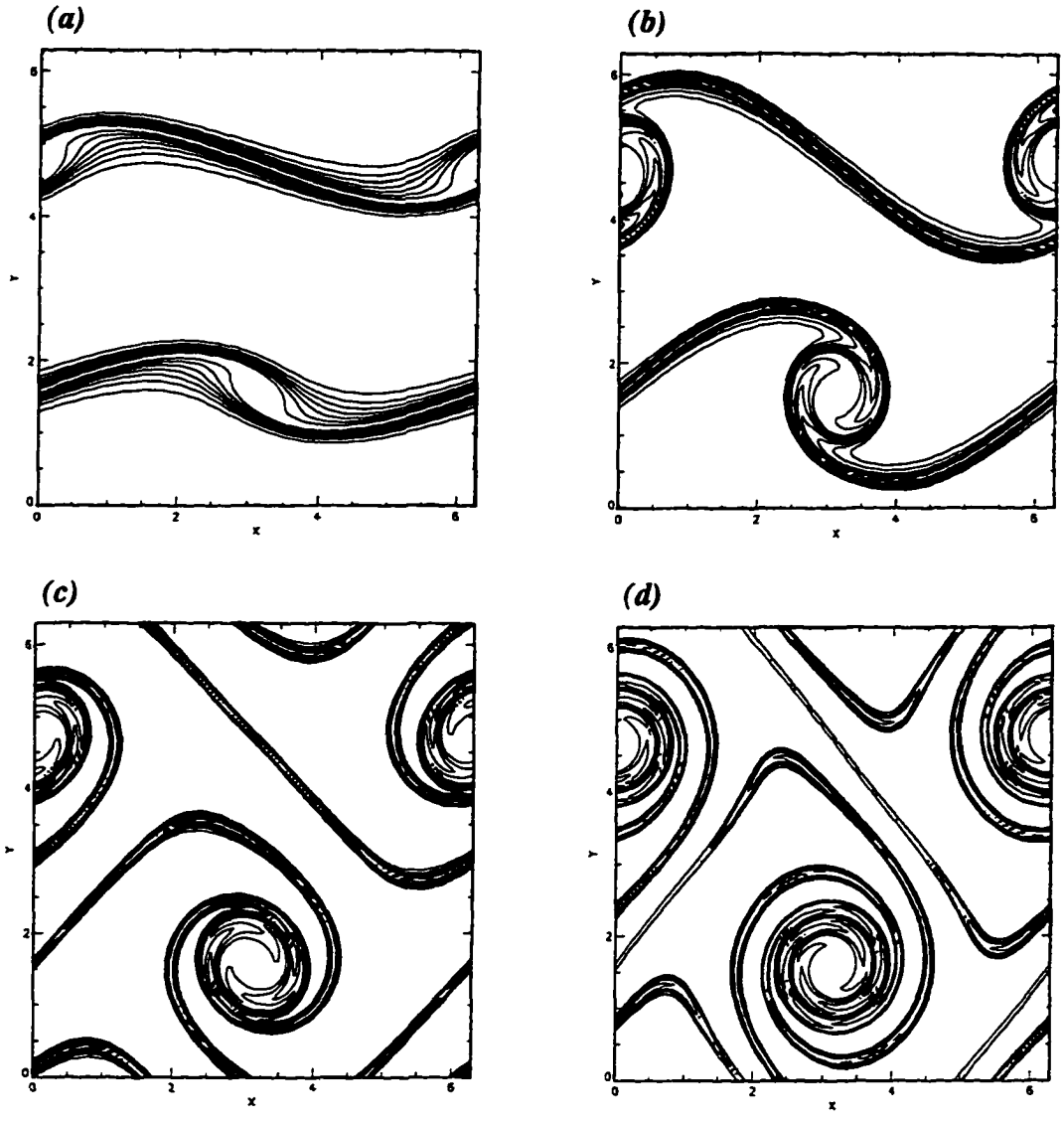

Fig 5.10 **Numerical solution of the double shear layer using sixth-order compact scheme with filtering on a 128^2 grid, *(a)* $t = 4$, *(b)* $t = 6$, *(c)* $t = 8$, and *(d)* $t = 10$.**

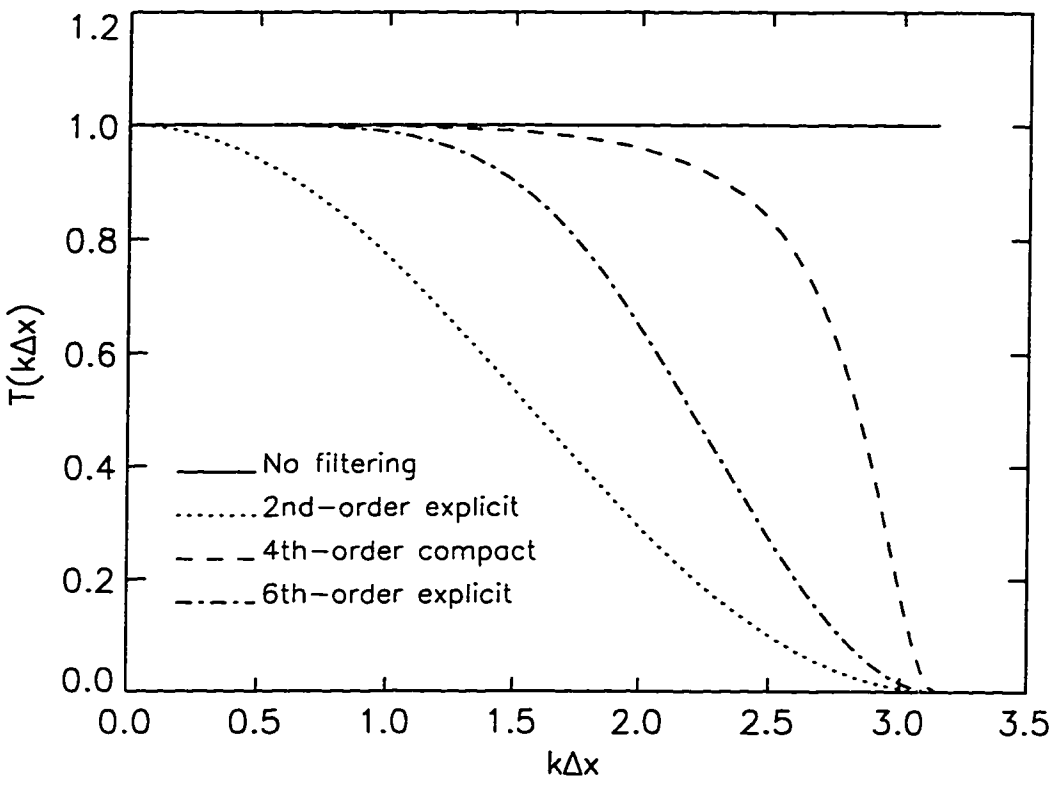

Fig 5.11 Transfer function for filter schemes.

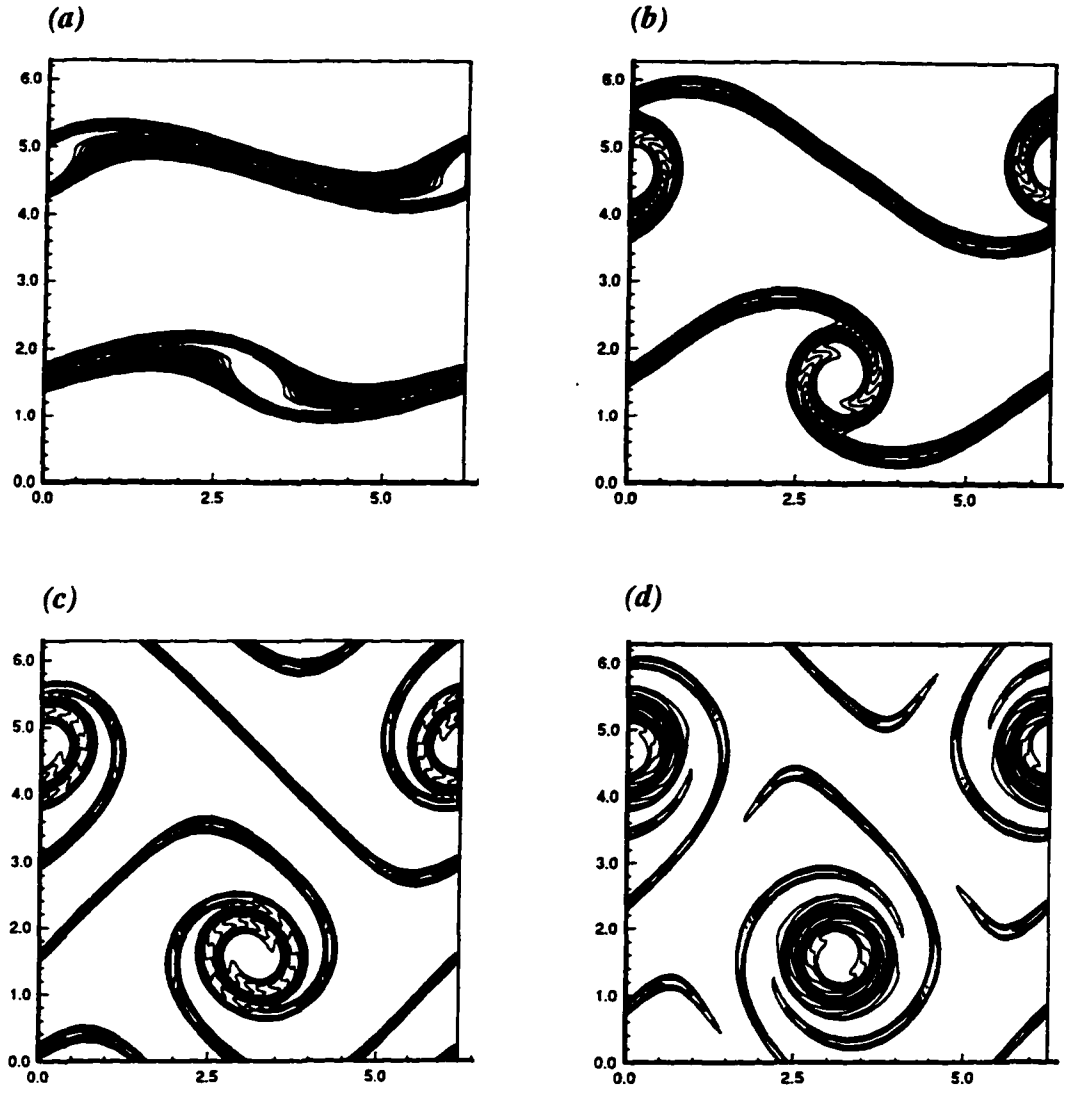

Fig 5.12 **Numerical solution of the double shear layer using fourth-order ENO scheme on a 128^2 grid from Weinan and Shu (1992), *(a)* $t = 4$, *(b)* $t = 6$, *(c)* $t = 8$, and *(d)* $t = 10$.**

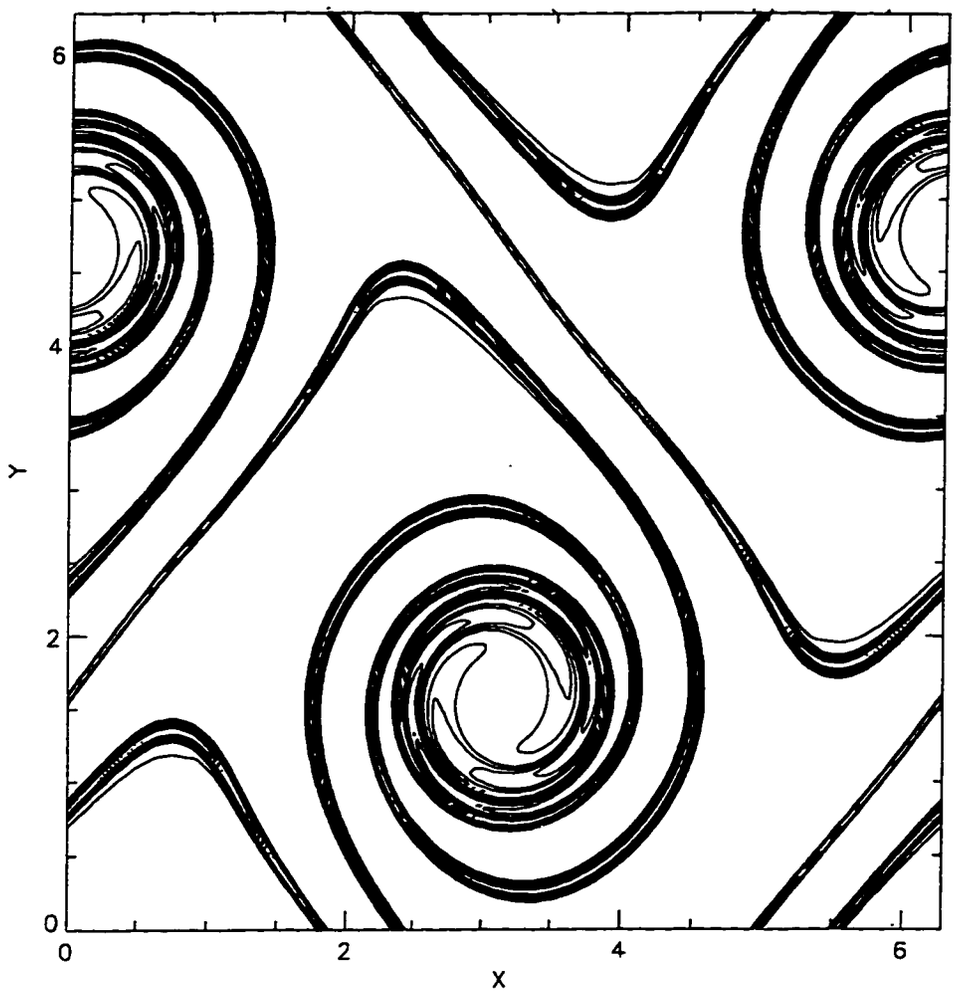

Fig 5.13 Numerical solution of the double shear layer using sixth-order compact scheme with filtering on a 256^2 grid at $t = 10$.

Chapter 6

DIRECT NUMERICAL SIMULATION - RESULTS

Results from the direct numerical simulation of rectangular jets at Reynolds number of $Re_{De} = 750$ are presented in this section. The Reynolds number of the jet flow is necessarily low so that all the scales of motion can be resolved with reasonable computational resources and no subgrid scale model is needed. The effect of Reynolds number on jet dynamics is addressed in the next chapter where large-eddy simulations are preformed at $Re_{De} = 75{,}000$. Emphasis is placed on LES of non-circular jets (Chap. 7) at higher Reynolds numbers where the flow is turbulent as occurs in experiment and nature. Spatial simulations are performed in this study where the domain is fixed in space and the flow enters and exits the domain through inflow and outflow boundaries, respectively. This is in contrast to a temporal simulation where the domain moves in the streamwise direction such that a small region of the flow is followed in time. The spatial reference frame is the one that occurs in nature and is thus preferable. It is also much more computationally demanding because the entire domain of interest must solved be simulated for all times.

6.1 Discrete Mode Forcing

As discussed in Sec. 2.2.1, time dependent boundary conditions are applied at the inflow to model the jet nozzle a short distance downstream of the exit ($x/D_e < 1$) and to promote the development of coherent structures within the computational domain. In this section, results are presented for simulations using discrete modes given by Eq. (2.19).

Simulations with discrete modes are used to study shear layer instabilities and the effects of forcing. Two cases are simulated with discrete modes corresponding to; *(i)* the fundamental mode, (ω = 0.22) at an rms intensity of 3% of the mean core velocity, U_o, and *(ii)* the fundamental mode (ω = 0.22) and the first subharmonic mode (ω = 0.11) at 1.5% intensity each. Cases *(iii) and (iv)* are presented in the next section and utilize the broad mode forcing at 3% and 15% total rms intensity, respectively. The domain and grid dimensions for the four runs are summarized in Table 6.1.

Table 6.1 Summary of parameters for DNS

Case	Forcing function	$L_x \times L_y \times L_z$	$N_x \times N_y \times N_z$
(i)	fund. @ 3%	12×5^2	129×65^2
(ii)	fund. + 1st Subh. @1.5% each	12×10^2	129×129^2
(iii)	broad @ 3%	12×10^2	129×129^2
(iv)	broad @ 15%	12×10^2	129×129^2

The domain length, L_x, listed in Table 6.1 includes a buffer layer of two diameters in length, giving an active computational domain of ten diameters. The streamwise grid spacing results in 10 points per fundamental wavelength. In Chap. 4 it was shown through the solution of several benchmark problems, that 8 points per wavelength provides adequate resolution with the fourth-order compact scheme.

Contours of vorticity magnitude for case *(i)* at t = 2 flow through times (the time to travel from inflow to outflow at the convective velocity) are shown in Figs. 6.1*a-e*. Contours in the major and minor axis planes (Figs. 6.1*a* and *b*) reveal that the shear layers near the inflow plane roll up at the fundamental frequency within the first diameter. For the region, $x/D_e > 5$, the fundamental mode has saturated and decayed. With no additional harmonic modes present in the forcing function, the jet does not transition to turbulence at

this Reynolds number. Near the outflow plane, $x/D_e - 10$, the jet width in the minor axis (x-y) plane becomes larger than that in the major axis (x-z) plane indicating that axis switching has taken place. Figs. 6.1*c* - *e* shows the vorticity magnitude at three cross-sectional planes ($x/D_e = 0$, 5, and 10), while Figs. 6.1*f* - *h* shows streamwise vorticity at three cross-sectional planes. ($x/D_e = 2.5$, 5, and 10). Even though there is no streamwise vorticity introduced at the inflow plane (not shown), by $x/D_e = 2.5$ (Fig. 6.1*f*) four pairs of streamwise vortices have formed in the higher curvature corner regions. This results in the distortion of the initially rectangular boundary layer at $x/D_e = 0$ to the diamond pattern at $x/D_e = 10$.

Vorticity contours for case *(ii)* at $t = 2$ flow through times show that the effect of adding the first subharmonic mode to the fundamental mode is to promote the formation of additional structures for the region, $x/D_e > 5$. In addition, the shear layer is dominated by intense vortices in the minor axis plane spaced at the first subharmonic wavelength. By examining the cross-sectional profiles in Fig. 6.2c-e it is apparent that rapid shear layer growth takes place in the major axis plane and that axis-switching does not take place. Cross-sectional contours of streamwise vorticity at $x/D_e = 5$ (Fig. 6.2g) show that four pair of streamwise vortices develop very close to the jet centerline which leads to a a partial bifurcation of the jet near $x/D_e = 10$. The streamwise vortices must be generated from the redistribution of azimuthal vorticity since they are not present at the inflow.

6.2 Broad Mode Forcing

Broad mode forcing is utilized to model naturally developing (unforced) jets with turbulent boundary layers. The resulting forcing function is somewhat random and does not contain symmetries present in discrete mode forcing. Figure 6.3 shows representative vorticity magnitude contours at $t = 2$ flow through times.

In contrast with simulations performed with discrete mode forcing, the shear layers do not roll up in a periodic fashion. Instead, non-symmetric, random structures are formed which are characteristic of naturally-developing jets. Contours at the outflow (Fig. 6.3f) show that the jet width in the minor axis plane is larger than that in the major axis plane, indicating that axis-switching takes place near the outflow plane.

The impact of the unsteady structures on the mean flow is examined by time-averaging the results of case *(iii)* with broad mode forcing at 3% intensity over a period of 8 flow through times. The results from the first flow through time are not included in the time-averaging so that transients resulting from the initial conditions are convected out of the domain. After the transient period, the flow field at every other grid point and every fourth time step is saved to disk. The results are then post-processed to compute statistical quantities such as first and second moment quantities, two-point correlations, and budgets. This procedure results in roughly 1188 samples in the period of 8 flow through times. The adequacy of sample size is addressed in the next chapter.

The time-averaged jet major and minor axis widths, entrainment, decay of centerline velocity, and fluctuating centerline velocity from case *(iii)* are shown in Fig. 6.4 as a function of streamwise coordinate. The results at this level of intensity show that significant unsteadiness does not occur until, $x/D_e \sim 7$. This results in a small growth of the jet widths and no distinctive end to the potential core region as observed in higher Reynolds number experimental jets at x/D_e = 4-5. Decay of centerline velocity plots from the DNS of a rectangular jet at Re_{De} = 800 of Miller et al. (1995) also reveal no distinctive end of the potential core within their computational domain of nine diameters.

In order to test the effect of forcing intensity, a fourth simulation is presented at a higher intensity of 15%. Jet widths in the major and minor axis planes, entrainment rate,

centerline velocity, and fluctuating velocity are given in Fig 6.5. Detailed profiles of time-averaged velocity, pressure, and Reynolds stress components for case *(iv)* are shown in Figs. 6.6 - 6.15. Time-averaged and fluctuating velocity components are normalized with the local velocity on the jet centerline, U_{CL} and transverse coordinates are normalized by the local jet width defined by the transverse distance where $U/U_{CL} = 0.5$. The location, Y_O, $Z_O = 0, 0$ denotes the position of the jet centerline.

Figure 6.5d shows that the effect of increasing the intensity of the inflow forcing function to 15% is to promote unsteadiness at $x/D_e \sim 5$. The centerline velocity also begins to decay slowly at roughly $x/D_e \sim 5$. Figure 6.6 shows time-averaged streamwise velocity along the minor and major axis. The experimental results of a jet issuing from a contoured rectangular nozzle of $AR = 2$ at $Re_{De} = 10^5$ (Quinn 1995) are also shown. This experimental jet shows axis-switching at $x/D_e \sim 12$. The profiles from the DNS at x/D_e =9 show good agreement with experimental profiles in the minor axis plane only. Fluctuating velocity profiles shown in Figs. 6.10-6.12 are generally underpredicted in comparison with the experimental profiles at higher Reynolds number. This is not surprising since the centerline fluctuating velocity is still increasing near the end of the computational domain of ten diameters (Fig. 6.5d) while the experimental value reaches its peak at $x/D_e = 5 - 6$ and then levels off.

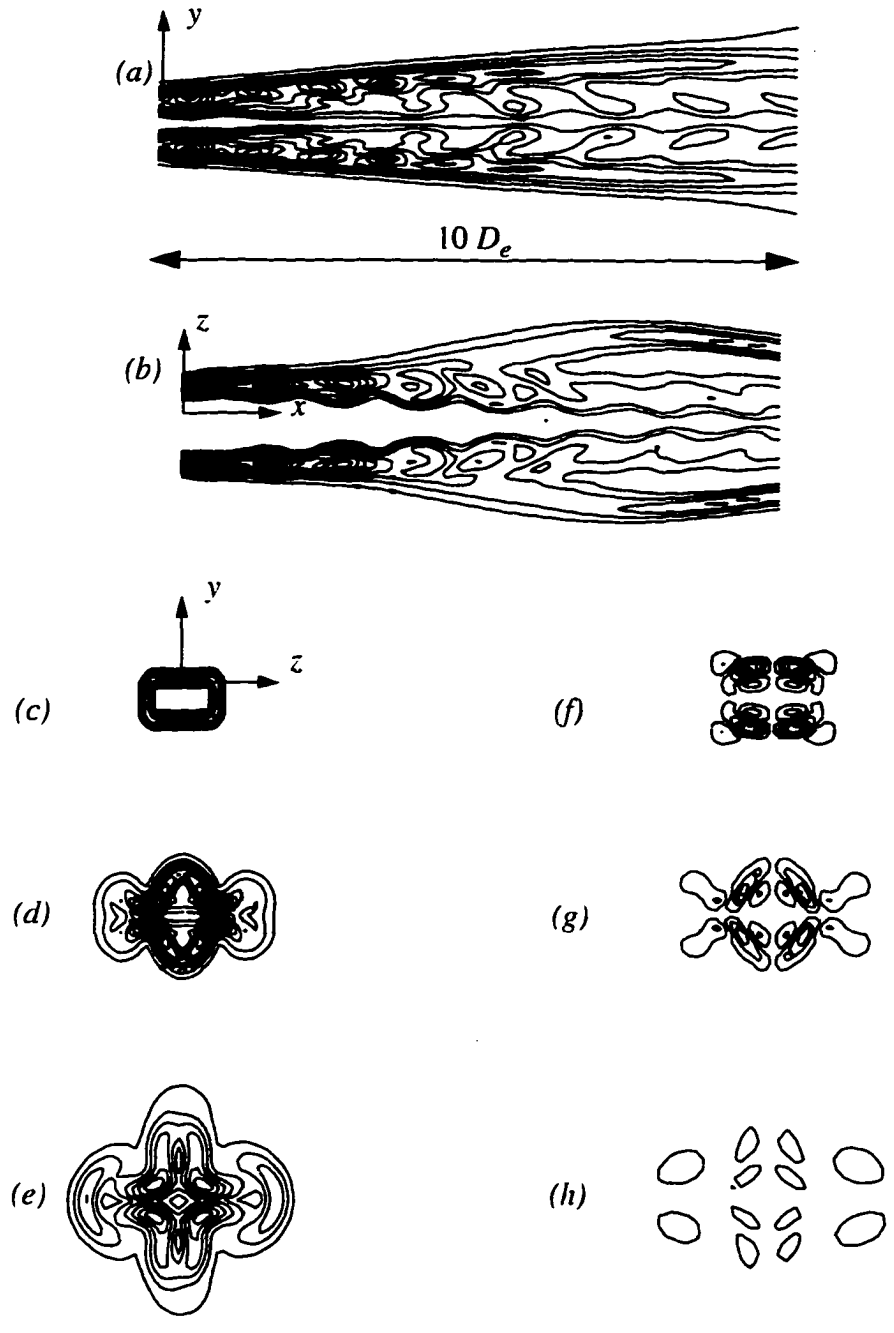

Fig 6.1 **Contours of vorticity magnitude *(a)* - *(e)* and streamwise vorticity *(f)* - *(h)* for case *(i)* at $t = 2$ flow through times for fundamental forcing function. *(a)* minor axis plane, $z/D_e = 0$, *(b)* major axis plane, $y/D_e = 0$, *(c)* cross flow plane, $x/D_e = 0$, *(d)* $x/D_e = 5$, *(e)* $x/D_e = 10$, *(f)* $x/D_e = 2.5$, *(g)* $x/D_e = 5$, and *(h)* $x/D_e = 10$.**

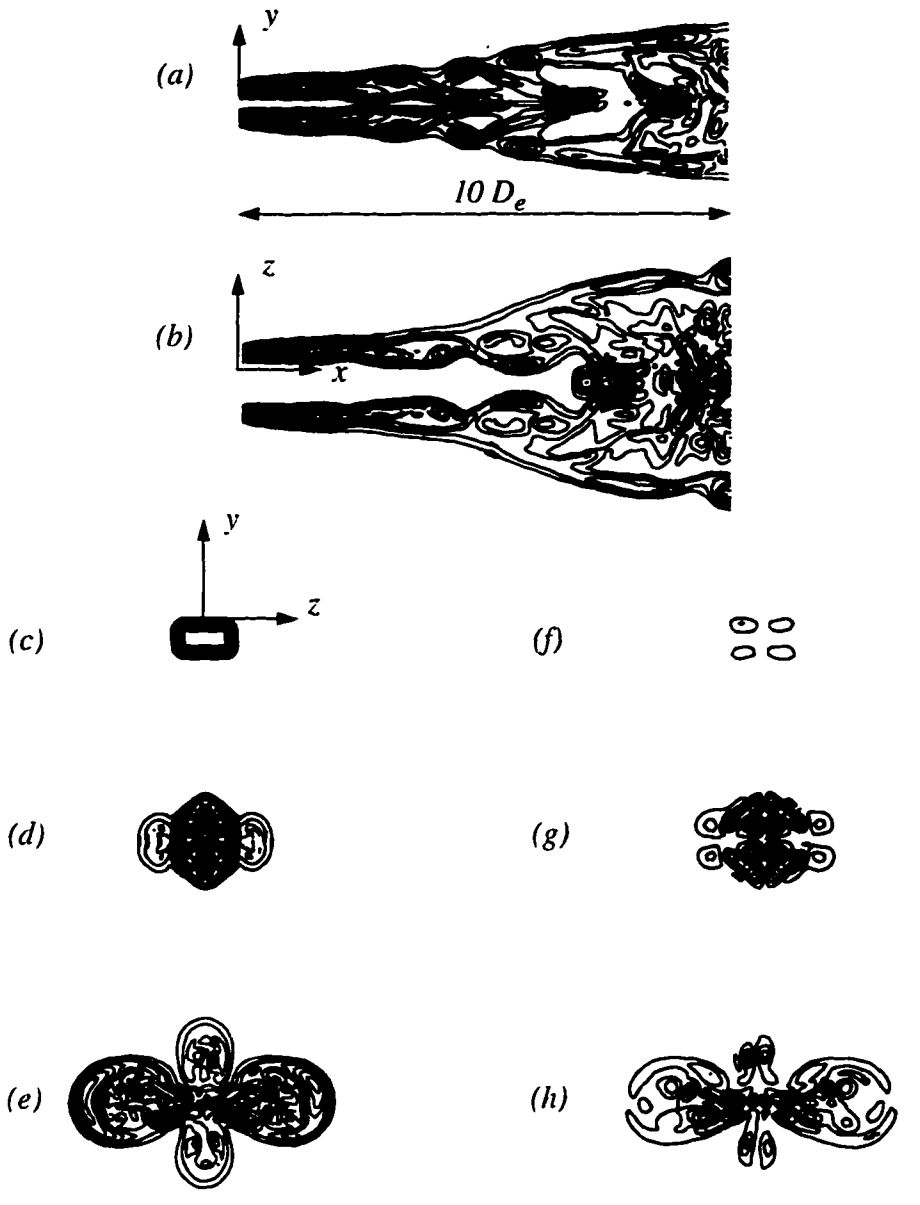

Fig 6.2 **Contours of vorticity magnitude *(a)* - *(e)* and streamwise vorticity *(f)* - *(h)* for case *(ii)* at t = 2 flow through times for fundamental and first subharmonic forcing function. *(a)* minor axis plane, $z/D_e = 0$, *(b)* major axis plane, $y/D_e = 0$, *(c)* cross flow plane, $x/D_e = 0$, *(d)* $x/D_e = 5$, *(e)* $x/D_e = 10$, *(f)* $x/D_e = 2.5$, *(g)* $x/D_e = 5$, and *(h)* $x/D_e = 10$.**

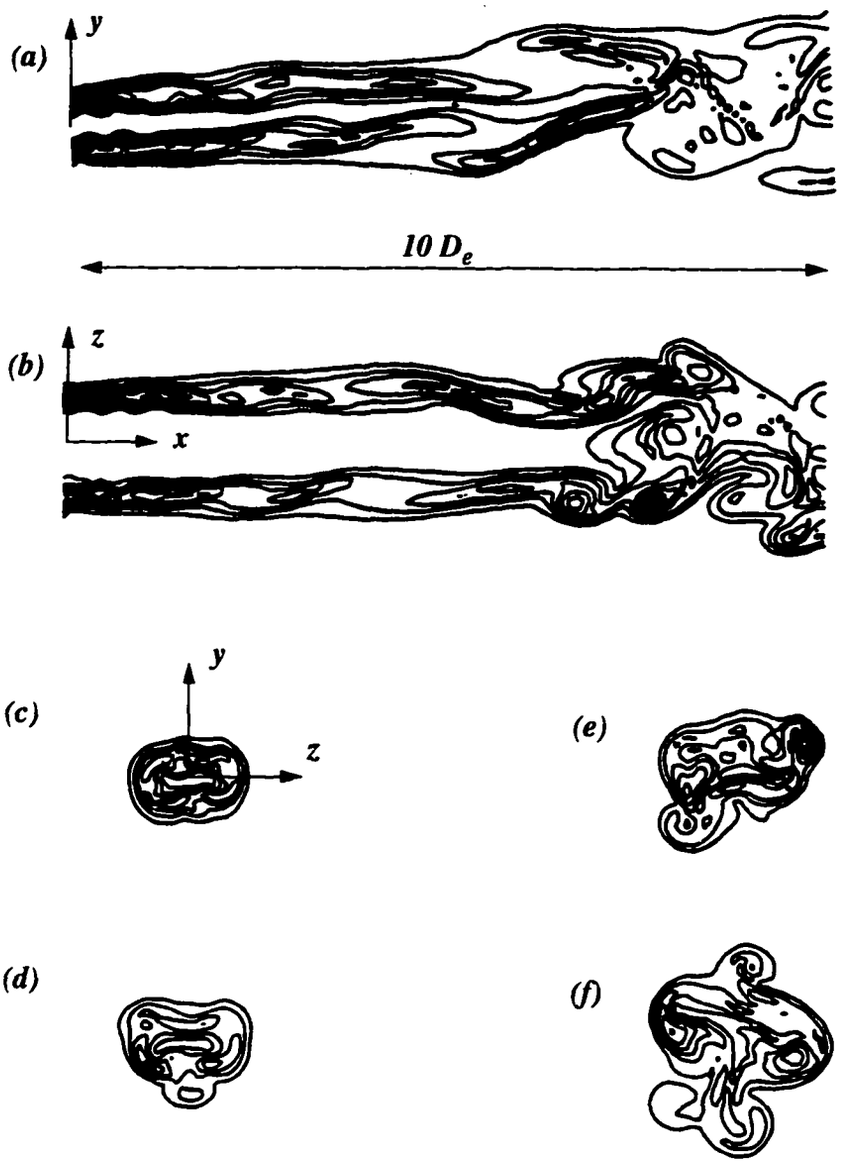

Fig 6.3 **Contours of vorticity magnitude for case *(iii)* at t = 2 flow through times for broad mode forcing function. *(a)* minor axis plane, z/D_e = 0, *(b)* major axis plane, y/D_e = 0, *(c)* cross flow plane, x/D_e =2.5, *(d)* x/D_e = 5, *(e)* x/D_e = 7.5, and *(f)* x/D_e = 10.**

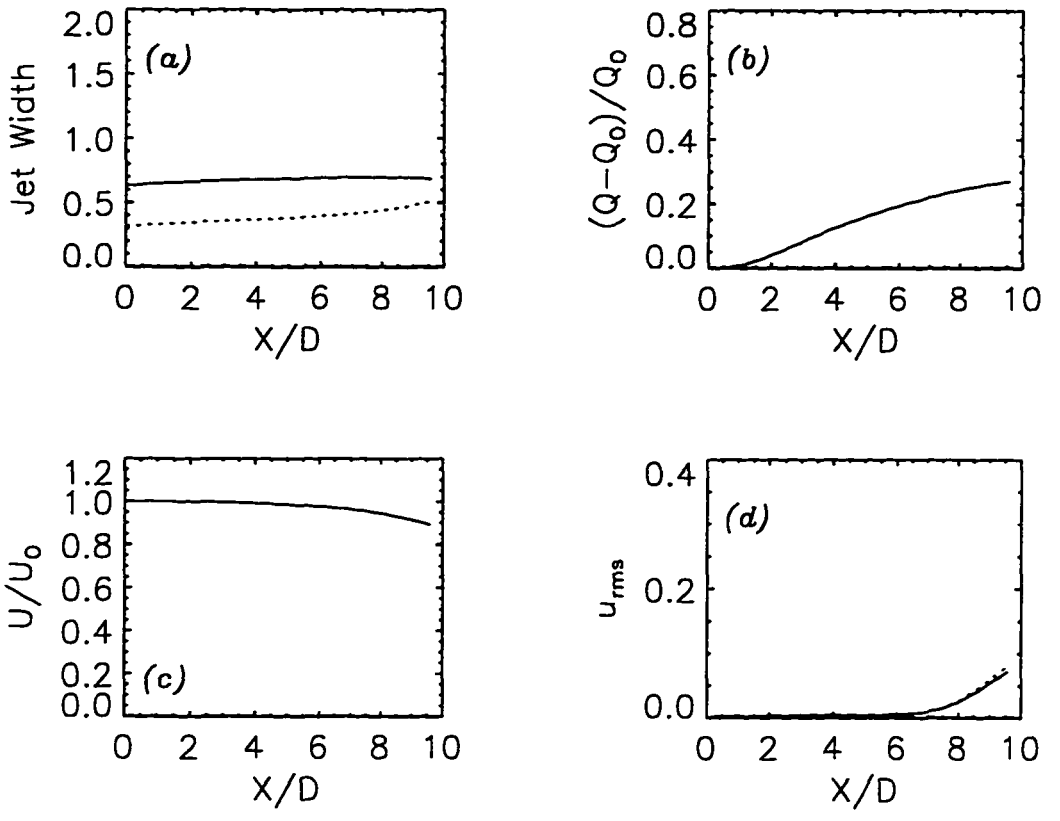

Fig 6.4 **Time-averaged quantities versus streamwise distance for DNS of rectangular jet with broad mode forcing at 3%; (a) jet widths (solid - major axis plane, dashed - minor axis plane), (b) entrainment ratio, (c) decay of centerline velocity, (d) fluctuating velocity (solid - u_{rms}/U_O, dashed - u_{rms}/U_{CL}).**

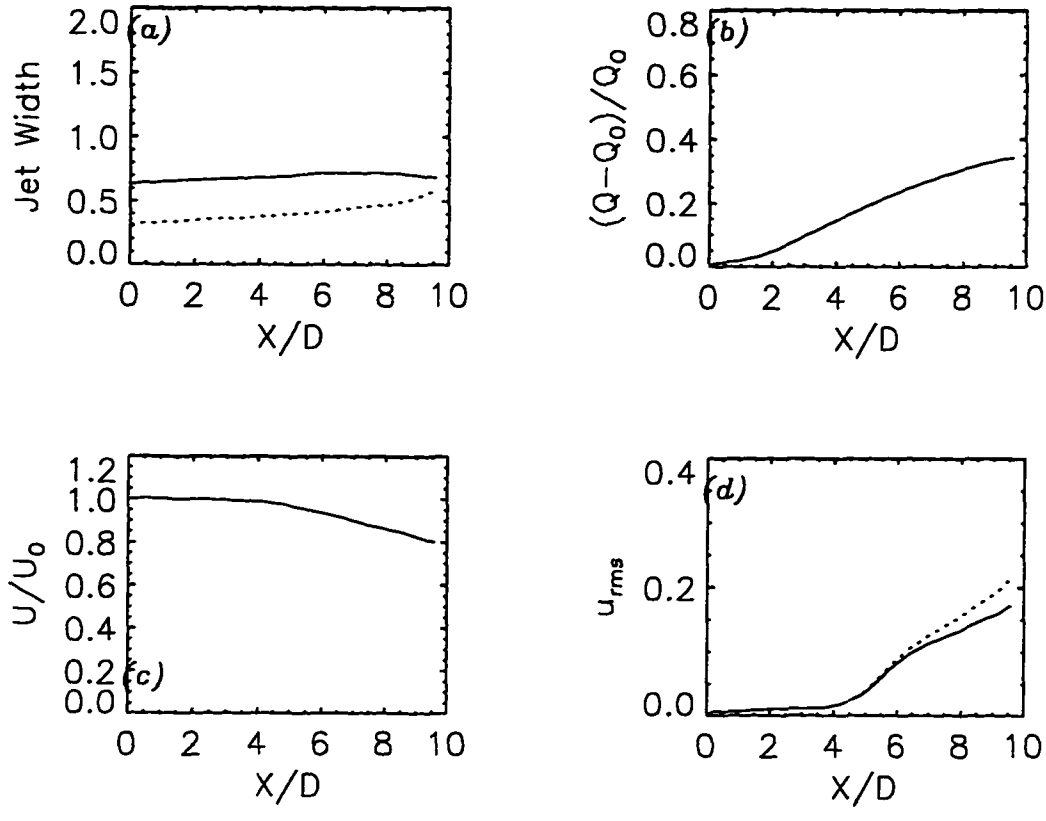

Fig 6.5 **Time-averaged quantities versus streamwise distance for DNS of rectangular jet with broad mode forcing at 15%; (a) jet widths (solid - major axis plane, dashed - minor axis plane), (b) entrainment ratio, (c) decay of centerline velocity, (d) fluctuating velocity (solid - u_{rms}/U_O, dashed - u_{rms}/U_{CL}).**

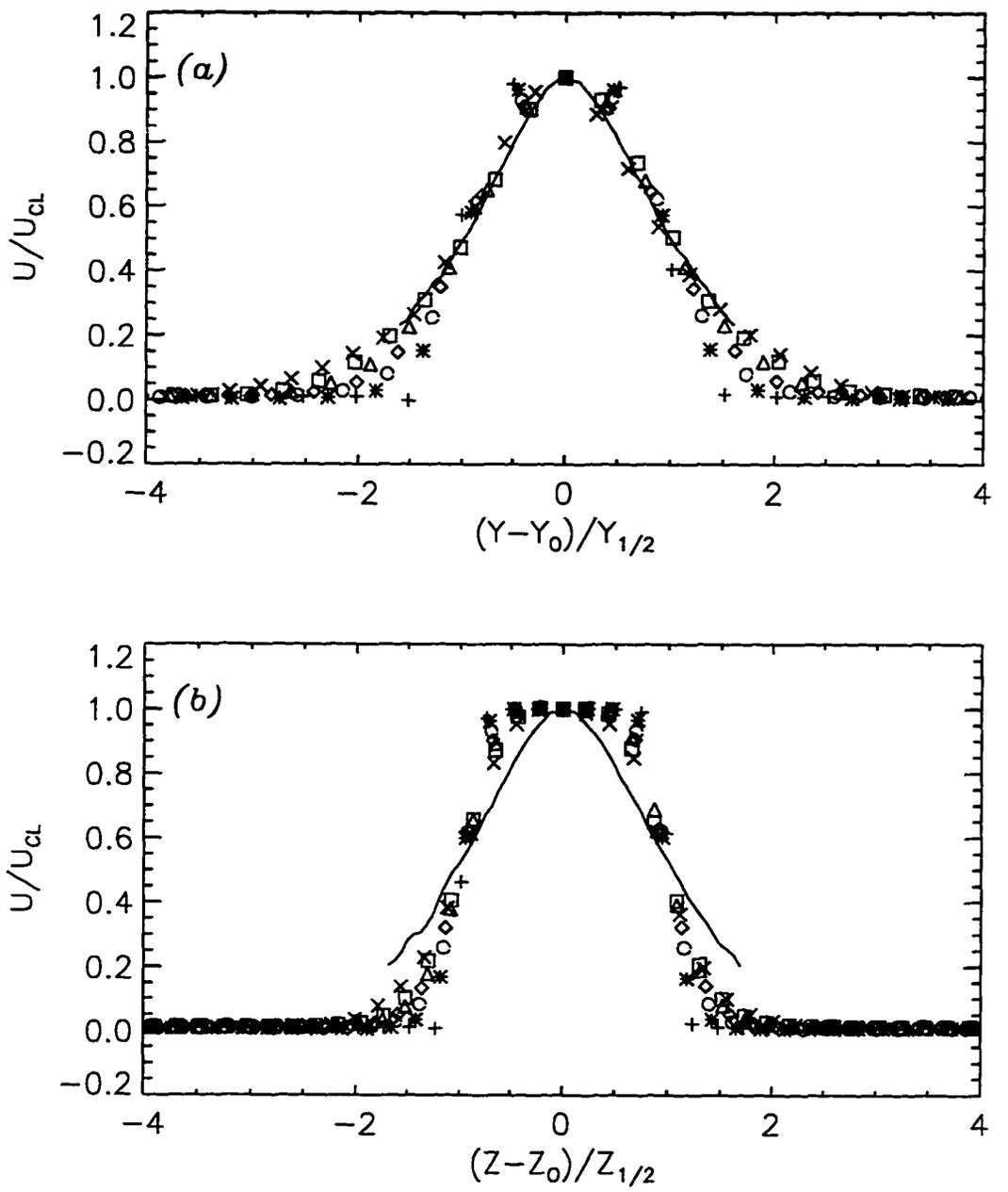

Fig 6.6 **Time-averaged streamwise velocity, *U*, for the DNS of rectangular jet, *(a)* minor axis and *(b)* major axis (solid - experiment of Quinn 1995, *x/D* = 10). *x/D* = ; +: 0.0 ; ✳: 1.5 ; ○: 3.0 ; ◇: 4.5 ; △: 6.0 ; □: 7.5 ; ×: 9.0.**

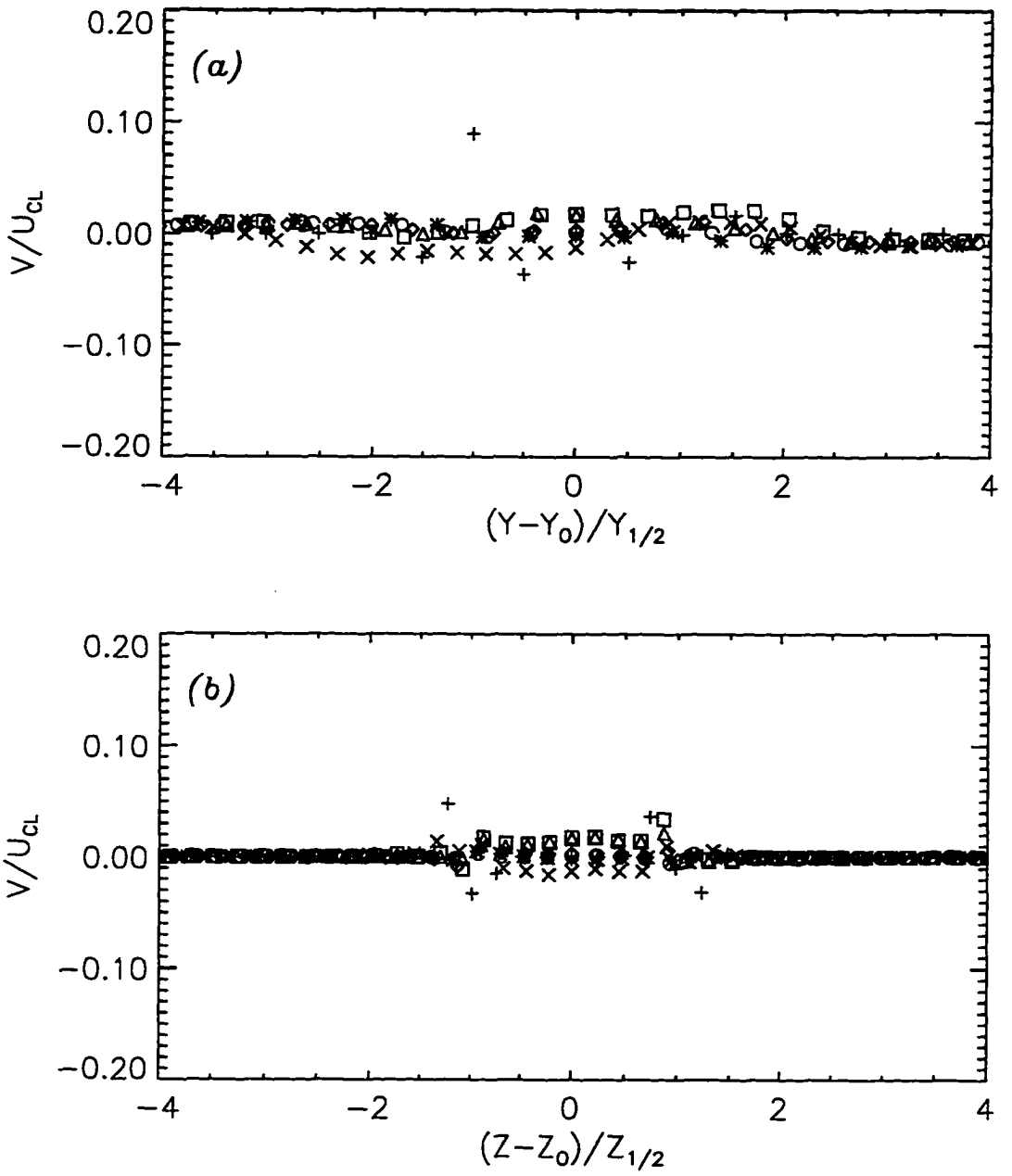

Fig 6.7 **Time-averaged lateral velocity, *V*, for the DNS of rectangular jet, *(a)* minor axis and *(b)* major axis. For symbols see Fig 6.6.**

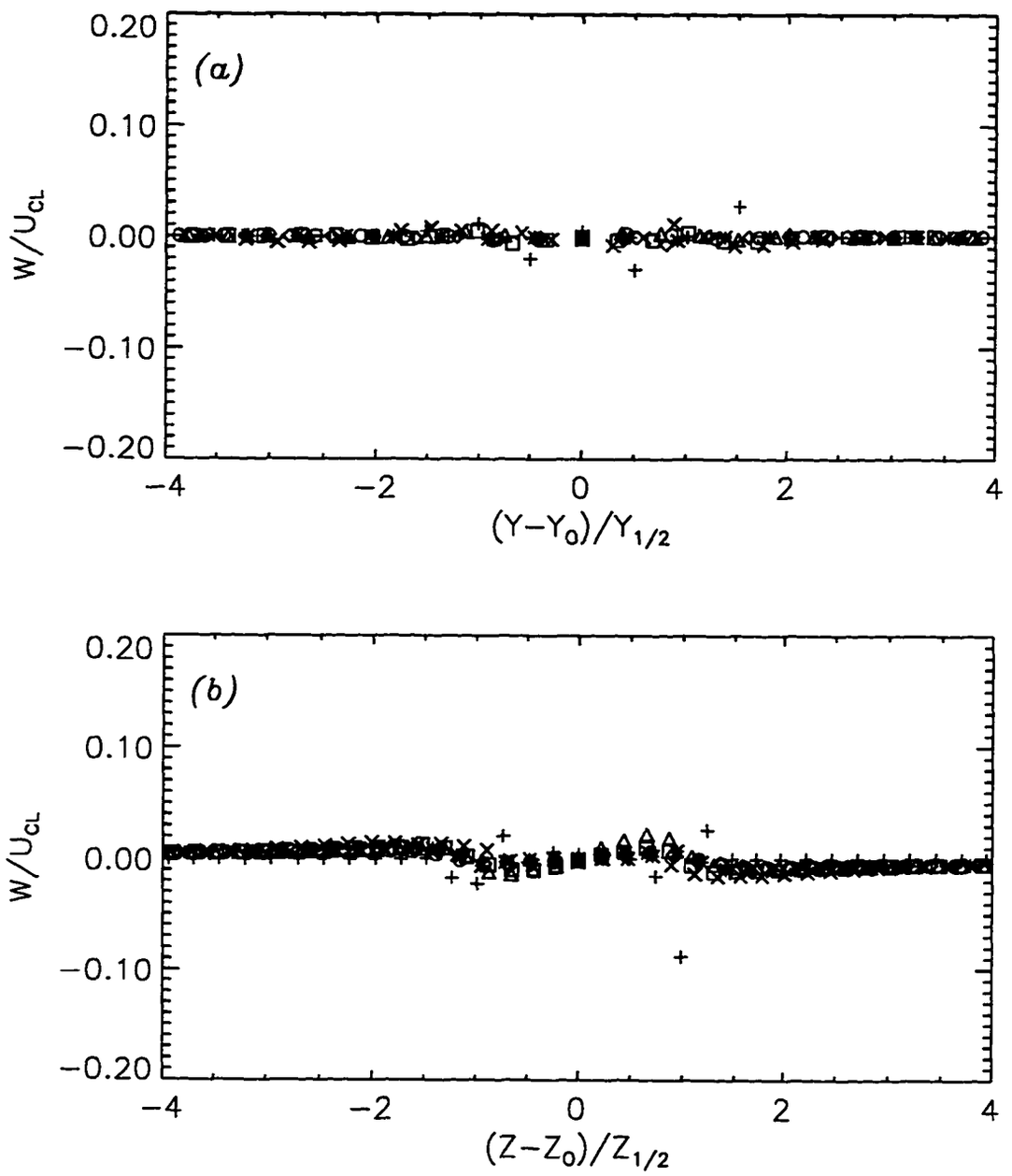

Fig 6.8 **Time-averaged transverse velocity, *W*, for the DNS of rectangular jet, *(a)* minor axis and *(b)* major axis. For symbols see Fig 6.6.**

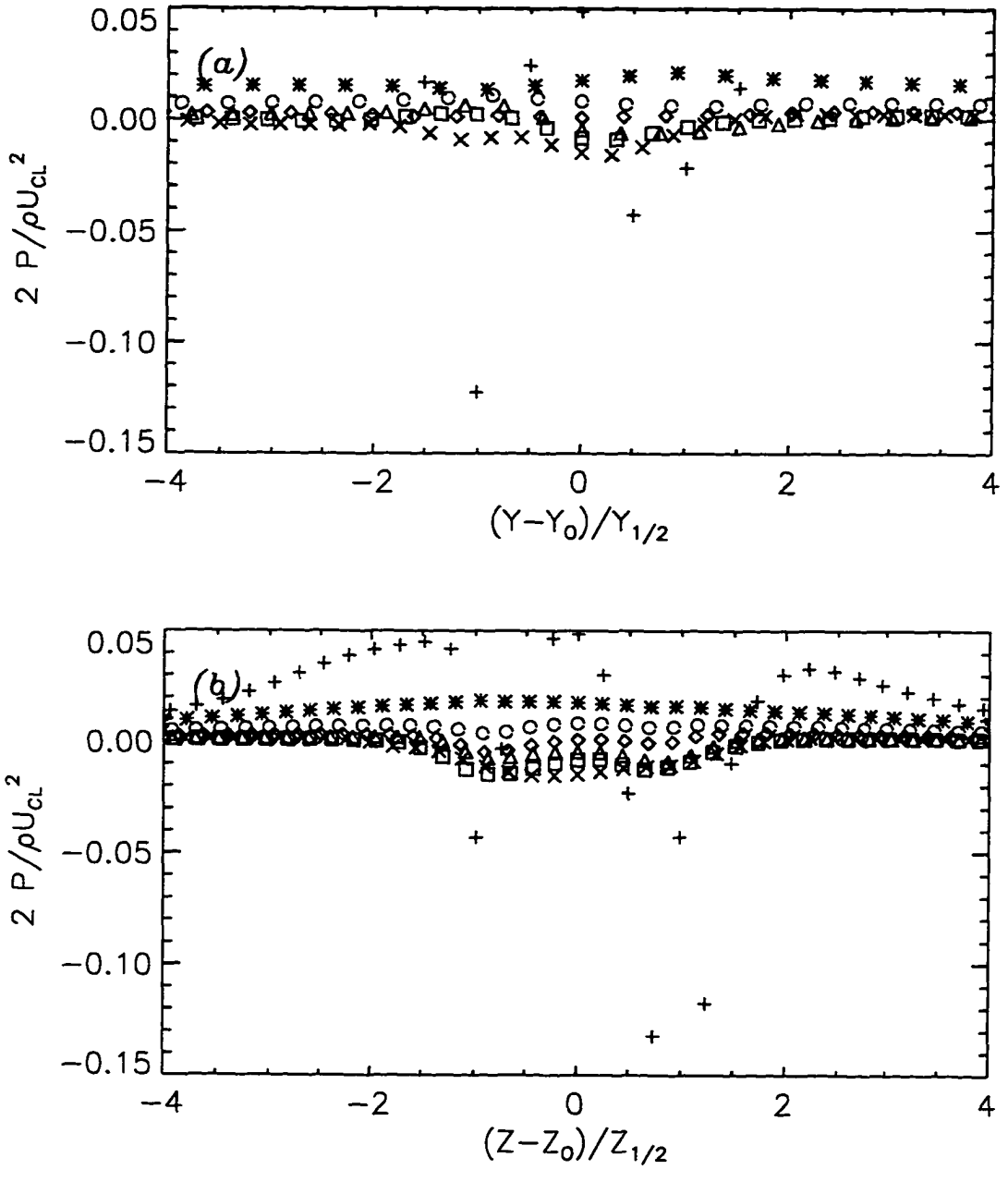

Fig 6.9 **Time-averaged pressure, *P*, for the DNS of rectangular jet, *(a)* minor axis and *(b)* major axis. For symbols see Fig 6.6.**

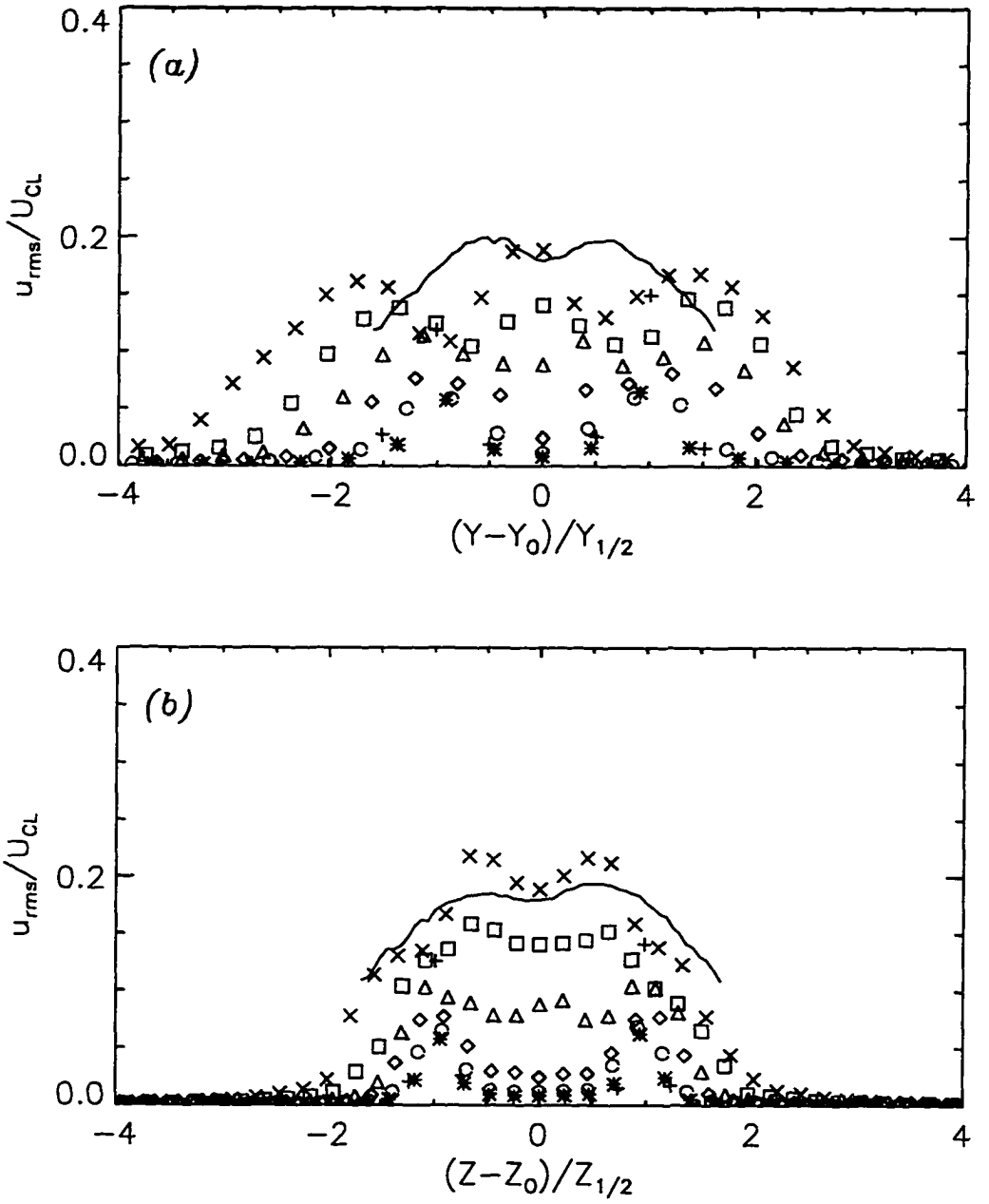

Fig 6.10 **Time-averaged fluctuating streamwise velocity, u_{rms}, for the DNS of rectangular jet, *(a)* minor axis and *(b)* major axis (solid - experiment of Quinn 1995, $x/D = 10$). For symbols see Fig 6.6.**

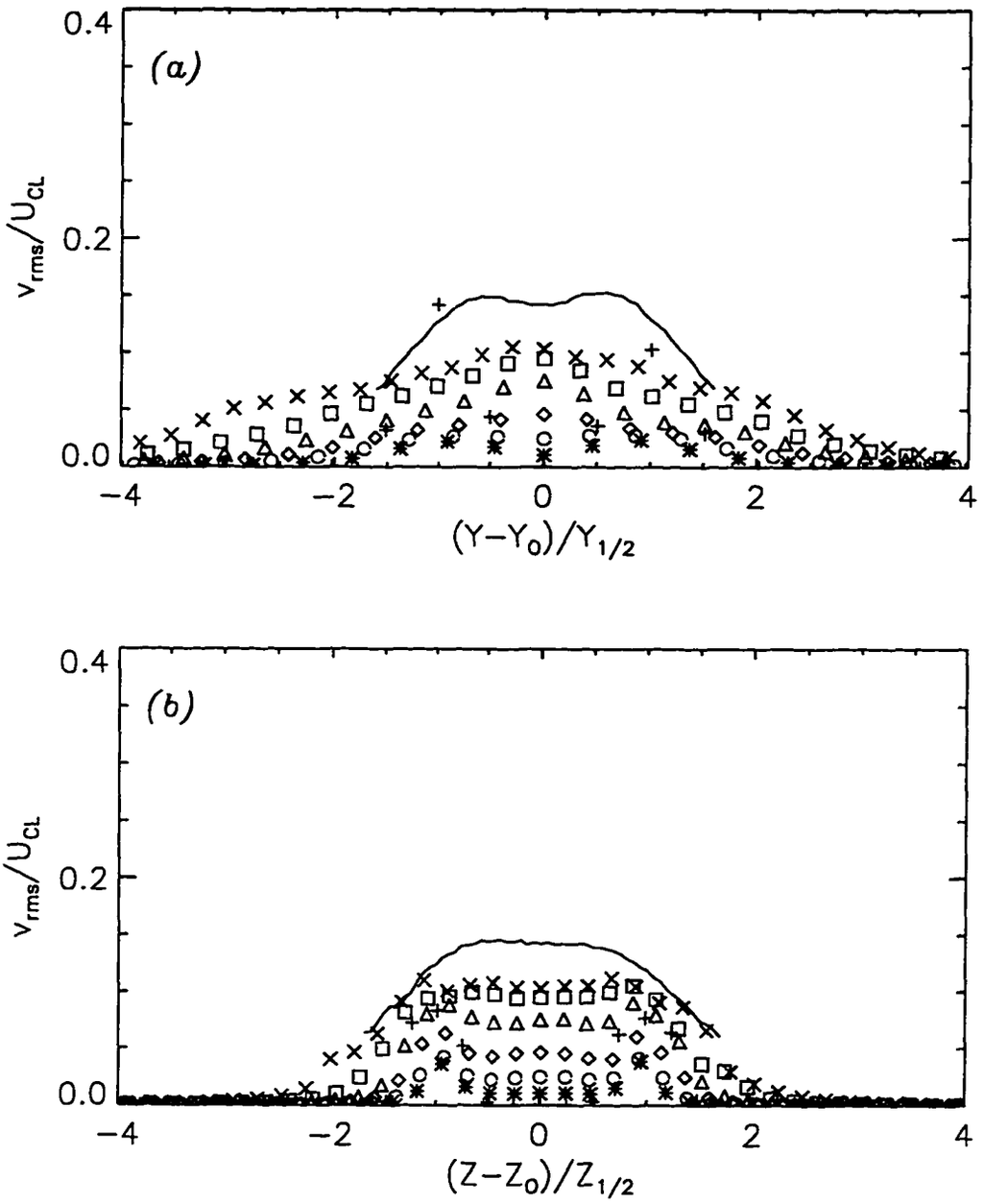

Fig 6.11 **Time-averaged fluctuating lateral velocity, v_{rms}, for the DNS of rectangular jet, *(a)* minor axis and *(b)* major axis (solid - experiment of Quinn 1995, $x/D = 10$). For symbols see Fig 6.6.**

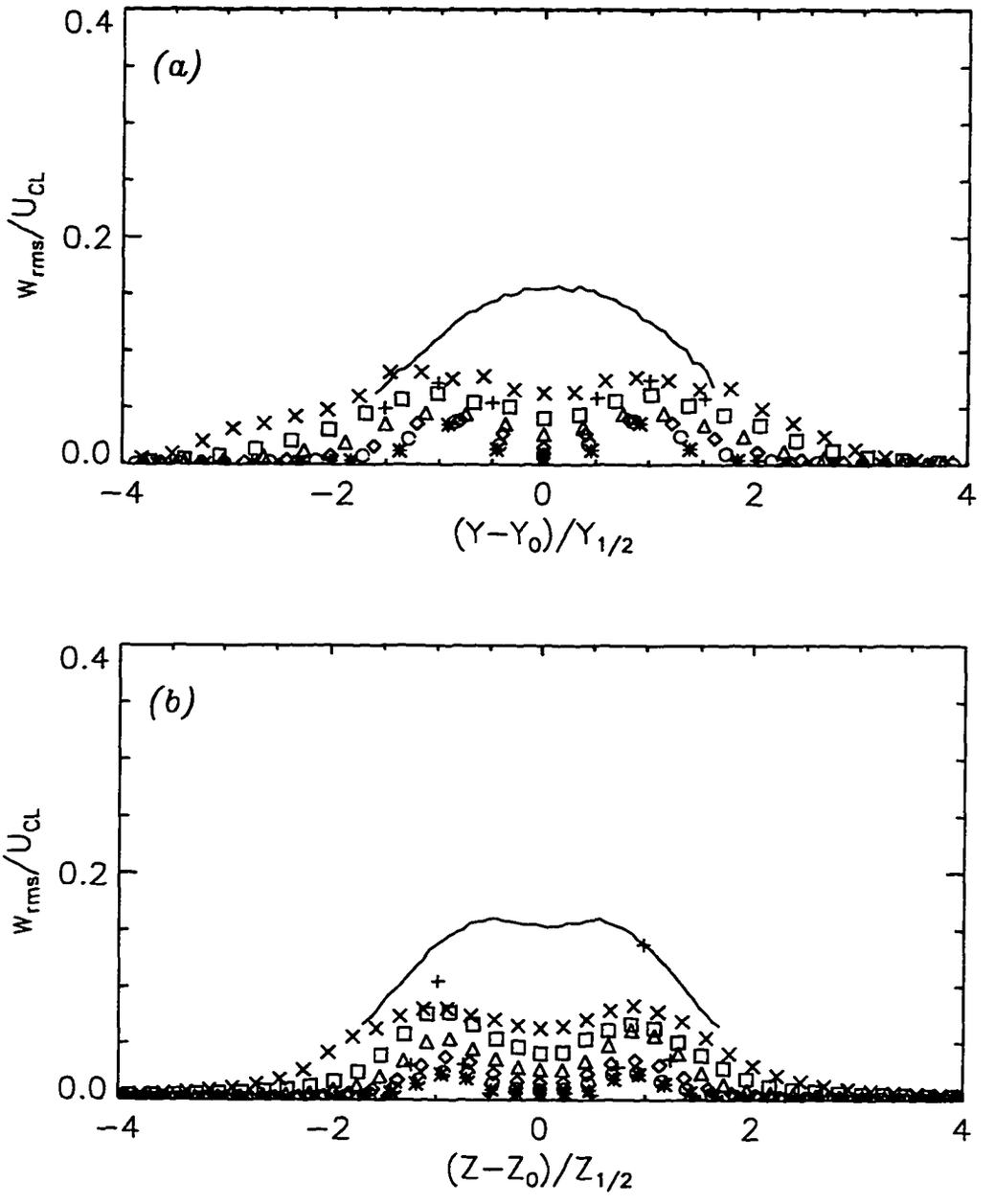

Fig 6.12 **Time-averaged fluctuating transverse velocity, w_{rms}, for the DNS of rectangular jet, *(a)* minor axis and *(b)* major axis (solid - experiment of Quinn 1995, $x/D = 10$). For symbols see Fig 6.6.**

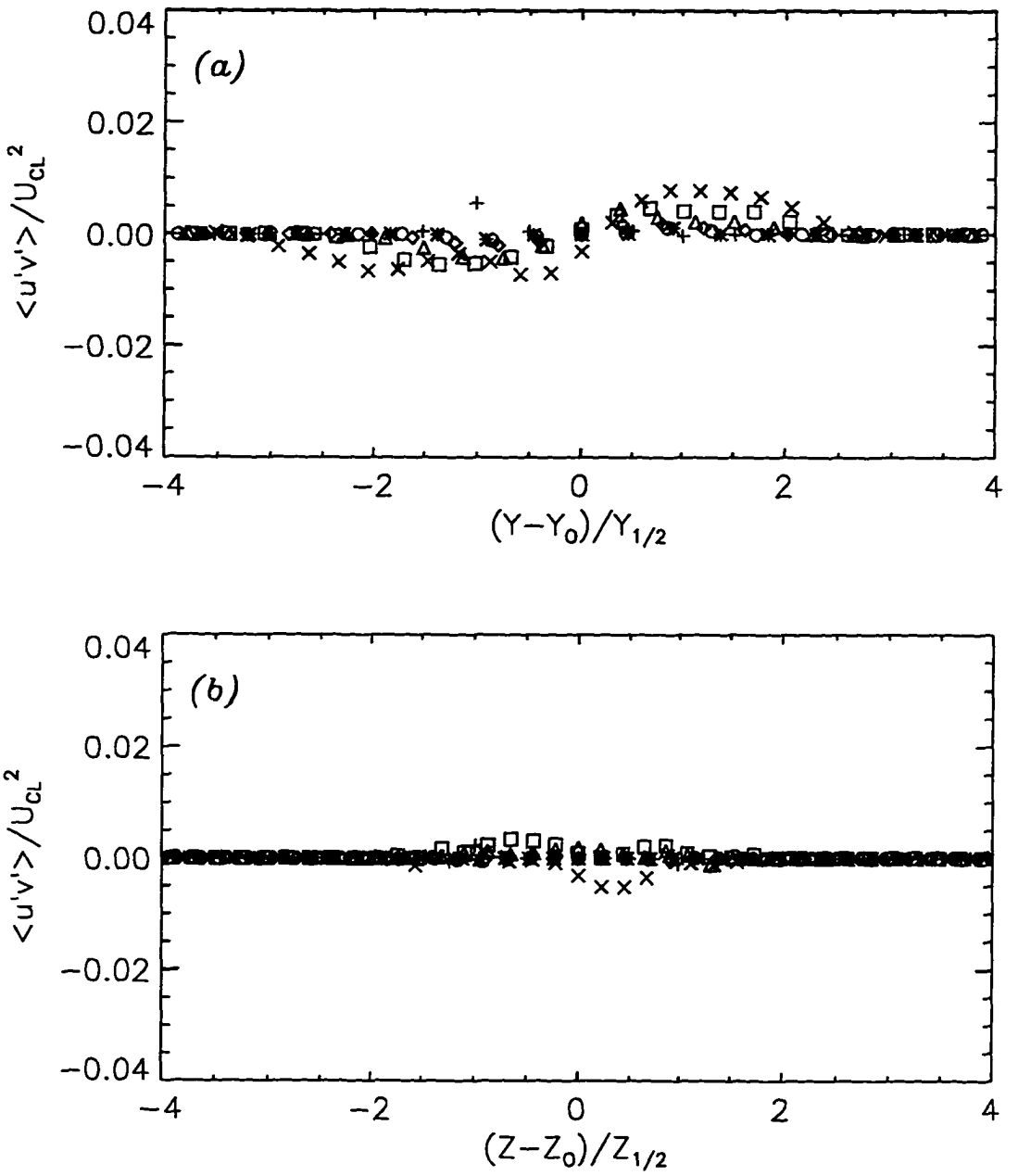

Fig 6.13 Time-averaged Reynolds shear stress, $\langle u'v' \rangle$, for the DNS of rectangular jet, *(a)* minor axis and *(b)* major axis. For symbols see Fig 6.6.

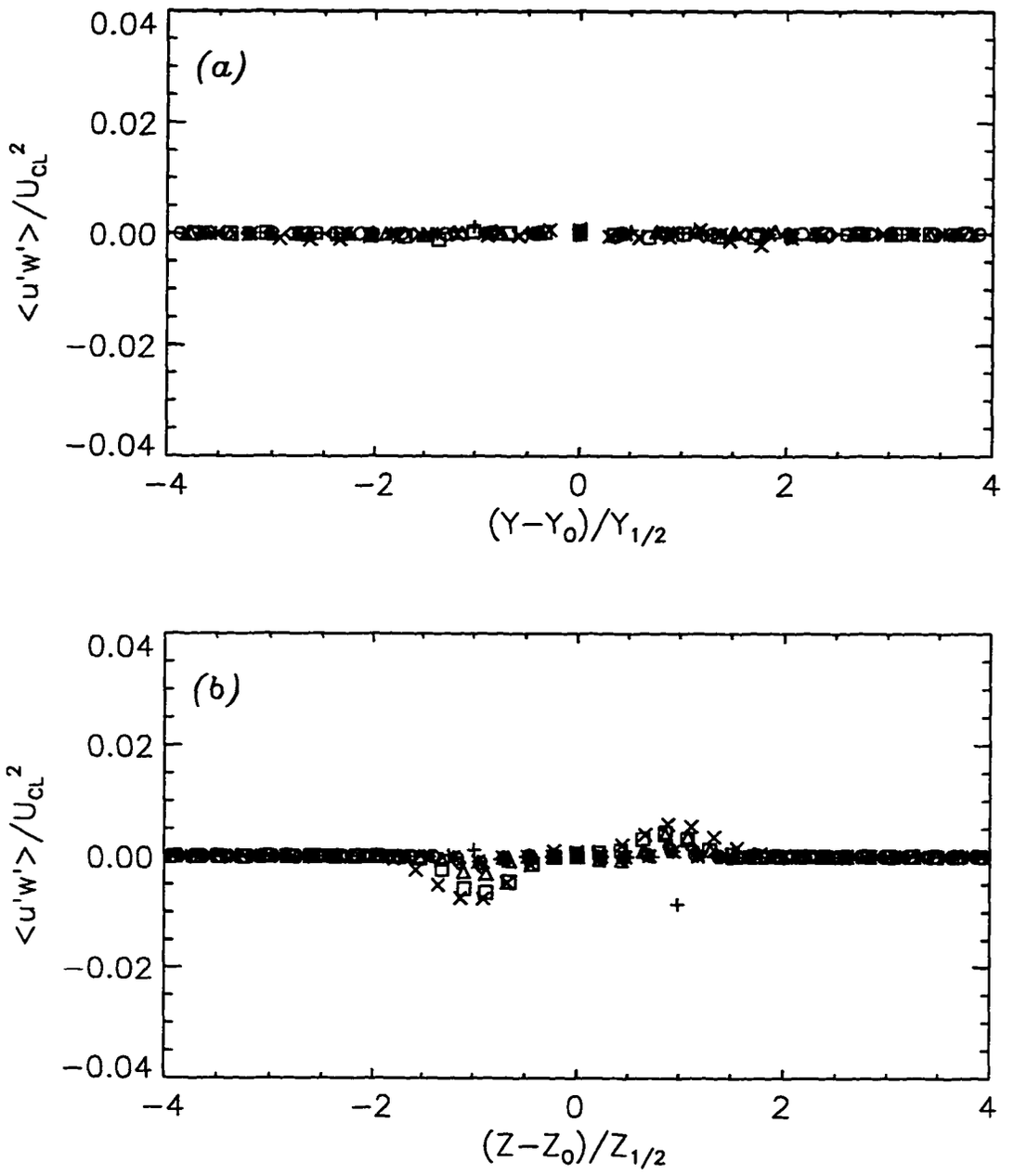

Fig 6.14 **Time-averaged Reynolds shear stress, $\langle u'w' \rangle$, for the DNS of rectangular jet, *(a)* minor axis and *(b)* major axis. For symbols see Fig 6.6.**

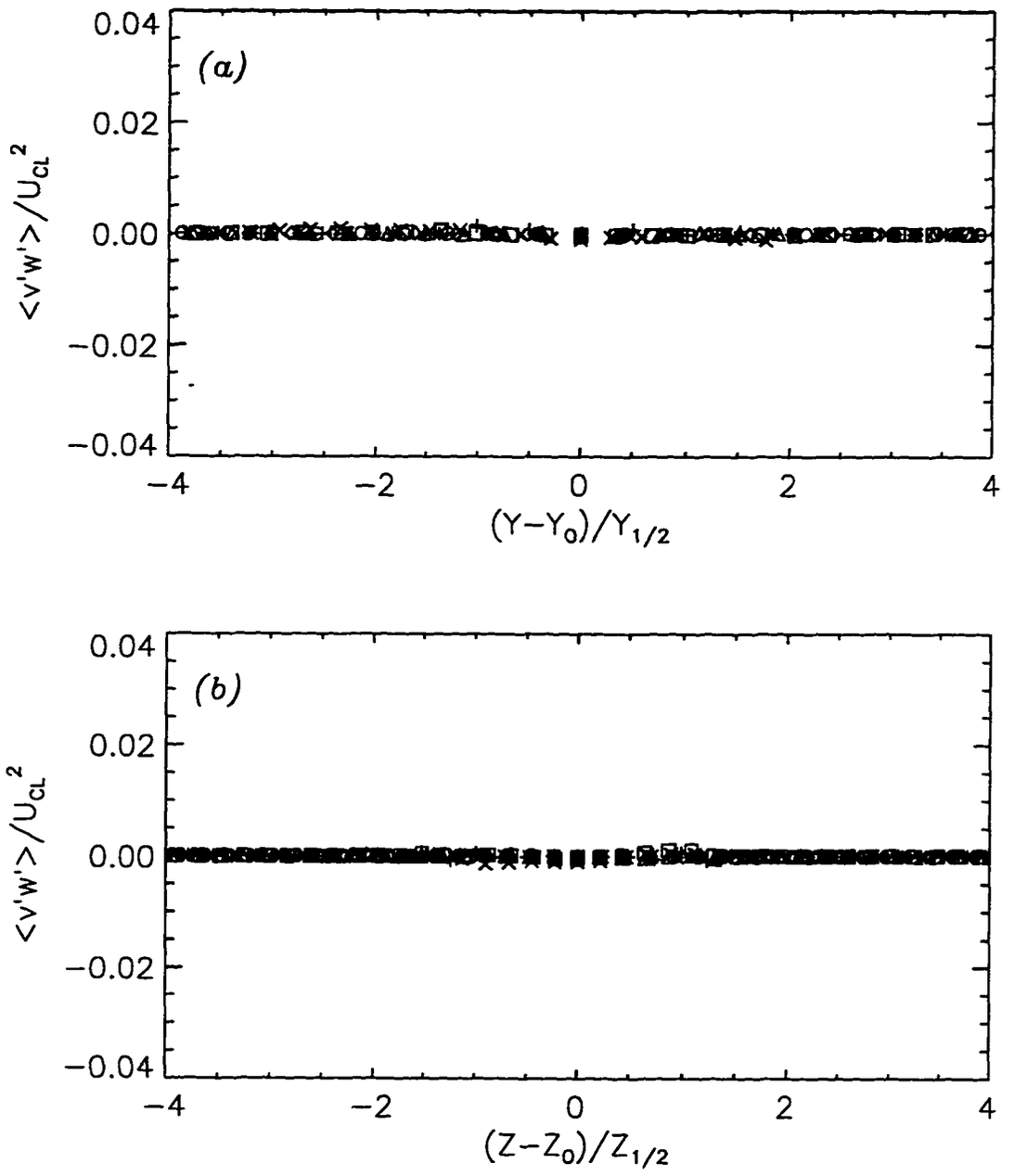

Fig 6.15 Time-averaged Reynolds shear stress, $\langle v'w' \rangle$, for the DNS of rectangular jet, *(a)* minor axis and *(b)* major axis. For symbols see Fig 6.6.

Chapter 7

LARGE EDDY SIMULATION-RESULTS

This chapter discusses the results of large eddy simulation (LES) of non-circular jets at a higher Reynolds number, Re_{De} = 75,000. At this Reynolds number, it is not practical with current computer resources to fully resolve all scales of motion of the jet flow. The Smagorinsky model outlined in Sec. 2.1.2 is included in the computation to account for unresolved scales. In addition, the velocity field is filtered every five time steps using the fourth-order compact filter outlined in Sect. 5.3.3. Filtering removes the highest wavenumber mode which is not accurately resolved, while passing through modes of low to moderate wavenumber. Results are presented for jets with initially rectangular and elliptical cross-sections with low aspect ratio, AR = 2. In addition, LES of a circular jet is performed to quantify the effects of non-uniform azimuthal curvature present in the non-circular jets.

7.1 Rectangular Jet

7.1.1 Simulation Parameters

In Sec. 2.2.1, the mean velocity of the rectangular jet at the inflow plane was specified. Broad mode forcing functions are used to promote unsteadiness and to model the naturally developing jet observed experimentally. A low level of forcing is used at this Reynolds number which corresponds to a maximum intensity at the inflow plane of $u_{rms}/\Delta x = 0.03$.

The domain dimensions are 12 x 10 x 10 and grid dimensions are 129^3. The last two diameters of streamwise domain length are used as a buffer domain giving an "active" computational length of 10 diameters in the streamwise directions. The grid is distributed uniformly in all three directions.

7.1.2 Effect of Grid Resolution

The effect of grid resolution on the LES results is presented in this section. In the LES approach, it is often difficult to separate the effect of truncation errors, aliasing errors, and SGS model errors as the grid is refined. This is contrasted with the DNS approach where all scales are resolved such that no SGS modeling errors are committed and the truncation error reduces at a known rate with grid refinement. Therefore, it is easier to isolate the effects of the numerical formation from those due to the physics of the problem.

The approach taken in the current study is to solve the problem numerically on a very coarse grid (denoted as the level 1 grid) using the same parameters identified in the previous sections. After roughly ten flow through times, the results on the coarsest grid are prolongated to a grid with double the number of grid points in each direction. Those results are used as initial conditions for a simulation on the level 2 grid which is run for ten flow through times. This process is repeated until it is no longer practical to double the number of grid points due to computer resource limitations. This procedure has the advantage of efficient use of computer resources in that solutions on the coarsest grid are very cheap due to the small number of grid points and large time step taken. Possible problems with the processing of the runs and the numerical formulation are identified with minimal computer resources, and confidence is gained in the solution procedure by the time the finest (and most expensive) grid level is reached. The prolongated result from the coarser grid

level also provides a "better" initial condition than starting from an artificially created initial condition which is inconsistent with the governing equations.

A by-product of this procedure is that results are generated on a number of grids with increasing resolution which can be used to address the issue of the sensitivity of the results to grid resolution. A summary for the grids used in the resolution study is given in Table 7.1. along with the number of streamwise points per fundamental wavelength. The increased resolution for the first three grid levels is obtained by doubling the number of grid points while keeping the domain dimensions constant. Continuing this trend to the fourth grid level would require 208 x 256^2 grid points which is very computationally expensive. A sufficiently long simulation on this grid would require roughly 350 Cray C-90 hours and 920 megawords of memory. An alternative is to examine the resolution of the first five diameters (on the fourth grid level only) by fixing the number of grid points and halving the domain dimensions. This region includes the entire potential core and the thin shear layer region near the inflow where resolution requirements are greatest.

Table 7.1 Summary of grids used in resolution study

Grid Level	Δx, Δy, Δz	N_x, N_y, N_z	L_x, L_y, L_z	*Points per wave*
1	0.386 x 0.313^2	26 x 32^2	10^3	2.5
2	0.193 x 0.156^2	52 x 64^2	10^3	5
3	0.096 x 0.078^2	104 x 128^2	10^3	10
4	0.048 x 0.039^2	104 x 128^2	5^3	20

Figure 7.1 shows the jet width, decay of centerline velocity, and fluctuating centerline velocity for the 4 grid resolutions. The results show that with the level 1 grid with roughly 2.5 points per fundamental wavelength, very little unsteady is resolved by the grid (see Fig. 7.1c). This results in a small spread rate in the minor axis plane and no axis-switching (lower curves, Fig. 7.1a). Increasing the grid resolution to the second level increased the

unsteadiness to 5% at x/De = 10. The results on the third level show a clear end to the potential core, followed by a leveling off of the unsteadiness. axis-switching is clearly shown in Fig. 7.1a. Increasing the grid resolution to the fourth level has a small impact on those trends. The biggest difference between the level 3 and 4 results is that the end of the potential core is shifted upstream by roughly 0.7 diameters (from 4.1D on level 3 to 3.4D on level 4). To show this point, the results on the third and fourth grid levels are replotted in Figs. 7.1d - f with the x/De coordinate shifted 0.7 diameters downstream for the fourth level. The graph shows that the results on the third level are relatively insensitive to grid refinement after the correction for potential core length. The discrepancy in the potential core length is most likely due to differences in the broad mode forcing function on the third and fourth grid level. The maximum rms intensity of the streamwise velocity perturbation is fixed at 3% of the core velocity for all grids. However, since the time step is halved with each grid refinement, the spectra content of the broad mode forcing is necessarily different on each grid. As a result of the grid resolution study, simulations in Chaps. 6 and 7 utilize the grid resolution of grid level 3. Future work should include a simulation on the 10^3 domain using 208 x 256^2 grid points, although it will be costly.

7.1.3 Velocity Spectra

Figure 7.2 displays time traces and power spectra for u, v, w, and p at six spatial locations throughout the computational domain. The first three locations correspond to the inflow plane (x/De = 0), roughly halfway (x/De = 4.13) and near the outflow plane (x/De = 8.34). The transverse location for the first three points is fixed in the center of the major axis shear layer (y, z = 0.31, 0), while the last three transverse locations are fixed in the minor axis shear layer, (y, z = 0, 0.63). The power spectra is computed by transforming the time traces from the temporal domain to the frequency domain, and are useful in determining the range of temporal scales and dominant frequencies. The results in Figs. 7.2a and

7.2*d* show that the forcing function is composed of a wide band of frequencies of similar strength. At five diameters (Figs. 7.2*b* and *e*) the power spectra show that a dominate frequency has emerged, while the highest frequency modes are several orders of magnitude smaller. Near the outflow (Figs. 7.1*c* and *f*) the range of scales is more broad suggesting that the flow is turbulent. A line with slope, $f^{-5/3}$, is included in the figures which is used to infer the presence of an inertial subrange and turbulent flow. The power spectra near the outflow (Figs. 7.2c and f) show roughly one decade with the $f^{-5/3}$ scaling.

7.1.4 Instantaneous Flow Field

Contours of streamwise velocity, pressure, vorticity magnitude, and streamwise vorticity at $t = 9$ flow through times are shown in Figs. 7.3 - 7.9. Negative contours are drawn with dashed lines while positive contours are drawn with solid lines. Local maximum and minimum values are also indicated in the figure. Contours in the minor axis plane (Fig. 7.3c) show that the shear layers roll up at roughly, $x/De = 3$, similar to a plane mixing layer. Pressure contours (Fig. 7.3b) show that the shear layers above and below the jet centerline roll up in an organized and staggered fashion. At $x/De = 4 - 5$, the unsteady structures from the upper and lower shear layers meet at the jet centerline ($y/D = 0$), thus signaling the end of the potential core. Downstream, the flow is characterized by smaller scale, less organized structures. For $x/De < 4$ the vorticity is dominated by the azimuthal components, i.e. there is no streamwise vorticity present. However, for $x/De > 4$, it is obvious that significant streamwise vorticity has been generated.

Figure 7.4c shows that shear layer roll up in the major axis plane is suppressed by roll up in the minor axis plane. Thus, the spreading of the jet in the major axis plane is suppressed resulting in a switching of the major and minor dimensions of the jet at $x/De = 7$.

The axis-switching at $t = 9$ is clearly seen by comparing streamwise velocity contours at the cross-section, $x/De = 2.44$ (Fig. 7.6) and $x/De = 9.75$ (Fig. 7.9).

7.1.5 Time-Averaged Flow Field

In the previous section, the flow field was examined at one instant in time to describe the formation and development of the unsteady structures. In this section, the impact of the unsteady structures on the mean flow is examined by time-averaging the results over a period of 11 flow through times. The results from the first flow through time are not included in the time-averaging so that transients resulting from the initial conditions are convected out of the domain. The results are then post-processed to compute statistical quantities. This procedure results in roughly 1634 samples in the period of 11 flow through times. The adequacy of sample size is addressed in the next section. The raw data files from the simulation occupy roughly 16 gigabytes of disk space.

Contours of Time-Averaged Flow Field

The time-averaged contours of streamwise velocity are shown in Fig. 7.10. Comparing contours of streamwise velocity confirms that axis-switching has indeed taken place at roughly seven diameters as was suggested by examining the instantaneous contours at $t =$ 9 flow through times. Figure 7.10e and f shows that roll up and interaction of structures result in rapid spreading in the minor axis plane only. The end of the potential core occurs at roughly $x/De = 4.5$, where the velocity along the jet centerline is no longer equal to the core velocity and begins to decrease due to entrainment of ambient fluid.

Profiles of First and Second Moment Quantities

In this section detailed profiles of time-averaged velocity, pressure and the six unique Reynolds stress components are shown. In addition, jet widths in the major and minor axis

planes, entrainment rate, centerline velocity and fluctuating centerline velocity are given. The numerical results are compared with available experimental results.

Time-averaged and fluctuating velocity components are normalized with the local velocity on the jet centerline, U_{CL} and transverse coordinates are normalized by the local jet width defined by the transverse distance where $U/U_{CL} = 0.5$. Figure 7.11a shows that axis-switching takes place at x/De = 6.8. Tsuchiya (1985) reported the axis-switching location of their 2:1 *AR* jet from a smoothly contoured nozzle to be $x/De = 6.0$. A second axis-switching was reported at $x/De = 25$ which is beyond the computational domain used in this study. Experiments of turbulent jets from contoured nozzles (Quinn 1995) show the first axis-switching to be as far as x/De = 12. A measure of entrainment into the jet (Fig. 7.11b) is provided by computing the difference in mass flux at the cross-section, x, and that at the inflow, $Q(x) - Q_0$, where $Q(x) = \int\int \rho U(x, y, z) dydz$ and $Q_0 = \int\int \rho U(0, y, z) dydz$. Figure 7.11c shows the decay of centerline velocity with streamwise distance. The end of the potential core is predicted at x/De = 4.0, which is in excellent agreement with the experimentally measured value of x/De = 4.1 by Tsuchiya (1985). The development of fluctuating velocity on the jet centerline is shown in Fig. 7.11d. For $x/De < 4$ the velocity fluctuations on the centerline are small. Near the end of the potential core, the fluctuating velocity rises sharply which is a result of the unsteady structures from the mixing layers meeting at the centerline. Downstream of the potential core, the fluctuating velocity is roughly constant when scaled with the local centerline velocity.

Profiles of time-averaged streamwise velocity are shown in Fig. 7.12 at various streamwise locations. For comparison, the experimental results of Quinn (1995) at x/De = 10 are included. The LES results at x/De = 9 are in excellent agreement with the experimental results. Self-similar profiles are predicted in the minor axis plane downstream of the potential core, while non-similar ones are predicted in the major axis plane. This

observation is consistent with the experimental studies of Sforza et al. (1966), Trentacoste and Sforza (1967), and Tsuchiya (1985). Figure 7.13 shows some self-similarity of the time-averaged lateral velocity component, V, along the y axis at the last two cross-sections ($x/De > 7$). Note that negative (positive) transverse velocity at the top (bottom) edge of the jet is consistent with fluid being entrained into jet. The lateral velocity along the z axis should be zero due to symmetry. The numerical results predict small lateral velocity along the z axis. Time-averaged transverse velocity profiles are shown in Fig. 7.14 which are clearly non-similar along the z axis. The transverse component should be close to zero along the y axis due to symmetry. Krothapalli et al. (1981) reported similar trends for rectangular jets from smoothly contoured nozzles at higher aspect ratios AR = 16.7. Time-averaged pressure profiles displayed in Fig. 7.15 show small positive values in the potential core followed by large negative values downstream of the potential core.

The normal components of the Reynolds stress tensor (plotted as *rms* values) are shown in Figs. 7.16 - 7.18, while the shear components are shown in Figs. 7.19 - 7.21. In general, profiles of the normal components are relatively flat along the y axis near the centerline, while off center peaks are present along the z axis downstream of the potential core. Upstream of the end of the potential core, the peaks in the normal components correspond to unsteadiness in the mixing layers separating the jet core from the ambient surroundings.

Peak values are higher (20 - 30%) than those reported for a rectangular jet by Quinn (1995). Similar trends exist for the shear components. The shear components of the Reynolds stresses show that the dominant components are predicted for $<u'v'>$ along the y axis (Fig. 7.19a) and $<u'w'>$ along the z axis (Fig. 7.20b).

7.1.6 Two-Point Velocity Correlations

In this section, results of two-point velocity correlations taken on the jet centerline at two cross-sections are presented. The correlations are used to estimate the size of the coherent structures along the jet centerline downstream of the potential core. In addition, the correlations are used to access the placement of the freestream boundaries in the computation. Large correlation coefficients at the edges of the computational domain indicate that freestream boundaries are too close to the centerline.

The transverse size of the coherent structures was estimated using two-point spatial correlations which requires prescribing the spatial separation, r, along the transverse direction with zero time separation. The two-point correlation is given by:

$$R_{ij}(\vec{r}_o + \vec{r}) = \frac{\langle \tilde{u}_i(\vec{r}_o, t)\tilde{u}_j(\vec{r}_o + \vec{r}, t)\rangle}{[\langle \tilde{u}_j(\vec{r}_o, t)^2\rangle \langle \tilde{u}_j(\vec{r}_o + \vec{r}, t)^2\rangle]^{1/2}} \tag{7.1}$$

where $< >$ denotes time-averaging, $\vec{r}_o = (x_o, y_o, z_o)$ denotes the location of the correlation, and $\vec{r}$ denotes the separation distance and direction of the correlation. An estimate of the structure size can be obtained by fitting a parabola through the data points near $y = 0$ and $z = 0$ in Figs. 7.22 - 7.24. In each figure, the top plot represents the correlation with the separation distance along the y axis, while the bottom plot is along the z axis. The correlations show that events near the jet centerline are uncorrelated with those near the edge of the domain, thus justifying the placement of the free stream boundaries in the computation.

7.1.7 Budgets

In this section a detailed term by term budget is presented for the resolved time-averaged momentum equations and the Reynolds stress transport equations. The imbalance in the terms of the resulting equation can then be used to access the adequacy of the sample

size. The momentum and Reynolds stress budgets can also be used for turbulence modeling of complex three-dimensional jets. Computation of budget terms for the plane mixing layer was performed by Rogers and Moser (1994). Demuren et al. (1996) used DNS data to develop turbulence models for the pressure diffusion in mixing layers and wakes.

Momentum Equation

The mean momentum equation for the resolved velocities is derived by time-averaging the filtered equations of motion given by Eq. (2.8). Omitting the details of the derivation, the result becomes:

$$\frac{\partial U_i}{\partial t} = -U_j\frac{\partial U_i}{\partial x_j} - \frac{\partial P}{\partial x_i} + \frac{1}{Re}\frac{\partial^2 U_i}{\partial x_j \partial x_j} - \left(\frac{\partial}{\partial x_j}\right)\langle u_i' u_j' \rangle - \left(\frac{\partial}{\partial x_j}\right)\langle q_{ij} \rangle \qquad (7.2)$$

where $U_i = \langle \bar{u}_i \rangle$ and $P = \langle \bar{\phi} \rangle$ denotes the time-averaged velocity and pressure, respectively. The first three terms on the RHS of Eq. (7.2) represent the convection, pressure gradient, and viscous diffusion terms, respectively.

For statistically stationary results, the terms on the RHS of Eq. (7.2) should sum to zero indicating that the time derivative of the average velocity is also zero. The fourth term on the RHS of (7.2) represents the resolved stresses due to unsteadiness of the velocity field and is similar to the Reynolds stress term in the Reynolds Averaged Navier-Stokes (RANS) equations. This term is computed directly in the large-eddy simulation approach. The last term on the RHS of Eq. (7.2) represents the contribution of the unresolved stresses. The concept of LES is that a large portion of the energy containing large scale stresses (fourth term on RHS) is resolved in the computation, compared with the unresolved portion which is modeled (last term on RHS).

Profiles of budget terms for the U momentum equation are shown in Fig. 7.25 along the y and z axis at the location, $x/De = 9$. Since the unresolved stresses, q_{ij}, are not available from the LES results, the eddy viscosity model given by Eq. (2.9) is used to compute the last term in Eq. (7.2). The resulting profiles in Figs. 7.25 - 7.30 have been passed through a filter to remove some high frequency noise which tends to obscure the trends. The sum of the terms on the RHS of Eq. (7.2) is represented by the symbols. The profiles show that the imbalance is relatively small compared to the convection and resolved Reynolds stress terms, and that the convection terms balance the Reynolds stress terms. The results also show that the unresolved SGS stresses are quite small compared with the resolved Reynolds stresses, validating the LES. The budgets for the V momentum equation in Fig. 7.26 show that along the y axis, the pressure gradient term balances the resolved Reynolds stress term at $y/D \sim \pm 2$.

The budget terms along the z axis are smaller in comparison as would be expected from symmetry arguments. Figure 7.27 shows similar trends for the W equation. The sense of the pressure gradient term for the V and W equation is consistent with fluid being entrained into the jet on a time-averaged basis.

Resolved Reynolds Stress Equation

The transport equations for the resolved Reynolds stresses are derived by first subtracting the filtered equations of motion, Eq. (2.8), from the time-averaged filtered equations, Eq. (7.2). The result is a transport equation for the i_{th} component of the resolved fluctuating velocity component. Time-averaging the quantity; $u_j' \cdot [u_i'\text{equation}] + u_i' \cdot [u_j'\text{equation}]$ gives the transport equation for the resolved Reynolds stresses. Again, omitting the details of the derivation:

$$\frac{\partial}{\partial t}\langle u_i'u_j'\rangle = -U_k\frac{\partial}{\partial x_k}\langle u_i'u_j'\rangle - \left[\langle u_j'u_k'\rangle\frac{\partial U_i}{\partial x_k} + \langle u_i'u_k'\rangle\frac{\partial U_j}{\partial x_k}\right]$$

$$-\frac{\partial}{\partial x_k}\langle u_i'u_j'u_k'\rangle - \left[\langle u_j'\frac{\partial \phi'}{\partial x_i}\rangle + \langle u_i'\frac{\partial \phi'}{\partial x_j}\rangle\right] - \frac{2}{Re}\langle\frac{\partial u_i}{\partial x_k}\frac{\partial u_j}{\partial x_k}\rangle + \frac{1}{Re}\frac{\partial^2\langle u_i'u_j'\rangle}{\partial x_j\partial x_j}$$

$$-\left[\langle u_j'\frac{\partial q_{ik}'}{\partial x_k}\rangle + \langle u_i'\frac{\partial q_{jk}'}{\partial x_k}\rangle\right] \qquad (7.3)$$

The first six terms on the RHS of Eq. (7.3) represent convection of the Reynolds stresses by the mean flow, turbulent production, turbulent dissipation, fluctuating velocity/ pressure gradient coupling, turbulent diffusion, and viscous diffusion, respectively. The last term on the RHS of Eq. (7.3) represents the contribution of the unresolved stresses to the resolved Reynolds Stresses equation. As with the momentum budget, the SGS model is used to estimate this term.

Figure 7.33 shows profiles of the $<u'u'>$ budget of the resolved Reynolds stress equation at the same location as the momentum budgets. It can be seen that a large positive production term is opposed by a negative velocity pressure gradient term. Convection and turbulent diffusion are also significant. Turbulent dissipation and viscous diffusion are small. The contribution of the SGS term is estimated to have a modest negative contribution. Budgets for the $<u'u'>$ and $<u'u'>$ are shown in Figs. 7.29 and 7.30a, respectively.

The results show that the imbalance is of the same order as some of the individual terms near the jet centerline. The imbalance is most likely due to the unresolved terms which are estimated. The dominate role of the very smallest scales (which are not resolved in LES) is in the dissipation of turbulent kinetic energy into heat. Since the smallest scales are not resolved, the turbulent dissipation term in Eq. (7.3) does not resemble the term in the fully resolved Reynolds stress equation. As a result, there is a large positive imbalance due to this discrepancy. Indeed, in some experimental studies which measure budgets of

the Reynolds stress equations, the imbalance is labeled as the turbulent dissipation because it cannot be accurately measured. The budget for the $<u'u'>$ equation from the DNS of the rectangular jet (case iii of Chap. 6) is shown in Fig. 7.30b. The overall balance of terms is better since the dissipation scales are resolved.

7.2 Elliptic Jet

In this section, the results of a large eddy simulation of a 2:1 *AR* elliptic jet at Re_{De} = 75,000 with broad mode forcing are presented. The grid and domain parameters are identical to those described for the LES of the rectangular jet. The jet boundary layer at the inflow is generated by using, $n = 2$ for the exponent of the super-elliptic coordinate system. Figure 7.31 shows that the mixing layer in the potential core of the elliptic jet rolls up preferentially in the minor axis plane at the expense of mixing in the major axis plane. The roll ups are not as orderly and well-defined as in the rectangular jet. Contours at the cross-section, $x/D_e = 4.88$ (Fig. 7.35d) reveal the generation of significant streamwise vorticity around the circumference of the jet boundary layer resulting in the distortion of the elliptic cross-section. It is apparent that the major and minor axis have already switched by the cross-section, $x/D_e = 9.75$ (Fig. 7.37).

Time-averaged contours of streamwise velocity shown in Fig. 7.38 reveal that axis-switching also takes place in the elliptic jet. Time-averaged results for the elliptic jet simulation are presented in Figs 7.39 - 7.49. The instantaneous results are averaged over eight flow through times resulting in a sample size of roughly 1200. The plot of jet widths (Fig. 7.39a) confirms that axis-switching has taken place at $x/D_e = 5.9$ and that the width in the major axis plane actually decreases slightly in agreement with the experimental results of unexcited 2:1 *AR* elliptic jets studied by Hussain and Husain (1989). The axis-switching location in that study occurred at roughly $x/D_e = 5.0$. Fig. 7.39b shows that the elliptic jet

entrains more fluid than the rectangular jet which is consistent with experimental observations. A summary of axis switching location is provided in Table 7.2 along with those from experiment.

Table 7.2 Summary of axis switching location from LES

Study	Geometry	AR	Location, x/D_e
Tsuchiya et al. (1985)	Rectangular	2	6.0
Quinn (1985)	"	"	11.0
Current	"	"	6.8
Hussain and Husain (1989)	Elliptic	"	5.0
Current	"	"	5.9

7.3 Round Jet

Large eddy simulation of a round jet is performed to provide a control for the simulations of rectangular and elliptic jets. Parameters for the round jet simulation are identical to those for the non-circular jets, with the obvious geometrical difference. For the round jet simulation, some asymmetry of profiles along the y and z axis exist beyond 6 diameters due to insufficient sample size. Perfectly symmetrical time-averaged profiles are difficult to achieve in experiments and computations of fully turbulent flow.

Contours of instantaneous streamwise velocity, pressure and vorticity for the round jet are shown in Figs. 7.50 and 7.51 in the x-y and x-z plane, respectively. Cross-sectional contours are shown in Figs. 7.52 - 7.56. The contours in the x-y and x-z plane show that regular, planar rings are not formed with the broad mode forcing function. Cross-sectional contours at x/D_e = 4.88 (Fig. 7.54) show significant generation of streamwise vorticity along the jet boundary layer resulting in a distortion of the initially circular profile. Further downstream, the vortices breakdown into small scale structures.

Time-averaged contours of streamwise velocity shown in Fig. 7.57 reveal that jet widths in the x-y and x-z planes grow at the same rate and axis-switching does not take place. Time-averaged quantities from the round jet simulation are shown in Fig. 7.58 for comparison with the non-circular jet simulations.

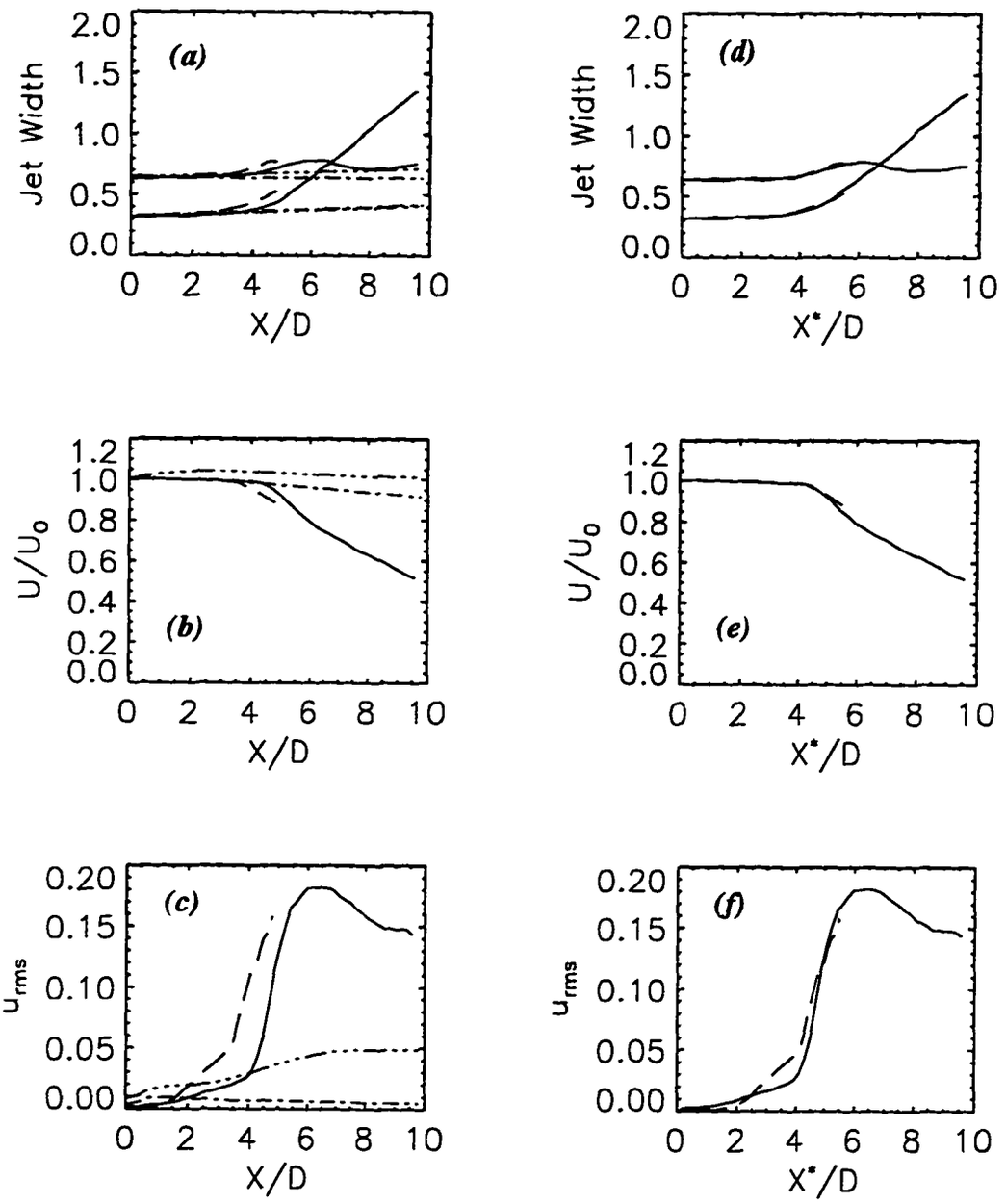

Fig 7.1 **Effect of grid resolution, *(a)* - *(c)* time-averaged quantities versus x, *(d)* - *(f)* level 4 corrected for length of potential core; (dot-dash : level 1 grid ; 3 dots-dash : level 2 grid ; solid : level 3 ; dash : level 4).**

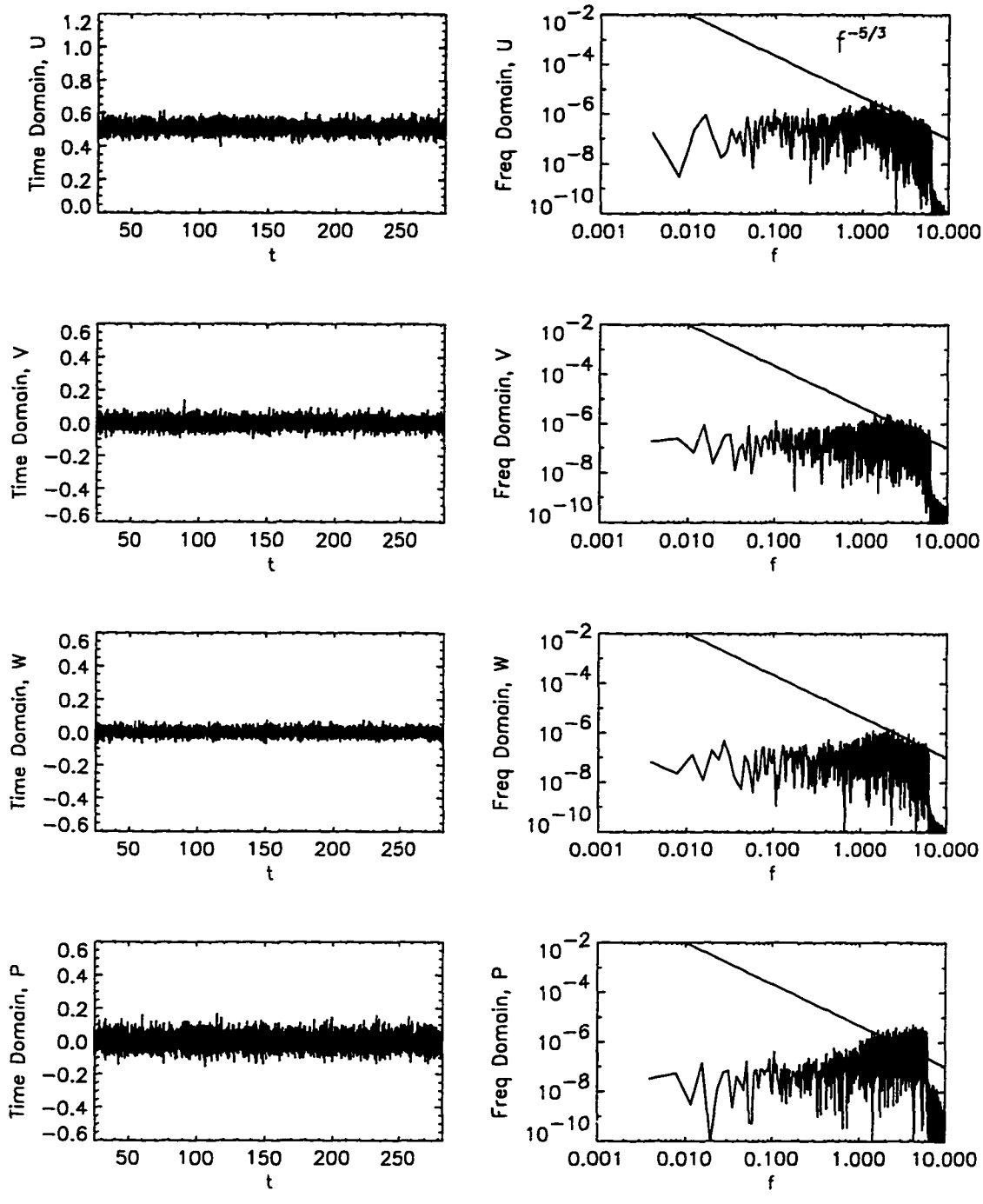

Fig 7.2a Time traces (first column) and power spectra (second column) for *U, V, W,* and *P* on minor axis, *(x, y, z)* = (0, 0.31, 0) Re_{De} = 75,000.

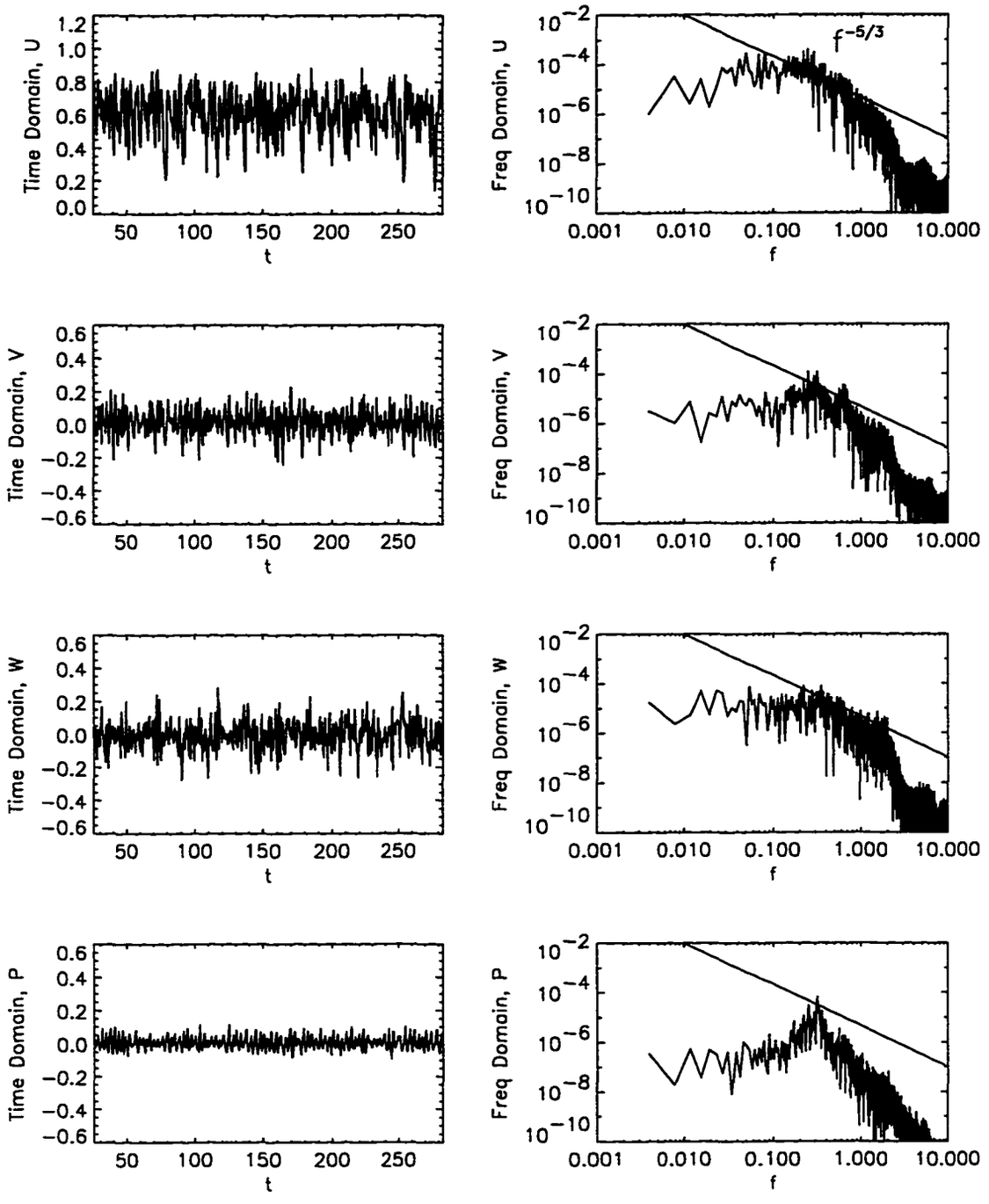

Fig 7.2b Time traces (first column) and power spectra (second column) for *U, V, W,* and *P* on minor axis, *(x, y, z)* = (4.13, 0.31, 0) Re_{De} = 75,000.

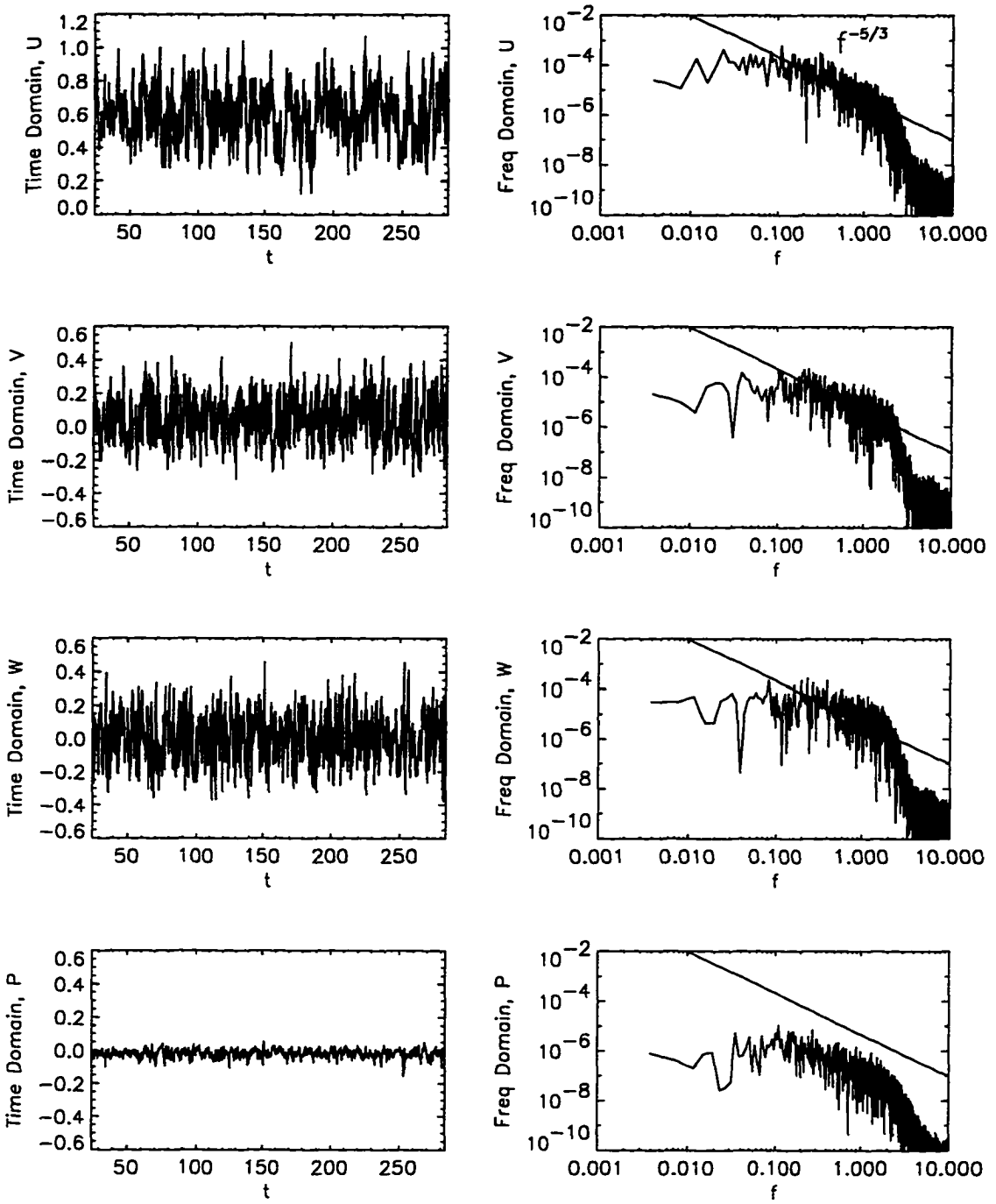

Fig 7.2c Time traces (first column) and power spectra (second column) for *U, V, W,* and *P* on minor axis, *(x, y, z)* = (8.34, 0.31, 0) Re_{De} = 75,000.

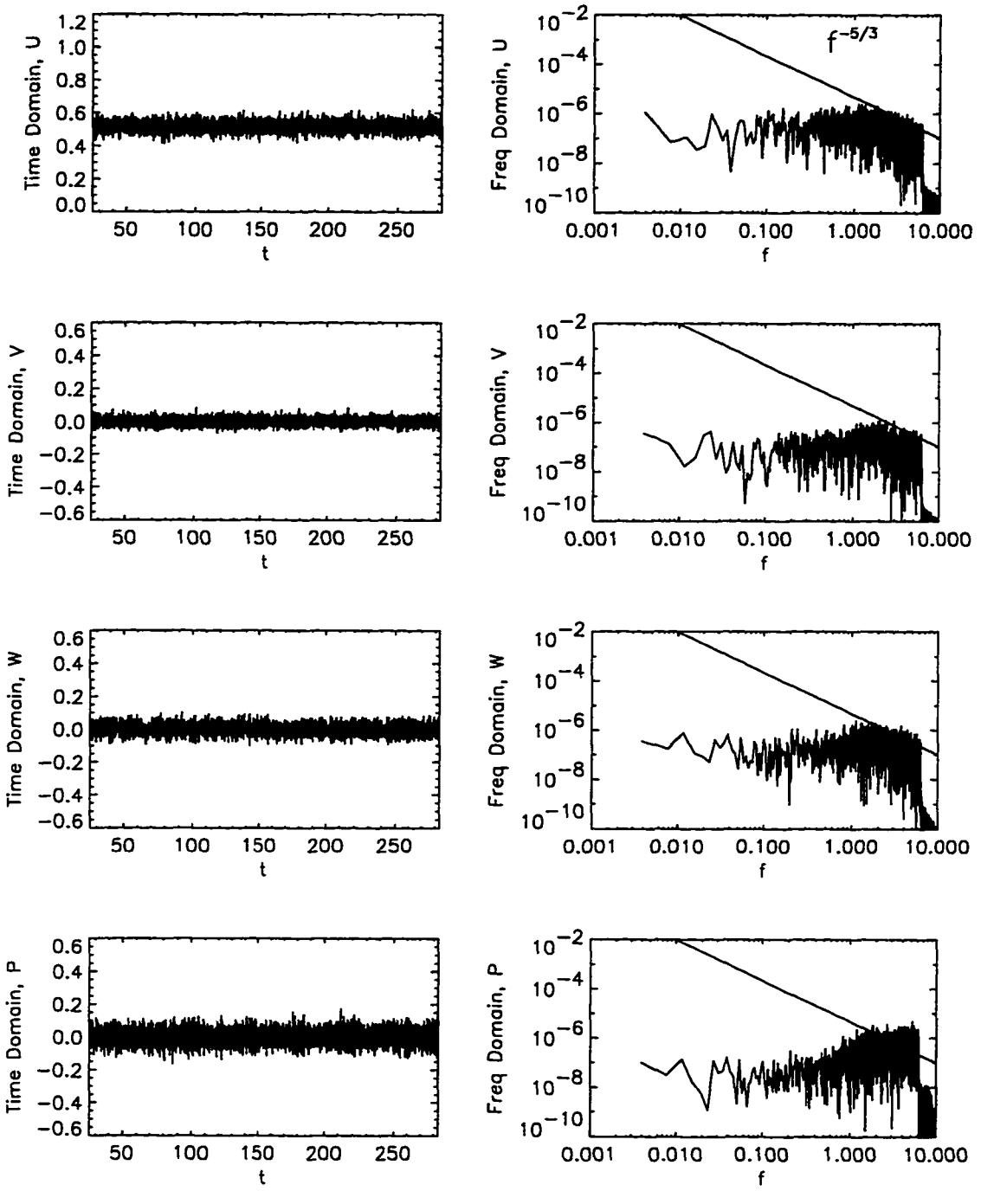

Fig 7.2d Time traces (first column) and power spectra (second column) for *U, V, W,* and *P* on major axis, *(x, y, z)* = (0, 0, 0.63) Re_{De} = 75,000.

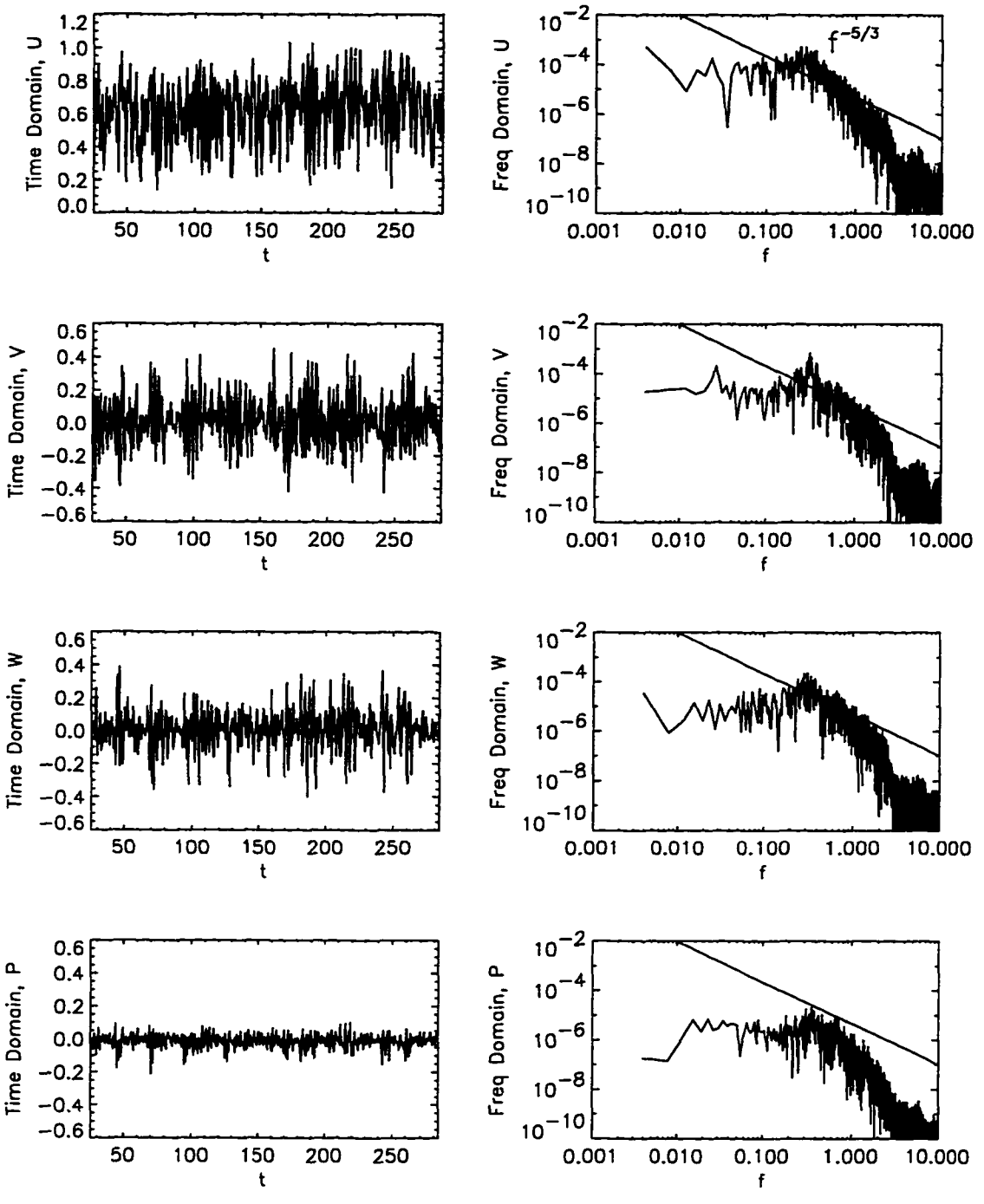

Fig 7.2e Time traces (first column) and power spectra (second column) for *U, V, W,* and *P* on minor axis, $(x, y, z) = (4.13, 0, 0.63)$ $Re_{De} = 75{,}000$.

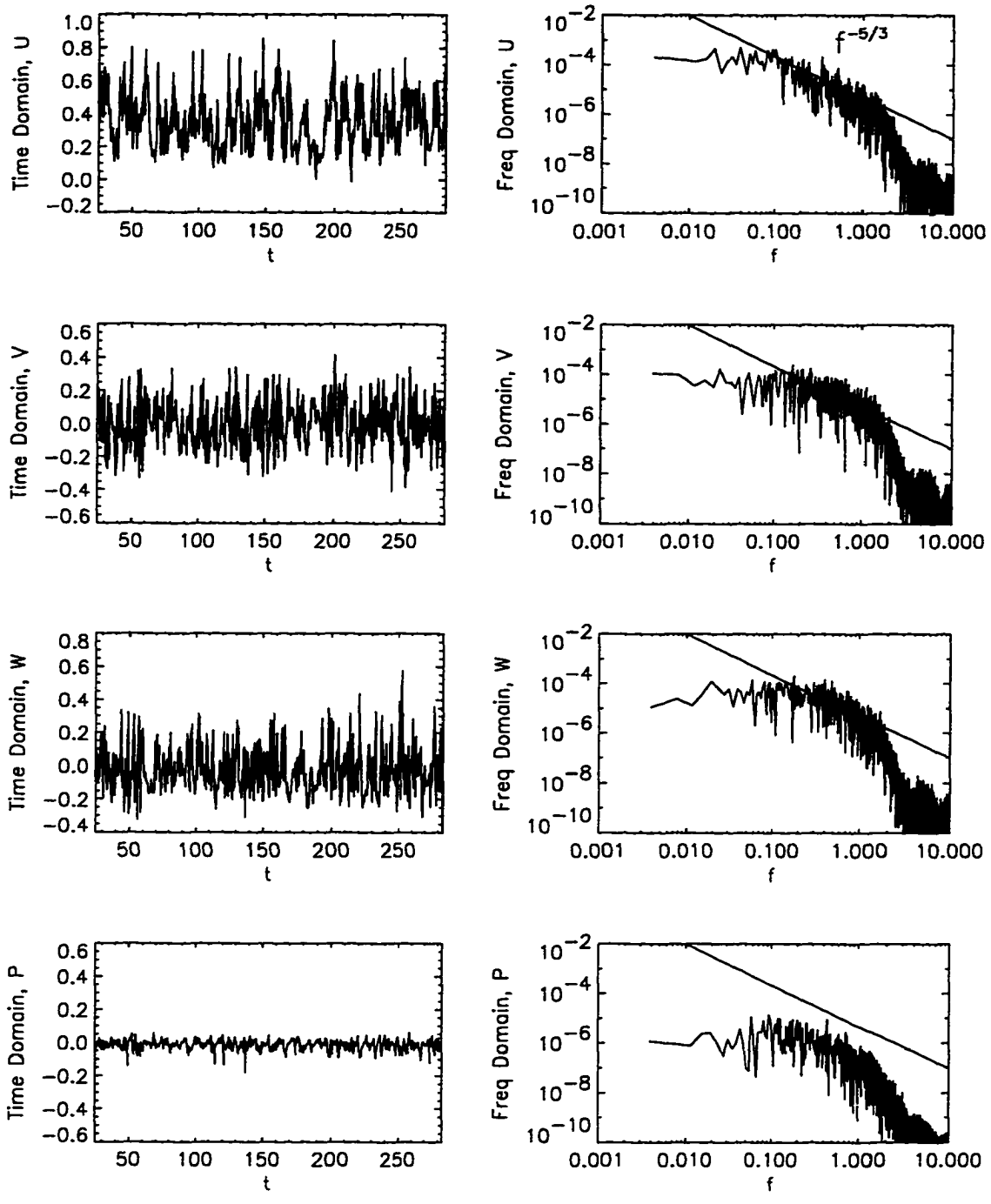

Fig 7.2f **Time traces (first column) and power spectra (second column) for *U, V, W,* and *P* on minor axis, *(x, y, z)* = (8.34, 0, 0.63) Re_{De} = 75,000.**

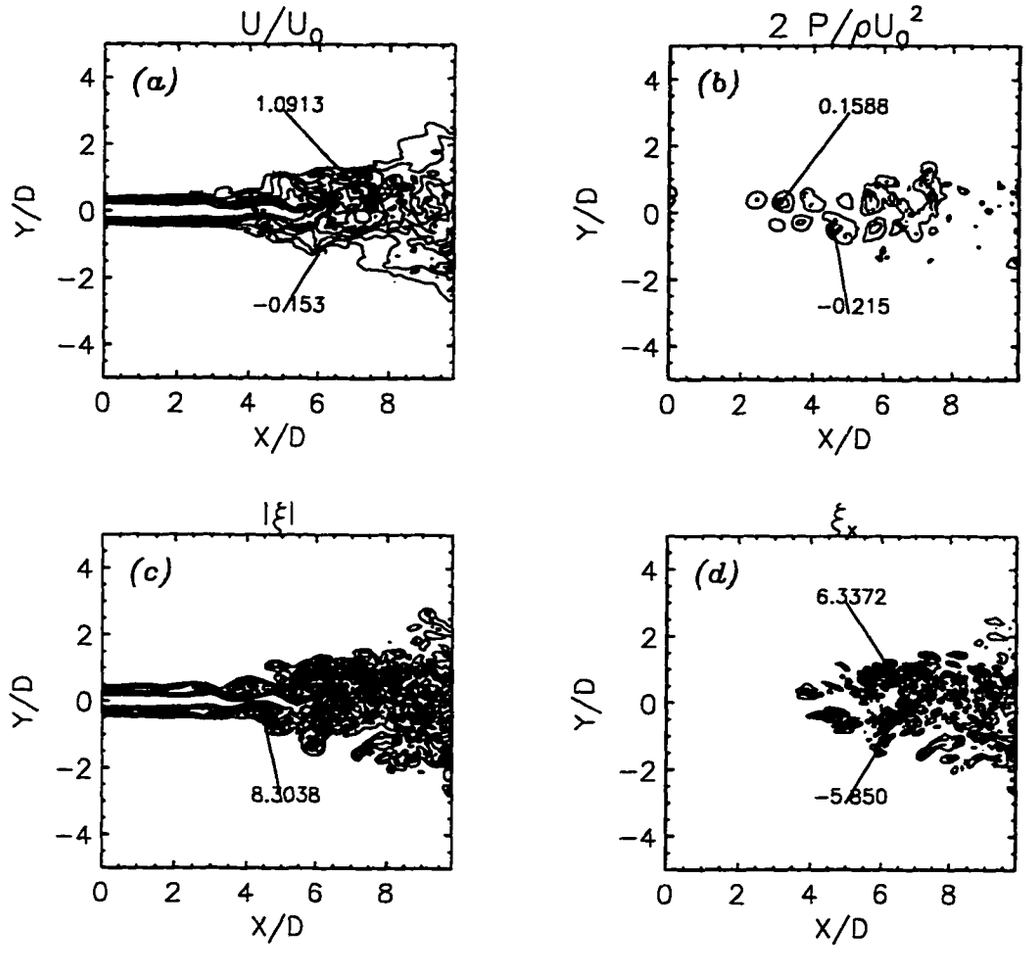

Fig 7.3 **Contours in the minor axis plane ($z/D = 0$) at $t = 9$ for LES of rectangular jet; *(a)* streamwise velocity, *(b)* pressure, *(c)* vorticity magnitude, and *(d)* streamwise vorticity.**

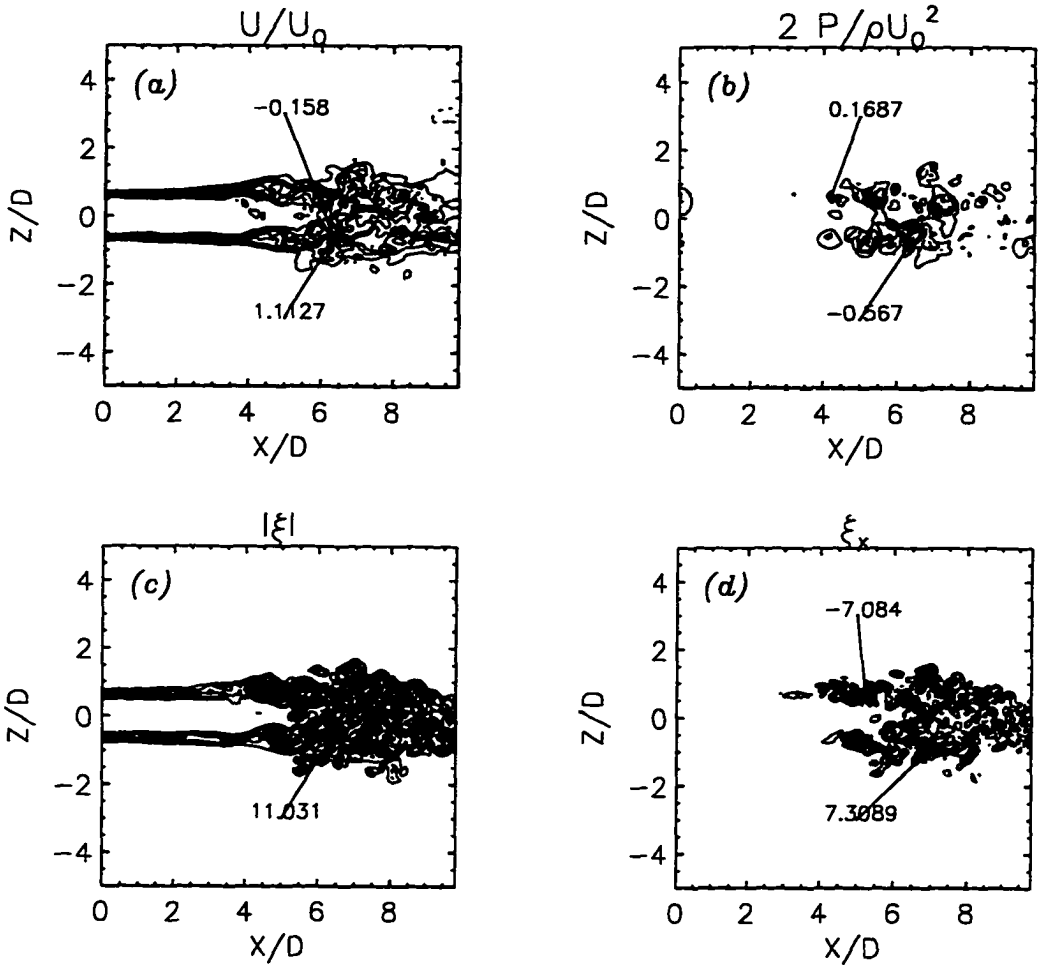

Fig 7.4 **Contours in the major axis plane ($z/D = 0$) at $t = 9$ for LES of rectangular jet; *(a)* streamwise velocity, *(b)* pressure, *(c)* vorticity magnitude, and *(d)* streamwise vorticity.**

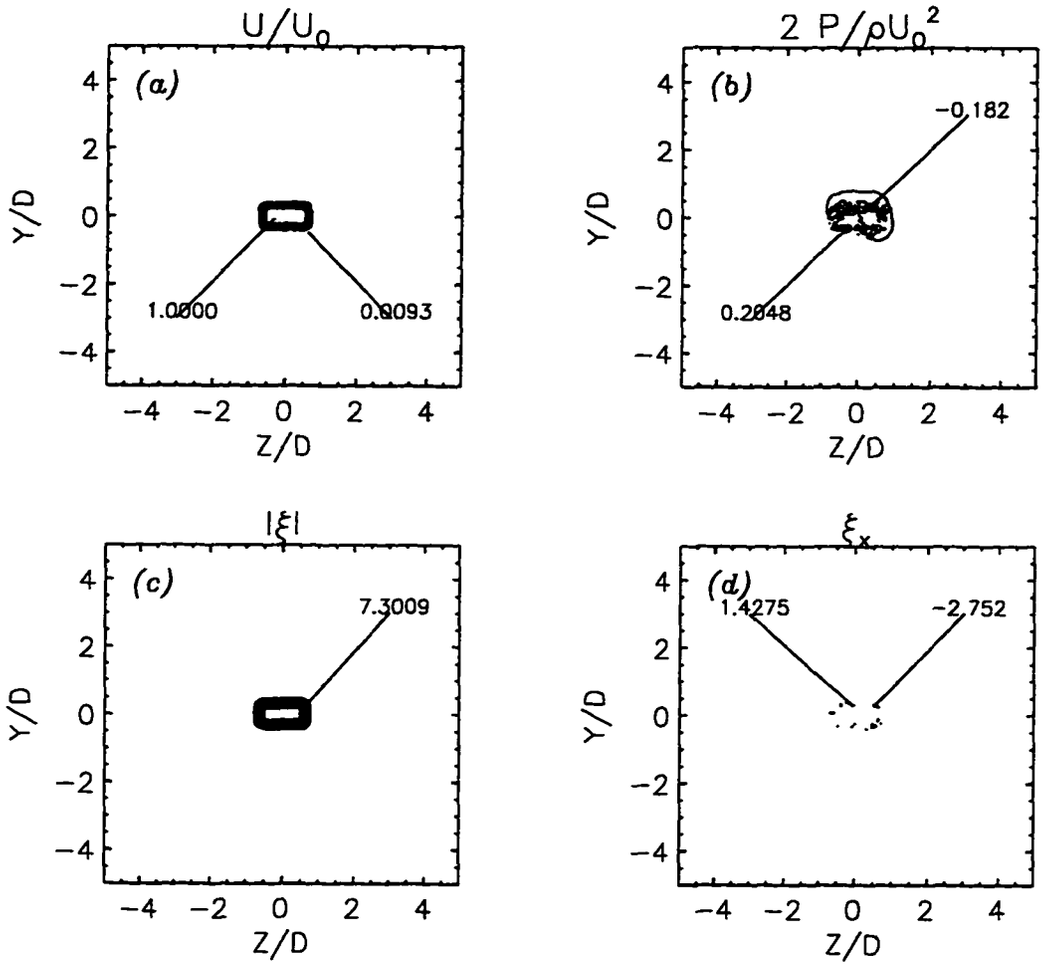

Fig 7.5 **Contours at the cross-section, x/*D* = 0, at *t* = 9 for LES of rectangular jet; *(a)* streamwise velocity, *(b)* pressure, *(c)* vorticity magnitude, and *(d)* streamwise vorticity.**

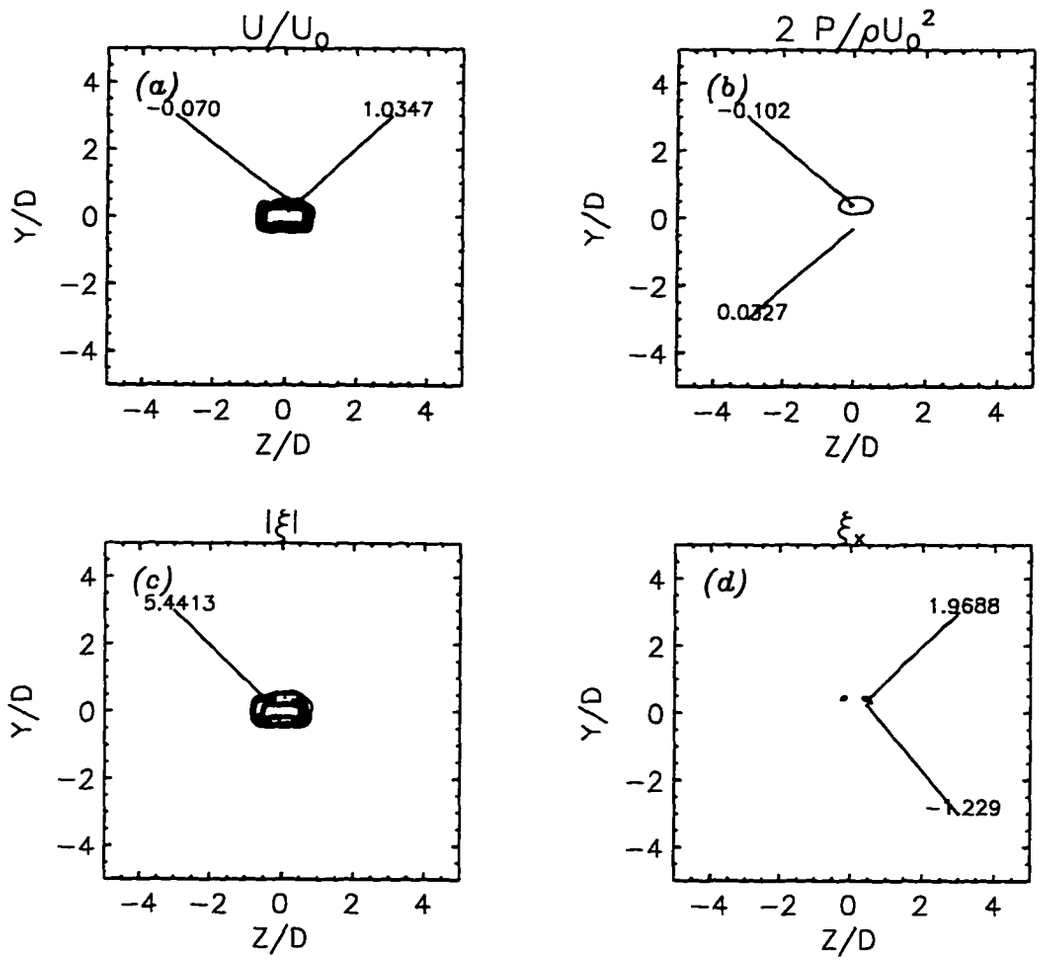

Fig 7.6 **Contours at the cross-section, x/*D* = 2.44, at *t* = 9 for LES of rectangular jet; *(a)* streamwise velocity, *(b)* pressure, *(c)* vorticity magnitude, and *(d)* streamwise vorticity.**

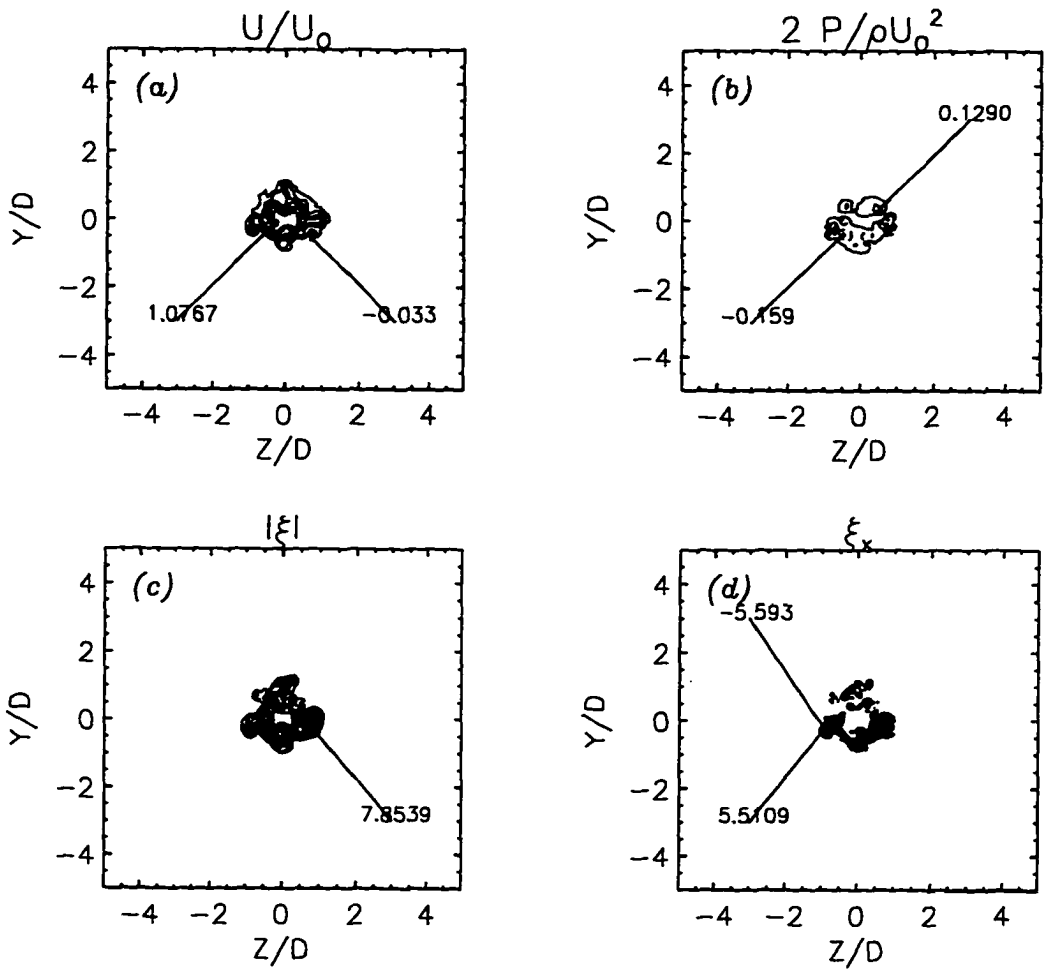

Fig 7.7 **Contours at the cross-section, x/*D* = 4.88, at *t* = 9 for LES of rectangular jet; *(a)* streamwise velocity, *(b)* pressure, *(c)* vorticity magnitude, and *(d)* streamwise vorticity.**

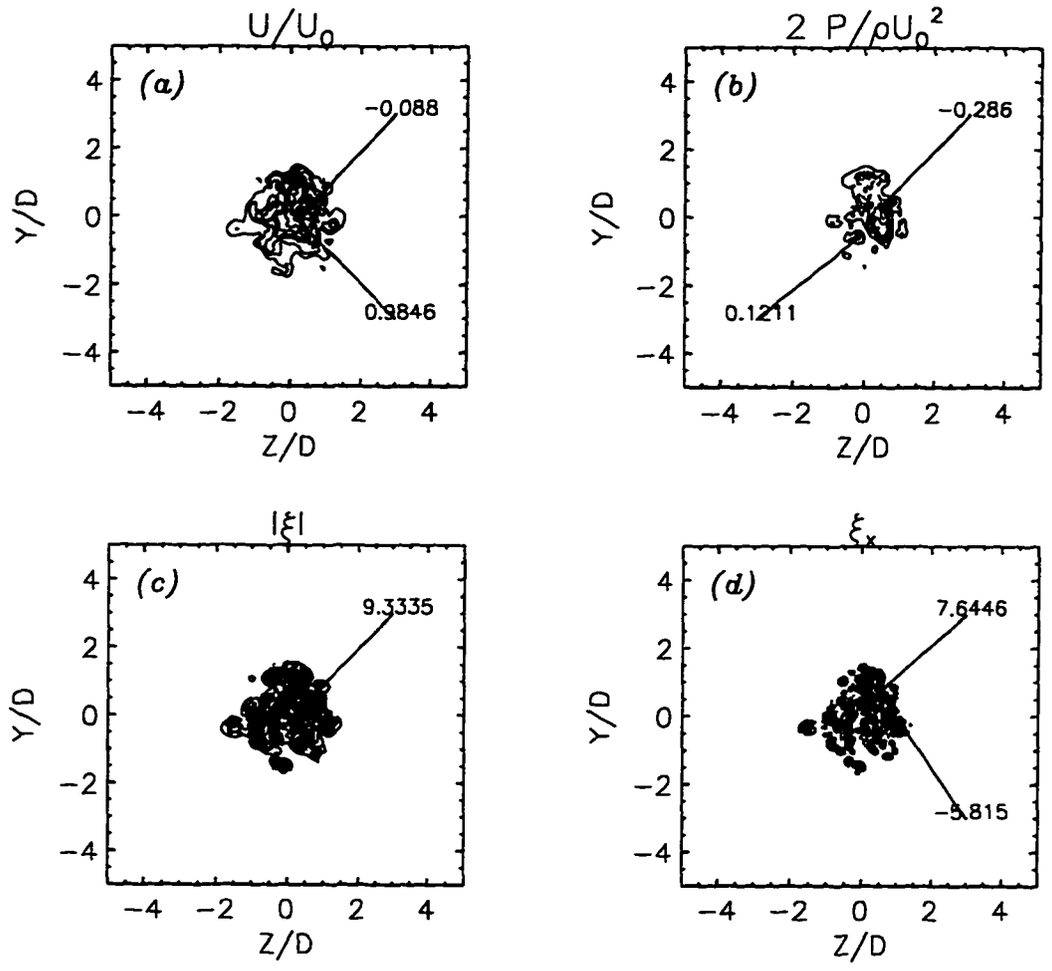

Fig 7.8 **Contours at the cross-section, x/*D* = 7.31, at *t* = 9 for LES of rectangular jet; *(a)* streamwise velocity, *(b)* pressure, *(c)* vorticity magnitude, and *(d)* streamwise vorticity.**

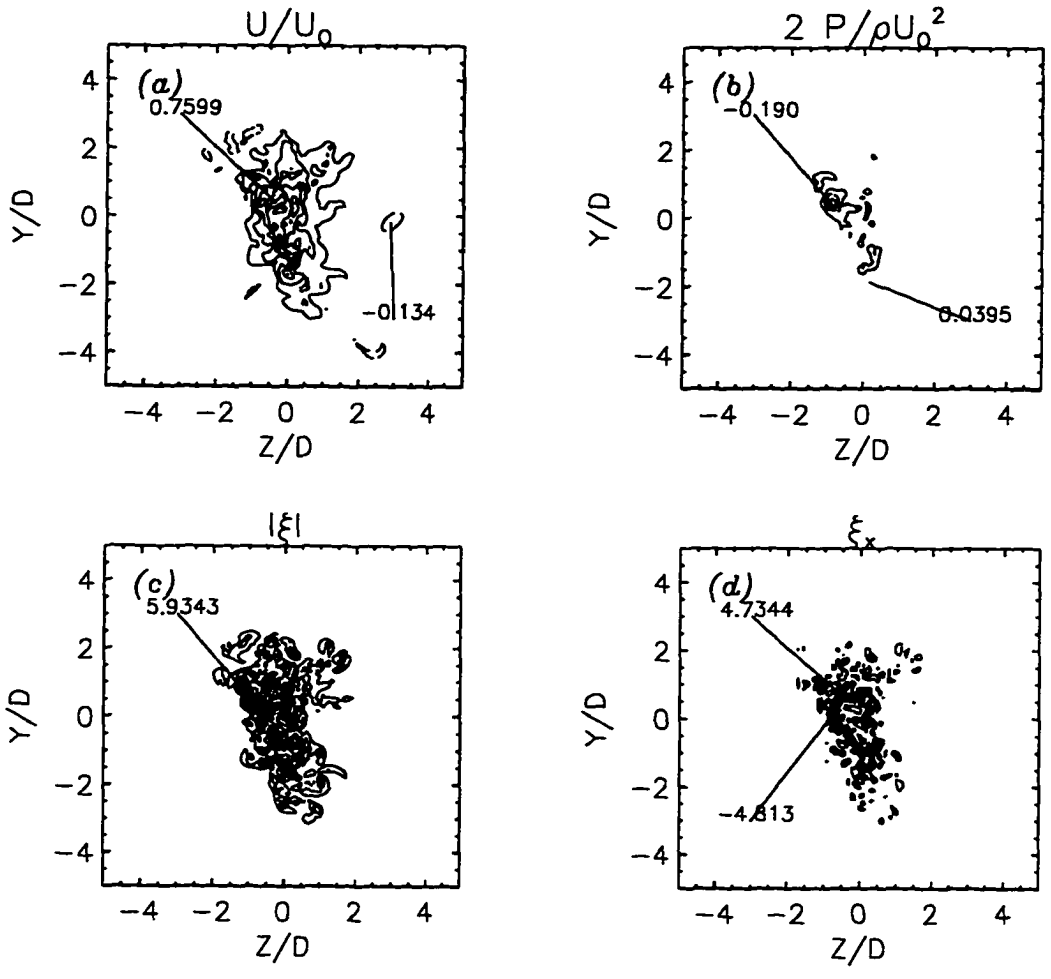

Fig 7.9 **Contours at the cross-section, x/*D* = 9.75, at *t* = 9 for LES of rectangular jet; *(a)* streamwise velocity, *(b)* pressure, *(c)* vorticity magnitude, and *(d)* streamwise vorticity.**

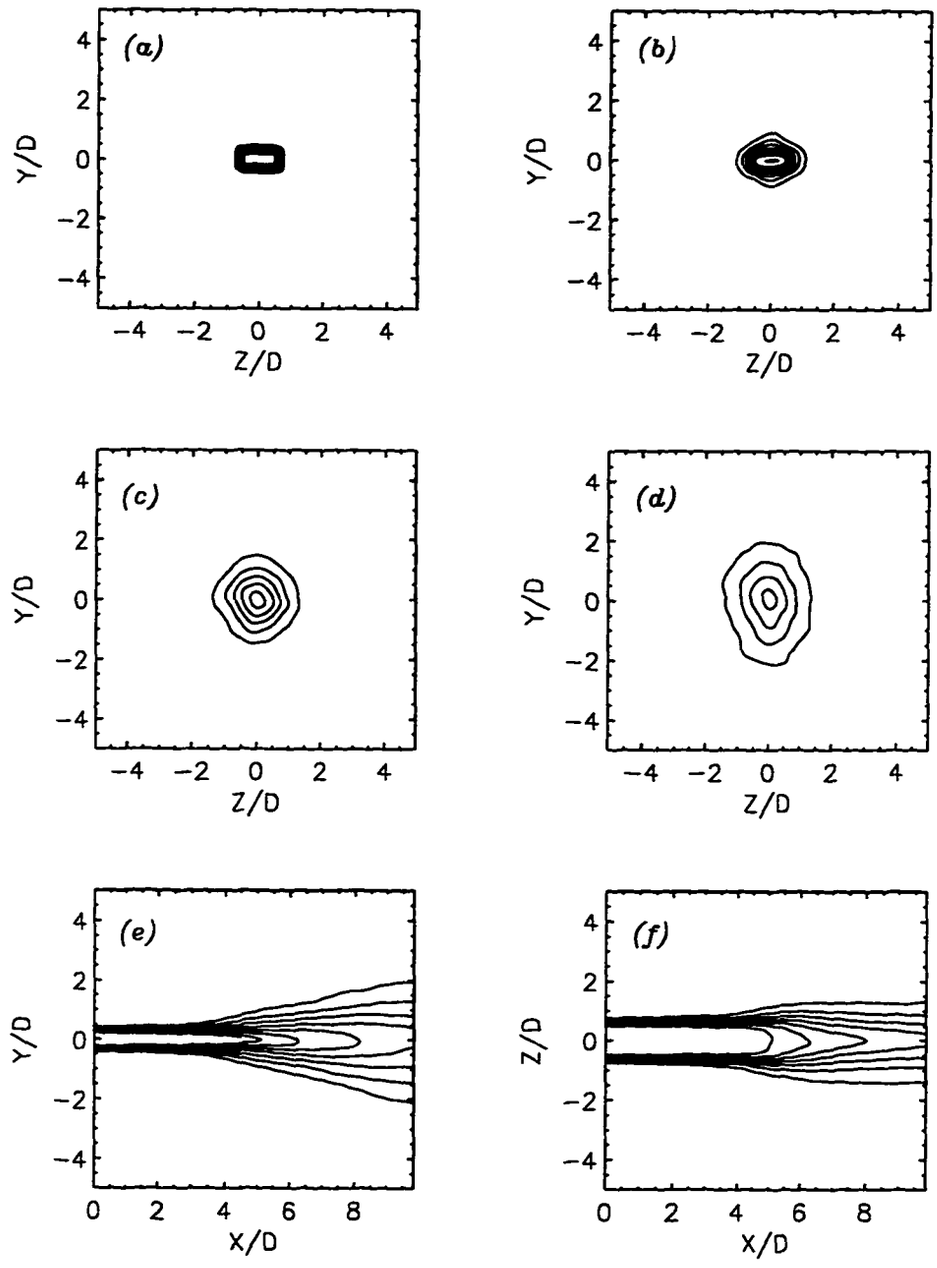

Fig 7.10 **Time-averaged contours of streamwise velocity for LES of rectangular jet; *(a)* $x/D = 0$, *(b)* $x/D = 4.88$, *(c)* $x/D = 7.31$, *(d)* $x/D = 9.75$, *(e)* minor axis plane, $z/D = 0$, *(f)* major axis plane, $y/D = 0$.**

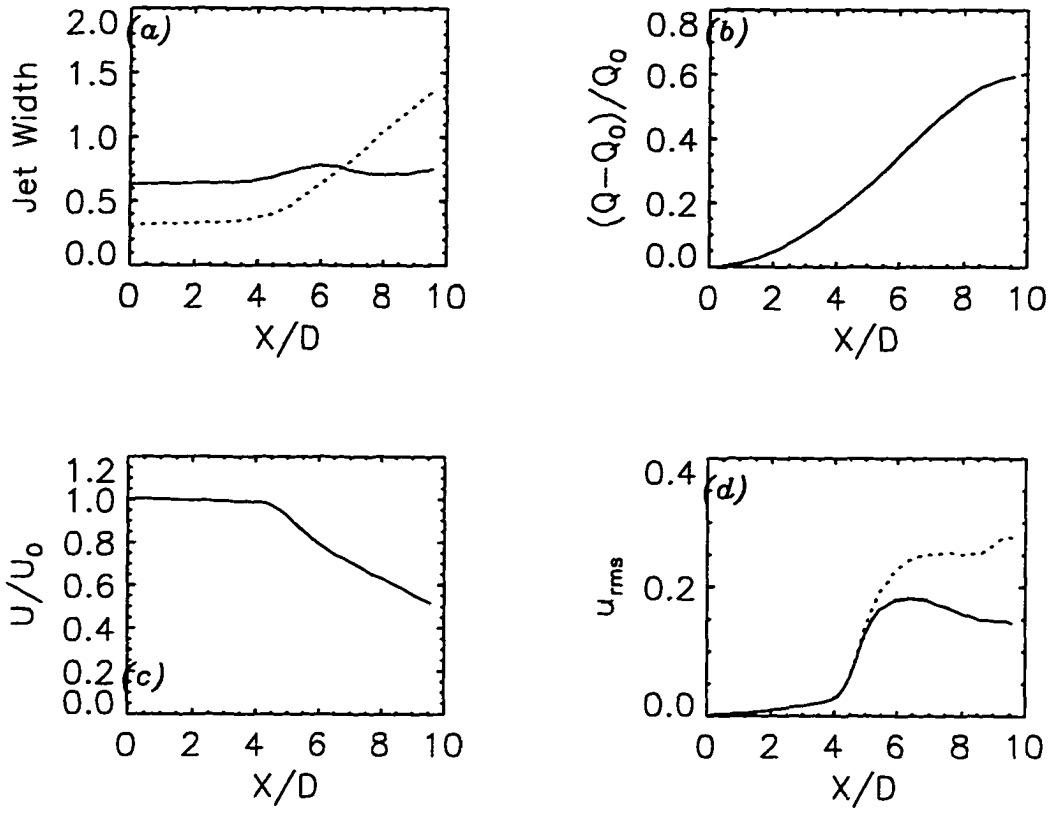

Fig 7.11 **Time-averaged quantities versus streamwise distance for LES of rectangular jet; (a) jet widths (solid - major axis plane, dashed - minor axis plane), (b) entrainment ratio, (c) decay of centerline velocity, (d) fluctuating velocity (solid - u_{rms}/U_O, dashed - u_{rms}/U_{CL}).**

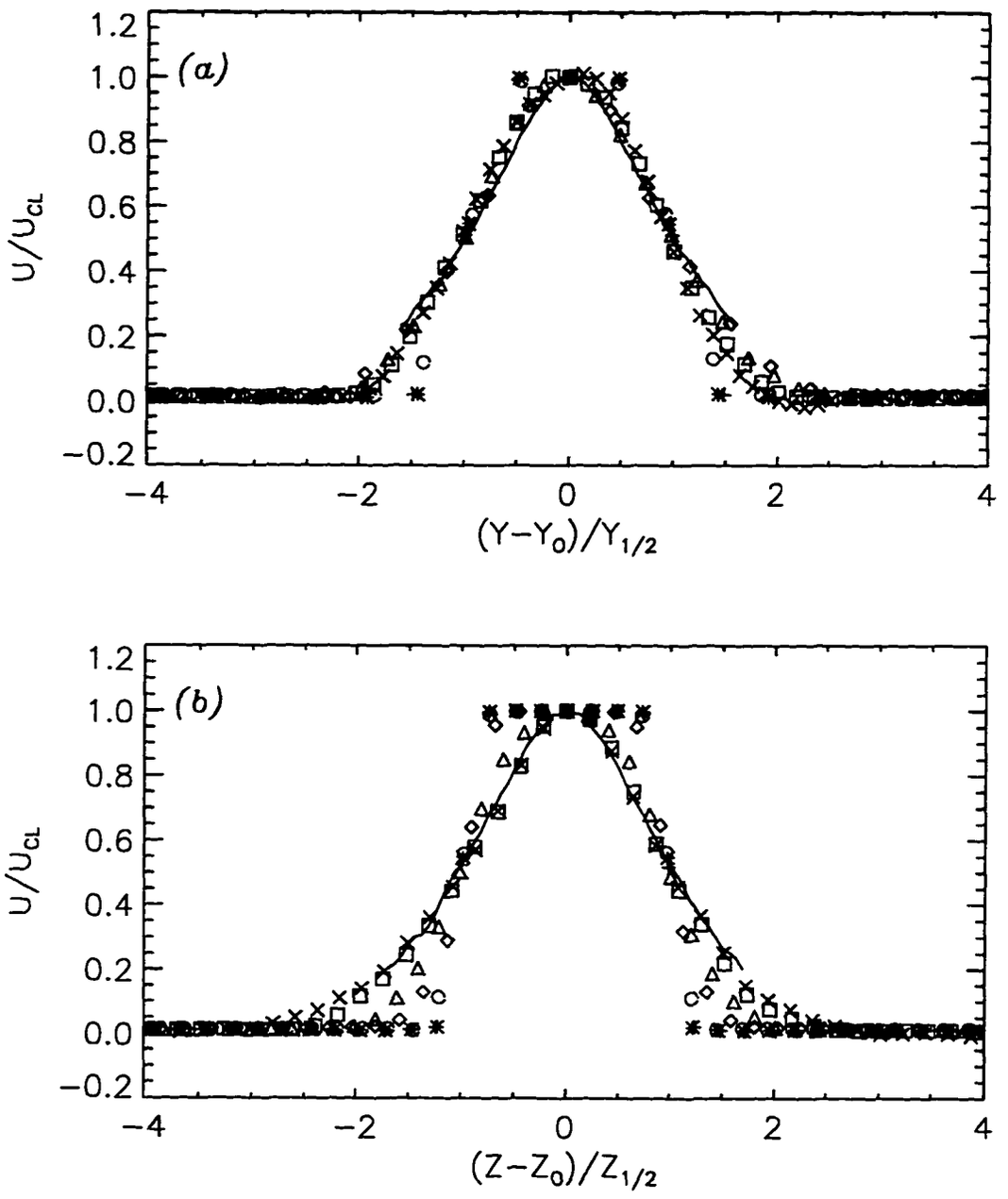

Fig 7.12 **Time-averaged streamwise velocity, *U*, for the LES of rectangular jet, *(a)* minor axis and *(b)* major axis (solid - experiment of Quinn 1995, *x/D* = 10). For symbols see Fig. 6.6.**

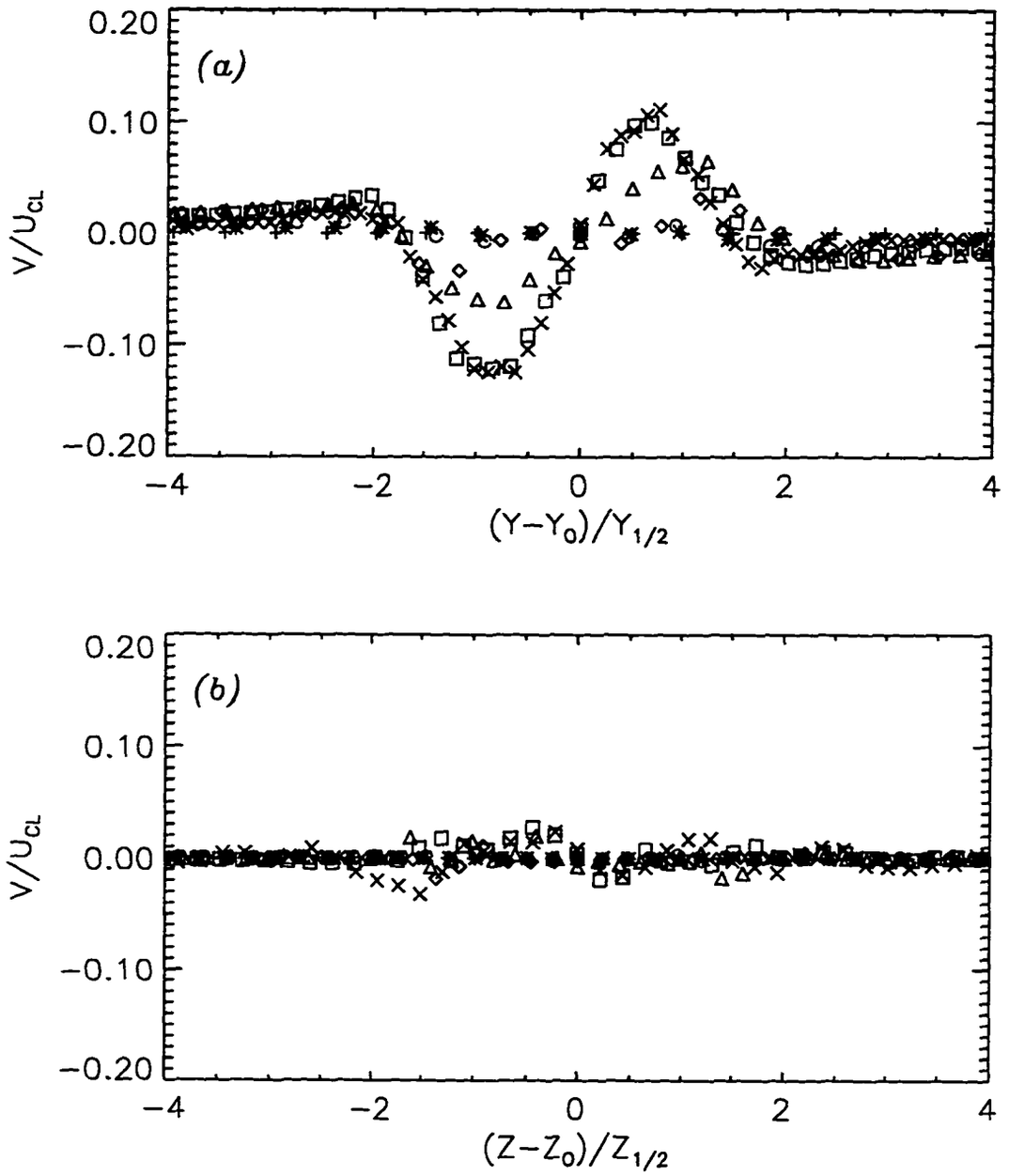

Fig 7.13 Time-averaged lateral velocity, *V*, for the LES of rectangular jet, *(a)* minor axis and *(b)* major axis. For symbols see Fig 6.6.

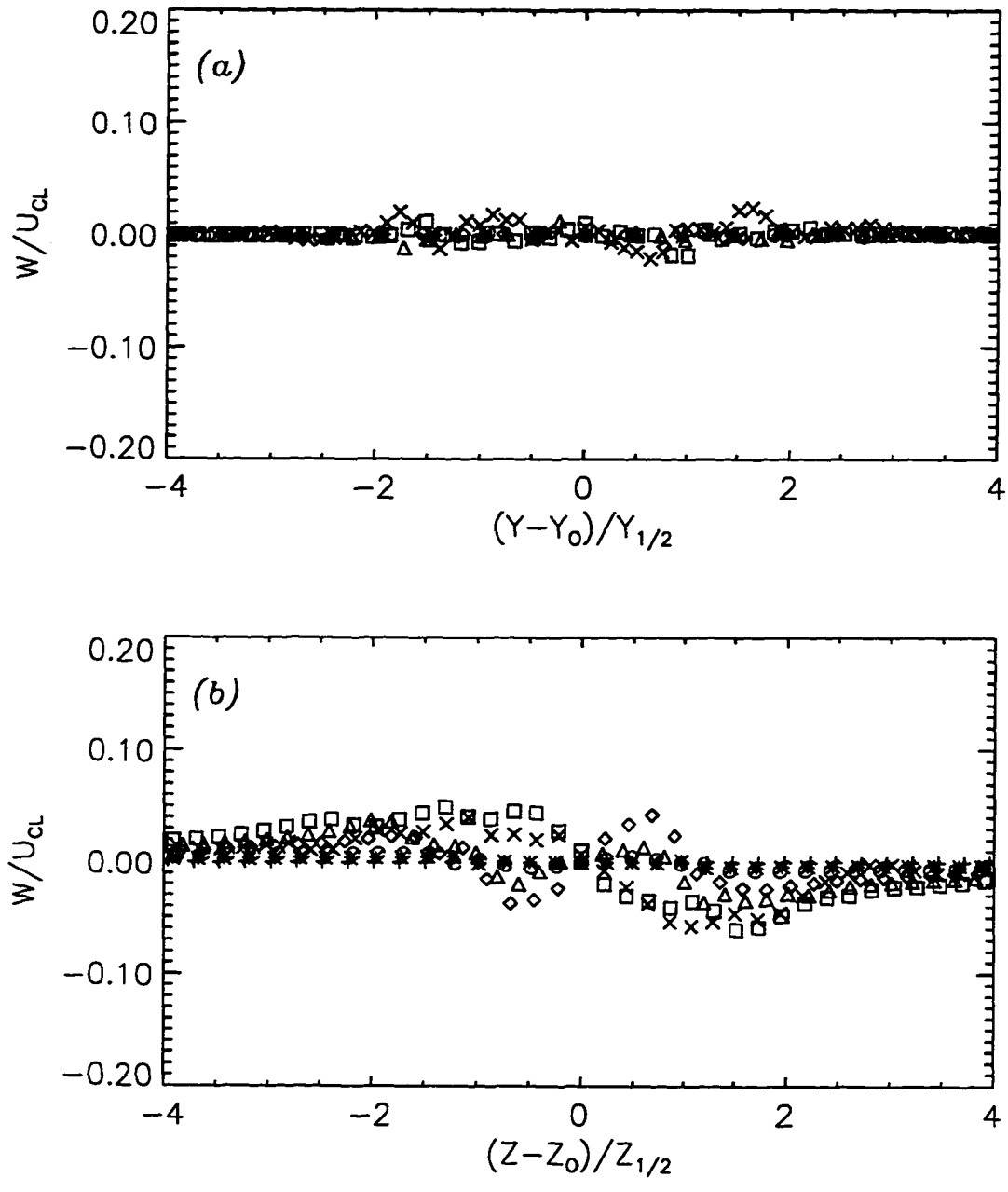

Fig 7.14 **Time-averaged transverse velocity, *W*, for the LES of rectangular jet, *(a)* minor axis and *(b)* major axis. For symbols see Fig 6.6.**

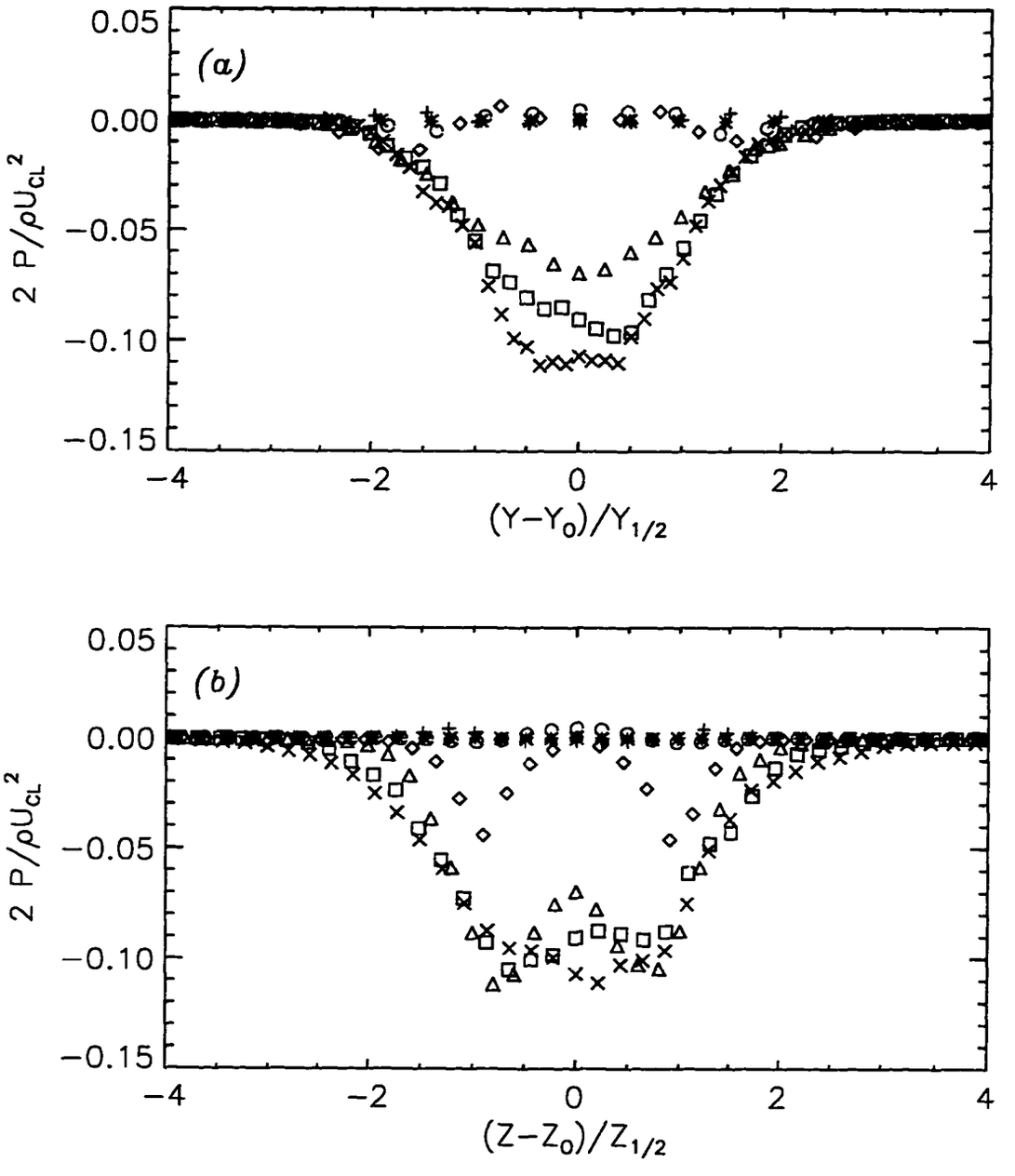

Fig 7.15 **Time-averaged pressure, *P*, for the LES of rectangular jet, *(a)* minor axis and *(b)* major axis. For symbols see Fig 6.6.**

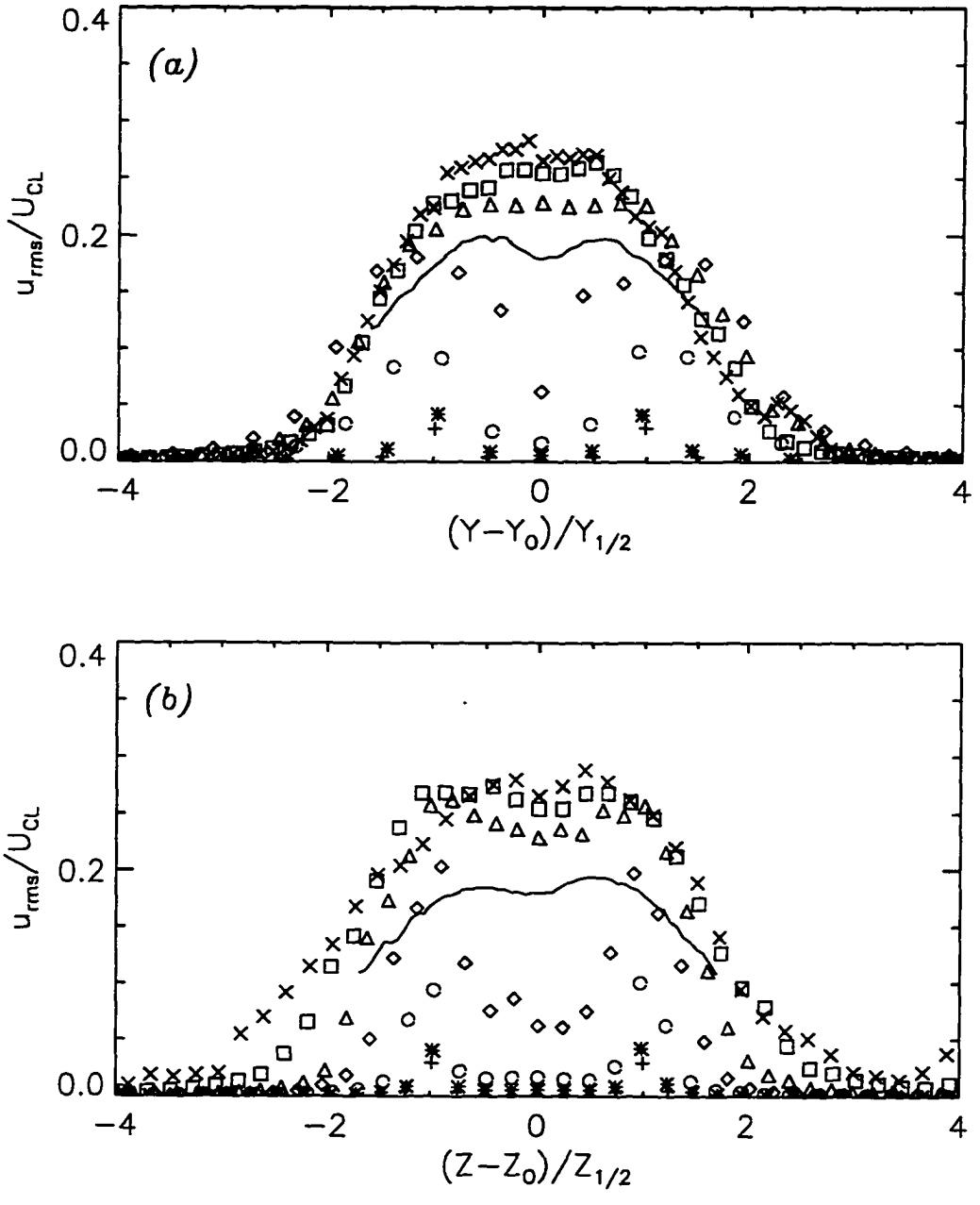

Fig 7.16 **Time-averaged fluctuating streamwise velocity, u_{rms}, for the LES of rectangular jet, *(a)* minor axis and *(b)* major axis (solid - experiment of Quinn 1995, x/D = 10). For symbols see Fig 6.6.**

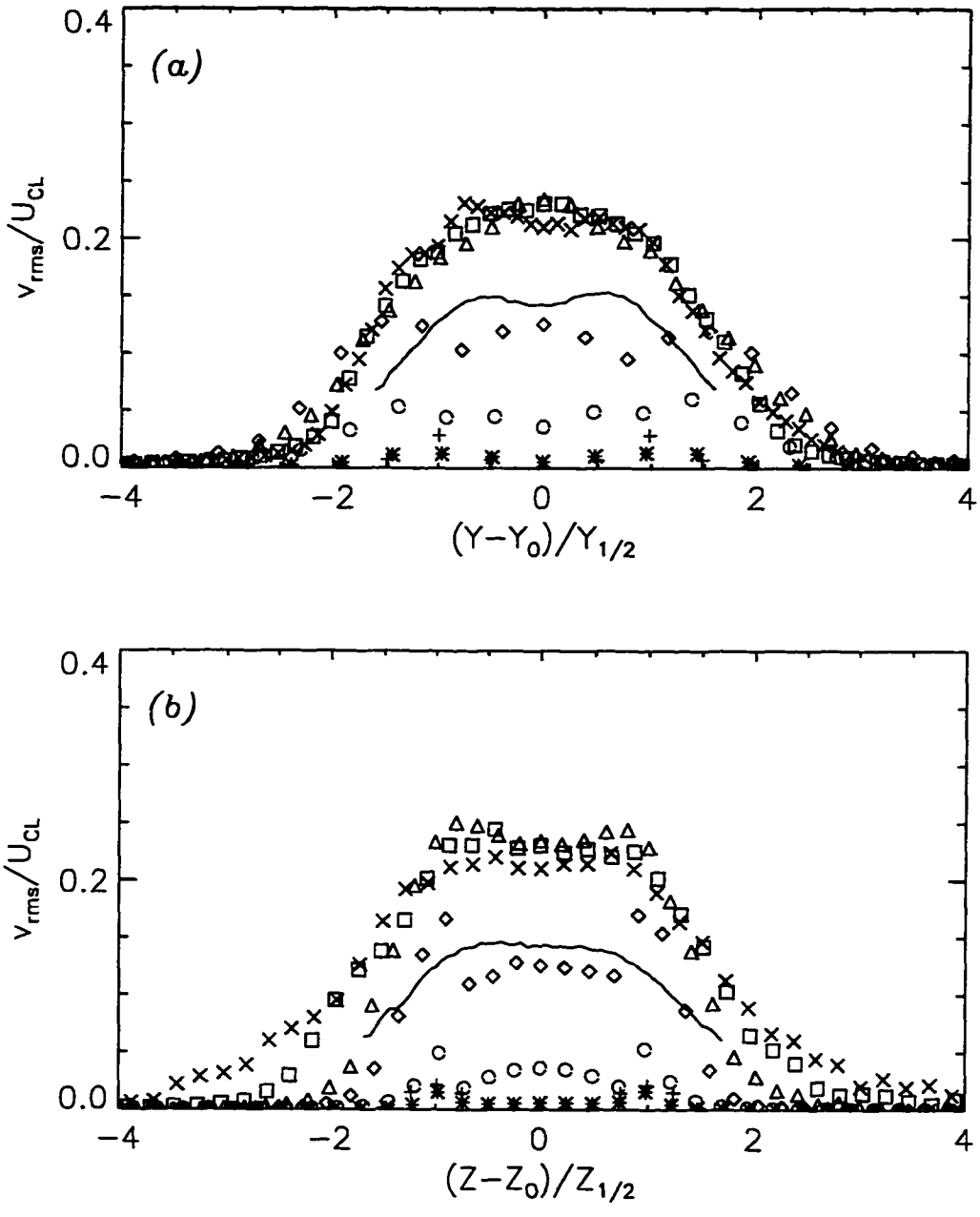

Fig 7.17 **Time-averaged fluctuating lateral velocity, v_{rms}, for the LES of rectangular jet, *(a)* minor axis and *(b)* major axis (solid - experiment of Quinn 1995, $x/D = 10$). For symbols see Fig 6.6.**

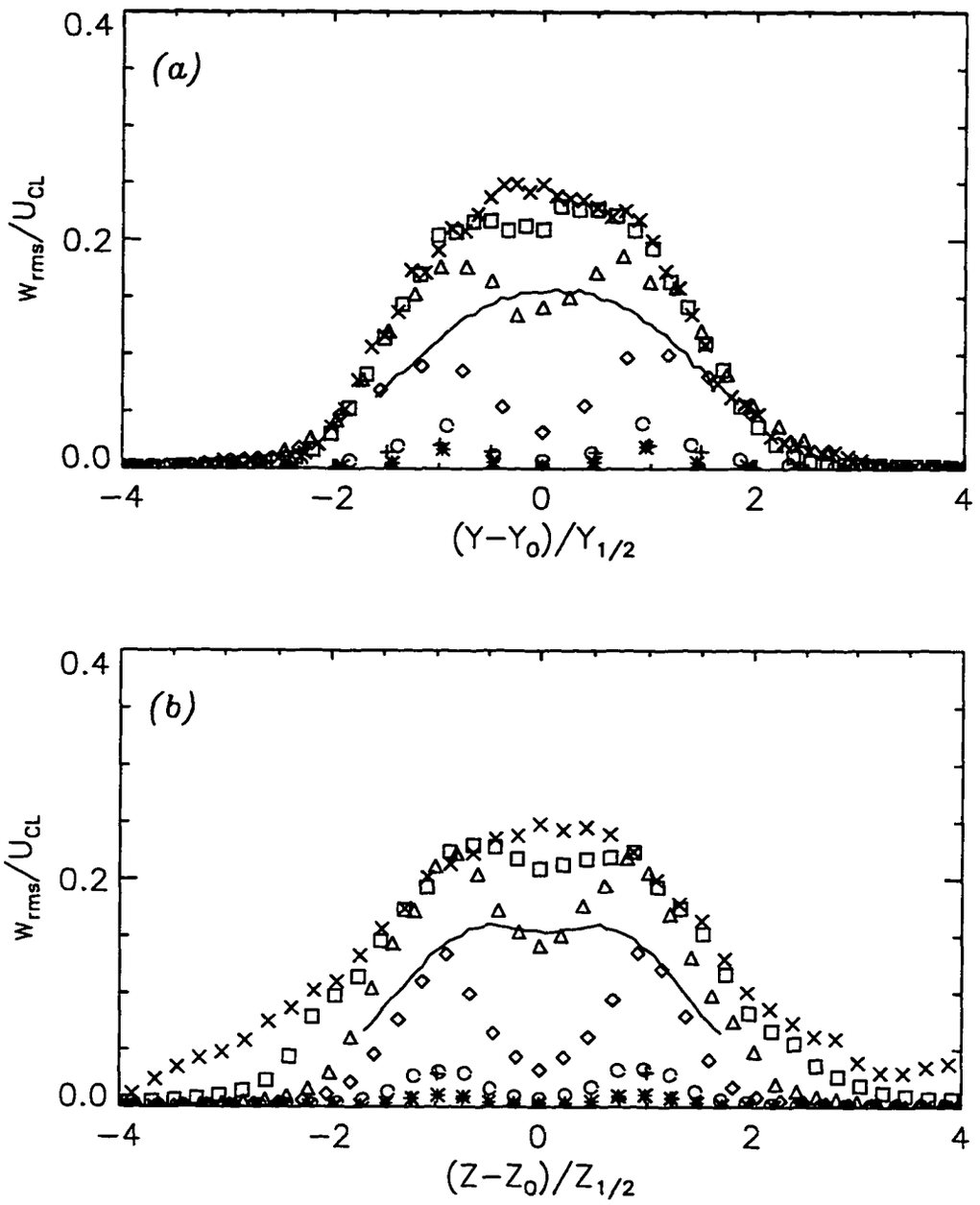

Fig 7.18 **Time-averaged fluctuating transverse velocity, w_{rms}, for the LES of rectangular jet, *(a)* minor axis and *(b)* major axis (solid - experiment of Quinn 1995, x/D = 10). For symbols see Fig 6.6.**

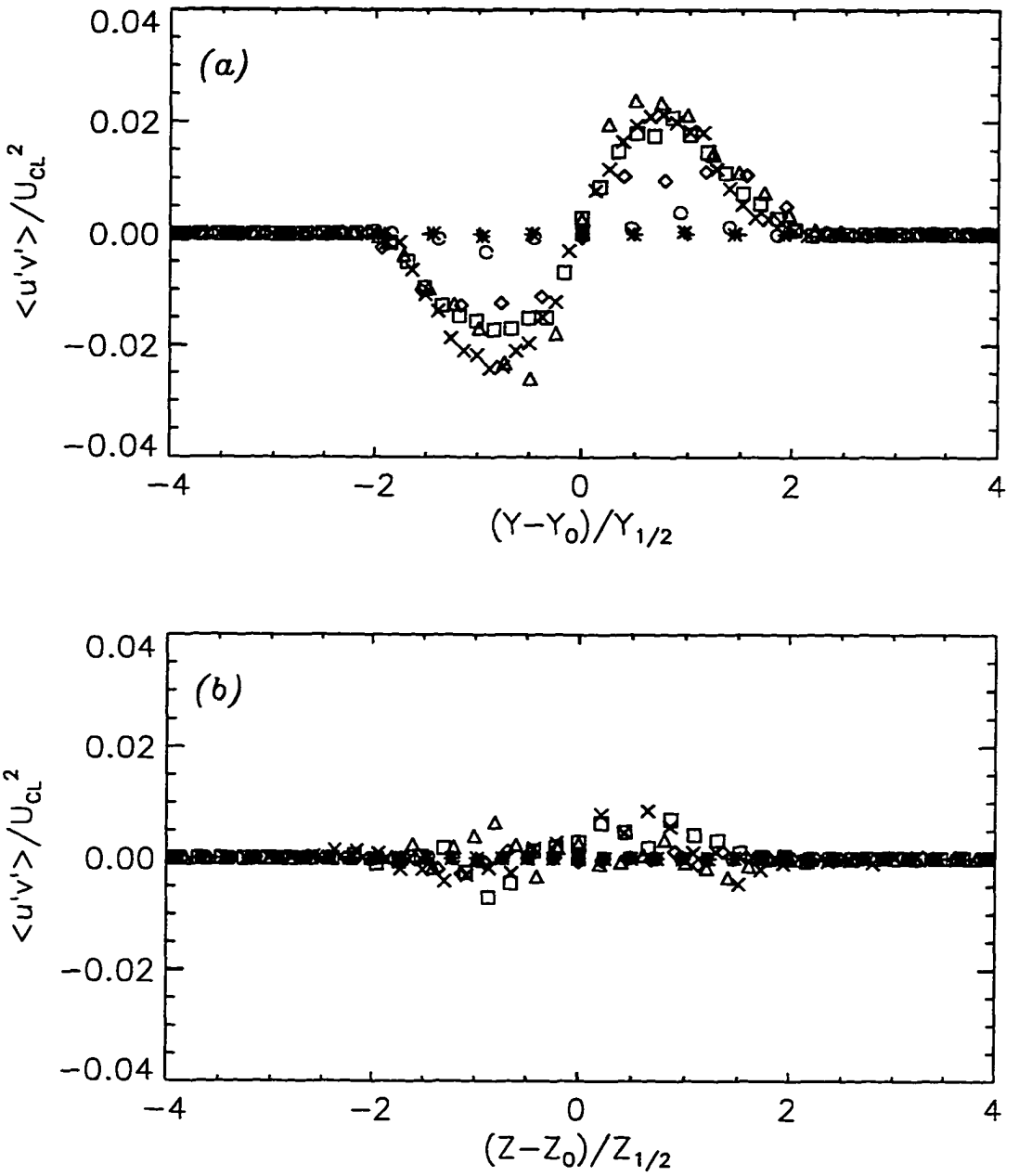

Fig 7.19 Time-averaged Reynolds shear stress, $\langle u'v' \rangle$, for the LES of rectangular jet, *(a)* minor axis and *(b)* major axis. For symbols see Fig 6.6.

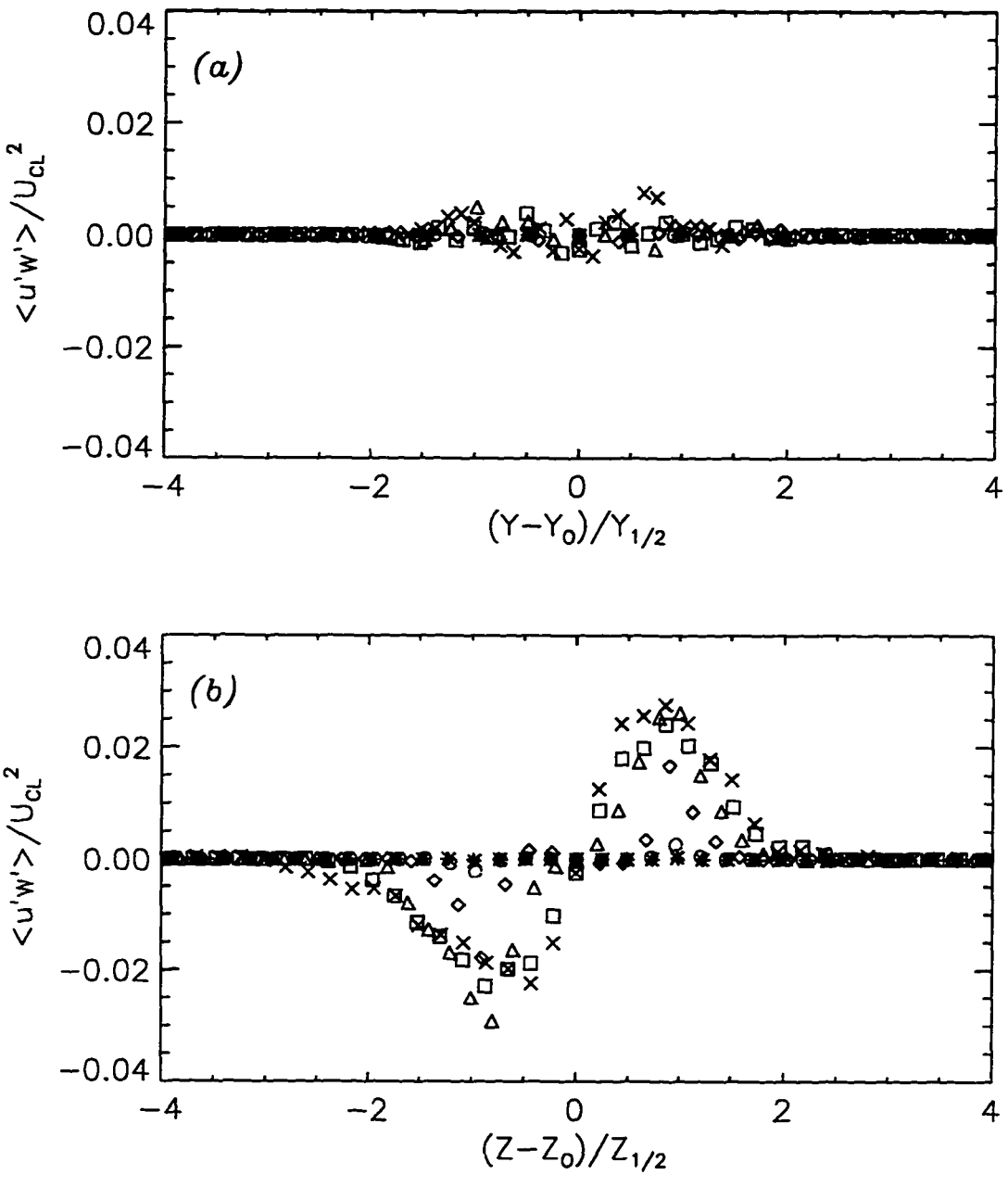

Fig 7.20 Time-averaged Reynolds shear stress, <u'w'>, for the LES of rectangular jet, *(a)* minor axis and *(b)* major axis. For symbols see Fig 6.6.

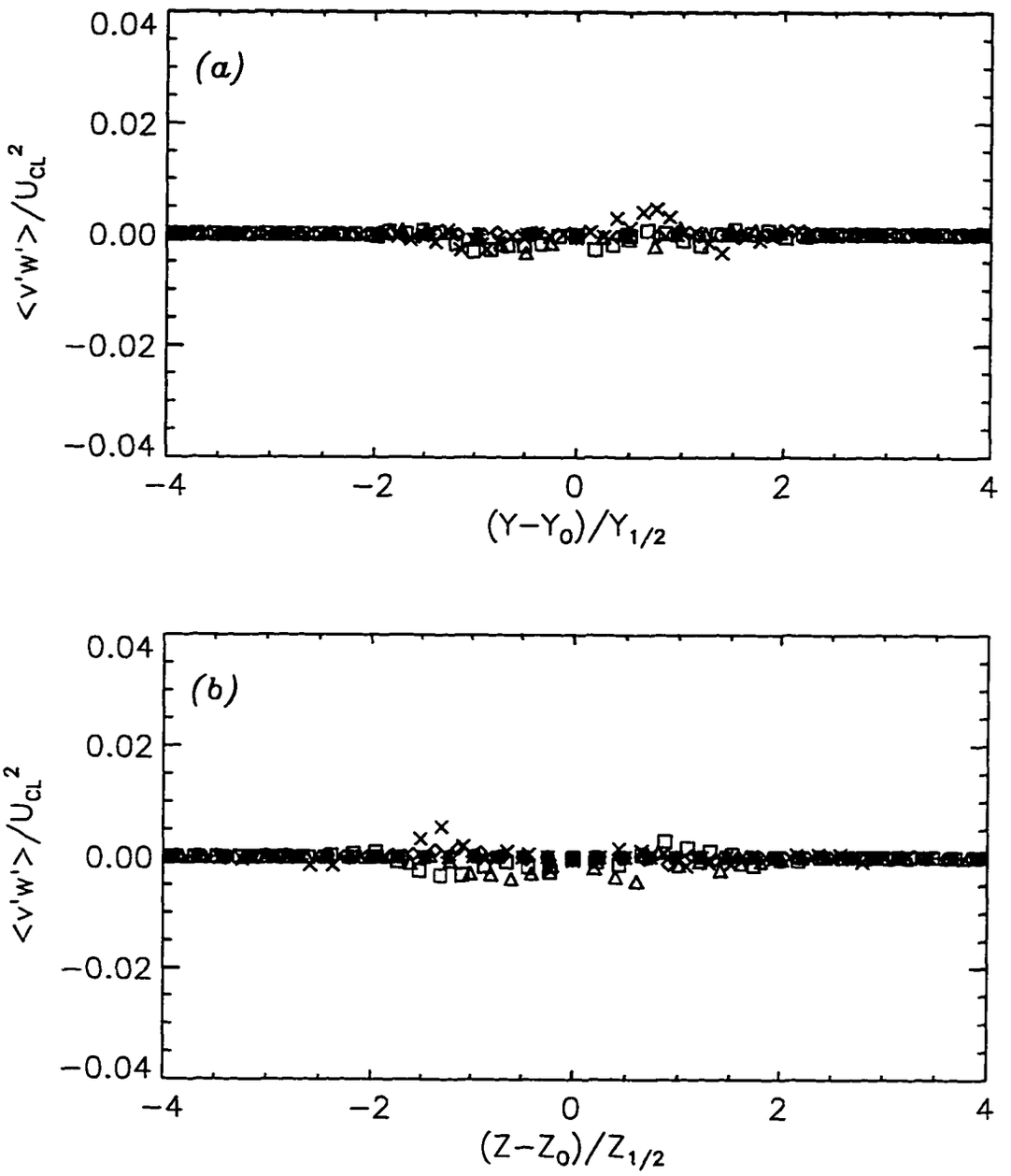

Fig 7.21 Time-averaged Reynolds shear stress, <v'w'>, for the LES of rectangular jet, *(a)* minor axis and *(b)* major axis. For symbols see Fig 6.6.

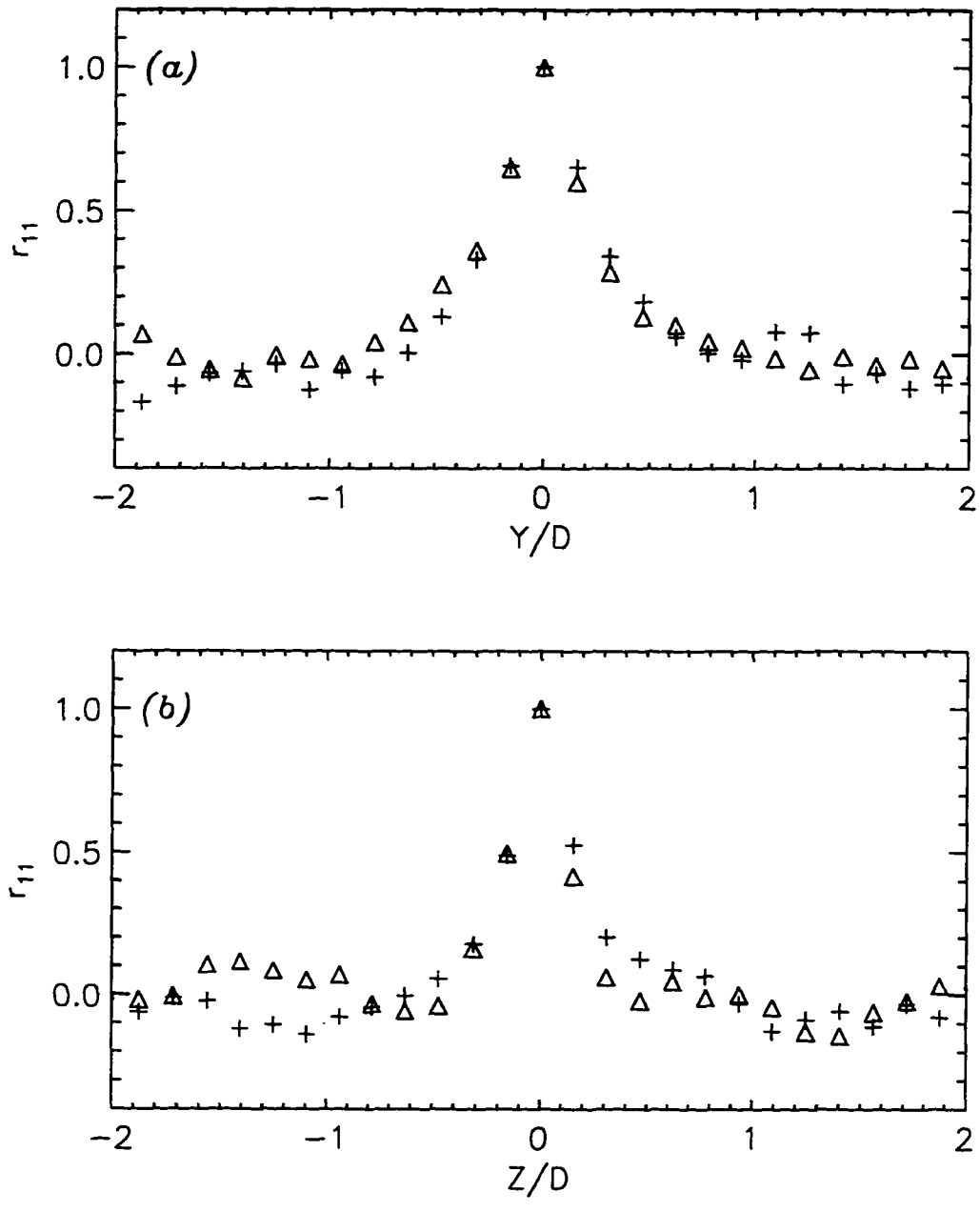

Fig 7.22 Two-point velocity correlation, r_{11}, for LES of rectangular jet *(a)* minor axis and *(b)* major axis, x/D_e = ; + 7.5 ; Δ 9.0.

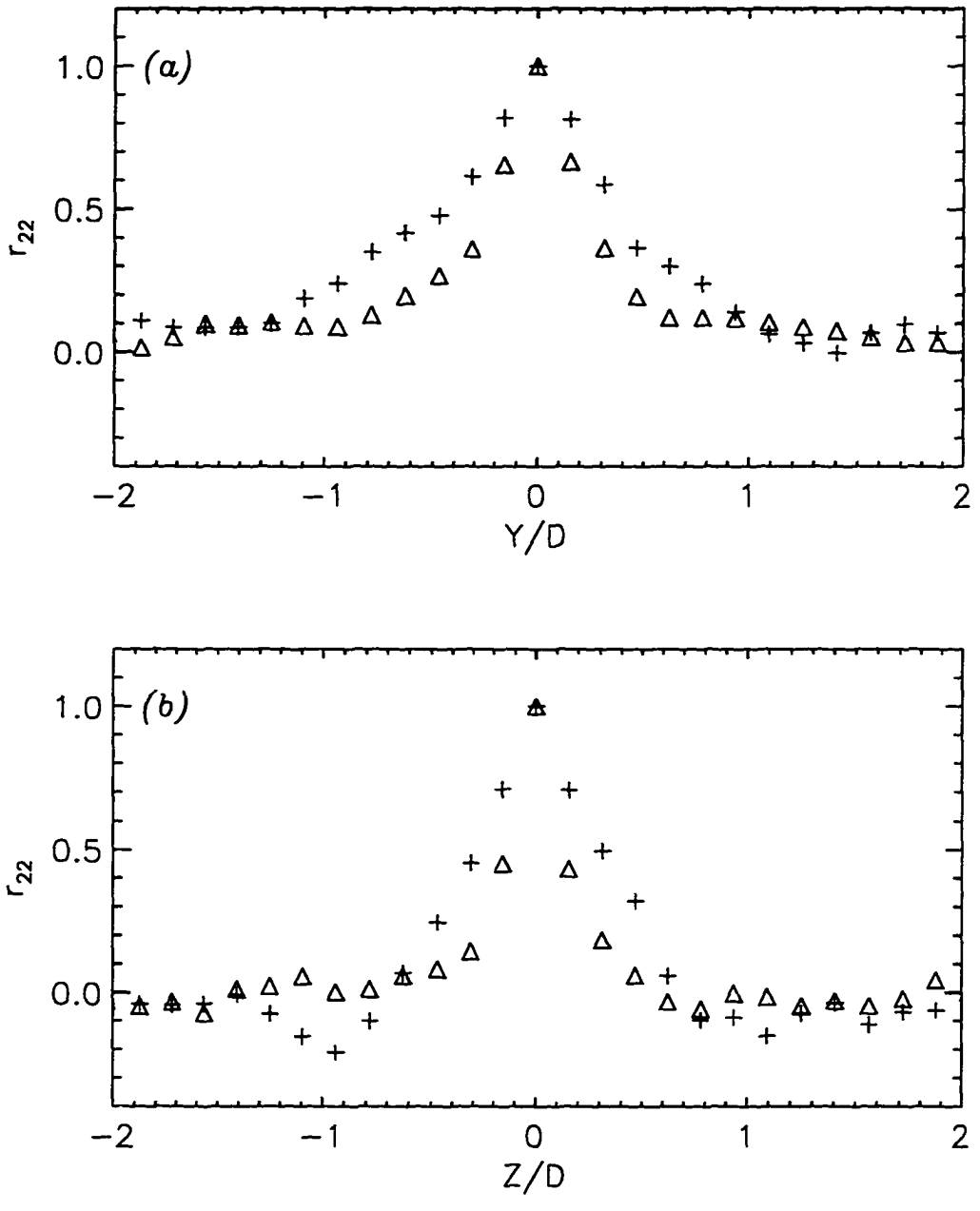

Fig 7.23 Two-point velocity correlation, r_{22}, for LES of rectangular jet *(a)* minor axis and *(b)* major axis. For symbols see Fig. 7.22.

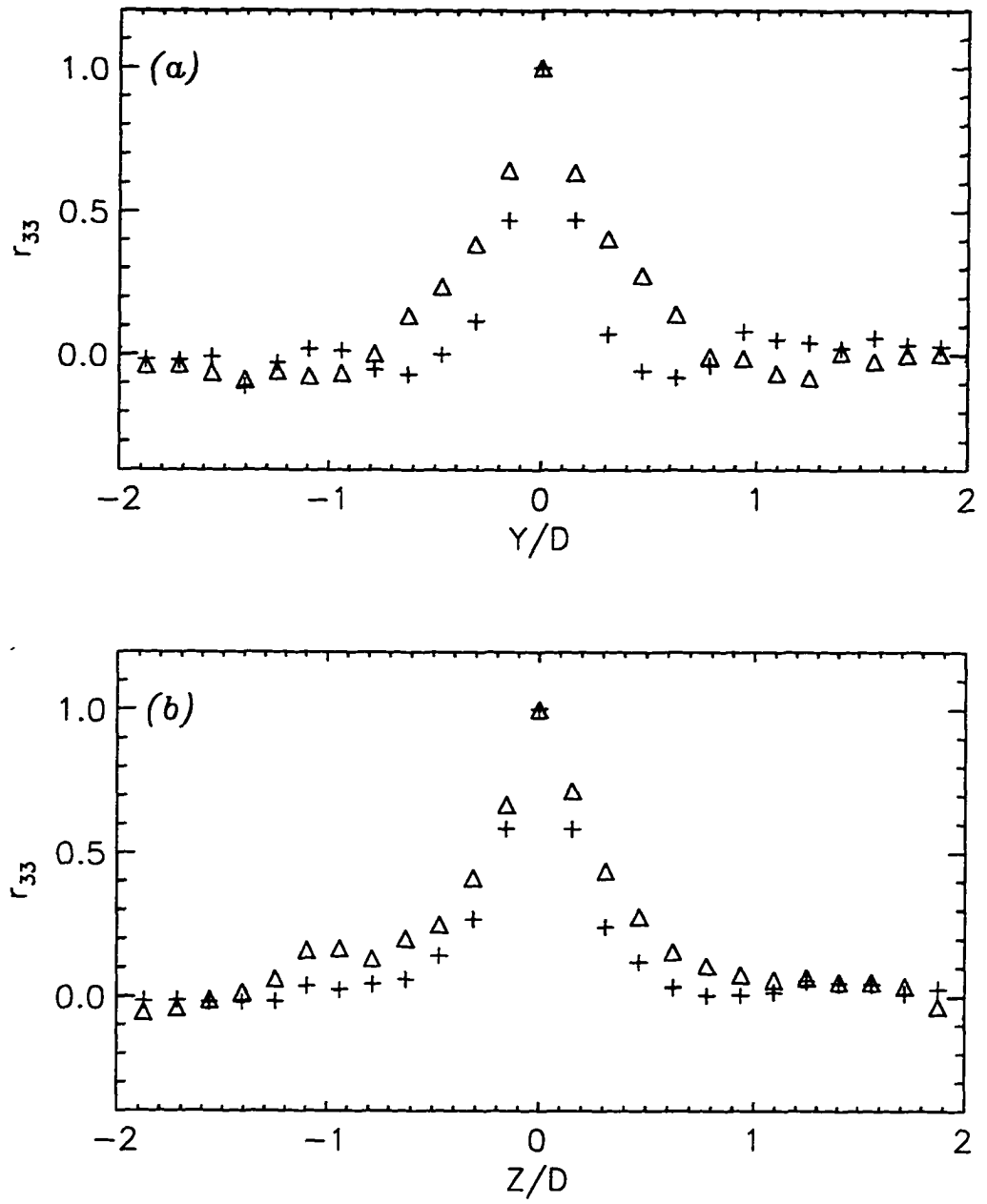

Fig 7.24 **Two-point velocity correlation, r_{33}, for LES of rectangular jet *(a)* minor axis and *(b)* major axis. For symbols see Fig. 7.22.**

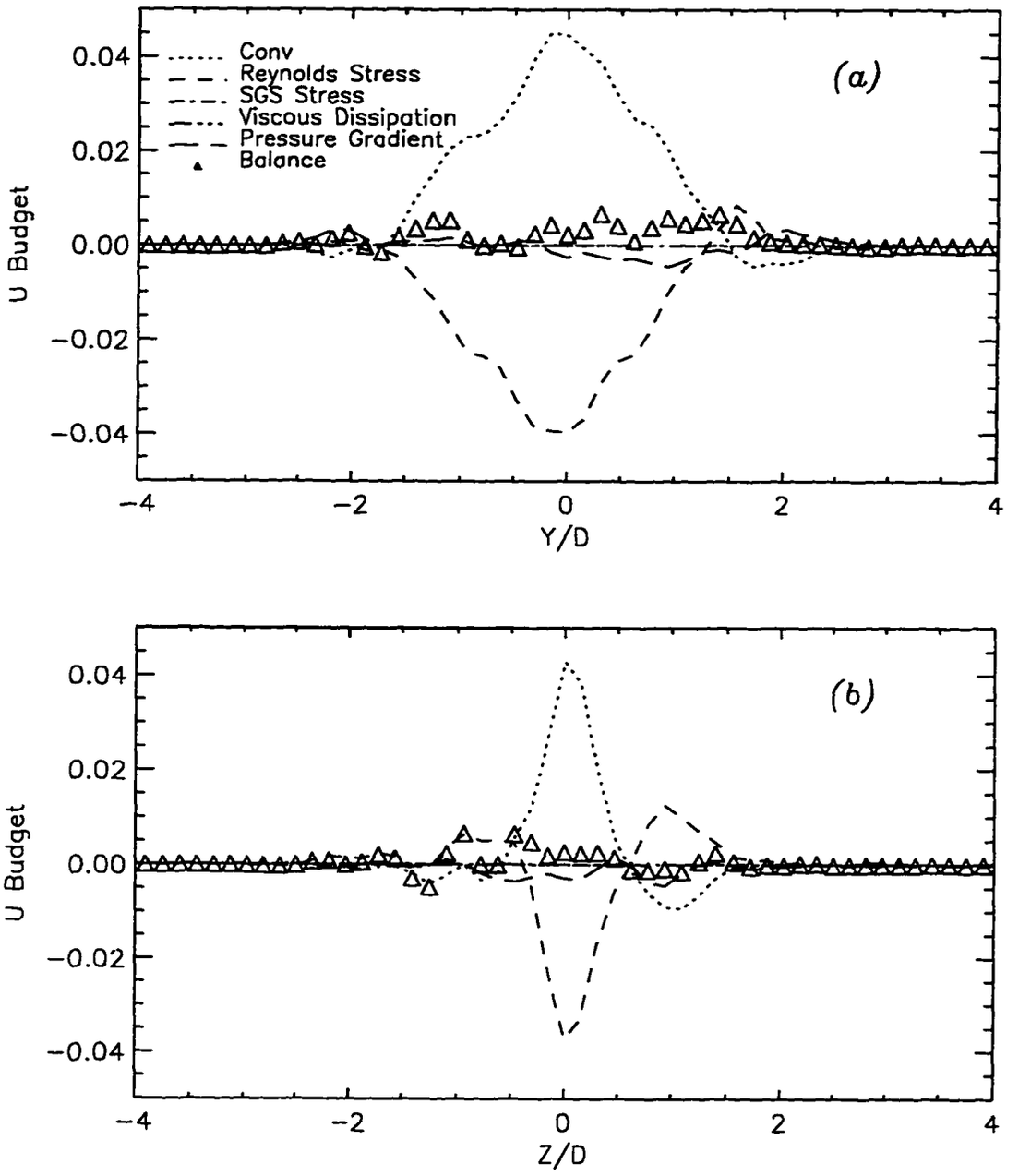

Fig 7.25 Budget terms for the U -momentum equation at x/D = 9.38 for LES of rectangular jet, *(a)* minor axis and *(b)* major axis.

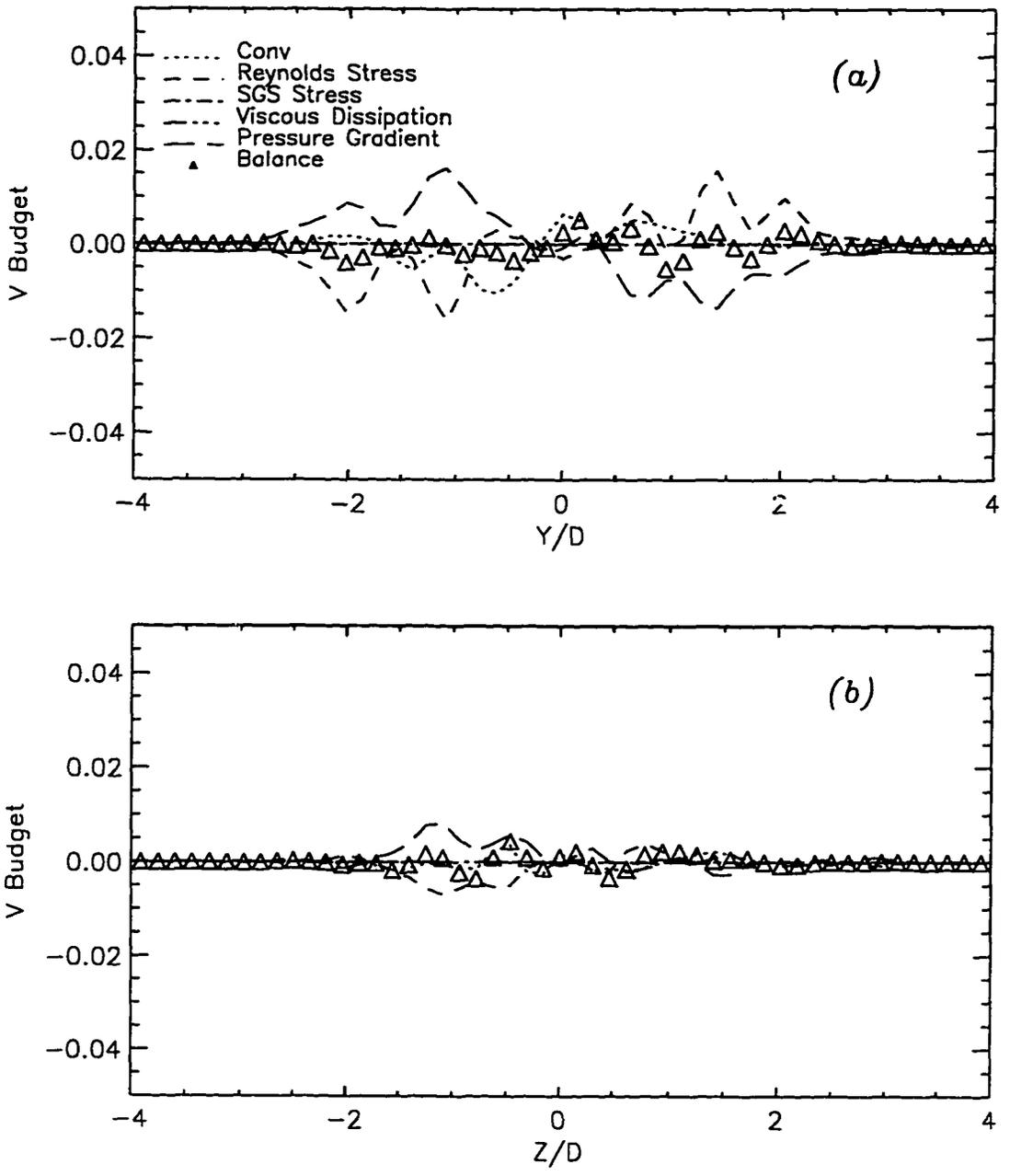

Fig 7.26 Budget terms for the *V*- momentum equation at *x/D* = 9.38, for LES of rectangular jet(*a*) minor axis and (*b*) major axis.

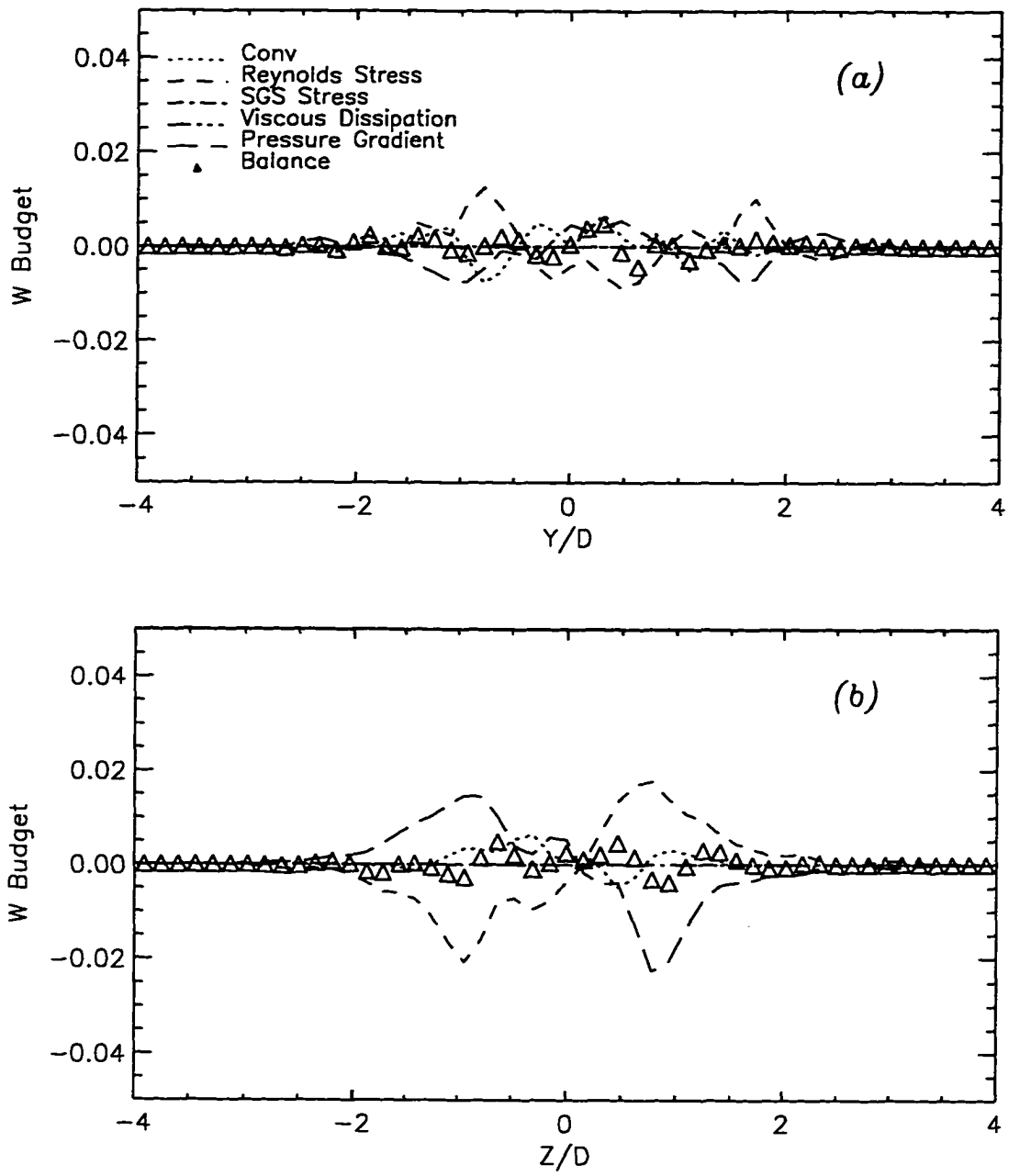

Fig 7.27 Budget terms for the W -momentum equation at x/D = 9.38, for LES of rectangular jet *(a)* minor axis and *(b)* major axis.

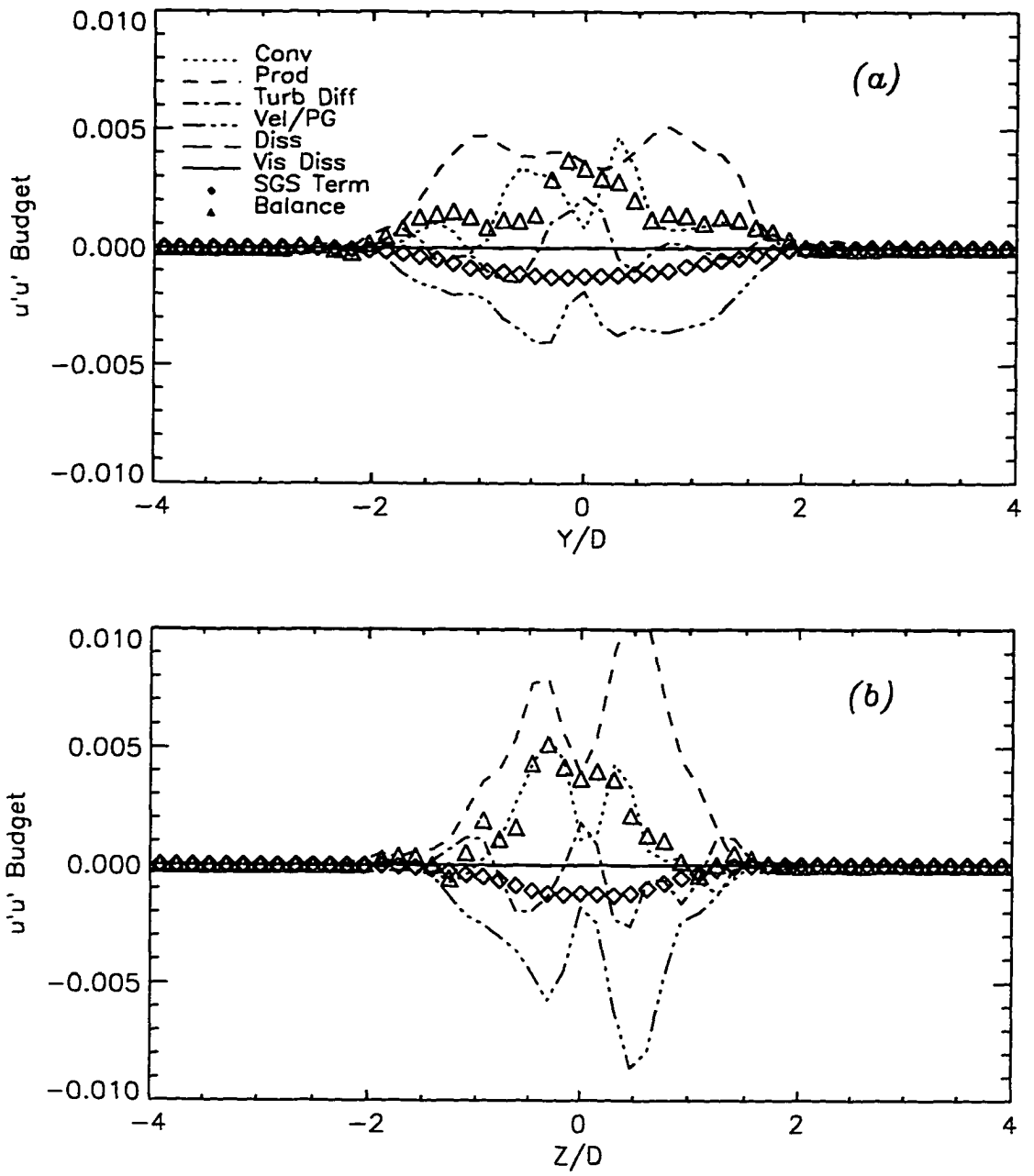

Fig 7.28 **Budget terms for the <u'u'> equation at x/D = 9.38, for LES of rectangular jet *(a)* minor axis and *(b)* major axis.**

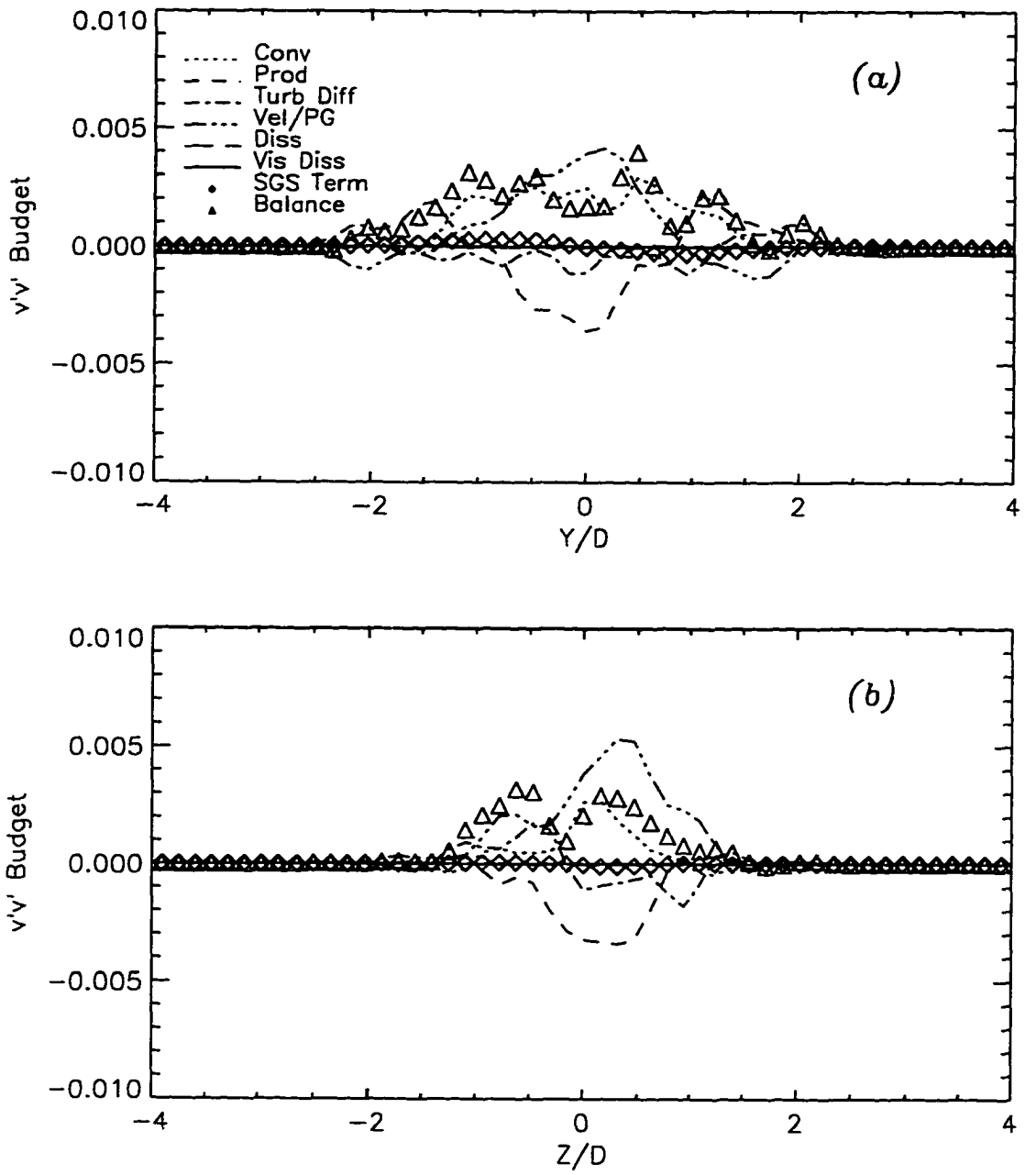

Fig 7.29 Budget terms for the <v'v'> equation at *x/D* = 9.38, for LES of rectangular jet *(a)* minor axis and *(b)* major axis.

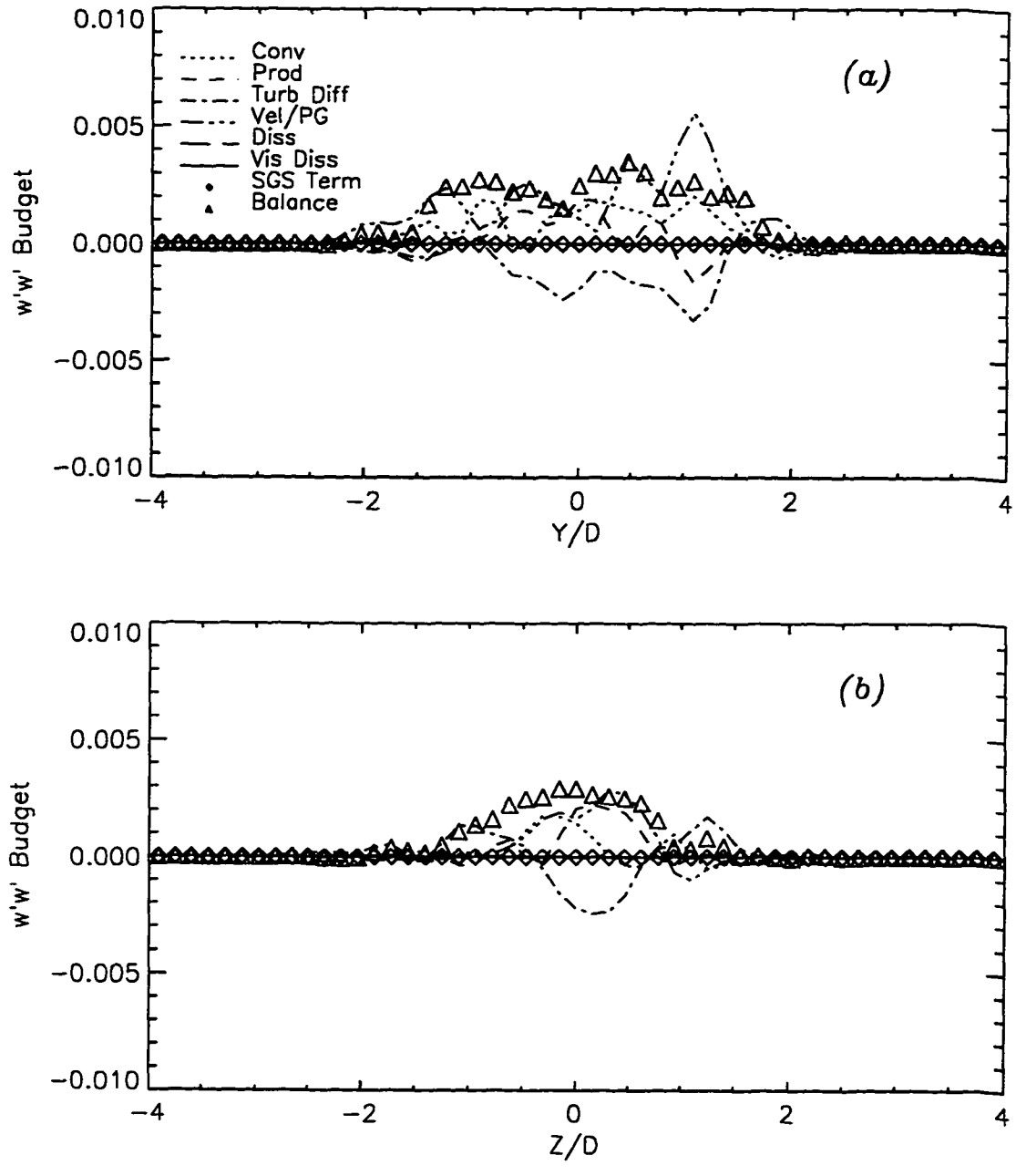

Fig 7.30a Budget terms for the <w'w'> equation at *x/D* = 9.38, for LES of rectangular jet *(a)* minor axis and *(b)* major axis.

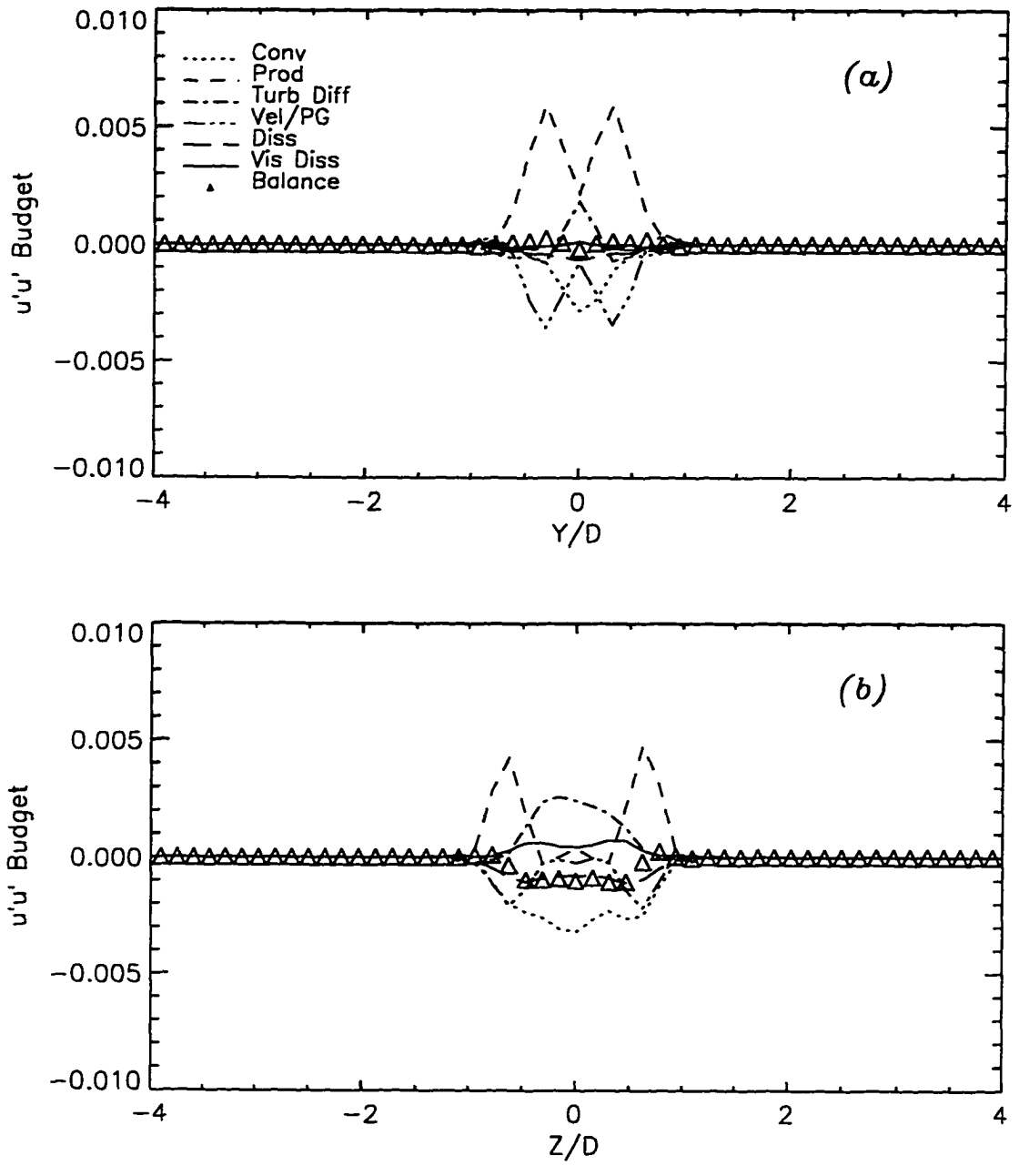

Fig 7.30b Budget terms for the <u'u'> equation at *x/D* = 9.38, for DNS of rectangular jet (case *iii*, Chap. 6) *(a)* minor axis and *(b)* major axis.

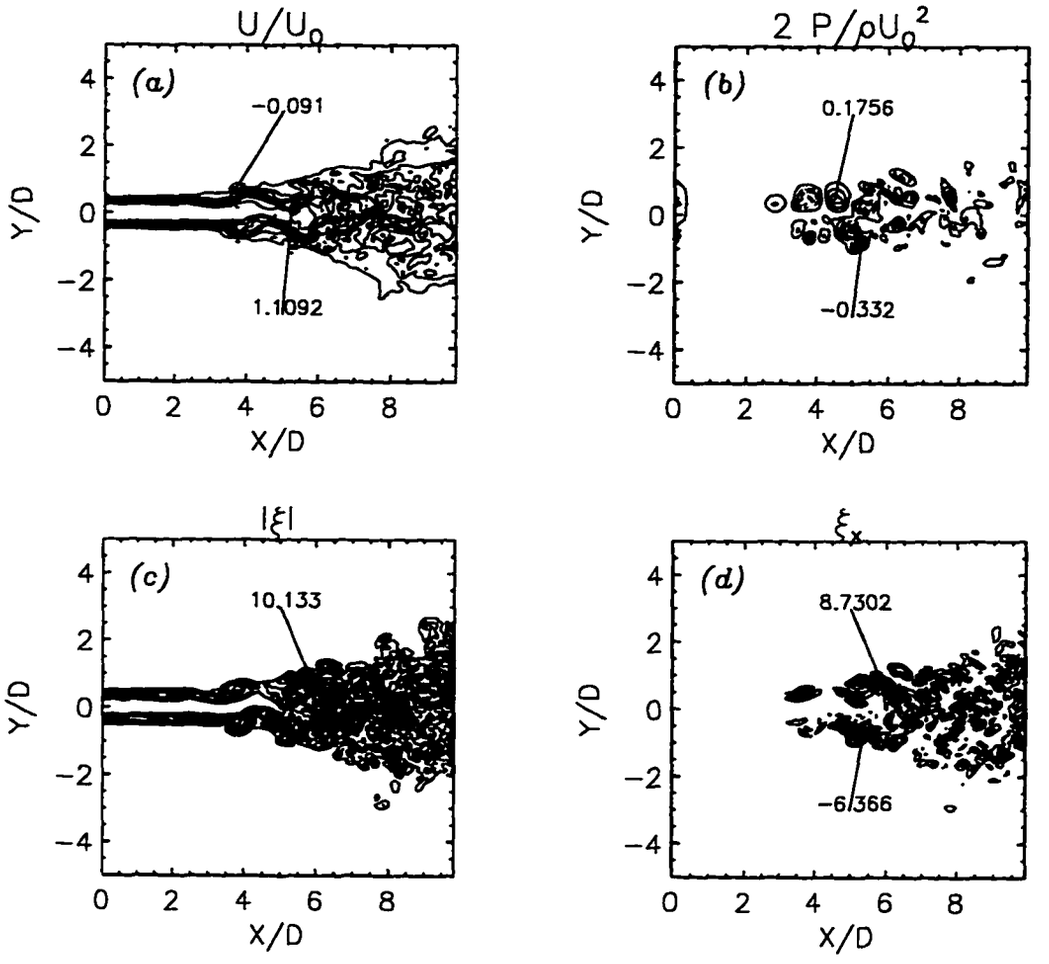

Fig 7.31 **Contours in the minor axis plane ($z/D = 0$) at $t = 3$ for LES of elliptic jet; *(a)* streamwise velocity, *(b)* pressure, *(c)* vorticity magnitude, and *(d)* streamwise vorticity.**

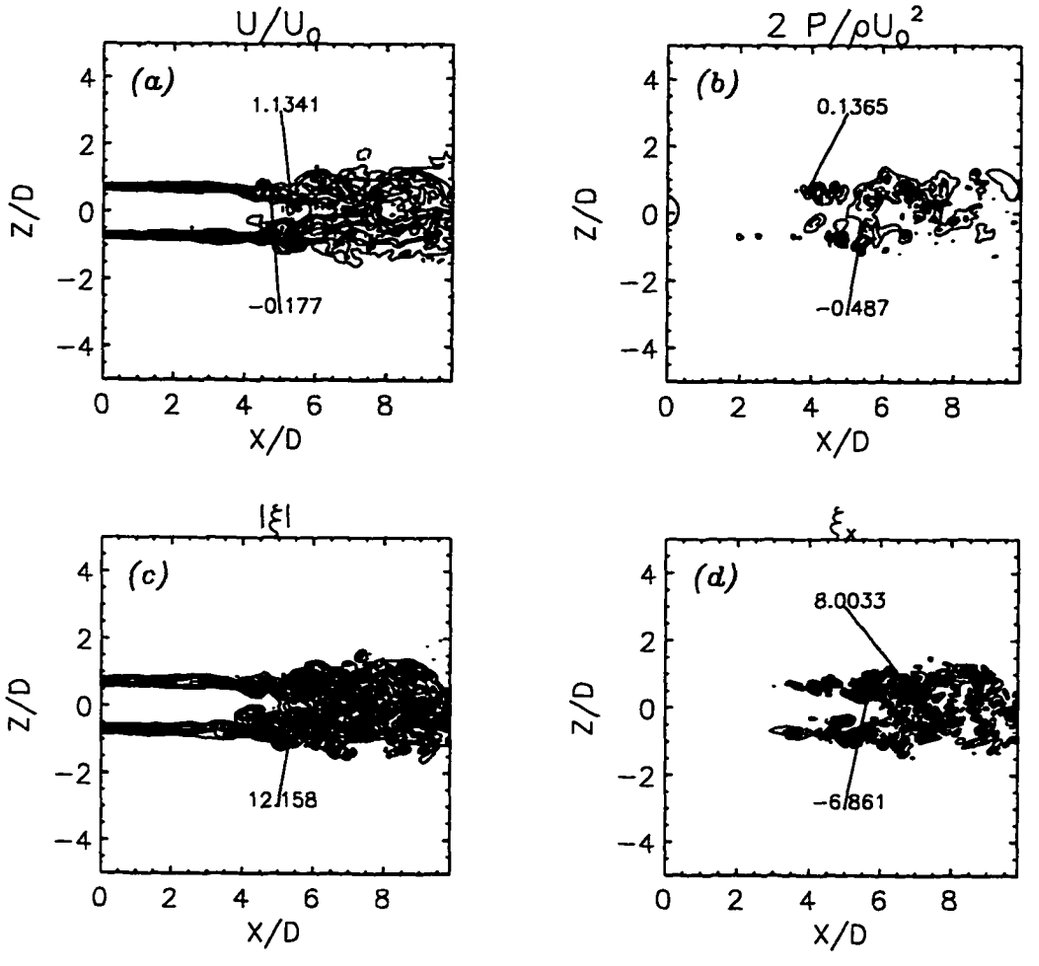

Fig 7.32 **Contours in the major axis plane ($z/D = 0$) at $t = 3$ for LES of elliptic jet; *(a)* streamwise velocity, *(b)* pressure, *(c)* vorticity magnitude, and *(d)* streamwise vorticity.**

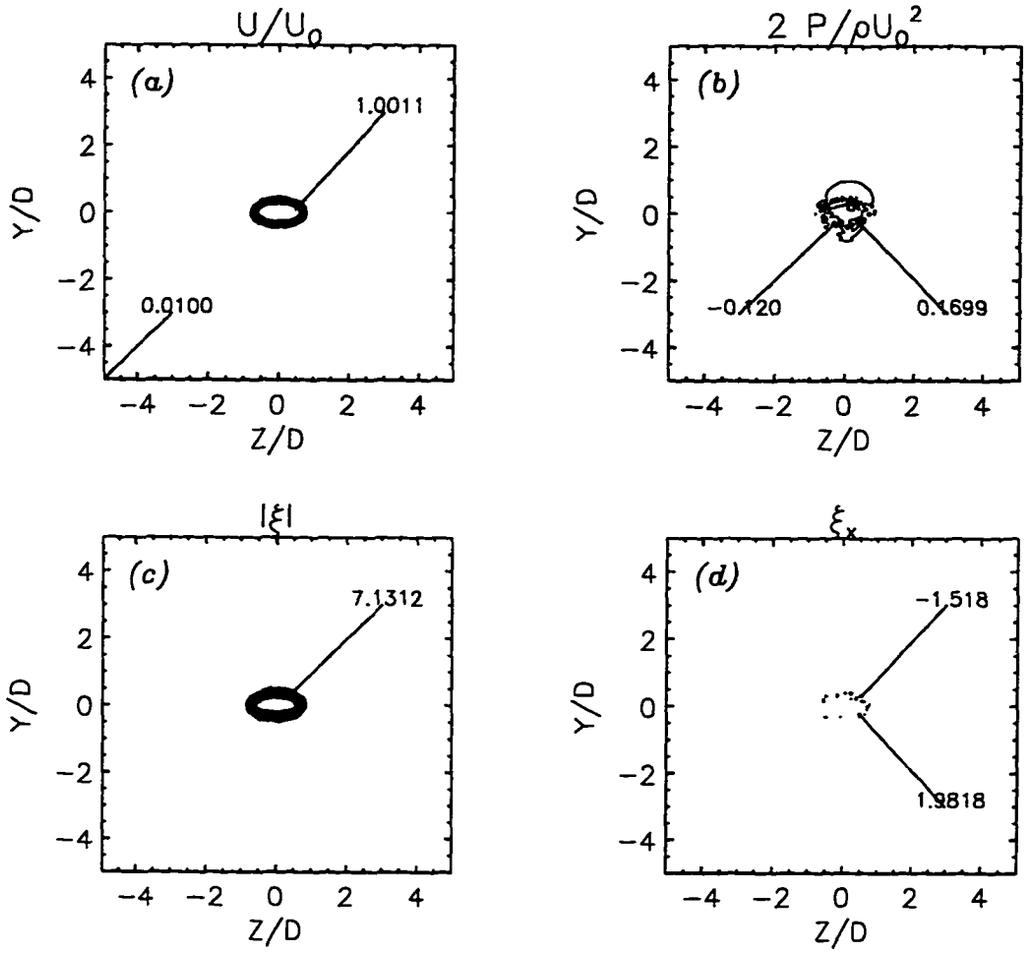

Fig 7.33 **Contours at the cross-section, x/*D* = 0, at *t* = 3 for LES of elliptic jet; *(a)* streamwise velocity, *(b)* pressure, *(c)* vorticity magnitude, and *(d)* streamwise vorticity.**

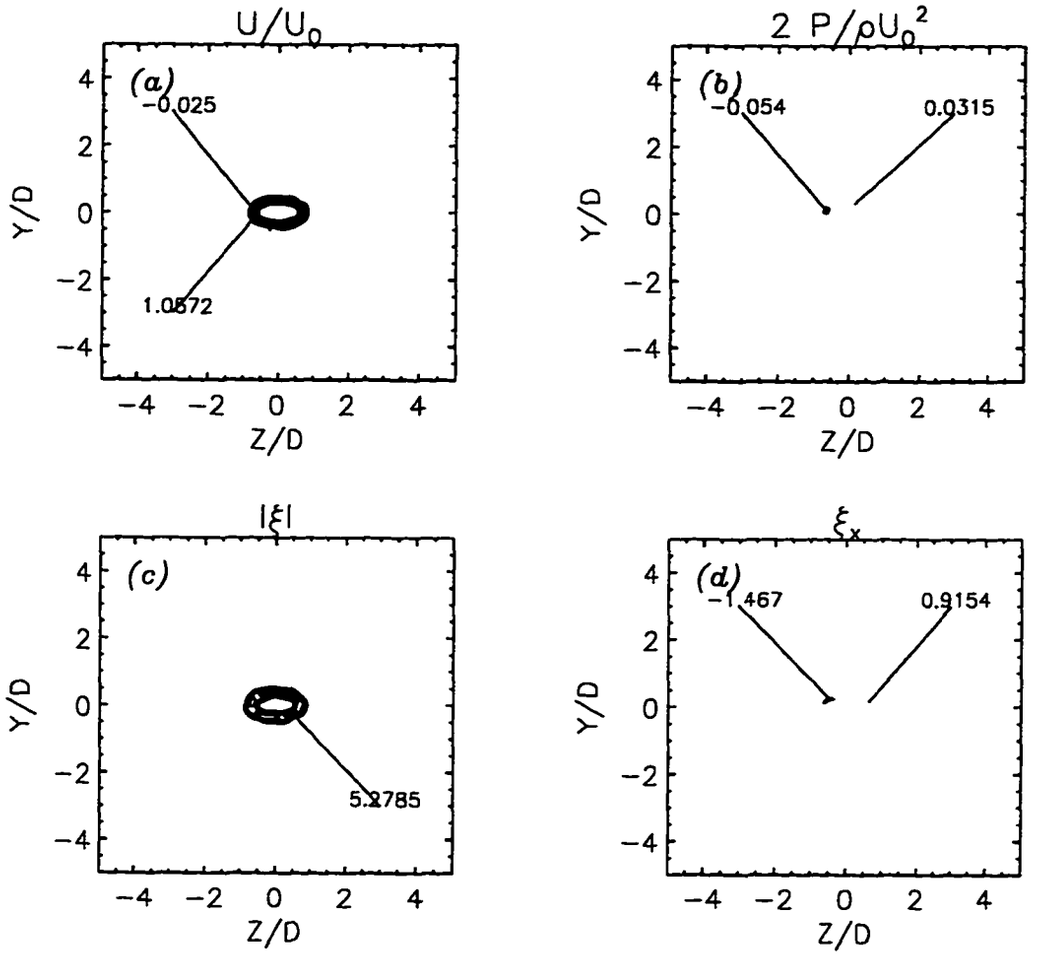

Fig 7.34 **Contours at the cross-section, x/*D* = 2.44, at *t* = 3 for LES of elliptic jet; *(a)* streamwise velocity, *(b)* pressure, *(c)* vorticity magnitude, and *(d)* streamwise vorticity.**

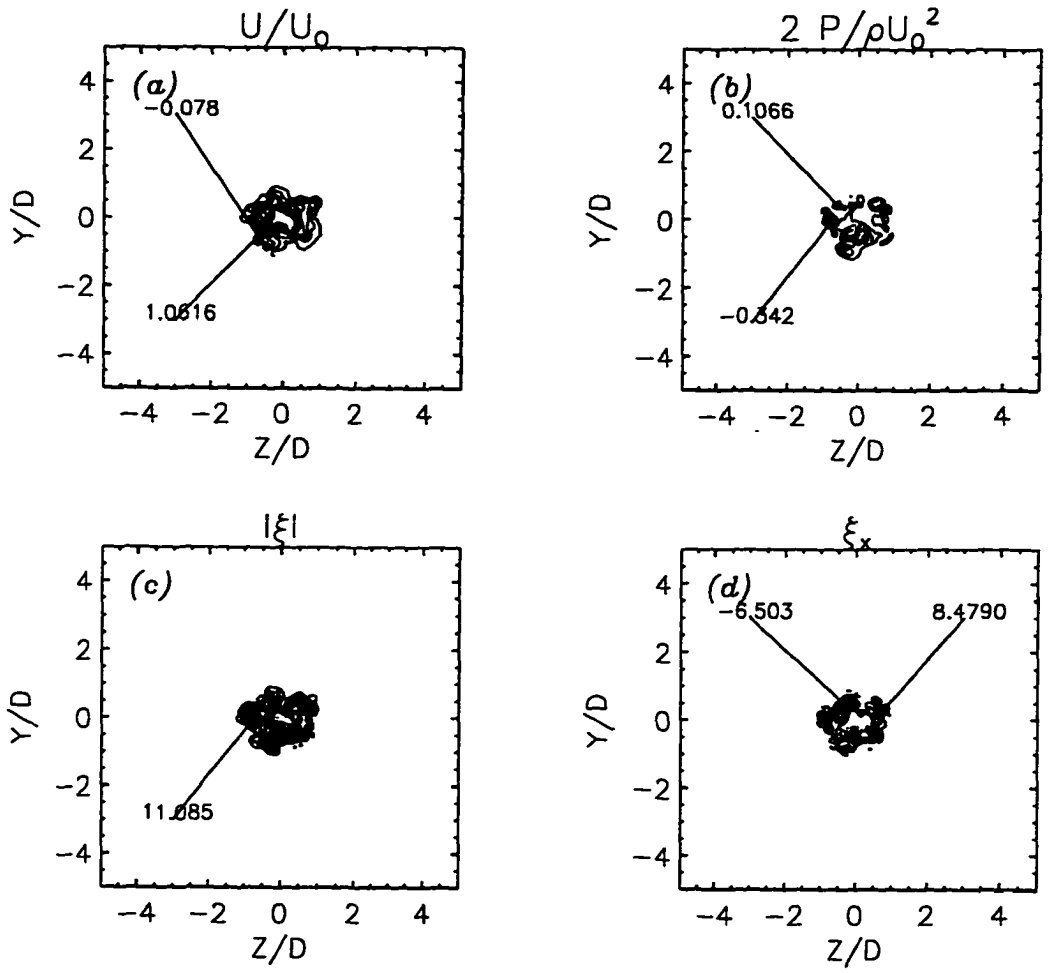

Fig 7.35 **Contours at the cross-section, x/*D* = 4.88, at *t* = 3 for LES of elliptic jet; *(a)* streamwise velocity, *(b)* pressure, *(c)* vorticity magnitude, and *(d)* streamwise vorticity.**

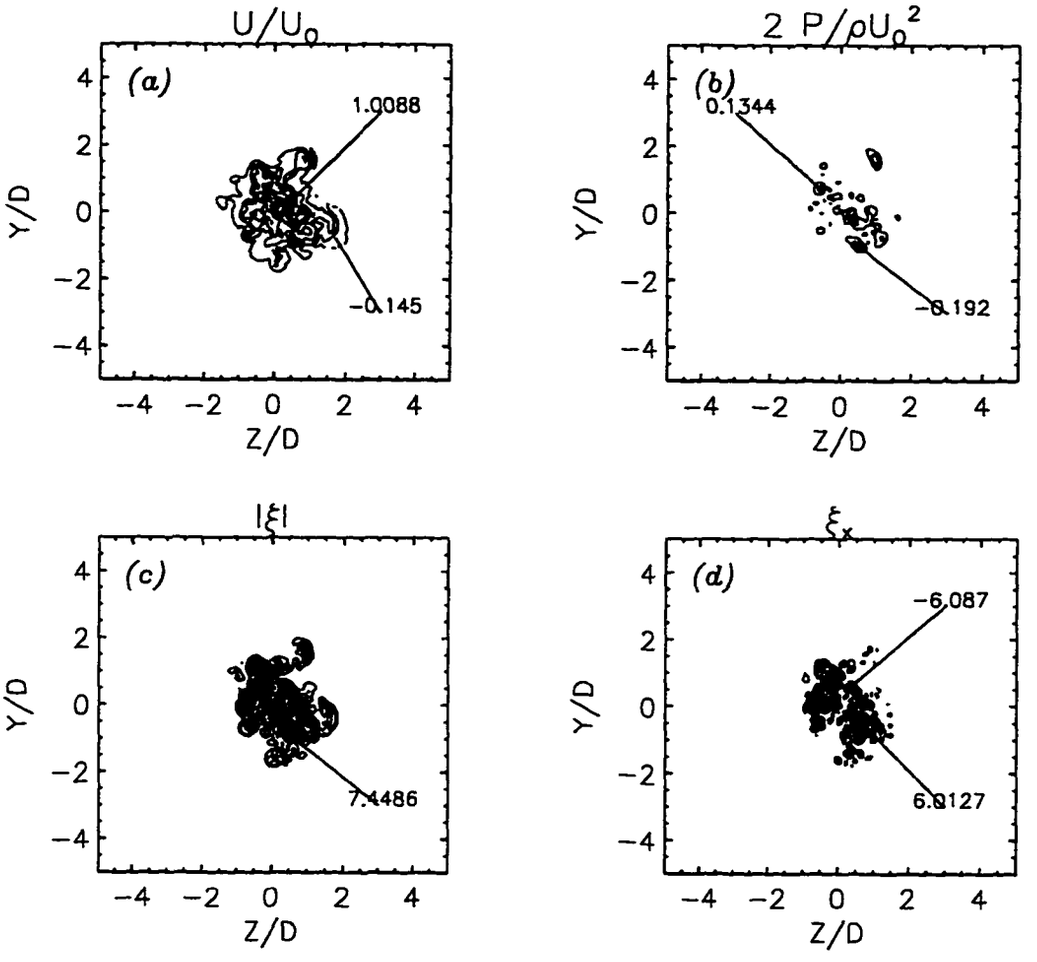

Fig 7.36 **Contours at the cross-section, x/*D* = 7.31, at *t* = 3 for LES of elliptic jet; *(a)* streamwise velocity, *(b)* pressure, *(c)* vorticity magnitude, and *(d)* streamwise vorticity.**

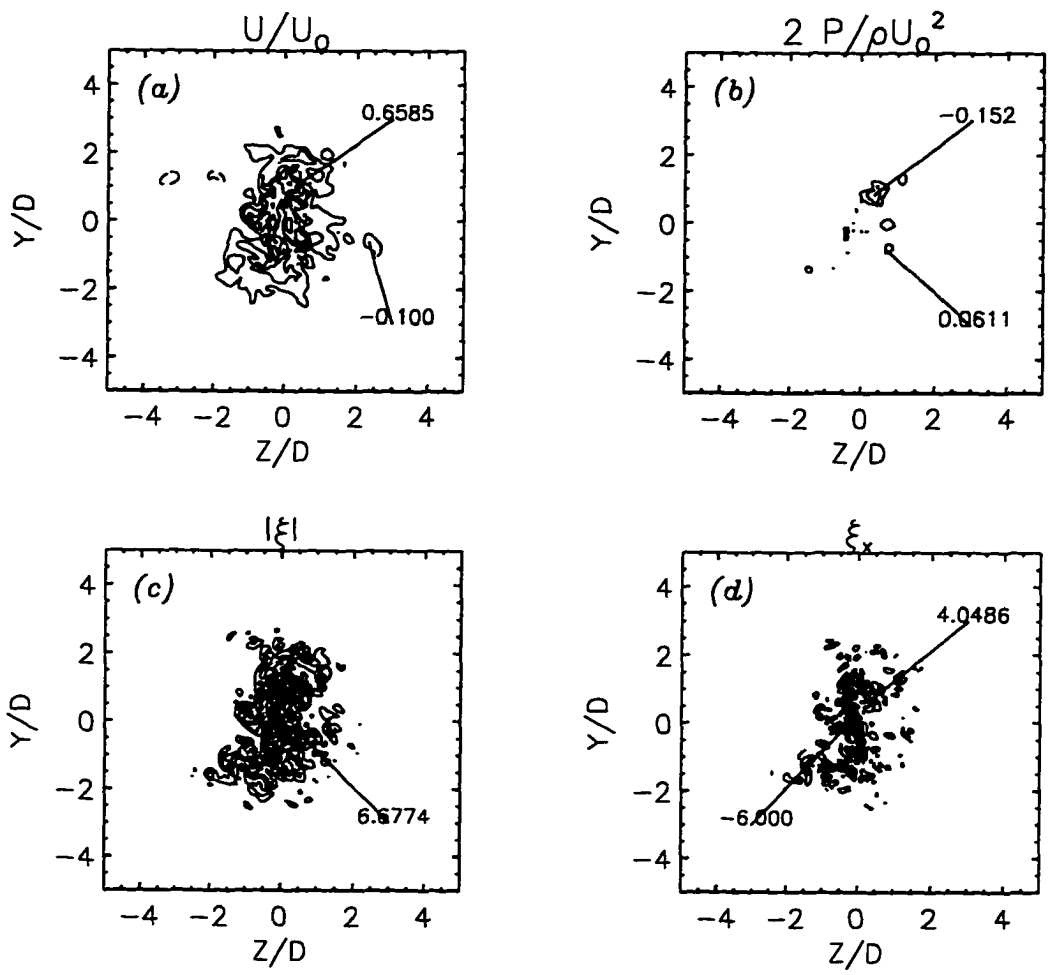

Fig 7.37 **Contours at the cross-section, x/*D* = 9.75, at *t* = 3 for LES of elliptic jet; *(a)* streamwise velocity, *(b)* pressure, *(c)* vorticity magnitude, and *(d)* streamwise vorticity.**

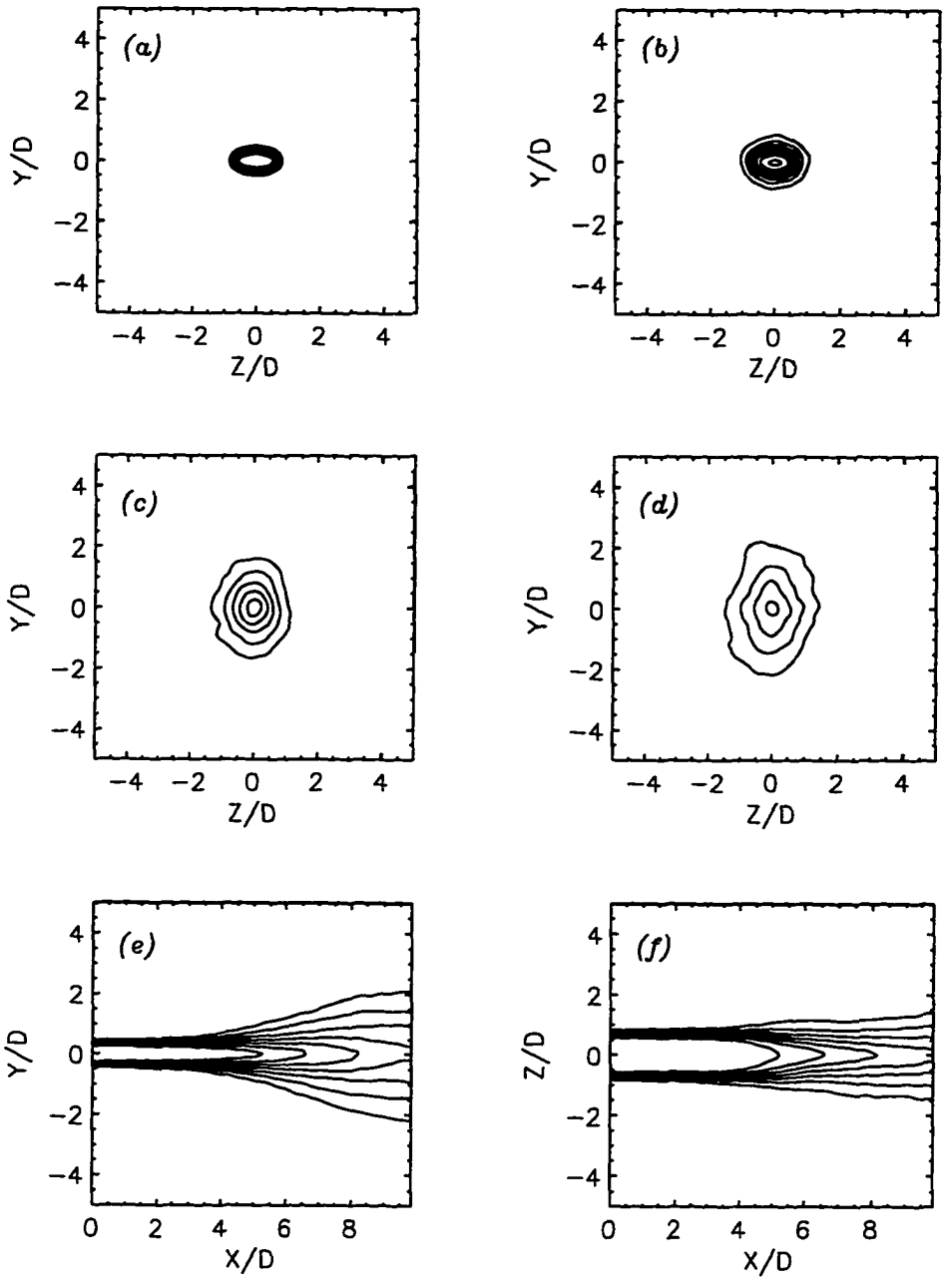

Fig 7.38 **Time-averaged contours of streamwise velocity for LES of elliptic jet; *(a)* $x/D = 0$, *(b)* $x/D = 4.88$, *(c)* $x/D = 7.31$, *(d)* $x/D = 9.75$, *(e)* minor axis plane, $z/D = 0$, *(f)* major axis plane, $y/D = 0$.**

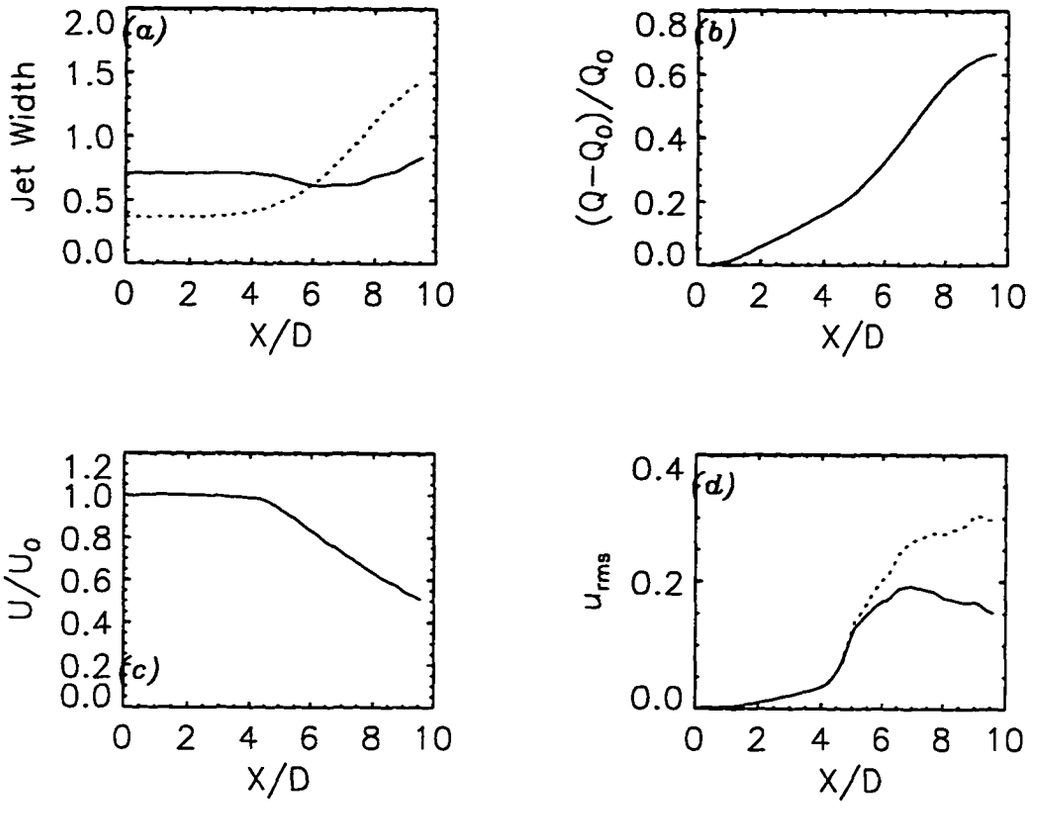

Fig 7.39 **Time-averaged quantities versus streamwise distance for LES of elliptic jet; (a) jet widths (solid - major axis plane, dashed - minor axis plane), (b) entrainment ratio, (c) decay of centerline velocity, (d) fluctuating velocity (solid - u_{rms}/U_O, dashed - u_{rms}/U_{CL}).**

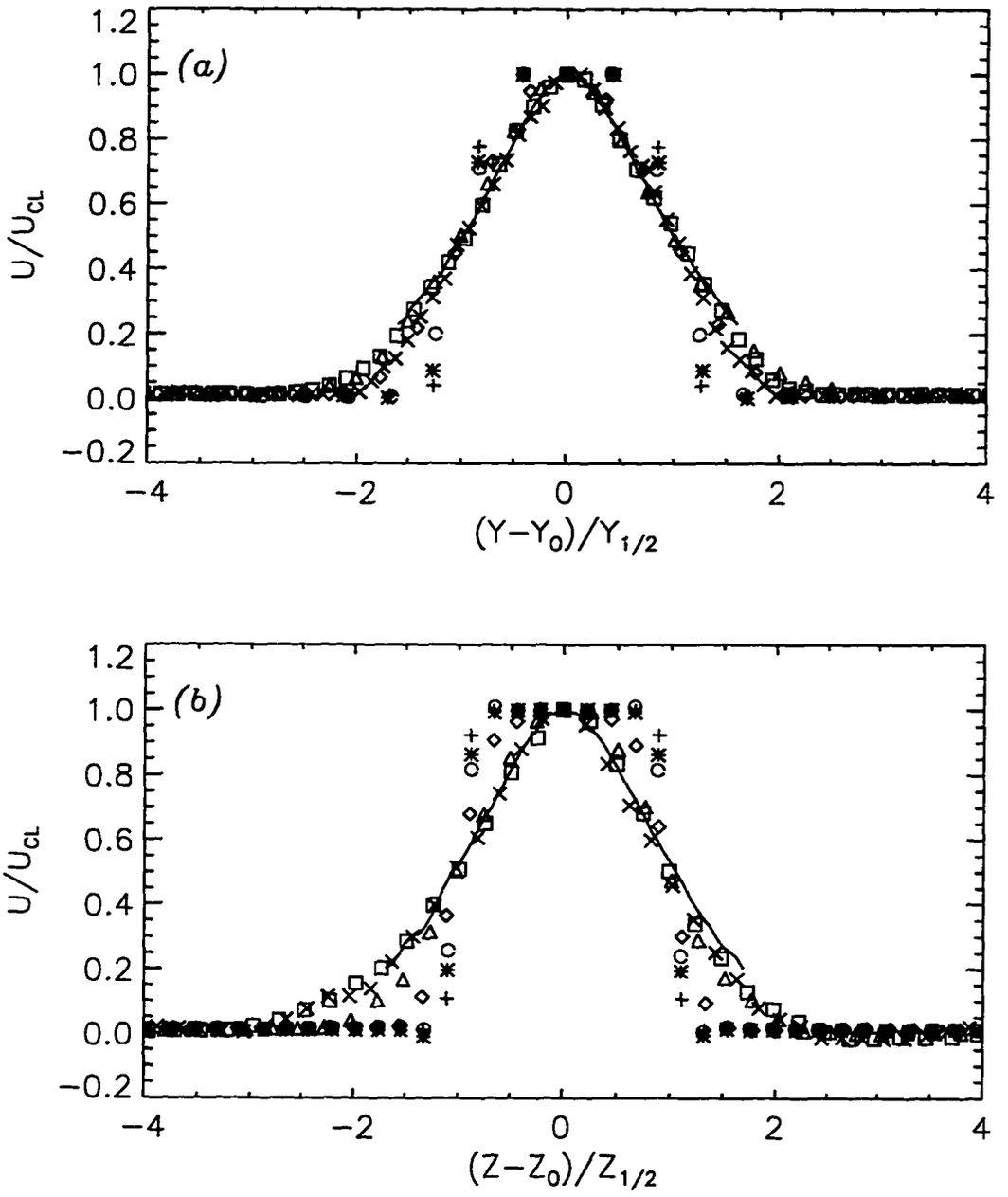

Fig 7.40 **Time-averaged streamwise velocity, *U*, for the LES of elliptic jet, *(a)* minor axis and *(b)* major axis (solid - experiment of Quinn 1995, *x/D* = 10).**

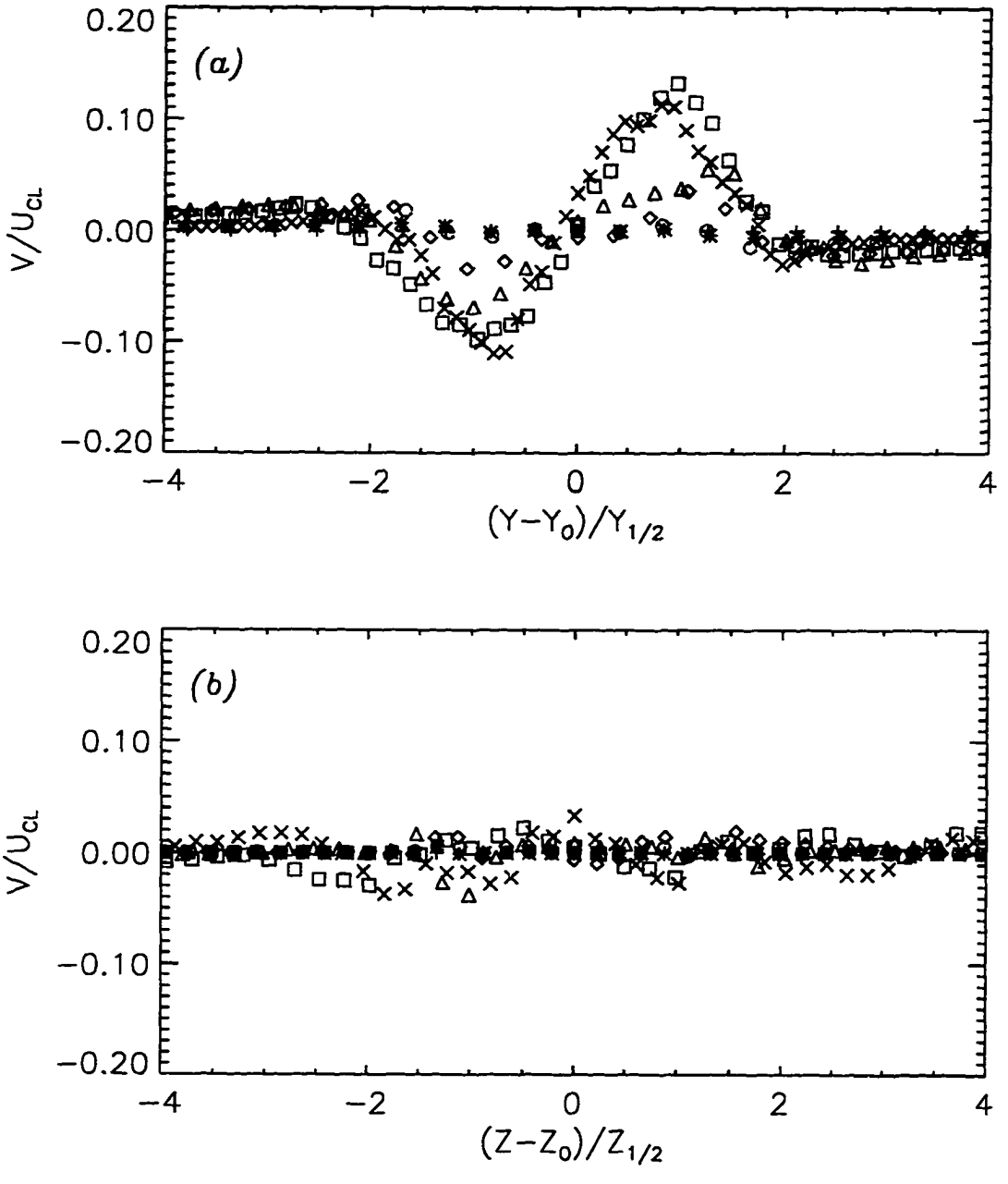

Fig 7.41 **Time-averaged lateral velocity, *V*, for the LES of elliptic jet, *(a)* minor axis and *(b)* major axis. For symbols see Fig 6.6.**

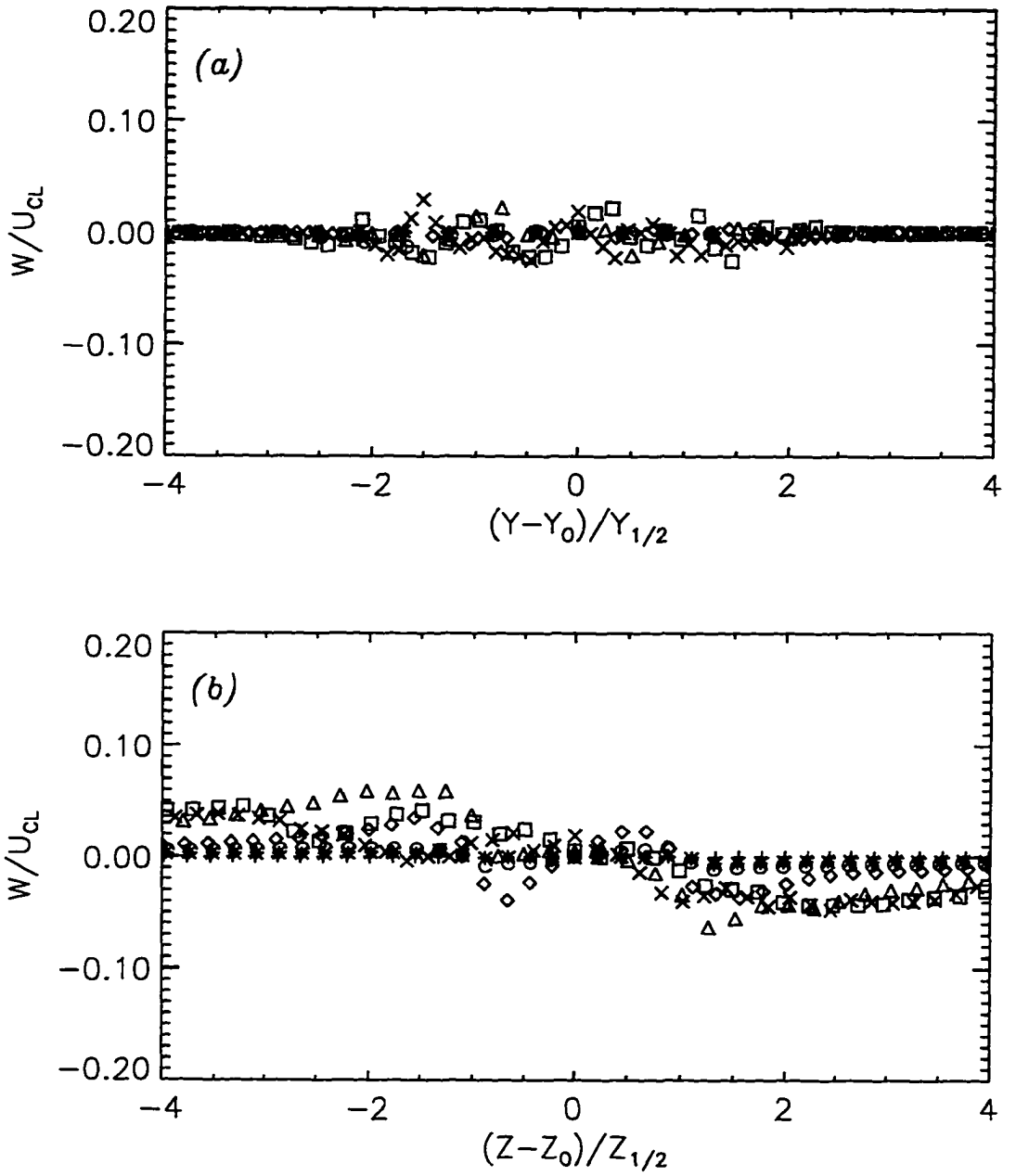

Fig 7.42 **Time-averaged transverse velocity, *W*, for the LES of elliptic jet, *(a)* minor axis and *(b)* major axis. For symbols see Fig 6.6.**

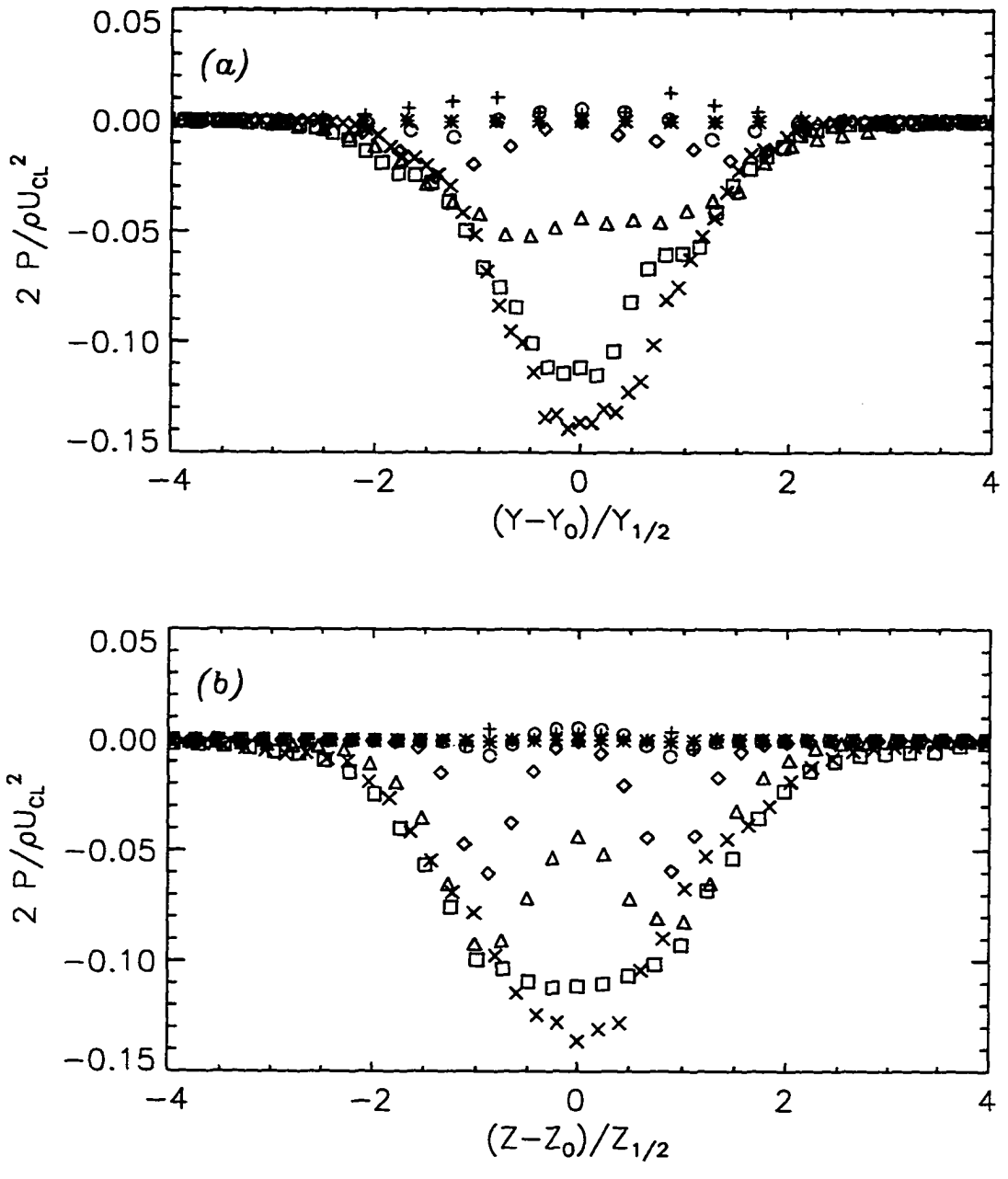

Fig 7.43 Time-averaged pressure, *P*, for the LES of elliptic jet, *(a)* minor axis and *(b)* major axis. For symbols see Fig 6.6.

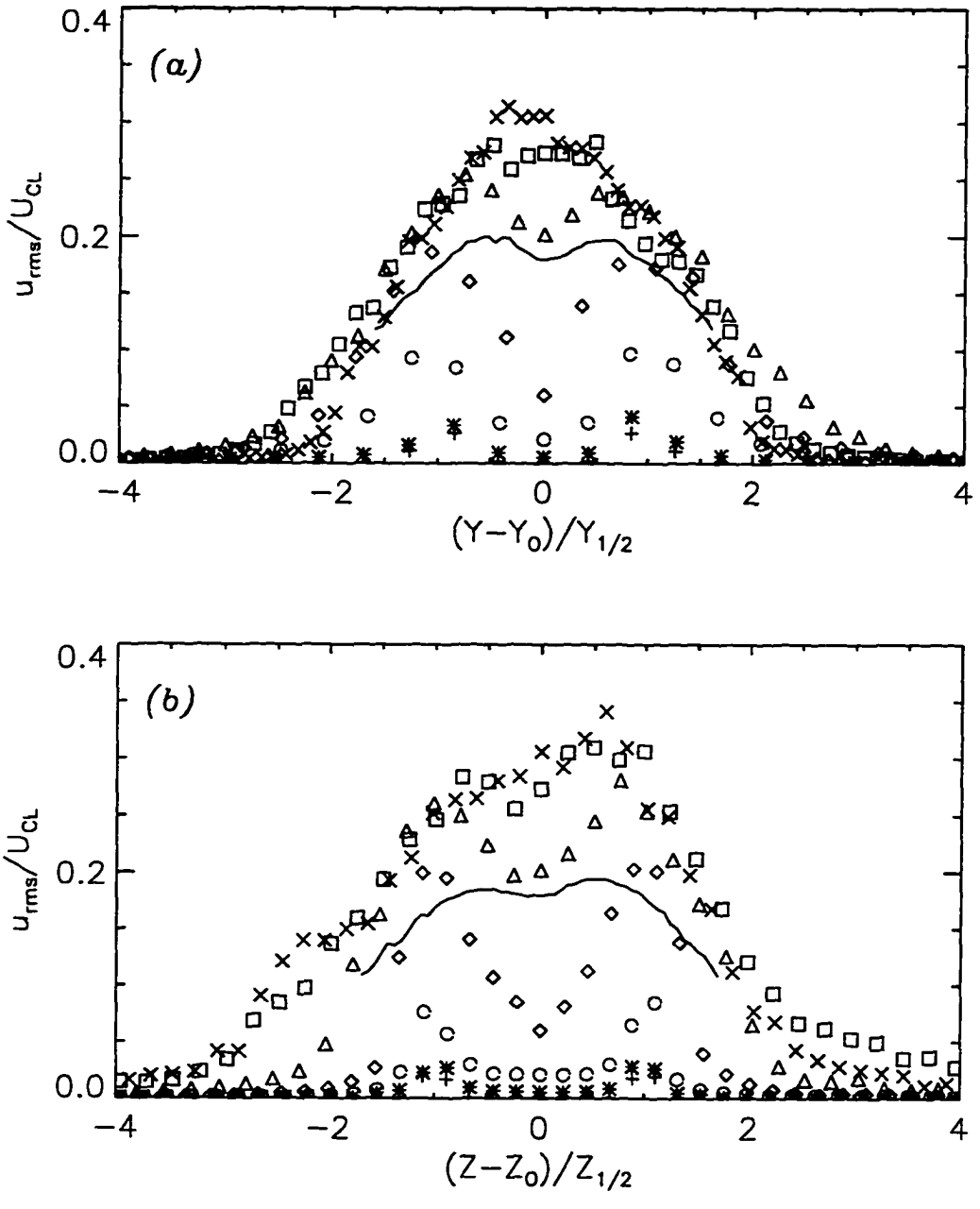

Fig 7.44 **Time-averaged fluctuating streamwise velocity, u_{rms}, for the LES of elliptic jet, *(a)* minor axis and *(b)* major axis (solid - experiment of Quinn 1995, $x/D = 10$). For symbols see Fig 6.6.**

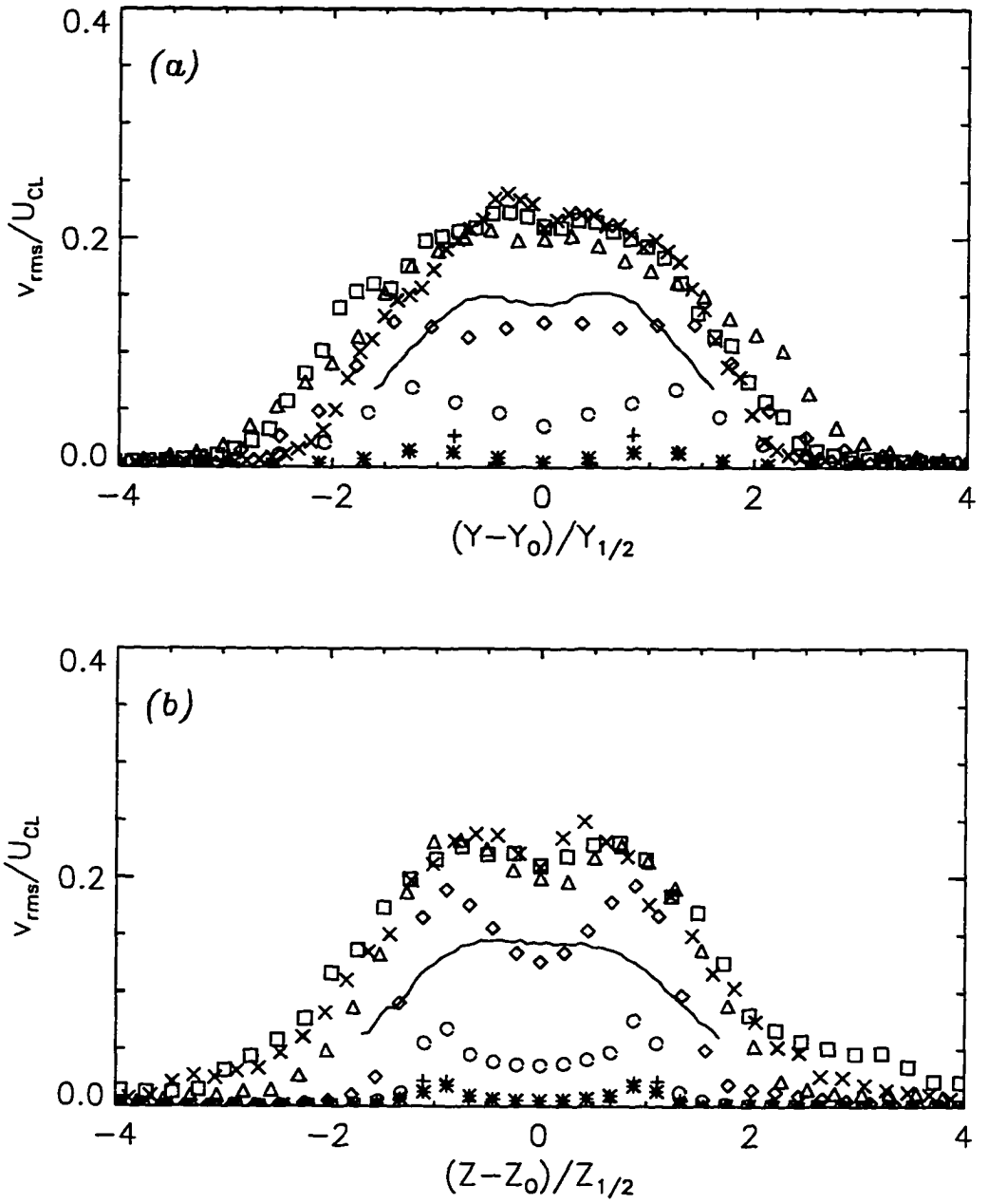

Fig 7.45 **Time-averaged fluctuating lateral velocity, v_{rms}, for the LES of elliptic jet, *(a)* minor axis and *(b)* major axis (solid - experiment of Quinn 1995, x/D = 10). For symbols see Fig 6.6.**

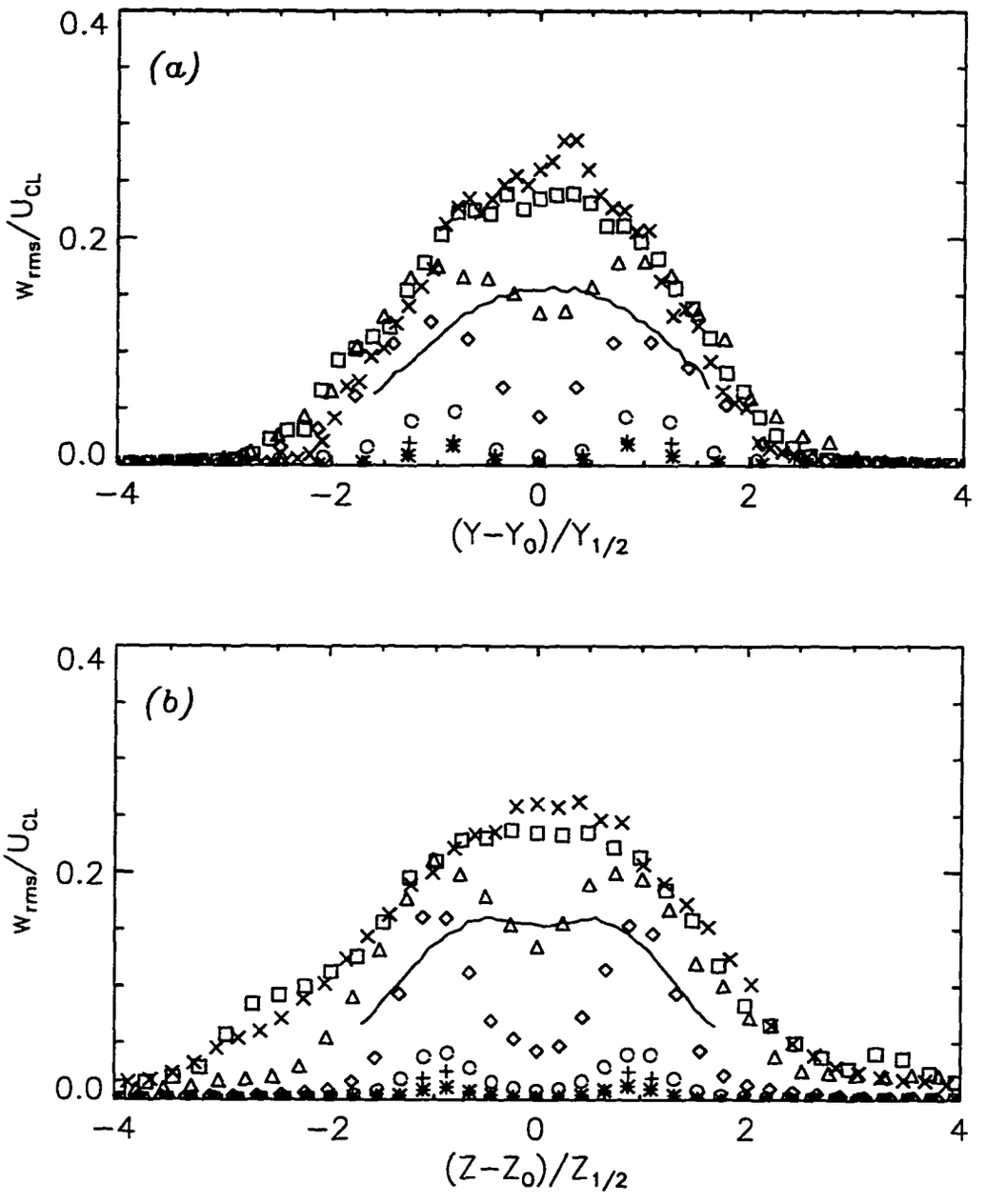

Fig 7.46 **Time-averaged fluctuating transverse velocity, w_{rms}, for the LES of elliptic jet, *(a)* minor axis and *(b)* major axis (solid - experiment of Quinn 1995, $x/D = 10$). For symbols see Fig 6.6.**

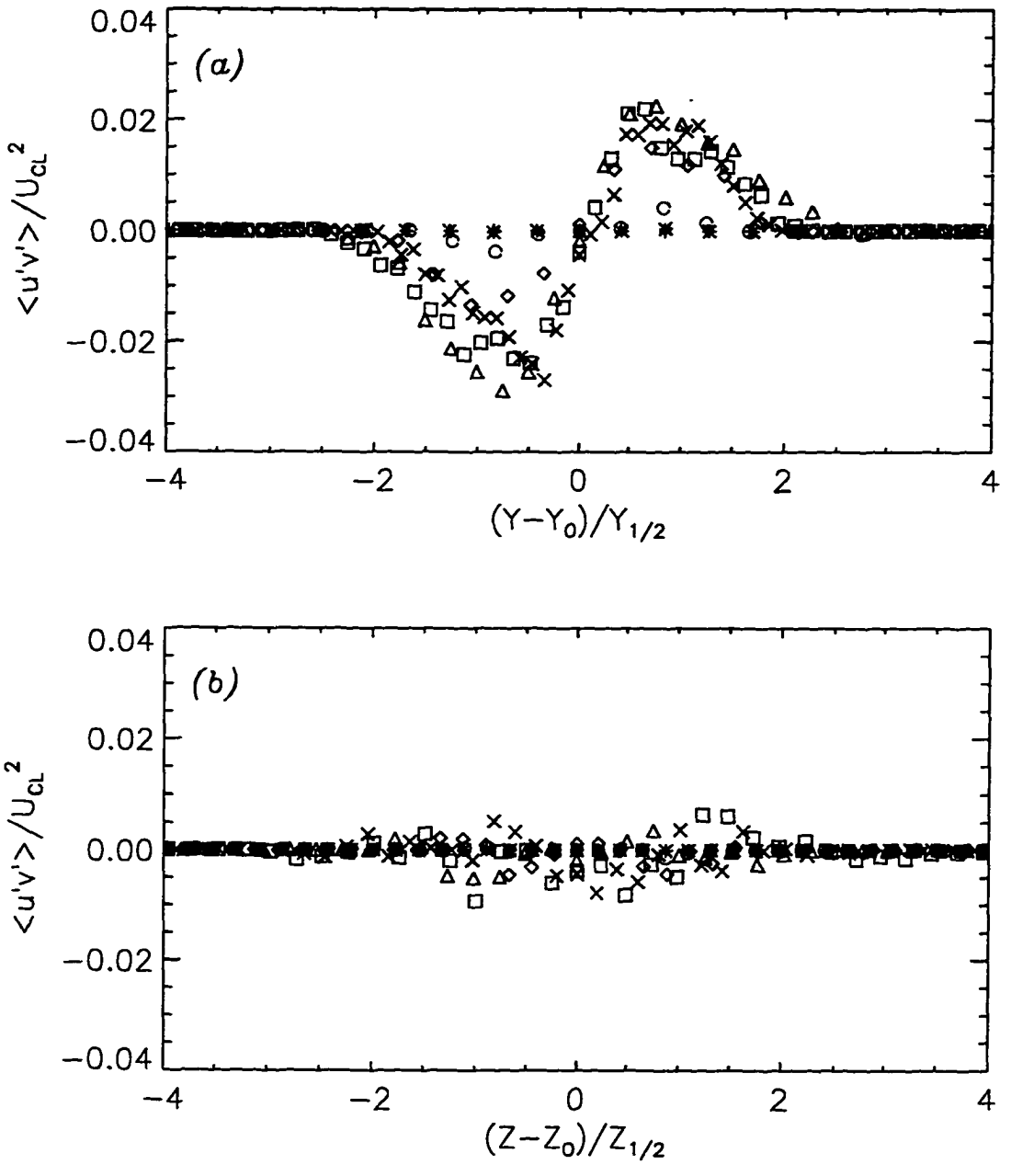

Fig 7.47 Time-averaged Reynolds shear stress, $\langle u'v' \rangle$, for the LES of elliptic jet, *(a)* minor axis and *(b)* major axis. For symbols see Fig 6.6.

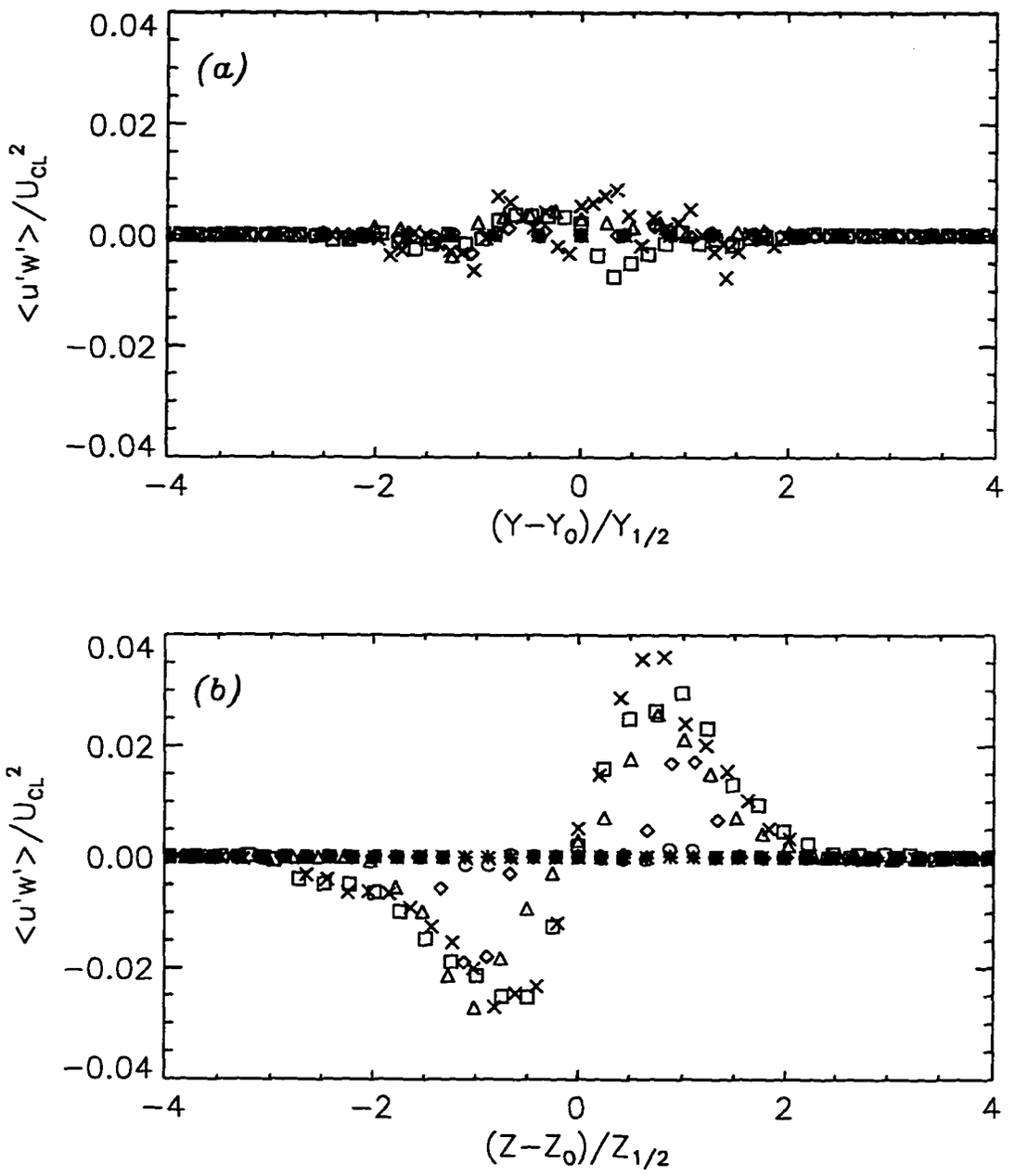

Fig 7.48 Time-averaged Reynolds shear stress, $\langle u'w' \rangle$, for the LES of elliptic jet, *(a)* minor axis and *(b)* major axis. For symbols see Fig 6.6.

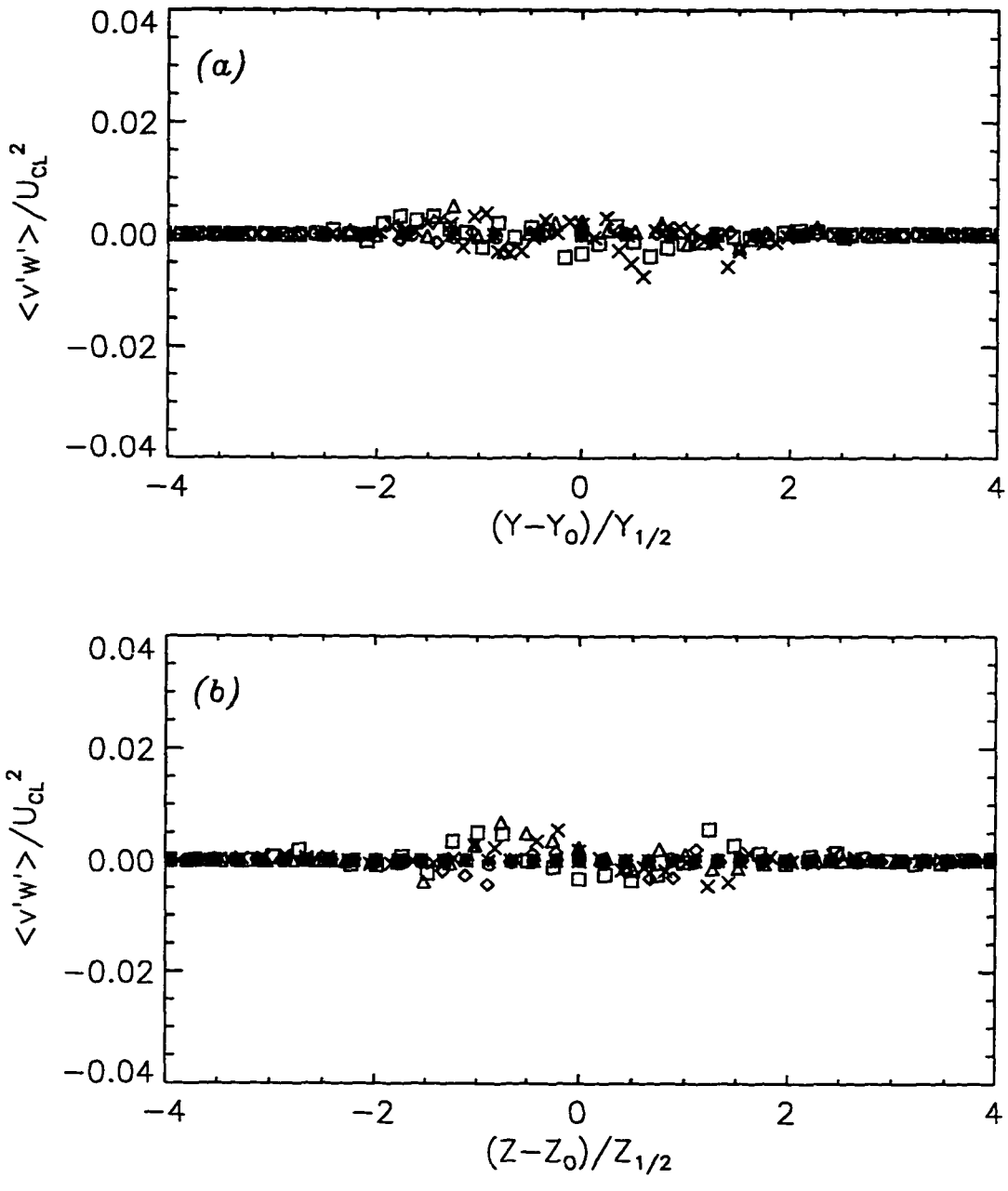

Fig 7.49 Time-averaged Reynolds shear stress, $\langle v'w' \rangle$, for the LES of elliptic jet, *(a)* minor axis and *(b)* major axis. For symbols see Fig 6.6.

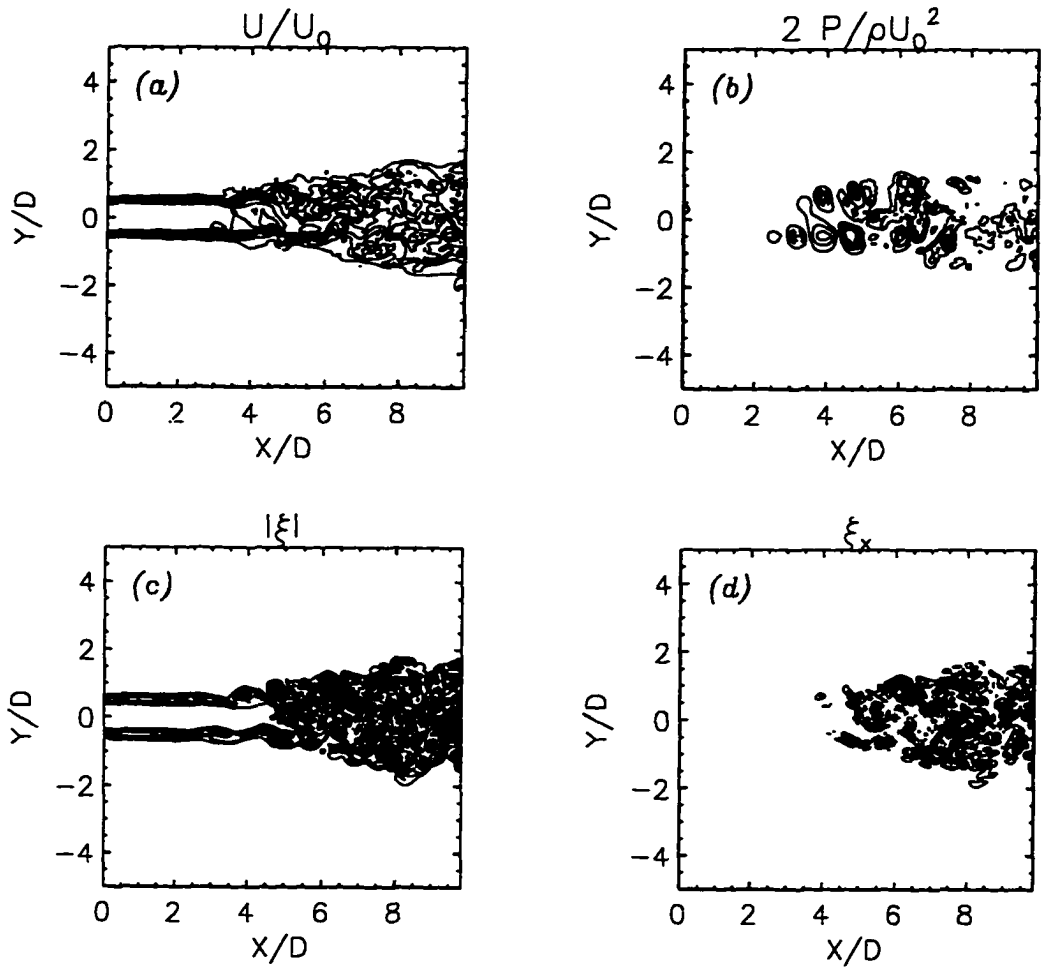

Fig 7.50 **Contours in the *X-Y* plane ($z/D = 0$) at $t = 3$ for LES of round jet; *(a)* streamwise velocity, *(b)* pressure, *(c)* vorticity magnitude, and *(d)* streamwise vorticity.**

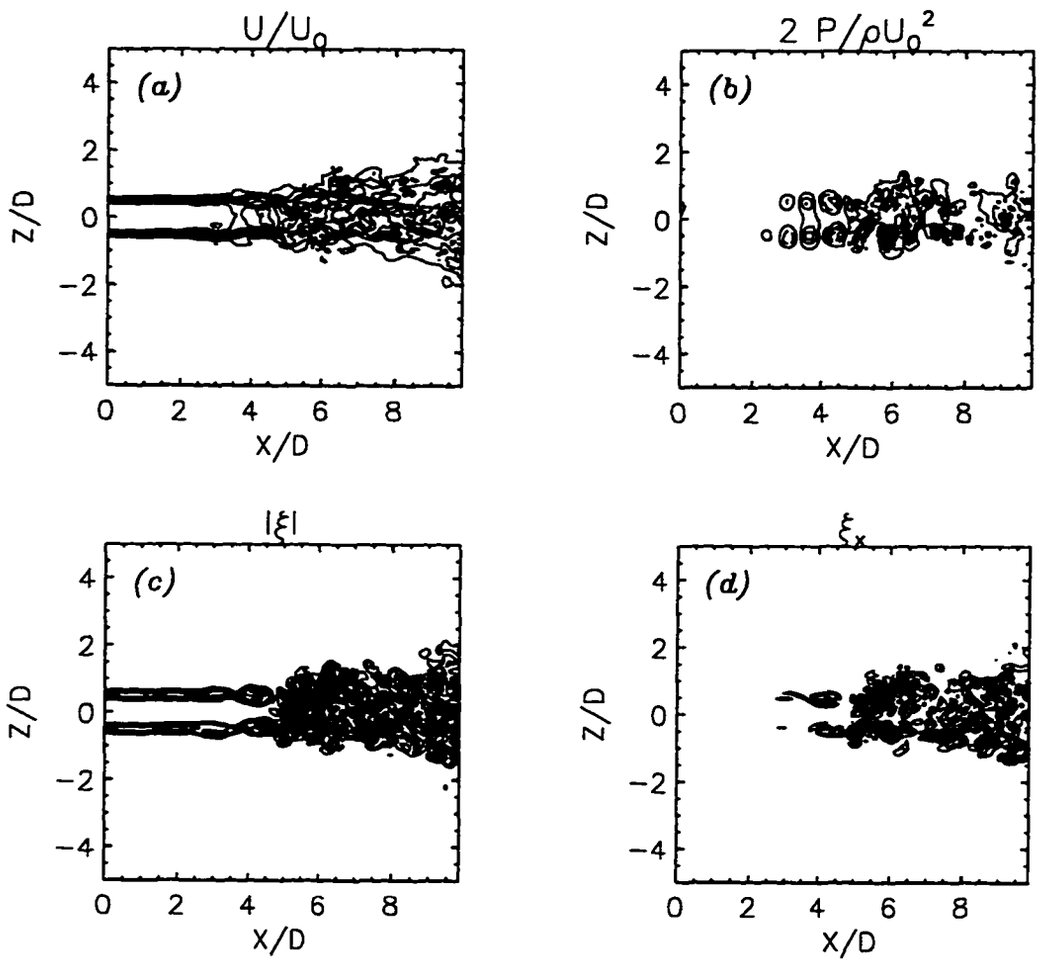

Fig 7.51 **Contours in the *X*-*Z* plane (*y*/*D* = 0) at *t* = 3 for LES of round jet; *(a)* streamwise velocity, *(b)* pressure, *(c)* vorticity magnitude, and *(d)* streamwise vorticity.**

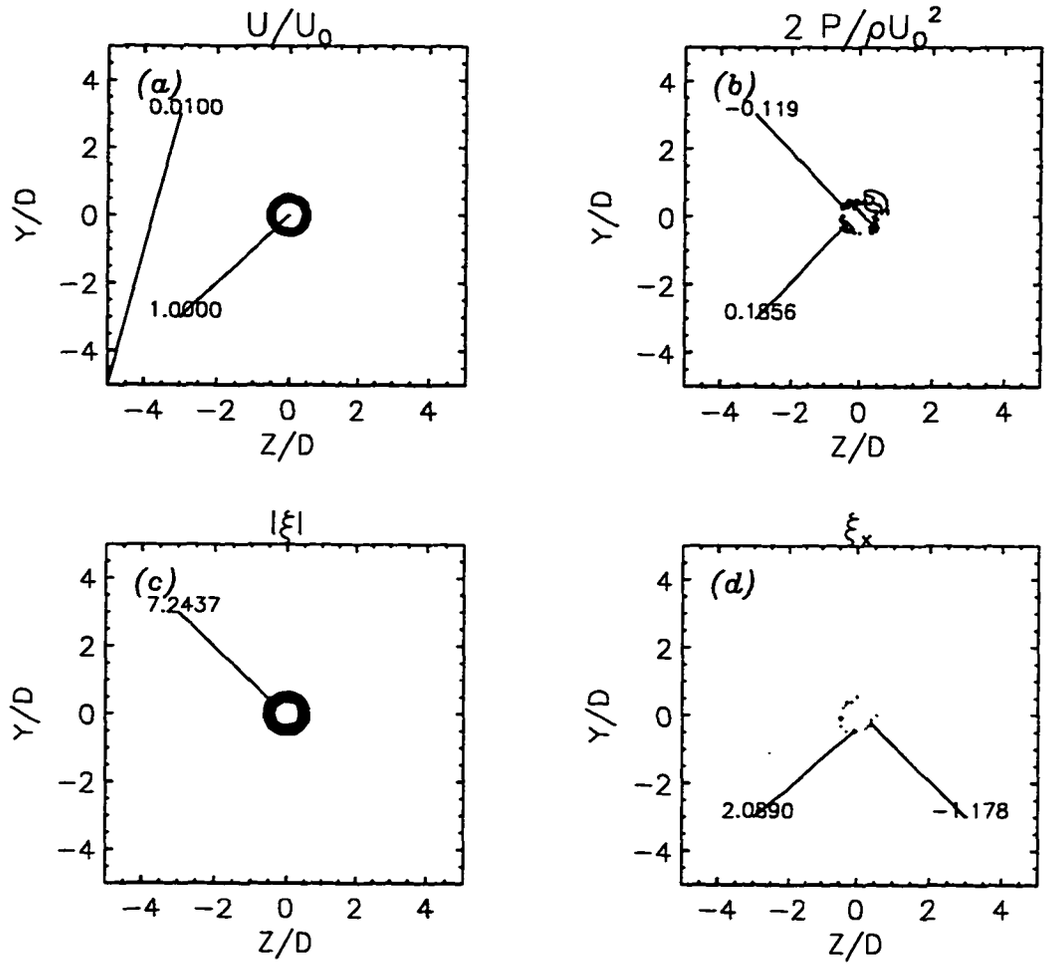

Fig 7.52 **Contours at the cross-section, x/*D* = 0, at *t* = 3 for LES of round jet; *(a)* streamwise velocity, *(b)* pressure, *(c)* vorticity magnitude, and *(d)* streamwise vorticity.**

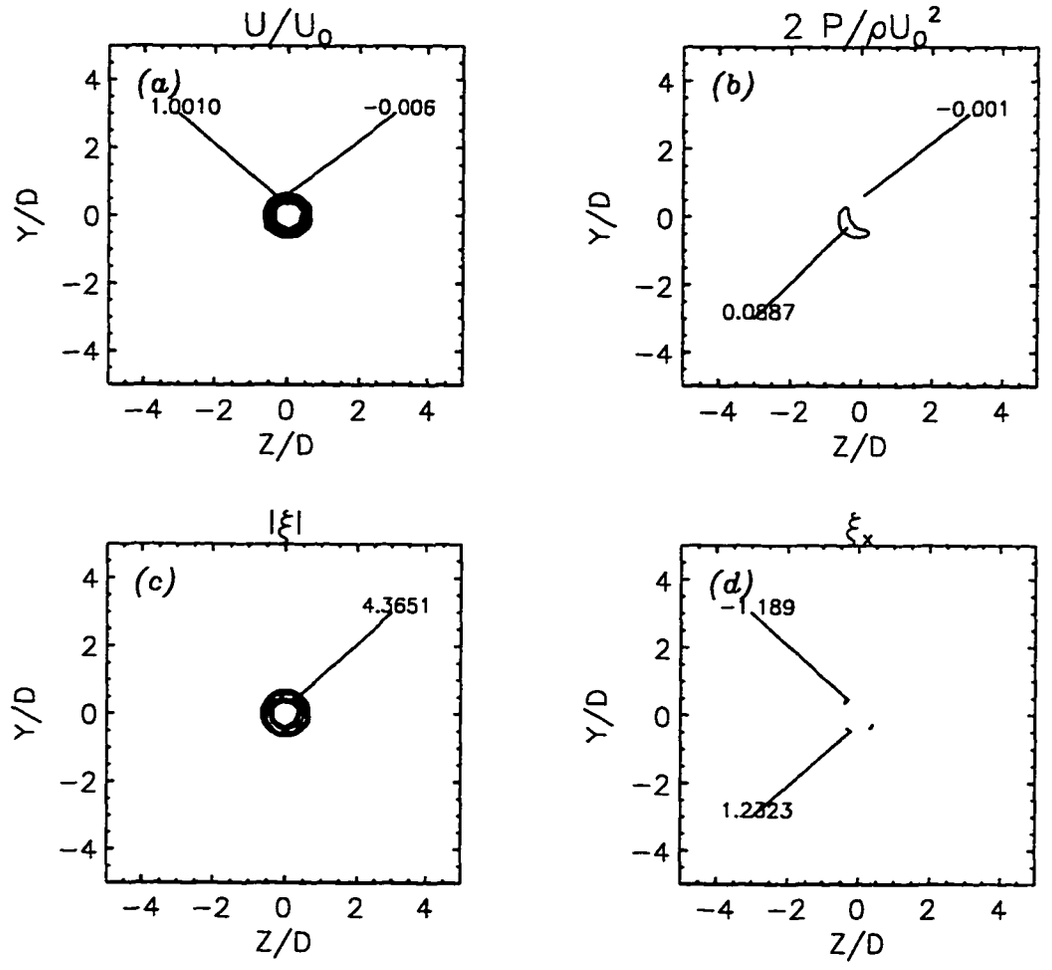

Fig 7.53 **Contours at the cross-section, x/*D* = 2.44, at *t* = 3 for LES of round jet; *(a)* streamwise velocity, *(b)* pressure, *(c)* vorticity magnitude, and *(d)* streamwise vorticity.**

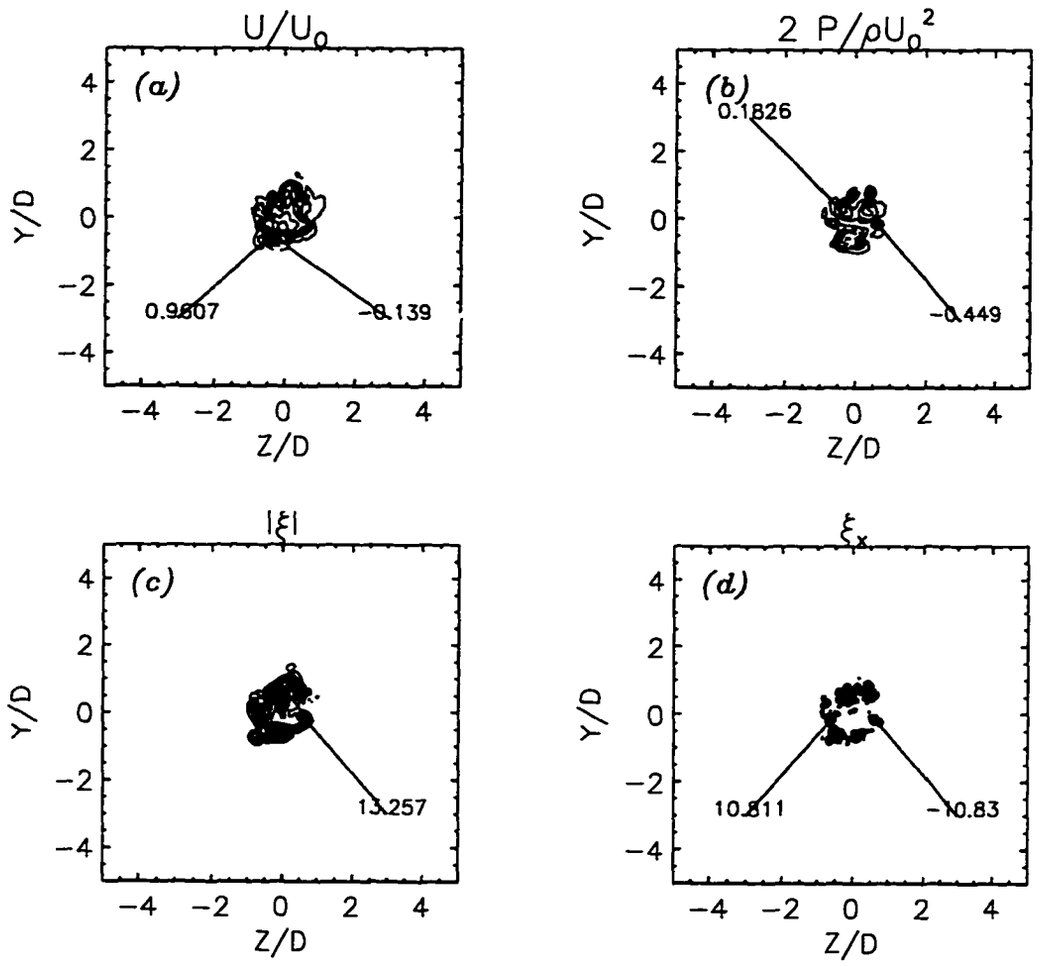

Fig 7.54 **Contours at the cross-section, x/*D* = 4.88, at *t* = 3 for LES of round jet; *(a)* streamwise velocity, *(b)* pressure, *(c)* vorticity magnitude, and *(d)* streamwise vorticity.**

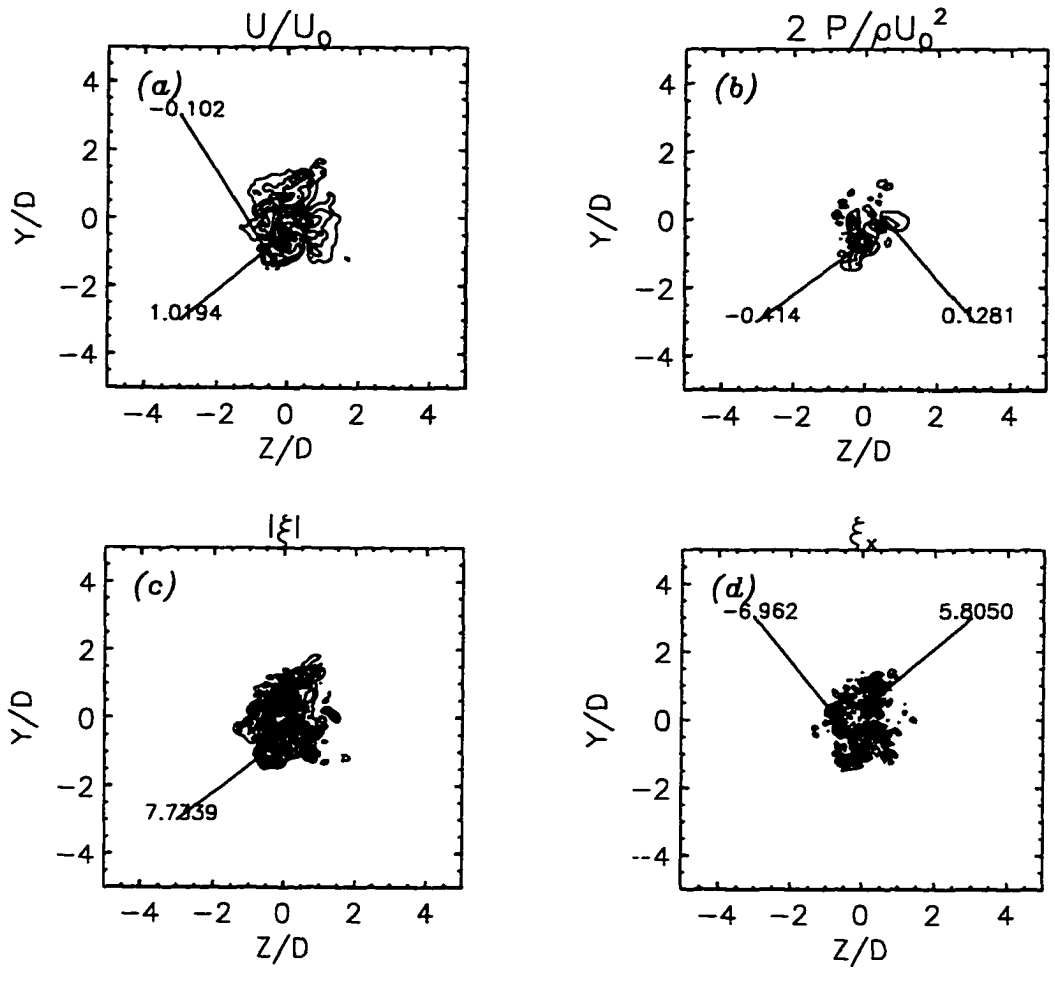

Fig 7.55 **Contours at the cross-section, x/*D* = 7.31, at *t* = 3 for LES of round jet; *(a)* streamwise velocity, *(b)* pressure, *(c)* vorticity magnitude, and *(d)* streamwise vorticity.**

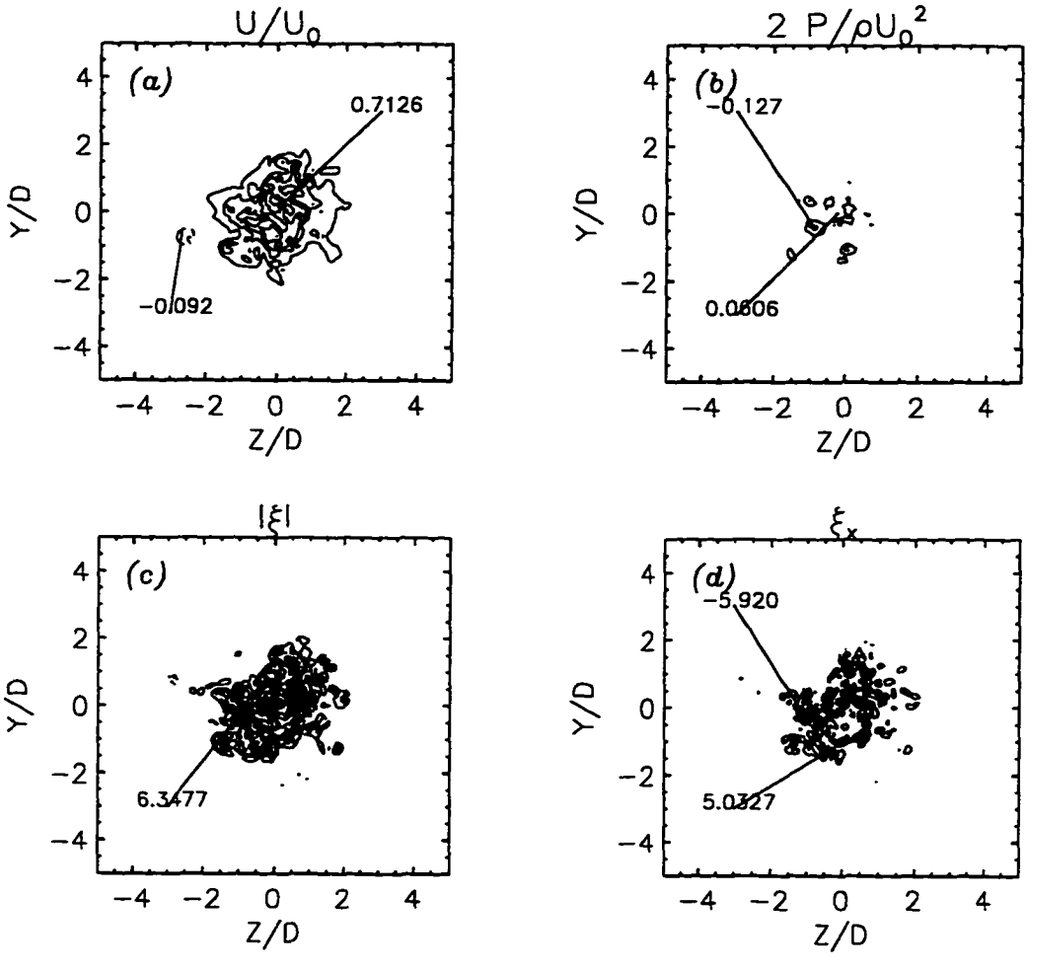

Fig 7.56 **Contours at the cross-section, x/*D* = 9.75, at *t* = 3 for LES of round jet; *(a)* streamwise velocity, *(b)* pressure, *(c)* vorticity magnitude, and *(d)* streamwise vorticity.**

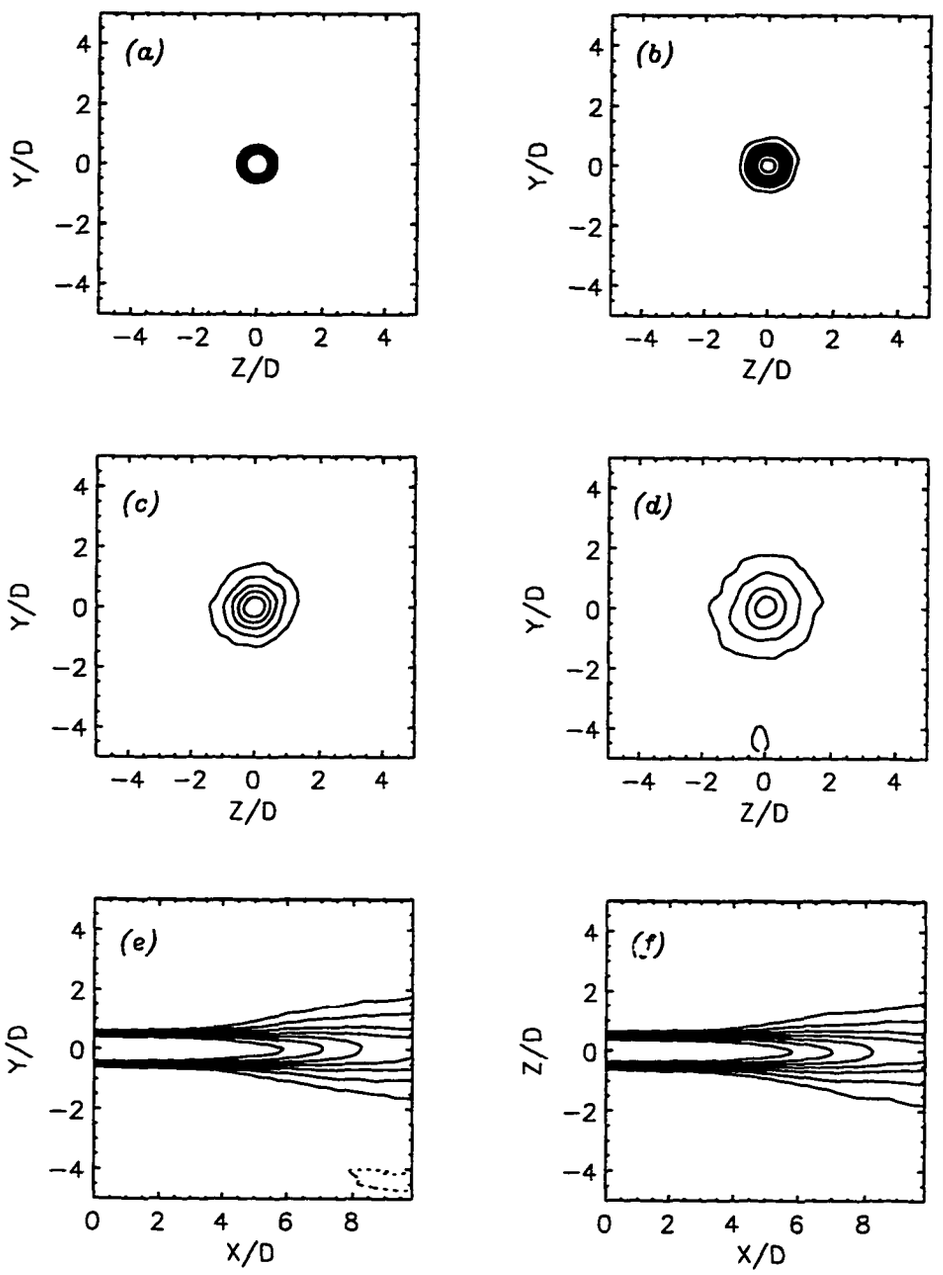

Fig 7.57 **Time-averaged contours of streamwise velocity for LES of round jet; *(a)* $x/D = 0$, *(b)* $x/D = 4.88$, *(c)* $x/D = 7.31$, *(d)* $x/D = 9.75$, *(e)* minor axis plane, $z/D = 0$, *(f)* major axis plane, $y/D = 0$.**

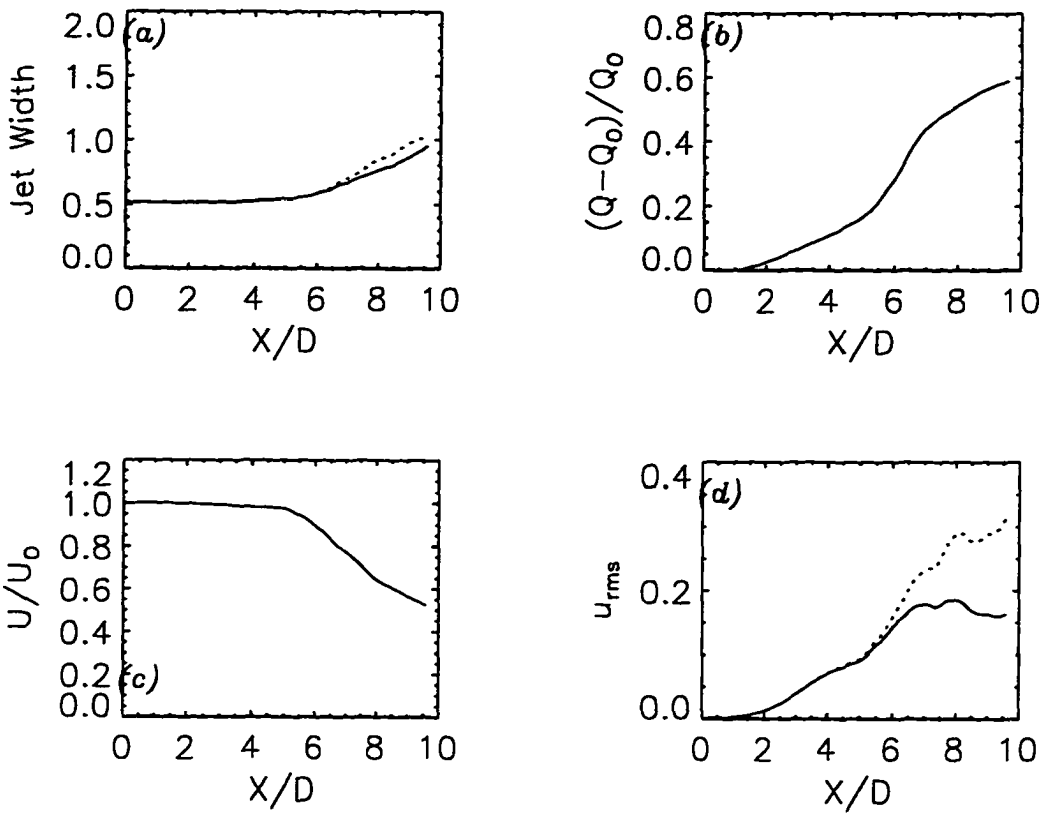

Fig 7.58 **Time-averaged quantities versus streamwise distance for LES of round jet; (a) jet widths (solid - major axis plane, dashed - minor axis plane), (b) entrainment ratio, (c) decay of centerline velocity, (d) fluctuating velocity (solid - u_{rms}/U_O, dashed - u_{rms}/U_{CL}).**

Chapter 8

SUMMARY AND CONCLUSIONS

Three-dimensional simulations of turbulent jets with rectangular and elliptical cross-section were simulated with a newly developed numerical formulation. At low Reynolds numbers the full Navier-Stokes equations were solved, while at higher Reynolds numbers the filtered equations of motion were solved along with a sub-grid scale model. The time-dependent results from the simulation are used to compute statistical quantities and to compare the results to experiment. The results are shown to agree favorably with experiment. Quantitative agreement with particular experiments should not be expected due to differences in initial conditions such as shape and aspect ratio of the jet nozzle, intensity level and spectral content of the jet exit boundary layer and Reynolds number. The present results show significant influence of the spectral content of perturbation in the inlet mixing layer. Indeed, features of the jet flow such as the axis switching location and the length of the potential core vary by as much as 60% from experiment to experiment.

Specific conclusions from the current study are outlined below. The first section describes conclusions about the numerical formulation, while the second section discusses conclusions based on the numerical simulation of complex jets. Contributions which make the present work unique are also highlighted. The final section outlines the suggestions for future work.

8.1 Numerical Formulation

Numerical Approximation of Convection Terms

It has been shown that many popular numerical approximations for convection terms lead to large dispersion and/or dissipation errors of the high-frequency modes, thus requiring upwards of 20-30 spatial points per wavelength for acceptable accuracy. Higher-order accurate compact schemes are used in this study which lead to greatly reduced dispersion errors and no dissipation errors. Solutions to relevant benchmark problems indicate that 6 - 8 points per wavelength are sufficient with the fourth-order compact scheme for acceptable accuracy. The implicit treatment of derivatives results in a global formulation closer to spectral methods than explicit finite difference schemes.

Enforcement of Continuity Equation with Higher-Order Compact Schemes

While compact schemes have been widely used for compressible simulations, their use for incompressible flows is complicated by the lack of an evolution equation for pressure. A numerical formulation was developed in the present study which solves a Poisson equation for pressure using a higher-order compact scheme. The improved accuracy and resolution characteristics was demonstrated through the solution of benchmark problems governed by the Euler and Navier-Stokes equations. It is confirmed that overall accuracy is limited by the weakest link.

Extension to Curvilinear Grids

The numerical formulation was extended to curvilinear grids which was used to concentrate grid points in the mixing layers of the rectangular jet near the inflow. Downstream of the potential core, the flow is fully turbulent. Clustering of the grid to resolve large gradients due to small scale structures is not possible without the use of time-varying, adaptive grids (which is outside the scope of the present study). Therefore, the grid is gradually

relaxed to uniform spacing in this region. Uniform grids enable manipulation of the discrete Poisson equation leading to a reduced stencil size and cost as compared with the curvilinear grids making the computational rate roughly one order of magnitude less. Part of the reason for the increase in computational rate is that convergence rates for the multigrid solution of the Poisson equation deteriorate with grid clustering and large aspect ratio. Therefore, the uniform grid formulation was utilized for most of the simulations presented in Chaps. 6 and 7.

8.2 Simulation of Complex Jets

Conclusions from the direct and large eddy simulations of complex jets are outlined in this section. Aspects of the current work which are different from the current state of the art are highlighted.

Effect of Reynolds Number

The results from the DNS of non-circular jets at low Reynolds numbers (Re = 750) in Chap. 6 show that many features of experiments at moderate to high Reynolds number are not captured. For example, low Reynolds number simulations in the present study and those by Miller et al (1995) show that the end of the potential core is not predicted within 10 diameters, while experiments and the simulations at higher Reynolds number of the current study show an end at roughly $x/D_e = 4$. Also transition to turbulent flow does not occur within the computational domain resulting in symmetrical structures and spikes in the velocity power spectra that are characteristic of laminar/transitional flow. It is clear that simulations at higher Reynolds numbers must be performed for comparison with experiment in the literature.

Streamwise Extent

Current state of the art for the large eddy simulation of square and rectangular jets at moderate to high Reynolds number is that due to Grinstein and DeVore (1992), Grinstein (1993), and Grinstein (1996). The streamwise extent of those simulations covers the very near field (i.e., only the potential core region, $x/D_e < 5$). The current study is unique in the sense that the near and medium fields are simulated. This allows the so-called characteristic decay region downstream of the potential core to be studied. In addition, the experimentally observed axis switching of the 2:1 rectangular jet at $x/D_e = 7$ is captured.

Subgrid Scale Model

The current study employs an explicit Smagorinsky subgrid scale model which allows the model effects to be quantified. Moreover, the effect of the unresolved scales was compared to those of the resolved scales by computing budget terms of the mean momentum equations. This analysis shows that the contribution of the unresolved stresses which are modeled are 15 times smaller than the those of the resolved stresses which are directly computed in the simulation.

Budgets for Mean Momentum and Reynolds Stress Equations

A numerical database of the time-dependent results from the simulations has been archived. The database was post-processed to compute statistical quantities and detailed budgets of the resolved mean momentum and Reynolds stress equations. In general, balance of the terms of the mean momentum equation are quite good. Balance of terms in the Reynolds stress equations was incomplete because of the under-prediction of turbulent dissipation which occurs mostly at small scales not resolved in the simulation. The database can be used to aid in the turbulence modeling of complex jets.

Effect of Initial Conditions

The results of the current study show that the initial conditions of the jet boundary layer at the inflow strongly effect the resulting dynamics. Forcing functions consisting of a single discrete mode show that the mixing layers in the potential core rolls up into planar vortex rings. At low Reynolds number, the fundamental mode saturates and decays, while at higher Reynolds number, transition to turbulence takes place. Axis-switching was observed in both cases. The addition of a subharmonic to the forcing function at low Reynolds number is shown to result in the formation of intense vortex ribs near the jet centerline which lead to a partial bifurcation of the jet. Axis switching was not observed in this case.

Forcing functions based on random, broad band modes show that the roll up of the mixing layers in the potential core is fundamentally different than that due to discrete forcing. Planar vortex rings are not formed with broad mode forcing and a staggered roll up of the upper and lower mixing layer in the minor axis plane only is observed. As a result, mixing in the major axis plane is suppressed leading to switching of the major and minor axis at $x/D_e = 6.6$ for the rectangular jet and $x/D_e = 5.9$ for the elliptic jet at higher Reynolds number. Naturally developing non-circular jets (i.e. without strong discrete forcing) are better modeled with broad mode forcing. Therefore, simulations forced with a single sinusoidal mode leading to the formation of planar vortex rings provide an incomplete description of the axis switching phenomenon in naturally developing jets. The results of the present study provide such a picture.

Effect of Non-Uniform Boundary Layer Curvature

Effects of non-uniform azimuthal curvature of the jet boundary layer at the nozzle are studied though large eddy simulations of rectangular, elliptic, and circular jets. The results show that the elliptic jet entrains more fluid into the jet core than the rectangular jet.

Grid Resolution

A grid resolution study was performed through simulations on 4 grid levels, by doubling the number of grid points on successive levels. The coarsest grid resolution (with 2.5 points per streamwise fundamental wavelength) does not capture unsteadiness (u_{rms} = 0.005 at x/D_e = 10) which is essential for accurate prediction of the potential core length and subsequent axis switching. Increasing the grid resolution to the second level results in an increased level of unsteadiness (u_{rms} = 0.05 at x/D_e = 10) but does not predict the end of the potential core or axis switching within the computational domain. The results from the level 3 grid (with 10 points per streamwise fundamental wavelength) show a well defined end of the potential core and axis switching in good agreement with experiment. The effect of increasing the grid resolution in the near field to the fourth level, does not significantly change those predictions. The main effect is that the prediction of the end of the potential core is shifted upstream by 0.7 diameters, which is most likely due to differences in the broad mode forcing function on the third and fourth grid levels. When the results on the fourth level are corrected for this difference, relatively grid independent results are achieved. The resolution requirement of roughly 10 streamwise grid points per wavelength reached through this exercise is consistent with conclusions from the solution of benchmark problems using compact schemes in Chap. 5.

8.3 Future Work

Future research directions are identified in this section. In the area of the numerical formulation, the efficiency of the Poisson solver with curvilinear grids could be improved which would lead to competitive computational rates as compared with the uniform grid formulation. This would be used take advantage of grid clustering capabilities in the very near field. The resolution after the end of the potential core would still be necessarily uniform due to the presence of small scale turbulent structures. Time-varying, adaptive meshes would be required to track those structures.

While the present numerical simulation extends the state of the art past the end of the potential core into the characteristic decay region, it would be desirable to simulate all 3 regions of the non-circular jet; *(i)* potential core, *(ii)* characteristic decay, and *(iii)* axisymmetric region. It would also be desirable to increase resolution to the fourth grid level of the resolution study for the entire domain length. Code improvements would be required to reduce the required wall clock time and memory for the simulation such as the use of parallel processing and Fortran buffer in/ buffer out statements (reading and writing to disk to save memory allocation). Parallelization should be a major goal of future work. The simulations can also be extended to solve compressible flows for acoustic predictions. There, accurate solutions are required for the unsteady flow field which is then used as the source term of an acoustic analogy equation.

REFERENCES

Briggs, W. L., 1987, *A Multigrid Tutorial*, Society for Industrial and Applied Mathematics, Philadelphia, Pennsylvania.

Carpenter, M. H. and Kennedy, C. A., 1994, "Fourth-Order, 2N-Storage Runge-Kutta Schemes," NASA TM 109112.

Crighton, D. G., 1973, "Instability of an Elliptic Jet," *Journal of Fluid Mechanics*, Vol. 59, pp. 665-672.

Demuren, A. 0., Rogers, M. M., Durbin, P., and Lele, S. K., 1996, "On Modeling Pressure Diffusion in Non-Homogeneous Shear Flows," *Proceedings of the Center for Turbulence Research, Summer Program.*

Demuren, A. O. and Wilson, R. V., 1994, "Estimating Uncertainty in Computations of Two-Dimensional Separated Flows," *Journal of Fluids Engineering*, Vol. 116, pp. 216-220.

Dhanak, M. R. and DeBernandis, B., 1981, "The Evolution of an Elliptic Vortex Ring," *Journal of Fluid Mechanics*, Vol. 100, pp. 189-216.

Gresho, P. M. and Sani, R. L., 1987, "On Pressure Boundary Conditions for the Incompressible Navier-Stokes Equations," *International Journal for Numerical Methods in Fluids*, Vol. 7, pp. 1111-1145.

Grinstein, F. F. and DeVore, C. R., 1992, "Coherent Structure Dynamics in Spatially-Developing Square Jets," AIAA Paper 92-3441.

Grinstein, F. F., 1993, "Vorticity in Spatially-Developing Rectangular Jets," AIAA Paper 93-3286.

Grinstein, F. F., 1995, "Self-Induced Vortex Ring Dynamics in Subsonic Rectangular Jets," *Physics of Fluids*, Vol. 7, No. 10, pp. 2519-2521

Grinstein, F. F., 1996, "Dynamics of Coherent Structures and Transition to Turbulence in Free Square Jets," AIAA Paper 96-0781.

Hardin, J. C., Ristorcelli, J. R., and C. K. W. Tam, 1995, *ICASE/LARC Workshop on Benchmark Problems in Computational Aeroacoustics CAA.*

Ho, C.-M. and Gutmark, E., 1987, "Vortex Induction and Mass Entrainment in a Small-Aspect-Ratio Jet," *Journal of Fluid Mechanics*, Vol. 179, pp. 383-405.

Hoffmann, K. A. and Chiang, S. T., 1993, *Computational Fluid Dynamics For Engineers - Volume I.*

Hu, F. Q., Hussaini, M. Y., and Manthey, J., 1994, "Low-Dissipation and -Dispersion Runge-Kutta Schemes for Computational Acoustics," ICASE Report 94-102.

Hussain, F. and Husain, H. S., 1989, "Elliptic Jets. Part 1. Characteristics of Unexcited and Excited Jets," *Journal of Fluid Mechanics*, Vol. 208, pp. 257-320.

Husain, H. S. and Hussain, F., 1991, "Elliptic Jets. Part 2. Dynamics of Coherent Structures: Pairing," *Journal of Fluid Mechanics*, Vol. 233, pp. 439-482.

Husain, H. S. and Hussain, F., 1993, "Elliptic Jets. Part 3. Dynamics of Preferred Mode Coherent Structure," *Journal of Fluid Mechanics*, Vol. 248, pp. 315-361.

Krothapalli, A., Baganoff, D., and Karamcheti, K., 1981, "On the Mixing of a Rectangular Jet," *Journal of Fluid Mechanics*, Vol. 107, pp. 201-220.

Koshigoe, S. and Tubis, A., 1986, "Wave Structures in Jets of Arbitrary Shape. I. Linear Inviscid Spatial Instability Analysis," *Physics of Fluids*, Vol. 29, pp. 3982-3993.

Koshigoe, S. and Tubis, A., 1987, "Wave Structures in Jets of Arbitrary Shape. II. Application of a Generalized Shooting Method to Linear Instability Analysis," *Physics of Fluids*, Vol. 30, pp. 1715-1723.

Koshigoe, S., Ho, C.-M., and Tubis, A., 1987, "Application of a Generalized Shooting Method to the Linear Stability Analysis of Elliptic Core Jets," AIAA Paper 87-2722.

Le, H. and Moin, P., 1994, "Direct Numerical Simulation of Turbulent Flow Over a Backward Facing Step," Report TF-58, Department of Mechanical Engineering, Stanford University.

Lele, S. K., 1992, "Compact Finite Difference Schemes with Spectral-Like Resolution," *Journal of Computational Physics*, Vol. 103, pp. 16-42.

Lowery, S. L. and Reynolds, W. C., 1986, "Numerical Simulation of a Spatially-Developing Mixing Layer," Report TF-26, Department of Mechanical Engineering, Stanford University.

McGuirk, J. J. and Rodi, W., 1979, "The Calculation of Three-Dimensional Turbulent Free Jets," In *Turbulent Shear Flows I*, Eds. F. Durst, B. E. Launder, F. W. Schmidt and J. H. Whitelow, pp. 71-83.

Miller, R. S., Madnia, C. K., and Givi, P., 1995, "Numerical Simulation of Non-Circular Jets," *Computers and Fluids*, Vol. 24, No. 1, pp. 1-25.

Morris, P. J., 1988, "Instability of Elliptic Jets," AIAA Journal, Vol. 26, pp. 172-178.

Orszag, S. A., 1971, "Numerical Simulation of Incompressible Flows within Simple Boundaries: Accuracy," *Journal of Fluid Mechanics*, Vol. 49, Part 1, pp. 75-112.

Quinn, W. R. and Militzer, J., 1988, "Experimental and Numerical Study of a Turbulent Free Square Jet," *Physics of Fluids*, Vol. 31, No. 5, pp. 1017-1025.

Quinn, W. R., 1989, "On the Mixing in an Elliptic Turbulent Free Jet," *Physics of Fluids A*, Vol. 1, No. 10, pp. 1716-1722.

Quinn, W. R., 1995, "Turbulent Mixing in a Free Jet Issuing from a Low Aspect Ratio Contoured Rectangular Nozzle," *The Aeronautical Journal of the Royal Aeronautical Society*, Vol. 99, No. 988, pp. 337-342

Rogers, M. M. and Moser, R. D., 1994, "Direct Simulation of a Self-Similar Turbulent Mixing Layer," *Physics of Fluids*, Vol. 6, No. 2, pp. 903-923.

Sfeir, A. A., 1976, "The Velocity and Temperature Fields of Rectangular Jets," *International Journal of Heat and Mass Transfer*, Vol. 19, pp. 1289-1297.

Sforza, P. M., Steiger, M. H., and Trentacoste, N., 1966, "Studies on Three-Dimensional Viscous Jets," AIAA Journal, Vol. 4, No. 5, pp. 800-806.

Smagorinsky, J., 1963, "General Circulation Experiments with Primitive Equations. I. The Basic Experiment," *Monthly Weather Review*, Vol. 91, No. 3, pp. 99-165.

Spencer, B. W. and Jones, B. G., 1971, "Statistical Investigations of Pressure and Velocity Fields in the Turbulent Two-Stream Mixing Layer," AIAA Paper 71-613.

Street, C. L. and Macaraeg, M. G., 1990, "Spectral Multi-Domain for Large-Scale Fluid Dynamic Simulations," *Applied Numerical Mathematics*, Vol. 6, pp. 123-139.

Stuart, J. T., 1967, "On Finite Amplitude Oscillations in Laminar Mixing Layers," *Journal of Fluid Mechanics*, Vol. 29, Part 3, pp. 417-440.

Tam, C. K. W. and Thies, A. T., 1993, "Instability of Rectangular Jets," *Journal of Fluid Mechanics*, Vol. 248, pp. 425-448.

Trentacoste, N. and Sforza, P. M., 1967, "Further Experimental Results for Three-Dimensional Free Jets," AIAA Journal, Vol. 5, pp. 885-891.

Tsuchiya, Y., Haneda, Y., Horikoshi, C., and Sato, T., 1985, "A Study on the Spread of the Rectangular Jets," *Bulletin of Japanese Society of Mechanical Engineering*, Vol. 28, No. 243, pp. 1933-1941.

Tsuchiya, Y., Horikoshi, C., Sato, T., and Takahashi, M., 1989, "A Study on the Spread of the Rectangular Jets,"*Japanese Society of Mechanical Engineering International Journal*, Ser. II, Vol. 32, No. 1, pp. 11-18.

Viets, H. and Sforza, P. M., 1972, "Dynamics of Bilaterally Symmetric Vortex Rings," *Physics of Fluids*, Vol. 15, No. 2, pp. 230-240.

Weinan, E. and Shu, C.-W., 1992, "A Numerical Resolution Study of High Order Essentially Non-Oscillatory Schemes Applied to Incompressible Flow," ICASE Report 92-39.

Williamson, J., 1980, "Low Storage Runge-Kutta Schemes," *Journal of Computational Physics*, Vol. 35, pp. 48-56.

Wilson, R. V., 1993, Numerical Simulation of Two-Dimensional, Spatially Developing Mixing Layers. Masters Thesis, Old Dominion University.

Wilson, R. V. and Demuren, A. O., 1996, "Two-Dimensional Spatially-Developing Mixing Layers," *Numerical Heat Transfer.*, Part A, Vol. 29, pp. 485-509.

Zaman, K. B. M. Q., 1996, "Axis Switching and Spreading of an Asymmetric Jet: The Role of Coherent Structure Dynamics," *Journal of Fluid Mechanics*, Vol. 316, pp. 1-27.